HYBRID FEEDBACK CONTROL FOR AUTONOMOUS ROBOT NAVIGATION WITH OBSTACLE AVOIDANCE

Spine title: Hybrid Feedback Control for Autonomous Robot Navigation with Obstacle Avoidance

(Thesis format: Monograph)

by

Mayur Sawant

Graduate Program
in
Department of Electrical and Computer Engineering

A thesis submitted in partial fulfillment
of the requirements for the degree of
Doctor of Philosophy (Ph.D.)

The School of Graduate and Postdoctoral Studies
The University of Western Ontario
London, Ontario, Canada

THE UNIVERSITY OF WESTERN ONTARIO
School of Graduate and Postdoctoral Studies

CERTIFICATE OF EXAMINATION

Examiners:

Supervisor:

Prof. Ricardo Sanfelice

Prof. Abdelhamid Tayebi

Prof. Meherdad Kermani

Co-Supervisor:

.....
Dr. Ilia Polushin

Dr. Yili Tang

Prof. Pei Yu

The thesis by

Mayur Sanjay Sawant

entitled:

Hybrid Feedback Control for Autonomous Robot Navigation with Obstacle Avoidance

is accepted in partial fulfillment of the
requirements for the degree of
Doctor of Philosophy (Ph.D.)

.....
Date

.....
Chair of the Thesis Examination Board

Abstract

This thesis provides some hybrid feedback based autonomous navigation algorithms. First, the problem of autonomous robot navigation in planar environments with arbitrarily-shaped convex obstacles is considered. The proposed navigation approach guarantees safe and global convergence to the target location through an appropriately designed switching strategy between two different modes, namely, the *move-to-target* mode and the *obstacle-avoidance* mode. A procedure for the implementation of the proposed hybrid feedback controller in *a priori* unknown environments is provided.

Subsequently, the problem of autonomous navigation in planar environments with non-convex obstacles is considered. An instrumental transformation that modifies (virtually) the non-convex obstacles, in a non-conservative manner, is introduced to facilitate the design of the obstacle-avoidance strategy. The proposed autonomous robot navigation scheme relies on a switching strategy between the *move-to-target* mode and the *obstacle-avoidance* mode. When initialized in the *move-to-target* mode, the proposed feedback control law guarantees safe and global convergence to the predefined target location in the modified obstacle-free workspace. The proposed controller has been successfully implemented in *a priori* unknown environments on the Turtlebot3 burger model in the Gazebo simulator using the ROS framework.

Finally, the problem of autonomous navigation in three-dimensional environments with arbitrarily-shaped convex obstacles is addressed. The proposed hybrid feedback control strategy, which consists in switching between the *move-to-target* and the *obstacle-avoidance* modes, guarantees safe and global autonomous robot navigation. A procedure for the implementation of the proposed autonomous navigation controller, in *a priori* unknown three-dimensional environments, is also provided.

Summary for Lay Audience

This thesis deals with the design of control algorithms allowing to safely guide a robot from any initial location to any target location in a given workspace. We consider three types of environments: two-dimensional environments with convex obstacles, two dimensional environments with arbitrarily shaped obstacles (possibly non-convex), and three-dimensional environments with arbitrarily shaped convex obstacles. The proposed control algorithms can also be implemented in *a priori* unknown environments, relying solely on information obtained from the sensors mounted on the robot.

To all those whom I love...

Acknowledgements

I would like to express my deepest gratitude to my supervisor, Prof. Abdelhamid Tayebi, for his unwavering support, motivation, and guidance throughout my academic journey. Prof. Tayebi's mentorship, timely feedback, and valuable suggestions have been instrumental in shaping my research and completing my thesis. His commitment to excellence and passion for research have been a constant source of inspiration.

I extend my thanks to my co-supervisor, Dr. Ilia Polushin, for his guidance and support, contributing significantly to the success of my research. I also want to acknowledge the invaluable contributions of my advisory committee members, Dr. Mehrdad R. Kermani and Prof. Rajni Patel, for their constructive comments and feedback on my work.

Special appreciation goes to Dr. Miaomiao Wang for his senior support, which has played a crucial role in my academic and research endeavors. I am grateful for the insightful discussions, encouragement, and support from my friends Vidhyaganesh Rangarajan, Mushtaque Shaikh, Nikita Thakur, and Komal Salgaonkar who have been part of this journey with me.

Lastly, I want to express my heartfelt thanks to my family for their unwavering support and encouragement. Their love and understanding have been my pillars of strength. This journey would not have been possible without their support.

Contents

Certificate of Examination ii

Abstract iii

Summary for Lay Audience iv

Acknowledgements vi

List of Figures xi

List of Symbols xvi

1 Introduction 1
- 1.1 Literature review . . . 2
  - 1.1.1 Collision-free path planning approach . . . 3
  - 1.1.2 Feedback-based approach . . . 4
- 1.2 Thesis contributions . . . 10
- 1.3 List of publications . . . 11
- 1.4 Thesis outline . . . 11

2 Background and Preliminaries 13
- 2.1 General notations . . . 13
- 2.2 Projection maps . . . 14
  - 2.2.1 Projection on a set . . . 14
  - 2.2.2 Sets with positive reach . . . 14
- 2.3 Geometric subsets of $\mathbb{R}^n$ . . . 14
  - 2.3.1 Line . . . 14
  - 2.3.2 Line segment . . . 15
  - 2.3.3 Hyperplane . . . 15
  - 2.3.4 Supporting hyperplane . . . 15
  - 2.3.5 Convex cone . . . 15
  - 2.3.6 Conic hull . . . 15
  - 2.3.7 Tangent cone and normal cone . . . 16
- 2.4 Hybrid system framework . . . 16
- 2.5 Preliminary lemmas . . . 17

3 Autonomous Navigation in Planar Environments with Convex Obstacles **19**
3.1 Introduction . . . 19
3.2 Problem formulation . . . 21
3.3 Hybrid control for obstacle avoidance . . . 22
3.3.1 Hybrid control law . . . 22
3.3.2 Geometric construction of the flow and jump sets . . . 24
Back region . . . 24
Gates . . . 24
Front region . . . 25
Side regions . . . 25
Flow and jump sets (*move-to-target* mode) . . . 25
Flow and jump sets (*obstacle-avoidance* mode) . . . 26
3.3.3 Mode selection map $\mathbf{L}(\mathbf{x}, m)$ . . . 27
3.4 Forward invariance and stability analysis . . . 28
3.5 Sensor-based implementation procedure . . . 32
3.6 Simulation results . . . 36
3.7 Conclusions . . . 41

4 Autonomous Navigation in Planar Environments with Non-Convex Obstacles **44**
4.1 Introduction . . . 44
4.2 Problem formulation . . . 45
4.3 Obstacle reshaping . . . 48
4.4 Hybrid control for obstacle avoidance . . . 54
4.4.1 Hybrid control design . . . 55
4.4.2 Geometric construction of the flow and jump sets . . . 56
Flow and jump sets (move-to-target mode) . . . 59
Flow and jump sets (*obstacle-avoidance* mode) . . . 59
4.4.3 Update law $\mathbf{L}(\mathbf{x}, \mathbf{h}, m)$ . . . 62
4.5 Stability analysis . . . 63
4.6 Sensor-based implementation procedure . . . 66
4.6.1 Switching to the *obstacle-avoidance* mode . . . 67
4.6.2 Moving in the *obstacle-avoidance* mode . . . 69
4.6.3 Switching to the *move-to-target* mode . . . 70
4.7 Simulation results . . . 70
4.7.1 Gazebo simulation . . . 74
4.8 Conclusions . . . 79

5 Autonomous Navigation in Environments with Three-dimensional Convex Obstacles **80**
5.1 Introduction . . . 80
5.2 Problem formulation . . . 82
5.3 Hybrid control for obstacle avoidance . . . 83
5.3.1 Hybrid control design . . . 83

5.3.2 Geometric construction of the flow and jump sets 84
Flow and jump sets (*move-to-target* mode) 85
Flow and jump sets (*obstacle-avoidance* mode) 86
5.3.3 Update law $\mathbf{L}(\mathbf{x}, \mathbf{h}, \mathbf{a}, m)$ 87
5.4 Stability analysis 89
5.5 Application to sphere worlds 90
5.6 Implementation procedure 92
5.7 Simulation results 94
5.8 Conclusions 96

6 Conclusions **99**
6.1 Summary 99
6.2 Perspective 100

Bibliography **101**

A Proofs of Chapter 2 **107**
A.1 Proof of Lemma 2.1 107
A.2 Proof of Lemma 2.2 107
A.3 proof of Lemma 2.3 108

B Proofs of Chapter 3 **109**
B.1 Proof of Lemma 3.1 109
B.2 Proof of Lemma 3.2 109
B.3 Proof of Lemma 3.3 111
B.4 Proof of Lemma B.1 113
B.5 Proof of Theorem 3.1 117
B.5.1 Proof of Lemma B.3 120
B.5.2 Proof of Lemma B.4 121
B.6 Proof of Proposition 3.1 122

C Proofs of Chapter 4 **124**
C.1 Proof of Lemma 4.1 124
C.2 Proof of Lemma 4.2 124
C.3 Proof of Lemma 4.3 125
C.4 Proof of Lemma 4.4 125
C.5 Proof of Lemma 4.5 126
C.5.1 Proof of claim 1 126
C.5.2 Proof of claim 2 129
C.6 Proof of Lemma 4.6 130
C.7 Proof of Lemma 4.7 130
C.8 Proof of Theorem 4.1 132
C.8.1 Proof of Lemma C.1 133
C.9 Proof of Proposition 4.1 134

D Proofs of Chapter 5 **135**

D.1 Proof of Lemma 5.1 135
D.2 Proof of Lemma 5.2 135
D.3 Proof of Lemma 5.3 136
D.4 Proof of Theorem 5.1 138
D.4.1 Proof of Lemma D.1 139
D.5 Proof of Theorem 5.2 143

List of Figures

1.1 The robot initialized at the origin (green dot) moving towards the target location (red dot) according to the negative gradient of the APF. The left figure shows safe convergence of the robot to the target location. The right figure illustrates the presence of undesired stable local minima. 5

1.2 The effect of the tuning parameter κ on the critical points of the navigation function φ given in (1.1). The left figure shows the presence of undesired stable local minima for $\kappa = 2$. The right figure shows the absence of undesired stable local minima for $\kappa = 4$. 6

1.3 The robot trajectory obtained using navigation function-based approach proposed in [Koditschek and Rimon, 1990]. 7

1.4 The left figure illustrates the process behind the construction of the local obstacle-free neighbourhood, represented by the shaded green color, using separating hyperplanes. The right figure provides a representation of the obstacle curvature assumption [Arslan and Koditschek, 2019, Assumption 2]. Obstacles $\mathcal{O}_1$ and $\mathcal{O}_3$ satisfy the assumption, whereas obstacle $\mathcal{O}_2$ does not. 8

1.5 Trajectories of a point robot obtained using the separating hyperplane-based approach [Arslan and Koditschek, 2019]. The left figure shows the trajectories of a point robot from 8 different locations (diamond symbols), converging to the target location at the origin. The right figure illustrates the presence of undesired local minima near the obstacles that do not satisfy the curvature condition. 9

3.1 Workspace $\mathcal{W}$ with two convex obstacles separated by the distance greater than or equal to $2(r_a + \gamma)$. The $\gamma-$neighbourhood of dilated obstacles is further partitioned into three region such that $\gamma > \gamma_s > \gamma_a > 0$. 21

3.2 Partitions of the local neighbourhood of obstacle $\mathcal{O}_i,\ i \in \mathbb{I}$ based on the location of the target. 24

3.3 Geometric representations of the flow and jump sets for different modes of operation related to obstacle $\mathcal{O}_i$, $i \in \mathbb{I}$. The left figures ($m = 0$) illustrate the case where the robot operates in the *move-to-target* mode and moves straight toward the target location. The middle figures ($m = -1$) illustrate the case where the robot, operating in the *obstacle-avoidance* mode, moves in the counter-clockwise direction with respect to $\partial\mathcal{O}_i$. The right figures ($m = 1$) illustrate the case where the robot, operating in the *obstacle-avoidance* mode, moves in the clockwise direction with respect to $\partial\mathcal{O}_i$. 27
3.4 The left figure shows a robot, with radius $r = 0.5m$, using a range-bearing sensor to locate the partial boundary of the obstacles within the sensing range $R_s = 2.5m$, wherein observed boundary of the nearest obstacle is shown in green and the observed boundaries of the remaining obstacles are represented by the blue colored curves. The right figure displays the range measurements obtained with a sensor located at $\mathbf{x}$ for $\theta \in [-\pi, \pi]$. Similar colors have been used to represent the correlation between the points on the boundary of the observed obstacles (left figure) and the rang/bearing measurements (right figure). 34
3.5 Construction of the rectangle $\square(\mathbf{x})$, used in (3.42), based on the location of the robot and the target location at the origin. 35
3.6 Robot safely navigating towards the target (red dot), along with three intermediate locations along the path. 38
3.7 Robot trajectories starting from different locations. 39
3.8 Trajectory of a robot, equipped with a range-bearing sensor, converging safely to the target location at the origin. The sensor measurements are affected by a Gaussian noise of 0 mean and $50mm$ standard deviation. . . 39
3.9 Distance of the center of the robot from the boundary of the obstacle occupied workspace as the robot converges to the target location. 40
3.10 The left figure represents the robot trajectories obtained using the sensor-based separating hyperplane approach [Arslan and Koditschek, 2019] showing the presence of stable undesired equilibria. The right figure presents the robot trajectories converging to the target location under the proposed hybrid navigation scheme. 41
3.11 The left figure shows the robot trajectories obtained using the hyperplane approach [Arslan and Koditschek, 2019]. The right figure shows the robot trajectories obtained using our proposed sensor-based hybrid feedback approach. 42
3.12 The left figure illustrates an obstacle-occupied workspace $\mathcal{O}_\mathcal{W} = \mathcal{O}_1 \cup \mathcal{O}_2$ that satisfies Assumption 3.1. The right figure depicts an obstacle-occpuied workspace that does not satisfy Assumption 3.1 43

4.1 Two examples of workspaces that do not satisfy Assumption 4.1. 46
4.2 (a) The original obstacle $\mathcal{O}_i \subset \mathbb{R}^2$. (b) Dilation of obstacle $\mathcal{O}_i$ by a structuring element $\mathcal{B}^\circ_\alpha(\mathbf{0}), \alpha > 0$. (c) Erosion of the dilated obstacle $\mathcal{O}_i \oplus \mathcal{B}^\circ_\alpha(\mathbf{0})$ by the same structuring element $\mathcal{B}^\circ_\alpha(\mathbf{0})$. 47

4.3 Workspace with two obstacles $\mathcal{O}_{\mathcal{W}} = \mathcal{O}_i \cup \mathcal{O}_j$ such that $d(\mathcal{O}_i, \mathcal{O}_j) < 2\alpha$. Left figure shows that the set $\mathcal{O}_{\mathcal{W}}^M$ is not a connected set. Right figure shows that the set $\mathcal{O}_{\mathcal{W}}^M$ is a connected set. 50

4.4 Workspace with two obstacle $\mathcal{O}_{\mathcal{W}} = \mathcal{O}_i \cup \mathcal{O}_j$ such that $d(\mathcal{O}_i, \mathcal{O}_j) < 2\alpha$. (a) $\mathcal{O}_{\mathcal{W}}$ does not satisfy Assumption 4.2. (b) $\mathcal{O}_{\mathcal{W}}$ satisfies Assumption 4.2. 51

4.5 Left figure shows the original obstacle $\mathcal{O}_i \subset \mathbb{R}^2$. Middle figure shows the modified obstacle $\mathcal{O}_i^M = \mathbf{M}(\mathcal{O}_i, \alpha)$ obtained using (4.4). Right figure shows the convex hull $\text{conv}(\mathcal{O}_i)$ for the obstacle $\mathcal{O}_i$. 52

4.6 The left figure shows an original workspace where a feasible path exists from location $\mathbf{x}$ to the origin. The right figure shows the modified workspace obtained using (4.4) with some $\alpha > r_a$, where there is no feasible path from the location $\mathbf{x}$ to the origin. 53

4.7 An obstacle-occupied workspace $\mathcal{O}_{\mathcal{W}}$ with three obstacles $\mathcal{O}_i, \mathcal{O}_j$ and $\mathcal{O}_k$, and the boundary of the modified obstacle $\mathcal{O}_{i,\alpha}^M$ obtained using a virtual ring with radius α, where $\mathcal{O}_{i,\alpha} = \mathcal{O}_i \cup \mathcal{O}_j \cup \mathcal{O}_k$, see (4.7). A video can be seen here https://youtu.be/mylrTOtYOSY 54

4.8 The left figure shows the partitioning of the region $\mathcal{N}_\gamma(\mathcal{D}_{r_a}(\mathcal{O}_i^M))$ into the *landing* region $\mathcal{R}_l = \mathcal{R}_{l,1} \cup \mathcal{R}_{l,2} \cup \mathcal{R}_{l,3}$, and the *exit* region $\mathcal{R}_e = \mathcal{R}_{e,1} \cup \mathcal{R}_{e,2} \cup \mathcal{R}_{e,3}$, using (4.12) and (4.14). The right figure shows the partitioning of the *exit* region into three sub-regions namely the *always exit* region $\mathcal{R}_a$, the *clockwise exit* region $\mathcal{R}_1$, and the *counter-clockwise exit* region $\mathcal{R}_{-1}$, using (4.15), (4.17) and (4.18), respectively. 56

4.9 Partitions of the neighbourhood of the modified obstacle $\mathcal{O}_{i,\alpha}^M$ based on the value of the inner product between the two vectors $-\mathbf{x}$ and $\mathbf{x} - \Pi(\mathbf{x}, \mathcal{O}_{i,\alpha}^M)$ and the tangent cone to the set $\mathcal{D}_{d(\mathbf{x},\mathcal{O}_{i,\alpha}^M)}(\mathcal{O}_{i,\alpha}^M)$ at $\mathbf{x}$. (a) The vector $-\mathbf{x}$ is pointing inside the tangent cone. (b) The vector $-\mathbf{x}$ is pointing outside the tangent cone. 57

4.10 Effects of ϵ, used in (4.22), on the construction of the sets $\mathcal{ER}_m^{\mathbf{h}}$, for $m \in \{-1, 1\}$ and a *hit point* $\mathbf{h} \in \mathcal{J}_0^{\mathcal{W}}$. The left figure shows that when $\epsilon = \epsilon_1$, the sets $\mathcal{ER}_m^{\mathbf{h}}, m \in \{-1, 1\}$, are non-empty. The right figure shows that when $\epsilon = \epsilon_2$, the sets $\mathcal{ER}_m^{\mathbf{h}}, m \in \{-1, 1\}$, are empty. 60

4.11 Flow and jump sets $\mathcal{F}_m^{\mathcal{W}}$, $\mathcal{J}_m^{\mathcal{W}}$, related to the set $\mathcal{O}_{i,\alpha}$ shown in Fig. 4.8. The left figure ($m = 0$) illustrates the case where the robot operates in the *move-to-target* mode and moves straight toward the target location. The middle figure ($m = 1$) illustrates the case where the robot, operating in the *obstacle-avoidance* mode, moves in the clockwise direction with respect to $\partial\mathcal{O}_{i,\alpha}^M$. The right figure ($m = -1$) illustrates the case where the robot, operating in the *obstacle-avoidance* mode, moves in the counter-clockwise direction with respect to $\partial\mathcal{O}_{i,\alpha}^M$. 61

4.12 The left figure illustrates a case in which the robot, operating in the *obstacle-avoidance* mode, moves initially in the clockwise direction from $\mathbf{h}_1$ to $\mathbf{l}_1$, and then in the counter-clockwise direction from $\mathbf{h}_2$ to $\mathbf{l}_2$ with respect to the nearest point on the modified obstacle $\mathcal{O}_{i,\alpha}^M$. The right figure illustrates a case in which the robot, operating in the *obstacle-avoidance* mode, moves in the clockwise direction with respect to the nearest point on the modified obstacle $\mathcal{O}_{i,\alpha}^M$. 62

4.13 Construction of the rectangle $\square(\mathbf{x}, \mathbf{0})$ based on the location of the robot and the target location at the origin. 68

4.14 Illustration of two possible situations that can occur when the robot, while operating in the *move-to-target* mode, enters in the $\beta-$neighbourhood of obstacles $\mathcal{O}_{\mathcal{W}}$, for some $\beta \in (r_a, \alpha)$. (a) When $\mathbf{card}(\mathcal{PJ}(\mathbf{x}, \mathcal{O}_{\mathcal{W}})) = 1$. (b) When $\mathbf{card}(\mathcal{PJ}(\mathbf{x}, \mathcal{O}_{\mathcal{W}})) > 1$. 69

4.15 A scenario in which, for the robot operating in the *obstacle-avoidance* mode, the virtual ring $\partial\mathcal{B}_{v_r}(\mathbf{c})$ encounters more than one intersection point with the obstacle-occupied workspace $\mathcal{O}_{\mathcal{W}}$ *i.e.*, $\mathbf{card}(\mathcal{PJ}(\mathbf{c}, \mathcal{O}_{\mathcal{W}})) > 1$. . . 70

4.16 Trajectory of a robot, initialized at $\mathbf{x}_0$, safely converging to the target location at the origin, while avoiding non-convex obstacles. 73

4.17 Distance of the robot's center from the boundary of the obstacle-occupied workspace for the simulation results shown in Fig. 4.16. 74

4.18 Robot trajectories starting from different locations 75

4.19 Robot safely navigating towards the target (red dot) in an environment that does not satisfy Assumption 4.2 76

4.20 Autonomous navigation of the Turtlebot in non-convex environment. . . 78

5.1 Geometrical representation of the *landing* region and the *exit* region. . . 85

5.2 The left figure depicts the set $\mathcal{N}_\gamma(\mathcal{D}_{r_a}(\mathcal{O}_i)) \cap \mathcal{P}(\mathbf{h}, \mathbf{a}) \cap \mathcal{P}_{\geq}(\mathbf{0}, \mathbf{R}(\mathbf{a})\mathbf{c}_i)$, shaded in a dark blue color. The right figure shows the direction of the modified obstacle-avoidance control vector, $\mathbf{v}_s(\mathbf{x}, \mathbf{a})$, at $\mathbf{x} \in \mathcal{N}_\gamma(\mathcal{D}_{r_a}(\mathcal{O}_i)) \cap \mathcal{P}(\mathbf{h}, \mathbf{a}) \cap \mathcal{P}_{\geq}(\mathbf{0}, \mathbf{R}(\mathbf{a})\mathbf{c}_i)$. 91

5.3 Trajectory of the robot safely converging to the origin. 95

5.4 Robot trajectories starting from different locations. 96

5.5 Distance of the center of the robot $\mathbf{x}$ from the boundary of the obstacle occupied workspace $\mathcal{O}_{\mathcal{W}}$. 97

5.6 Robot trajectories safely navigating around spherical obstacles and converging to the target location at the origin. 97

5.7 The left figure shows the change in the distance between the robot $\mathbf{x}$ and the boundary of the obstacle-occupied workspace $\mathcal{O}_{\mathcal{W}}$. The right figure shows monotonic decrease of the distance between the robot $\mathbf{x}$ and the target location at the origin. 98

B.1 Illustration of a robot trajectory (blue curve) not intersecting the half-line $\mathcal{L}_{>}(\mathbf{0}, \nu_{-1}(\mathbf{s}))$ (red line) while operating in the *obstacle-avoidance* mode in the flow set $\mathcal{F}_1^k \times \{1\} \times \{k\}$. The velocity vector at the current location of the robot (green dot) always points to the positive half-space $\mathcal{P}_{\geq}(\mathbf{0}, \nu_1(\mathbf{x}))$ (shaded blue region). 113
B.2 The geometric representation of the *obstacle-avoidance* mode flow set $\mathcal{F}_1^k$ related to an obstacle $\mathcal{O}_k, k \in \mathbb{I}$. The left figure shows the partitions of the set $\partial\mathcal{F}_1^k$. The right figure depicts the partitions of the set $\mathcal{F}_1^k$. 114
B.3 1) Trajectory $\mathbf{x}(t)$ starting from $\mathbf{x}_1$, illustrates the property stated in (B.18) *i.e.,* with consecutive intersections with the half-line $\mathcal{L}_{>}(\mathbf{0}, \nu_1(\mathbf{s}))$, the state $\mathbf{x}$ approaches towards the origin. 2) Trajectory $\mathbf{x}(t)$ starting from $\mathbf{x}_2$, does not intersect with the half-line $\mathcal{L}_{>}(\mathbf{0}, \nu_{-1}(\mathbf{s}))$, as $\mathbf{x}(0,0) \notin \mathcal{M}_0$ and $m(0,0) = 0$, as per Lemma 3.3. 118

C.1 Illustration of the case where $\mathbf{x} \in \partial\mathcal{W}_\alpha$ and $\mathbf{p} \in \mathcal{W}_\alpha$ such that $\mathbf{p} - \mathbf{x} \notin \mathbf{T}_{\mathcal{W}_\alpha}(\mathbf{x})$. 125
C.2 The diagrammatic representation for the Case A in the proof of Lemma 4.5. (a) $d(\mathbf{0}, \mathcal{O}_{i,\alpha}^M) \geq \beta$, (b) $r_a < d(\mathbf{0}, \mathcal{O}_{i,\alpha}^M) < \beta$. 127
C.3 The diagrammatic representation for the Case B in the proof of Lemma 4.5. (a) $d(\mathbf{0}, \mathcal{O}_{i,\alpha}^M) \geq \beta$, (b) $r_a < d(\mathbf{0}, \mathcal{O}_{i,\alpha}^M) < \beta$. 128

D.1 The partition of the set $\mathcal{N}_\gamma(\mathcal{D}_{r_a}(\mathcal{O}_i)) \cap \mathcal{P}(\mathbf{h}, \mathbf{a})$. 141

List of Symbols

- $\mathbb{N}$ denotes the set of natural numbers.
- $\mathbb{R}, \mathbb{R}_{\geq 0}$ and $\mathbb{R}_{>0}$ denote the set of real, non-negative real and positive real numbers, respectively.
- $\mathbb{R}^n$ is the set of $n-$dimensional vectors.
- $\mathbb{R}^{n\times m}$ is the set of real-valued $n \times m$ matrices.
- $\mathbf{I}_n$ denotes $n-$dimensional Identity matrix.
- $A^\top$ denotes the transpose of matrix $A \in \mathbb{R}^{n\times m}$.
- $\|\mathbf{x}\|$ represents the Euclidean norm of vector $\mathbf{x} \in \mathbb{R}^n$.
- $\mathcal{B}_r(\mathbf{p}) := \{\mathbf{x} \in \mathbb{R}^n | \|\mathbf{x} - \mathbf{p}\| \leq r\}$ is the Euclidean ball of radius $r > 0$, centered at $\mathbf{p} \in \mathbb{R}^n$.
- $\mathbb{S}^n := \{\mathbf{x} \in \mathbb{R}^{n+1} | \|\mathbf{x}\| = 1\}$ is the unit $n-$sphere embedded in $\mathbb{R}^{n+1}$.
- $\mathsf{SO}(3) := \{R \in \mathbb{R}^{3\times 3} | \mathbf{det}(R) = 1, RR^\top = R^\top R = \mathbf{I}_3\}$ is the Special Orthogonal group of order 3 where $\mathbf{I}_3$ denotes the three-dimensional identity matrix.
- $\mathcal{A} \oplus \mathcal{B} := \{\mathbf{a} + \mathbf{b} | \mathbf{a} \in \mathcal{A}, \mathbf{b} \in \mathcal{B}\}$ represents the dilation of $\mathcal{A}$ by $\mathcal{B}$, where $\mathcal{A} \subset \mathbb{R}^n$ and $\mathcal{B} \subset \mathbb{R}^n$.
- $\mathcal{A} \ominus \mathcal{B} := \{\mathbf{x} \in \mathbb{R}^n | \mathbf{x} + \mathbf{b} \in \mathcal{A}, \forall \mathbf{b} \in \mathcal{B}\}$ represents the erosion of $\mathcal{A}$ by $\mathcal{B}$, where $\mathcal{A} \subset \mathbb{R}^n$ and $\mathcal{B} \subset \mathbb{R}^n$.
- $\mathcal{D}_r(\mathcal{A}) = \mathcal{A} \oplus \mathcal{B}_r(\mathbf{0})$ represents the $r-$dilated version of the set $\mathcal{A}$, where $r \in \mathbb{R}_{\geq 0}$ and $\mathcal{A} \subset \mathbb{R}^n$.
- $\mathcal{N}_r(\mathcal{A}) = \mathcal{D}_r(\mathcal{A}) \setminus \mathcal{A}^\circ$ denotes the $r-$neighborhood of the set $\mathcal{A}$, where $r \in \mathbb{R}_{>0}$ and $\mathcal{A} \subset \mathbb{R}^n$.
- $d(\mathbf{x}, \mathcal{A}) = \min_{\mathbf{q}\in\mathcal{A}} \|\mathbf{x} - \mathbf{q}\|$ denotes the Euclidean distance of $\mathbf{x}$ from the closed set $\mathcal{A}$, where $\mathbf{x} \in \mathbb{R}^n$ and $\mathcal{A} \subset \mathbb{R}^n$.
- $\mathcal{PJ}(\mathbf{x}, \mathcal{A}) := \{\mathbf{q} \in \mathcal{A} | \|\mathbf{x} - \mathbf{q}\| = d(\mathbf{x}, \mathcal{A})\}$ is the set of all locations from the set $\mathcal{A} \subset \mathbb{R}^n$ that are closest to the point $\mathbf{x} \in \mathbb{R}^n$.

- $\mathcal{L}_s(\mathbf{p}, \mathbf{q}) := \{\mathbf{x} \in \mathbb{R}^n | \mathbf{x} = \lambda\mathbf{p} + (1-\lambda)\mathbf{q}, \lambda \in [0,1]\}$ is the line segment joining $\mathbf{p}$ and $\mathbf{q}$, where $\mathbf{p} \in \mathbb{R}^n$ and $\mathbf{q} \in \mathbb{R}^n$.
- $\mathcal{P}(\mathbf{p}, \mathbf{q}) := \{\mathbf{x} \in \mathbb{R}^n | \mathbf{q}^\top(\mathbf{x} - \mathbf{p}) = 0\}$ is the hyperplane passing through $\mathbf{p}$ and orthogonal to $\mathbf{q}$, where $\mathbf{p} \in \mathbb{R}^n$ and $\mathbf{q} \in \mathbb{R}^n \setminus \{\mathbf{0}\}$.
- $\psi(\mathbf{p}, \mathbf{q})$ denotes the angle measured from the vector $\mathbf{p}$ to $\mathbf{q}$, where the measurement in the counterclockwise direction is considered positive.
- $\mathbf{P} : \mathbb{R}^3 \to \mathbb{R}^{3\times3}$, $\mathbf{P}(\mathbf{a}) := \mathbf{I}_3 - \mathbf{a}\mathbf{a}^\top/\|\mathbf{a}\|^2$ is the orthogonal projection operator.

Chapter 1

Introduction

The ongoing developments in the field of self-driving vehicles, swarm robotics and humanoid robotics have surged research interests in the domain of autonomous robotics. Autonomous robots with various features are being developed for a multitude of applications such as nurse robots for patient care [Tanioka et al., 2017], autonomous underwater vehicles (AUVs) for marine life exploration [Leonard and Bahr, 2016], unmanned aerial vehicles (UAVs) for remote surveillance [Jain et al., 2021] and package delivery [Mehndiratta et al., 2018], autonomous ground vehicles (AGVs) for public transport [Poczter et al., 2014], to name a few. Depending upon the nature of the application, mobile robots can be used to perform various tasks such as trajectory tracking, rendezvous, formation control, coverage control, boundary patrol, *etc.* However, most of these complex tasks can be boiled down to a sequence of point navigation problems wherein given an initial and a final location within an obstacle-free space, the robot has to navigate towards the destination without colliding with the obstacles and the other robots in the environment.

There have been a considerable amount of literature dedicated towards solving this navigation problem, with configuration space motion planning [Choset et al., 2005] being among the earliest. Here, the configuration of a robot corresponds to its location and orientation at any given instant of time. With an explicit representation of the robot's configuration space, several planning and control schemes such as those based on the exact cell decomposition approaches [LaValle, 2006], [Boissonnat and Yvinec, 1998] are used to safely navigate the robot towards its destination. However, obtaining the exact description of the configuration space in terms of standard geometric models is a difficult task. On the other hand, approximate decomposition techniques such as slice projection (SP) [Lozano-Perez, 1990] and hierarchical approximate cell decomposition (HACD) [Brooks and Lozano-Perez, 1985], avoid this issue by constructing an approximation of the configuration space as a union of simpler geometric shapes such as hyper-rectangles and polytopes, at the expense of accuracy and completeness. Sampling-based motion planning techniques [Kavraki et al., 1996], [LaValle, 1998] provide an alternative solution to circumvent the aforementioned issue since they require an implicit definition of the configuration space, which is generally much easier to obtain. These path planning methodologies provide a feasible path that has to be tracked, as closely as possible, by another feedback control scheme. On the other hand, feedback-based autonomous naviga-

tion strategies can simultaneously handle the path-finding and path-following tasks. The feedback-based autonomous navigation approach relying on the artificial potential field (APF), originally introduced in [Khatib, 1986], is one of the most popular approaches in mobile robotics. However, it suffers from the well-known problem of undesired local minima. In [Koditschek and Rimon, 1990], [Koditschek and Rimon, 1992], the authors proposed a class of APF-based controllers, relying on some appropriately designed navigation functions (NF), which with a proper parameter tuning can overcome the drawbacks of the APF approach and lead to a safe and almost[1] global asymptotic convergence to the target location. The original work was limited to the navigation of a point-mass robot, in a sphere world [2] assuming perfect knowledge of the environment. Since then there have been considerable developments in the field of robot navigation using NFs. Alternatively, some research works such as those in [Arslan and Koditschek, 2019], [Berkane et al., 2021a] address the robot navigation problem with collision avoidance, without an explicit design of the navigation function, instead they exploit the topological properties of the environment to provide a navigation control scheme.

Most of the available research work dealing with feedback-based autonomous navigation, with collision avoidance, assume either global information availability [Koditschek and Rimon, 1992], [Berkane et al., 2021a] or obstacles with simple geometries [Lionis et al., 2007], [Vrohidis et al., 2018]. Another deficiency of the NF-based robot navigation approach is that it does not guarantee global convergence due to the undesired unstable equilibria it generates [Koditschek and Rimon, 1990]. Moreover, their extensions to a multi-robot environment cluttered with stationary and\or moving obstacles is challenging.

1.1 Literature review

Autonomous navigation approaches can mainly be classified into two categories, namely, the collision-free path planning based approach and the planning-free feedback-based approach. The first approach, referred to as collision-free path planning based approach, consists of a high-level planning task which generates the collision-free path to be followed by a low-level feedback controller. This approach, is interesting in applications where the vehicle's surrounding environment is static and *a priori* known. The second approach, referred to as the planning-free feedback-based approach, consists in dealing (simultaneously) with the collision avoidance and path following problems as the vehicle moves. This approach allows the integration of the obstacle avoidance task and the low-level control task through environment sensing (or knowledge) feedback. Among this second class, one can find two main sub-classes, namely, the *a priori* known-environment based approach and the reactive sensor based approach. However, there is no result in the literature, providing a sensor-based reactive navigation strategy, with provable global stability guarantees, for robots navigating in unknown environments with arbitrarily shaped static (or dynamic) obstacles.

[1] For all initial conditions except a set of zero Lebesgue measure.

[2] An Euclidean sphere world of dimension n is formed by removing from the interior of a large n-dimensional ball a finite number of non-overlapping smaller balls.

1.1.1 Collision-free path planning approach

In the path planning based approaches, one constructs a roadmap of the obstacle-free space, independent of any particular initial and final configuration of the robot. Then given any valid initial and final configuration of the robot, the roadmap is searched for a feasible path joining these configurations. Depending on the roadmap construction process, these approaches can mainly be subdivided into two categories, *i.e.,* sampling-based approaches and combinatorial approaches. In the case of sampling-based motion planning the main idea is to avoid the explicit construction of the obstacle regions, and instead conduct a search that probes the robot's workspace with a sampling scheme. This probing is enabled by a collision detection module, which the motion planning algorithms consider as a black box. This enables the development of planning algorithms that are independent of the particular geometric models of the obstacles [LaValle, 2006]. This technique includes methodologies such as probabilistic roadmaps (PRMs) [Kavraki et al., 1996] and rapidly exploring random trees (RRTs) [LaValle, 1998]. The PRM approach consists of two distinct phases; a learning phase and a query phase. In the learning phase, the robot's configuration space is sampled for collision-free configurations, which are added as nodes to a graph whose edges correspond to feasible paths between these configurations. These paths are computed using a simple and fast local planner. This graph is referred to as the probabilistic roadmap. In the query phase, any given initial and goal configurations of the robot are connected to two nodes of the roadmap. The roadmap is then searched for a path joining these two nodes [Kavraki et al., 1996]. The randomized sampling technique proposed in [Kavraki et al., 1996], did not consider the effects of configuration-obstacle, which created bottlenecks in the region where configuration obstacles are closely spaced. Several research works have tried to improve the sampling procedure to provide better representation of the obstacle-free configuration space. In [Boor et al., 1999], a Gaussian sampling strategy was proposed that guarantees configurations with a Gaussian distribution around obstacle surfaces. This method has a parameter that controls the distribution and how near the nodes are to the obstacles. In [Yeh et al., 2012], a PRM generation with obstacle-based sampler is proposed to provide uniform distribution of the nodes near the obstacle region. The PRM approach utilizes a local planner to connect different nodes, however for the case of complicated nonholonomic and dynamical systems, a simplistic local planner may be insufficient to establish connection between any given pair of nodes. To that end, the RRTs method, which was originally introduced in [LaValle, 1998], [LaValle and Kuffner Jr, 2001], provides a sampling-based alternative to PRM, allowing one to address the navigation problem for more intricate classes of constrained dynamical systems. In [Karaman and Frazzoli, 2011], the authors have carried out a performance analysis of the quality of the solution returned by the above-mentioned algorithms as a function of the number of samples and provided an optimal variant of the approach. Recently, in [Arslan et al., 2017], a novel sensor-based steering algorithm was designed which used local Voronoi decomposition of the workspace to significantly improve the path planning performance of sampling based algorithms near difficult regions such as narrow passages.

On the other hand, the combinatorial approaches to motion planning find paths through the continuous configuration space without resorting to approximations. Due to

this property, they are alternatively referred to as exact algorithms. In contrast to the sampling-based approach, the motion planning algorithms based on the combinatorial approach can either find a path between two valid configurations, if it exists, otherwise declare that no feasible path is present [LaValle, 2006]. In [Lozano-Pérez and Wesley, 1979], [Brooks and Lozano-Perez, 1985], the authors utilized an approximate cell division technique to develop an algorithm to find the collision-free path between any two obstacle-free robot configurations. If a given cell is partially occupied by the configuration obstacle then it is sub-divided to obtain better approximation of the configuration obstacle-free region. Such hierarchical approximate cell decomposition (HACD) process allows fast exploration of the configuration space. Another approach is the use of slice projection (SP) methodology, presented in [Lozano-Perez, 1987], [Lozano-Perez, 1990], wherein the robot's configuration space is partitioned into slices with respect to a given axis *e.g.*, the robot's orientation and then projecting those slices to obtain safe, lower dimensional under-approximations of the robot's free space. A major advantage of the SP methodology over the HACD methodology is that SP generates, in general, a smaller amount of cells since the geometry represented by a slice does not need to be any further approximated by simpler shapes, although, this comes at the cost of requiring more elaborate techniques, compared to rectangloids, in order to safely navigate within a projected slice.

1.1.2 Feedback-based approach

One of the earliest works in the field of feedback-based autonomous robot navigation is the work by Oussama Khatib [Khatib, 1986]. This approach makes use of an artificial potential function (APF) which is the summation of an attractive potential function with goal location as the global minimum and a repulsive potential function whose value is inversely proportional to the distance between the robot and obstacle-occupied workspace. It was shown that by guiding a robot using the control law of the form of a negative gradient of the APF ensures, in most of the cases, convergence to the desired goal location while avoiding collisions with the obstacles as shown in Fig. 1.1 (left). However, as shown in 1.1 (right), despite its intuitive nature, this class of controllers suffers unavoidably from the presence of unwanted equilibria induced by the workspace's topology and whose region of attraction may not be trivial.

In their seminal work [Koditschek and Rimon, 1990], Rimon and Koditschek presented a family of APFs called Navigation functions (NFs) for point and sphere worlds[3]. The NF proposed in [Koditschek and Rimon, 1990, (1)] is of the following form:

$$\varphi = \frac{\gamma(\mathbf{x})}{(\gamma(\mathbf{x})^{\kappa} + \beta(\mathbf{x}))^{\frac{1}{\kappa}}}, \tag{1.1}$$

where $\mathbf{x} \in \mathbb{R}^n$ is the location of the robot and $\kappa > 0$ is the tuning parameter. In (1.1), $\gamma : \mathbb{R}^n \to \mathbb{R}$ is a convex attractive potential function with the goal location as the global minimum. The repulsive potential function $\beta : \mathbb{R}^n \to \mathbb{R}$ is the product of the Euclidean

[3]An Euclidean sphere world of dimension n is formed by removing from the interior of a large $n-$dimensional ball a finite number of non-overlapping smaller balls

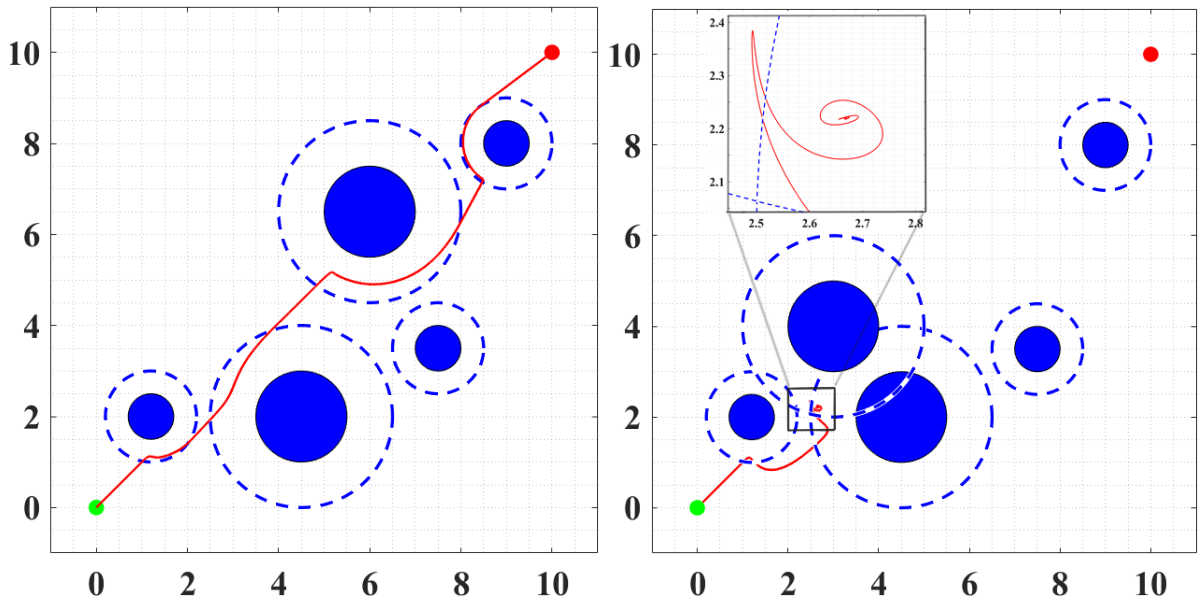

Figure 1.1: The robot initialized at the origin (green dot) moving towards the target location (red dot) according to the negative gradient of the APF. The left figure shows safe convergence of the robot to the target location. The right figure illustrates the presence of undesired stable local minima.

distances between the robot and the workspace obstacles. A properly tuned NF avoids the generation of undesired stable local minima, as illustrated in Fig. 1.2. The figure shows the contour plot of the navigation function φ given in (1.1) that shows no undesired stable minima in the workspace for higher values of κ.

However, NF-based autonomous navigation approaches generate undesired unstable local minima (saddle points). In fact, [Koditschek and Rimon, 1990] demonstrated that in the case of a single point-mass robot navigating in a sphere world, the control law of the form of negative gradient of the NF, with proper tuning of the parameter κ, ensures almost global convergence to the target location, *i.e.,* there exists a set of initial locations, with zero Lebesgue measure, from which the robot gets stuck away from the target location, as depicted in Fig. 1.3.

Later in [Koditschek and Rimon, 1992], the authors presented a constructive transformation for mapping workspace cluttered by trees of star-shaped obstacles[4] into sphere worlds. This extended the applicability of the NF-based autonomous navigation approaches to workspaces containing star-shaped obstacles.

Since then the NF framework has been successfully adapted to resolve the limitations related to the original work such as parameter tuning and global information requirements, and to extend its applicability to more general problem settings involving multiple robots. In [Lionis et al., 2007], [Verginis and Dimarogonas, 2021], the authors proposed the concept of locally computable NF wherein the parameter tuning requirement is removed by restricting the obstacles' influence within their local neighbourhood. In [Filippidis and Kyriakopoulos, 2011], the authors provided the construction of an ad-

[4]A star is a set which possesses a point from which all the rays cross the boundary only once.

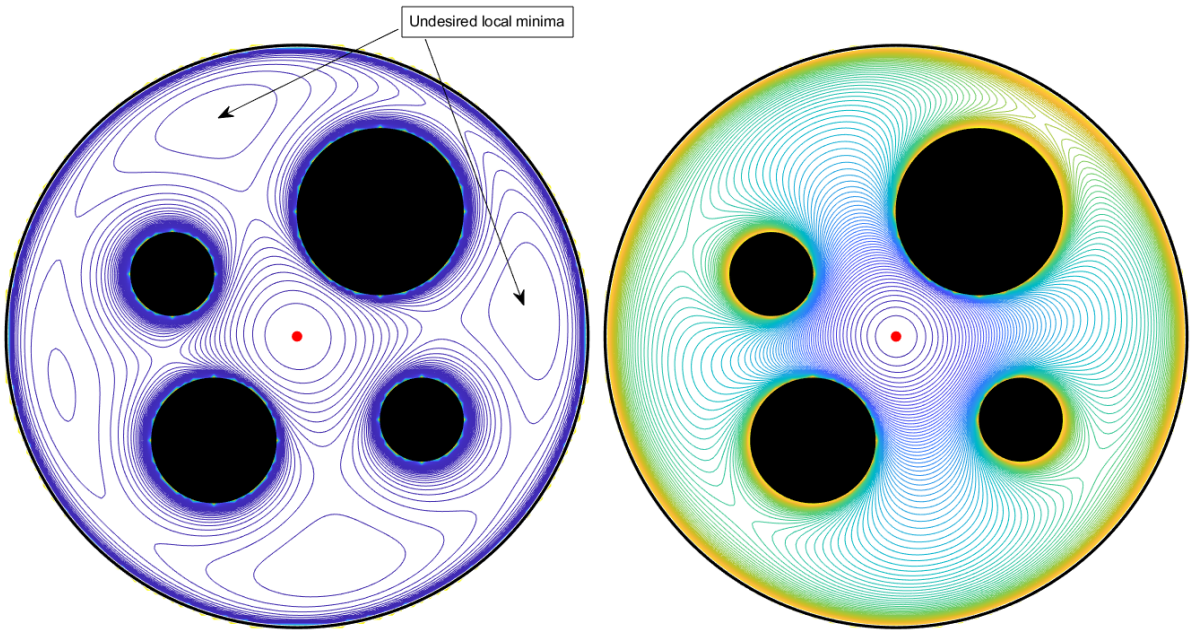

Figure 1.2: The effect of the tuning parameter κ on the critical points of the navigation function φ given in (1.1). The left figure shows the presence of undesired stable local minima for $\kappa = 2$. The right figure shows the absence of undesired stable local minima for $\kappa = 4$.

justable NF, in sphere words, where the robot can update its NF for each new obstacle encountered within a spherical sensing region. This work also extended the applicability of the NF for an unbounded workspace and introduced an online parameter tuning algorithm. In [Filippidis and Kyriakopoulos, 2012], [Filippidis and Kyriakopoulos, 2013], the authors provided a sufficient condition based on the curvature of the obstacle boundary which extended the applicability of NF to obstacles with focally admissible surfaces without the need of a diffeomorphism. It is shown that with a proper parameter tuning, the environment which may not be diffeomorphic to the sphere world but contains obstacles which are sufficiently curved, is almost globally navigable.

Another research work [Paternain et al., 2017], extended the NF-based approach for ellipsoidal obstacles wherein the authors provided a sufficient condition on the eccentricity of the obstacles. However, this methodology is limited to obstacles which are not too flat. Recently, in [Kumar et al., 2022], the authors removed the flatness limitation presented in [Paternain et al., 2017], by providing a controller, in an ellipsoidal world, which locally transforms the region near the obstacle into a spherical region by using the information related to the Hessian of the ellipsoid. In [Sun and Tanner, 2015], the NF-based approach is adapted for the case of a moving target. For a robot operating in a sphere world, governed by double integrator dynamics, with proper parameter tuning, the authors provide almost global convergence guarantees to a circular disk around the moving target, using the control of the form of the negative gradient of the time-varying navigation function. This work was then extended in [Li and Tanner, 2018] to star worlds, wherein the author introduced a novel computationally efficient diffeomorphism between a given

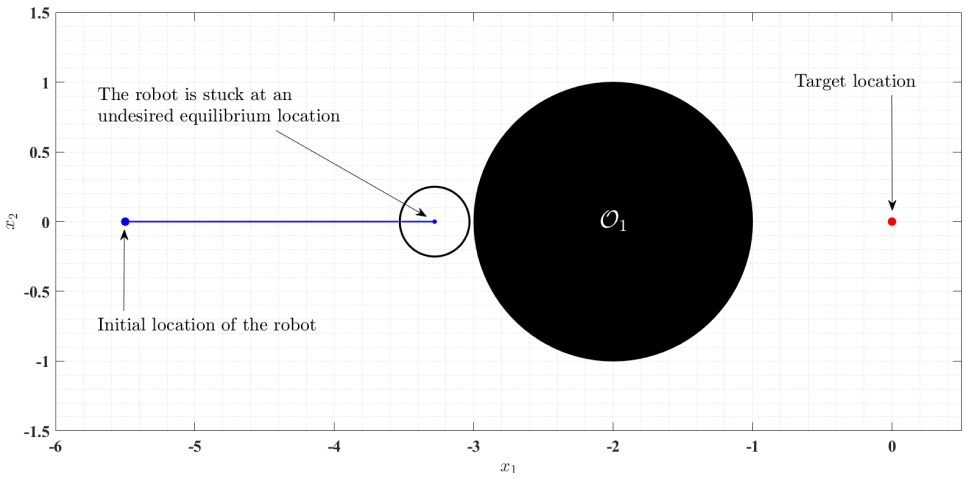

Figure 1.3: The robot trajectory obtained using navigation function-based approach proposed in [Koditschek and Rimon, 1990].

star world and the respective sphere world. Recently, in [Chen et al., 2020], the authors extended the work in [Sun and Tanner, 2015] to the case of moving obstacles in a sphere world satisfying certain workspace validity assumptions.

One of the drawbacks of the above-mentioned NF-based approaches is their inability to abstract the time needed to carry out a navigation task, which restricts one to employ NF-based autonomous navigation strategies in a time critical environment. This issue is tackled in [Loizou, 2011b], [Loizou, 2017], wherein the authors proposed a new concept of navigation transformation which consists in a diffeomorphism which transforms a given sphere world into a point world such that the spherical obstacles are mapped to an isolated set of points. In the point world, the final trajectory between any two locations is simply represented by the line segment joining those two points. This allows one to create time abstracting navigation controllers, for almost all pairs of valid initial and target locations, due to the capability to analytically obtain collision-free distance-to-the-target Euclidean metrics. In [Kim and Khosla, 1992], the authors proposed a harmonic function (HF) based approach for the obstacle avoidance problem for a mobile robot in a known environment. The main idea is to consider a robot as a particle suspended in a fluid with a uniform flow having a sink at the desired target location with source at the boundaries of the obstacles. In [Loizou, 2011a], the authors provided a methodology for the design of a harmonic potential-based NF, with almost global convergence properties, in *a priori* known environments which are diffeomorphic to the point world. The proposed NF is *correct-by-construction i.e.,* it does not have undesired local minima by design. Recently, this work was extended in [Loizou and Rimon, 2021], for unknown environments with a sensor-based robot navigation approach. However, similar to [Paternain et al., 2017], the complete shape of the obstacles is assumed to become known when the robot visits their respective neighborhoods. Most of the NF-approaches in the literature are only applicable to environments with either unknown spherical obstacles or known obstacles which are diffeomorphic to a sphere. Moreover, these NF-based approaches generate undesired unstable equilibria (saddle points) away from the predefined target location due to the

topological obstruction induced by the motion space in the presence of obstacles for any smooth transversal vector field, as shown in [Koditschek and Rimon, 1990], which renders these approaches at best almost globally convergent.

There are several research works which do not explicitly define the navigation function, but instead directly design vector fields based on the topological properties of the environment to satisfy the predefined objectives. For example, in [Arslan and Koditschek, 2016], [Arslan and Koditschek, 2019], the authors proposed a novel sensor-based reactive[5] navigation approach for a single robot operating in an unknown environment with sufficiently curved convex obstacles. The central idea is to construct a compact obstacle-free local neighbourhood around the robot by identifying the hyperplanes separating the robot body from the obstacles in the surrounding, as shown by the shaded green color in Fig. 1.4(left), and then guiding the robot towards the projection of the target location onto the boundary of this compact set. If the workspace satisfies the obstacle curvature condition [Arslan and Koditschek, 2019, Assumption 2], see Fig. 1.4(right), then for almost all initial locations, the robot trajectories obtained using the separating hyperplane-based approach converge asymptotically to the target location, while strictly decreasing the Euclidean distance to the target location [Arslan and Koditschek, 2019, Theorem 3], see Fig. 1.5 (left). When the environment consists of obstacles that do not satisfy the obstacle curvature condition [Arslan and Koditschek, 2019, Assumption 2], which is the case with obstacles $\mathcal{O}_1$ and $\mathcal{O}_2$ in Fig. 1.5(right), the hyperplane-based approach generates undesired local minima, as can be seen in Fig. 1.5 (right).

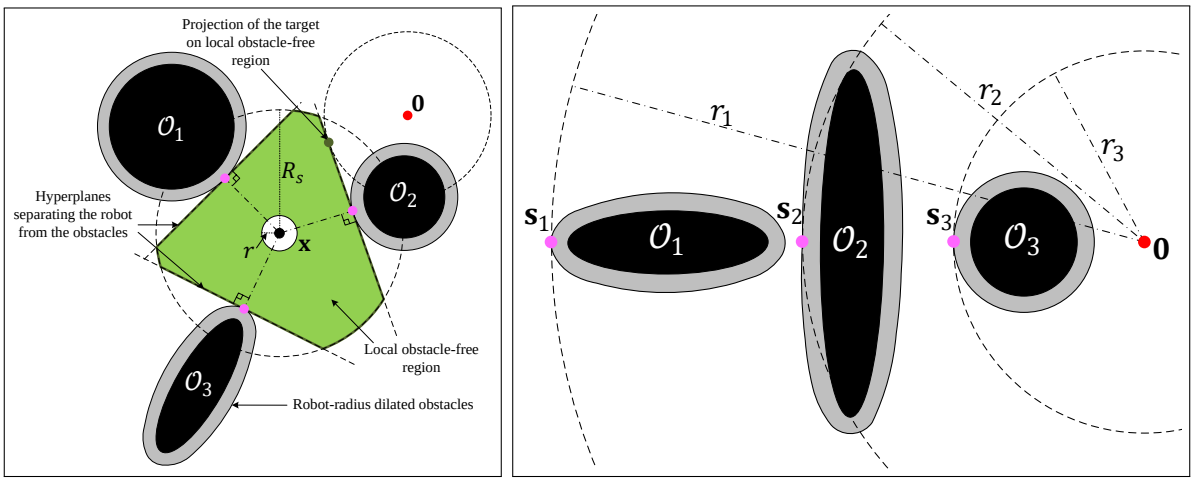

Figure 1.4: The left figure illustrates the process behind the construction of the local obstacle-free neighbourhood, represented by the shaded green color, using separating hyperplanes. The right figure provides a representation of the obstacle curvature assumption [Arslan and Koditschek, 2019, Assumption 2]. Obstacles $\mathcal{O}_1$ and $\mathcal{O}_3$ satisfy the assumption, whereas obstacle $\mathcal{O}_2$ does not.

[5]the term *reactive* means that motion is generated by a vector field arising from some closed-loop feedback policy issuing online force or velocity commands in real time as a function of the instantaneous robot state.

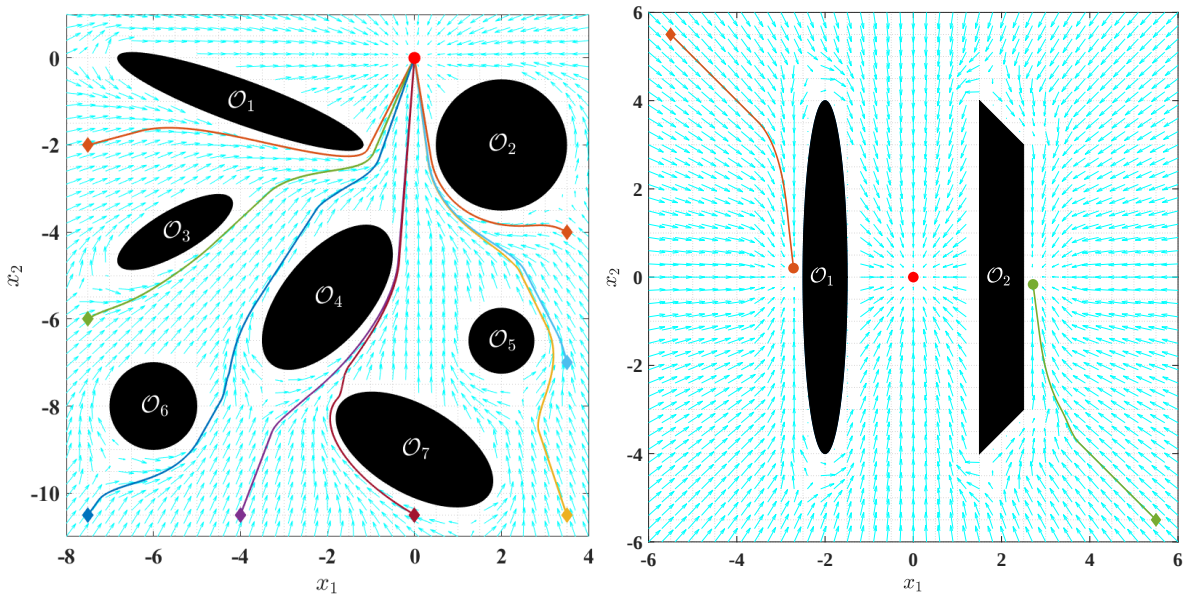

Figure 1.5: Trajectories of a point robot obtained using the separating hyperplane-based approach [Arslan and Koditschek, 2019]. The left figure shows the trajectories of a point robot from 8 different locations (diamond symbols), converging to the target location at the origin. The right figure illustrates the presence of undesired local minima near the obstacles that do not satisfy the curvature condition.

This work is then extended in [Vasilopoulos and Koditschek, 2018] to the case of two-dimensional partially known non-convex environment wherein geometric information regarding the non-convex obstacles is assumed to be *a priori* known. When the robot visits the neighbourhood of these known obstacles, a diffeomorphic transformation is used to convert them into disk-shaped obstacles. In [Berkane, 2021], the author proposed a controller design based on Nagumo's theorem [Nagumo, 1942], [Blanchini et al., 2008] for general convex obstacles. In this work, the authors ensured the forward invariance of the obstacle-free space by projecting the *ideal* velocity control vector, pointing towards the target, onto the tangent cone at the boundary of the obstacle whenever it points towards the obstacle. However, similar to the NF-based approaches, this approach suffers from the presence of undesired equilibria. To tackle this issue, the authors in [Berkane et al., 2019] proposed a hybrid controller which renders the target location globally asymptotically stable in the case of a single spherical obstacle. The robot operates in the *move-to-target* mode[6] when it is away from the obstacle, and switches to the *obstacle-avoidance* mode in the close proximity of the obstacle. The strategy is similar to the bug path planning algorithms [Lumelsky and Stepanov, 1986]. This work is then extended in [Berkane et al., 2021a] to the case of known environments with sufficiently disjoint ellipsoidal obstacles, leading to global asymptotic stabilization of the target location. The switching mechanism proposed in [Berkane et al., 2019], [Berkane, 2021], [Berkane et al., 2021a] generates discontinuous control laws in the case of single inte-

[6]The *move-to-target* mode is referred to as the mode where the control applied to robot is the ideal control pointing towards the target in the absence of obstacles.

grator dynamics. In [Vrohidis et al., 2018], the authors proposed a discontinuous vector field design in a sphere world, for a robot modeled as a single integrator, that ensures obstacle avoidance and facilitates the use of the prescribed performance control technique to impose predetermined convergence to the desired location.

1.2 Thesis contributions

The contributions presented in this dissertation are summarized as follows:

- In Chapter 3, a hybrid feedback controller for autonomous robot navigation in two-dimensional environments with arbitrarily-shaped convex obstacles is proposed. Existing approaches such as NF-based approaches [Paternain et al., 2017], [Verginis and Dimarogonas, 2021], [Kumar et al., 2022], the separating hyperplane-based approach [Arslan and Koditschek, 2019], and the control Lyapunov barrier function based approach [Reis et al., 2020], are tailored for sufficiently curved obstacles with smooth boundaries. Due to the topological obstruction induced by the motion space [Koditschek and Rimon, 1990], the above-mentioned approaches provide at best almost global asymptotic stability guarantees. Additionally, their direct application to environments with flat obstacles with nonsmooth boundaries can generate undesired stable local minima, as shown in Fig. 1.5 (right). In contrast, the proposed hybrid feedback autonomous navigation scheme, consisting of two modes of operation, namely, the *move-to-target* mode and *obstacle-avoidance* mode), is applicable to robots navigating in environments with arbitrarily-shaped convex obstacles (including obstacles with nonsmooth boundaries). Most importantly, the proposed hybrid control scheme is endowed with global asymptotic stability guarantees. The proposed hybrid feedback controller can be implemented in a priori unknown environments using the measurements obtained via a range-bearing sensor mounted on the robot. The obtained results have been published in [Sawant et al., 2023a] and [Sawant et al., 2022a].

- In Chapter 4, a hybrid feedback controller, endowed with global asymptotic stability guarantees, for autonomous robot navigation in two-dimensional environments with arbitrarily-shaped non-convex obstacles, is presented. An instrumental obstacle reshaping technique is introduced to (virtually) modify the obstacles, in a less conservative manner (without necessarily convexifying them), in a way that ensures uniqueness of the closest point on the modified obstacles from the robot's center– a useful feature for our obstacle avoidance technique. The existing autonomous robot navigation algorithms assume that the non-convex obstacles have smooth boundaries (references), and/or the robot can pass through any pair of obstacles, see for instance [Arslan and Koditschek, 2019, Assumption 1], [Berkane et al., 2021a, Section V-C3] and [Verginis and Dimarogonas, 2021, Assumption 2]. In contrast, the proposed control strategy applies to environments with arbitrary shaped non-convex obstacles and does not require the obstacles to be pairwise separated as long as there exists a safe path between the initial and the target locations. Moreover,

the proposed autonomous navigation algorithm can be implemented in *a priori* unknown environments using the measurements obtained via a range-bearing sensor mounted on the robot.
The work in this chapter has been reported in [Sawant et al., 2022b] and [Sawant et al., 2023b].

- In Chapter 5, we propose a hybrid feedback controller for safe autonomous robot navigation in three-dimensional environments with arbitrarily-shaped convex obstacles. In comparison with the continuous control schemes presented in [Koditschek and Rimon, 1992], [Paternain et al., 2017], [Arslan and Koditschek, 2019], which guarantee safety and almost global asymptotic stability, the proposed hybrid feedback controller is endowed with safety and global asymptotic stability guarantees. We also propose a modification to the hybrid feedback controller, tailored for the sphere world, that ensures a monotonic decrease of the distance between the robot's center and the target location. The proposed autonomous navigation algorithm can be implemented in *a priori* unknown environments, relying on range-bearing measurements. The results presented in this chapter have been reported in [Sawant et al., 2024].

1.3 List of publications

The materials presented in this dissertation are based on the following publications:

Journal Articles:

- M. Sawant, S. Berkane, I. Polushin and A. Tayebi, "Hybrid Feedback for Autonomous Navigation in Planar Environments with Convex Obstacles," *IEEE Transactions on Automatic Control*, 68(12), pp. 7342 - 7357, 2023.

- M. Sawant, I. Polushin and A. Tayebi, "Hybrid Feedback Control Design for Non-convex Obstacle Avoidance," *IEEE Transactions on Automatic Control*, 2023, (Submission no. 23-0869, accepted).

Peer-Reviewed Conference Proceedings:

- M. Sawant, A. Tayebi and I. Polushin, "Autonomous Navigation in Environments with Arbitrary Non-convex Obstacles," In *Proc. of 61st IEEE Conference on Decision and Control (CDC)*, Cancun, Mexico, pp. 7208-7213, 2022.

- M. Sawant, I. Polushin and A. Tayebi, "Hybrid Feedback for Three-dimensional Convex Obstacle Avoidance," *Submitted to 64th IEEE Conference on Decision and Control (CDC)*, Milan, Italy, 2024 (Under review).

1.4 Thesis outline

The thesis is organized as follows:

Chapter 2 presents the notations, background and preliminaries used throughout the thesis. Section 2.1 provides general notations used in the thesis. Section 2.2 presents tools allowing to obtain the closest points on a given set from any given location. Section 2.3 provides mathematical definitions of several geometrical subsets of $\mathbb{R}^n$ used throughout this work. Section 2.4 provides the hybrid systems framework used in this work.

Chapter 3 is dedicated to the design and stability analysis of the hybrid feedback controller for point-mass robots operating in planar environments with arbitrarily-shaped convex obstacles. Section 3.3 deals with the design of the hybrid feedback controller. Section 3.4, deals with the forward invariance and the stability properties of the resulting hybrid closed-loop system. Section 3.5 presents an implementation procedure for the proposed hybrid feedback controller in *a priori* unknown environments. This is followed by computer simulation results in Section 3.6.

Chapter 4 considers the problem of autonomous robot navigation in planar environments with arbitrarily-shaped obstacles (possibly non-convex). Section 4.3 provides an instrumental obstacle reshaping technique that will be used for the design of the obstacle-avoidance strategy presented in Section 4.4. Section 4.5, deals with the forward invariance and the stability properties of the resulting hybrid closed-loop system. Section 4.6 presents a sensor-based implementation procedure in *a priori* unknown environments. This is followed by computer simulation results in Section 4.7.

Chapter 5 deals with the design of a hybrid feedback controller for robots operating in three-dimensional environments with arbitrarily-shaped convex obstacles. Section 5.3, deals with the control design. Section 5.4, deals with the forward invariance and stability properties of the resulting hybrid closed-loop system. Section 5.5 offers a modified version of the hybrid feedback controller tailored for sphere worlds. Section 5.6 presents a sensor-based implementation procedure in *a priori* unknown environments. Section 5.7 provides some simulation results.

Chapter 6 summarizes the findings of this thesis and presents some possible future directions.

Appendices A, B, C and **D** contain the detailed proofs of lemmas and theorems stated throughout the thesis.

Chapter 2

Background and Preliminaries

2.1 General notations

The sets of real, non-negative real and natural numbers are denoted by $\mathbb{R}$, $\mathbb{R}_{\geq 0}$ and $\mathbb{N}$, respectively. We identify vectors using bold lowercase letters. The Euclidean norm of a vector $\mathbf{p} \in \mathbb{R}^n$ is denoted by $\|\mathbf{p}\|$, and an Euclidean ball of radius $r > 0$ centered at $\mathbf{p}$ is represented by $\mathcal{B}_r(\mathbf{p}) = \{\mathbf{q} \in \mathbb{R}^n | \|\mathbf{q} - \mathbf{p}\| \leq r\}$. Given two vectors $\mathbf{p} \in \mathbb{R}^2$ and $\mathbf{q} \in \mathbb{R}^2$, we denote by $\psi(\mathbf{p}, \mathbf{q})$ the angle from $\mathbf{p}$ to $\mathbf{q}$. The angle measured in counter-clockwise manner is considered positive, and vice versa. Given two locations $\mathbf{p}, \mathbf{q} \in \mathbb{R}^n$, the notation $\mathbf{path}(\mathbf{p}, \mathbf{q})$ represents a continuous path in $\mathbb{R}^n$, which joins these locations. A set $\mathcal{A} \subset \mathbb{R}^n$ is said to be pathwise connected if for any two points $\mathbf{p}, \mathbf{q} \in \mathcal{A}$, there exists a continuous path, joining $\mathbf{p}$ and $\mathbf{q}$, that belongs to the same set *i.e.*, there exists a $\mathbf{path}(\mathbf{p}, \mathbf{q}) \subset \mathcal{A}$ [Willard, 2012, Definition 27.1]. The set of $n-$dimensional unit vectors is given by $\mathbb{S}^{n-1} := \{\mathbf{p} \in \mathbb{R}^n | \|\mathbf{p}\| = 1\}$. The three-dimensional Special Orthogonal group is defined by $\mathsf{SO}(3) := \{R \in \mathbb{R}^{3\times 3} | R^\top R = \mathbf{I}_3, \mathbf{det}(R) = 1\}$. For a given vector $\mathbf{x} := [x_1, x_2, x_3]^\top \in \mathbb{R}^3$, we define $\mathbf{x}^\times$ as the skew-symmetric matrix, which is given by

$$\mathbf{x}^\times = \begin{bmatrix} 0 & -x_3 & x_2 \\ x_3 & 0 & -x_1 \\ -x_2 & x_1 & 0 \end{bmatrix}. \tag{2.1}$$

For two sets $\mathcal{A}, \mathcal{B} \subset \mathbb{R}^n$, the relative complement of $\mathcal{B}$ with respect to $\mathcal{A}$ is denoted by $\mathcal{A} \setminus \mathcal{B} = \{\mathbf{a} \in \mathcal{A} | \mathbf{a} \notin \mathcal{B}\}$. Given a set $\mathcal{A} \subset \mathbb{R}^n$, the symbols $\partial\mathcal{A}, \mathcal{A}^\circ$, $\mathcal{A}^c$ and $\bar{\mathcal{A}}$ represent the boundary, interior, complement and the closure of the set $\mathcal{A}$, respectively, where $\partial\mathcal{A} = \bar{\mathcal{A}} \backslash \mathcal{A}^\circ$. The number of elements in a set $\mathcal{A}$ is given by $\mathbf{card}(\mathcal{A})$. Let $\mathcal{A}$ and $\mathcal{B}$ be subsets of $\mathbb{R}^n$, then the dilation of $\mathcal{A}$ by $\mathcal{B}$ is denoted by $\mathcal{A} \oplus \mathcal{B} = \{\mathbf{a} + \mathbf{b} | \mathbf{a} \in \mathcal{A}, \mathbf{b} \in \mathcal{B}\}$, and the erosion of $\mathcal{A}$ by $\mathcal{B}$ is denoted by $\mathcal{A} \ominus \mathcal{B} = \{\mathbf{x} \in \mathbb{R}^n | \mathbf{x} + \mathbf{b} \in \mathcal{A}, \forall \mathbf{b} \in \mathcal{B}\}$ [Haralick et al., 1987]. Additionally, the set $\mathcal{B}$ is referred to as a structuring element. Given a positive scalar $r > 0$, the $r-$dilated version of the set $\mathcal{A} \subset \mathbb{R}^n$ is denoted by $\mathcal{D}_r(\mathcal{A}) = \mathcal{A} \oplus \mathcal{B}_r(\mathbf{0})$. The $r-$neighbourhood of the set $\mathcal{A}$ is then denoted by $\mathcal{N}_r(\mathcal{A}) = \mathcal{D}_r(\mathcal{A}) \setminus \mathcal{A}^\circ$.

2.2 Projection maps

2.2.1 Projection on a set

Given a closed set $\mathcal{A} \subset \mathbb{R}^n$ and a point $\mathbf{x} \in \mathbb{R}^n$, the Euclidean distance of $\mathbf{x}$ from the set $\mathcal{A}$ is evaluated as

$$d(\mathbf{x}, \mathcal{A}) = \min_{\mathbf{q} \in \mathcal{A}} \|\mathbf{x} - \mathbf{q}\|. \tag{2.2}$$

The set $\mathcal{PJ}(\mathbf{x}, \mathcal{A}) \subset \mathcal{A}$, which is defined as

$$\mathcal{PJ}(\mathbf{x}, \mathcal{A}) = \{\mathbf{q} \in \mathcal{A} | \|\mathbf{x} - \mathbf{q}\| = d(\mathbf{x}, \mathcal{A})\}, \tag{2.3}$$

is the set of points in the set $\mathcal{A}$ which are at the distance of $d(\mathbf{x}, \mathcal{A})$ from $\mathbf{x}$. If $\mathbf{card}(\mathcal{PJ}(\mathbf{x}, \mathcal{A}))$ is one, then the element of the set $\mathcal{PJ}(\mathbf{x}, \mathcal{A})$ is denoted by $\Pi(\mathbf{x}, \mathcal{A})$.

2.2.2 Sets with positive reach

Given a closed set $\mathcal{A} \subset \mathbb{R}^n$, the set $\mathrm{Unp}(\mathcal{A})$, which is defined as

$$\mathrm{Unp}(\mathcal{A}) = \{\mathbf{x} \in \mathbb{R}^n | \mathbf{card}(\mathcal{PJ}(\mathbf{x}, \mathcal{A})) = 1\}, \tag{2.4}$$

denotes the set of all $\mathbf{x} \in \mathbb{R}^n$ for which there exists a unique point in $\mathcal{A}$ nearest to $\mathbf{x}$. Then, for any $\mathbf{x} \in \mathcal{A}$, the reach of set $\mathcal{A}$ at $\mathbf{x}$, denoted by $\mathbf{r}(\mathcal{A}, \mathbf{x})$ [Rataj and Zähle, 2019, Pg 55], is defined as

$$\mathbf{r}(\mathcal{A}, \mathbf{x}) := \sup\{r \geq 0 | \mathcal{B}_r^\circ(\mathbf{x}) \subset \mathrm{Unp}(\mathcal{A})\}. \tag{2.5}$$

The reach of set $\mathcal{A}$ is then given by

$$\mathbf{reach}(\mathcal{A}) := \inf_{\mathbf{x} \in \mathcal{A}} \mathbf{r}(\mathcal{A}, \mathbf{x}). \tag{2.6}$$

If a closed set has reach greater than or equal to $r > 0$, then any location less than r distance away from the set will have a unique closest point on the set.

2.3 Geometric subsets of $\mathbb{R}^n$

2.3.1 Line

Let $\mathbf{q} \in \mathbb{R}^n \backslash \{\mathbf{0}\}$ and $\mathbf{p} \in \mathbb{R}^n$, then a line passing through $\mathbf{p}$ in the direction of $\mathbf{q}$ is defined as

$$\mathcal{L}(\mathbf{p}, \mathbf{q}) := \{\mathbf{x} \in \mathbb{R}^n | \mathbf{x} = \mathbf{p} + \lambda \mathbf{q}, \lambda \in \mathbb{R}\}. \tag{2.7}$$

If $\lambda \geq 0$ (respectively, $\lambda > 0$), then we get the positive half-line $\mathcal{L}_{\geq}(\mathbf{p}, \mathbf{q})$ (respectively, $\mathcal{L}_{>}(\mathbf{p}, \mathbf{q})$). Similarly, we define the negative half-lines for $\lambda \leq 0$ and $\lambda < 0$ as $\mathcal{L}_{\leq}(\mathbf{p}, \mathbf{q})$ and $\mathcal{L}_{<}(\mathbf{p}, \mathbf{q})$, respectively.

2.3.2 Line segment

Let $\mathbf{p} \in \mathbb{R}^n$ and $\mathbf{q} \in \mathbb{R}^n$, then a line segment joining $\mathbf{p}$ and $\mathbf{q}$ is given by

$$\mathcal{L}_s(\mathbf{p}, \mathbf{q}) := \{\mathbf{x} \in \mathbb{R}^n | \mathbf{x} = \lambda\mathbf{p} + (1-\lambda)\mathbf{q}, \lambda \in [0,1]\}. \tag{2.8}$$

2.3.3 Hyperplane

Given $\mathbf{p} \in \mathbb{R}^n$ and $\mathbf{q} \in \mathbb{R}^n \backslash \{\mathbf{0}\}$, a hyperplane passing through $\mathbf{p}$ and orthogonal to $\mathbf{q}$ is given by

$$\mathcal{P}(\mathbf{p}, \mathbf{q}) := \{\mathbf{x} \in \mathbb{R}^n | \mathbf{q}^\intercal(\mathbf{x} - \mathbf{p}) = 0\}. \tag{2.9}$$

The hyperplane divides the Euclidean space $\mathbb{R}^n$ into two half-spaces *i.e.*, a closed positive half-space $\mathcal{P}_{\geq}(\mathbf{p}, \mathbf{q})$ and a closed negative half-space $\mathcal{P}_{\leq}(\mathbf{p}, \mathbf{q})$ which are obtained by substituting '$=$' with '$\geq$' and '$\leq$' respectively, in the right-hand side of (2.9). We also use the notations $\mathcal{P}_{>}(\mathbf{p}, \mathbf{q})$ and $\mathcal{P}_{<}(\mathbf{p}, \mathbf{q})$ to denote the open positive and the open negative half-spaces such that $\mathcal{P}_{>}(\mathbf{p}, \mathbf{q}) = \mathcal{P}_{\geq}(\mathbf{p}, \mathbf{q}) \backslash \mathcal{P}(\mathbf{p}, \mathbf{q})$ and $\mathcal{P}_{<}(\mathbf{p}, \mathbf{q}) = \mathcal{P}_{\leq}(\mathbf{p}, \mathbf{q}) \backslash \mathcal{P}(\mathbf{p}, \mathbf{q})$.

2.3.4 Supporting hyperplane

Given a closed convex set $\mathcal{A} \subset \mathbb{R}^n$, $\mathbf{p} \in \partial\mathcal{A}$ and $\mathbf{q} \in \mathbb{R}^n \backslash \{\mathbf{0}\}$, a hyperplane $\mathcal{P}(\mathbf{p}, \mathbf{q})$ is a supporting hyperplane [Boyd et al., 2004] to $\mathcal{A}$ at point $\mathbf{p}$, if

$$\mathbf{q}^\intercal(\mathbf{x} - \mathbf{p}) \leq 0, \ \forall \mathbf{x} \in \mathcal{A}. \tag{2.10}$$

In this case, the vector $\mathbf{q}$ is normal to the set $\mathcal{A}$ at $\mathbf{p}$, the supporting hyperplane $\mathcal{P}(\mathbf{p}, \mathbf{q})$ is tangent to $\mathcal{A}$ at $\mathbf{p}$, and the negative half-space $\mathcal{P}_{\leq}(\mathbf{p}, \mathbf{q})$ contains $\mathcal{A}$.

2.3.5 Convex cone

Given $\mathbf{c} \in \mathbb{R}^n, \mathbf{p}_1 \in \mathbb{R}^2 \backslash \mathbf{c}$ and $\mathbf{p}_2 \in \mathbb{R}^2 \backslash \mathbf{c}$, a convex cone [Boyd et al., 2004] $\mathcal{C}(\mathbf{c}, \mathbf{p}_1, \mathbf{p}_2)$ with its vertex at $\mathbf{c}$ and its edges passing through $\mathbf{p}_1$ and $\mathbf{p}_2$ is defined as

$$\mathcal{C}(\mathbf{c}, \mathbf{p}_1, \mathbf{p}_2) := \{\mathbf{x} \in \mathbb{R}^2 | \mathbf{x} = \mathbf{c} + \lambda_1(\mathbf{p}_1 - \mathbf{c}) + \lambda_2(\mathbf{p}_2 - \mathbf{c}), \forall\lambda_1 \geq 0, \forall\lambda_2 \geq 0\}. \tag{2.11}$$

2.3.6 Conic hull

Given a set $\mathcal{A} \subset \mathbb{R}^n$ and a point $\mathbf{x} \in \mathbb{R}^n$, the conic hull [Boyd et al., 2004, Section 2.1.5] $\mathcal{CH}(\mathbf{x}, \mathcal{A})$ for the set $\mathcal{A}$, with its vertex at $\mathbf{x}$ is defined as

$$\mathcal{CH}(\mathbf{x}, \mathcal{A}) := \bigcup_{\mathbf{p}, \mathbf{q} \in \mathcal{A}} \mathcal{C}(\mathbf{x}, \mathbf{p}, \mathbf{q}). \tag{2.12}$$

The conic hull $\mathcal{CH}(\mathbf{x}, \mathcal{A})$ is the smallest convex cone with its vertex at $\mathbf{x}$ that contains the set $\mathcal{A}$ *i.e.*, $\mathcal{A} \subset \mathcal{CH}(\mathbf{x}, \mathcal{A})$.

2.3.7 Tangent cone and normal cone

Given a closed set $\mathcal{A} \subset \mathbb{R}^n$, the tangent cone to $\mathcal{A}$ at a point $\mathbf{x} \in \mathbb{R}^n$ [Aubin et al., 2011, Definition 11.2.1] is defined by

$$\mathbf{T}_{\mathcal{A}}(\mathbf{x}) := \left\{ \mathbf{w} \in \mathbb{R}^n \middle| \liminf_{\tau \to 0^+} \frac{d(\mathbf{x} + \tau \mathbf{w}, \mathcal{A})}{\tau} = 0 \right\}. \tag{2.13}$$

The tangent cone to the set $\mathcal{A}$ at $\mathbf{x}$ is the set that contains all the vectors whose directions point from $\mathbf{x}$ either inside or tangent to the set $\mathcal{A}$. Given a tangent cone to a set $\mathcal{A}$ at a point $\mathbf{x}$, the normal cone to the set $\mathcal{A}$ at the point $\mathbf{x}$, as defined in [Rataj and Zähle, 2019, Pg 58], [Aubin et al., 2011, Pg 475], is given by

$$\mathbf{N}_{\mathcal{A}}(\mathbf{x}) := \left\{ \mathbf{p} \in \mathbb{R}^n \middle| \mathbf{p}^\intercal \mathbf{w} \leq 0, \forall \mathbf{w} \in \mathbf{T}_{\mathcal{A}}(\mathbf{x}) \right\}. \tag{2.14}$$

2.4 Hybrid system framework

A hybrid dynamical system [Goebel et al., 2012] is represented using differential and difference inclusions for the state $\xi \in \mathbb{R}^n$ as follows:

$$\mathcal{H} : \begin{cases} \dot{\xi} \in \mathbf{F}(\xi), & \xi \in \mathcal{F}, \\ \xi^+ \in \mathbf{J}(\xi), & \xi \in \mathcal{J}, \end{cases} \tag{2.15}$$

where

- $\mathcal{F} \subset \mathbb{R}^n$ is the *flow set*,
- $\mathcal{J} \subset \mathbb{R}^n$ is the *jump set*,
- the *flow map* $\mathbf{F} : \mathbb{R}^n \rightrightarrows \mathbb{R}^n$ describes the continuous flow on $\mathcal{F}$,
- the *jump map* $\mathbf{J} : \mathbb{R}^n \rightrightarrows \mathbb{R}^n$ describes the discrete jump on $\mathcal{J}$.

Note that $\rightrightarrows$ denotes a set-valued mapping, and ξ^+ denotes the value of ξ after an instantaneous jump. The hybrid system (2.15) is defined by its data and denoted as $\mathcal{H} = (\mathcal{F}, \mathbf{F}, \mathcal{J}, \mathbf{J})$.

The solutions to a hybrid system are obtained on a *hybrid time domain* parameterized by the amount of time $t \in \mathbb{R}_{\geq 0}$ spent in the *flow set* and by the number of jumps $j \in \mathbb{N}$ of the state. A *hybrid time domain* $\mathbb{E} \subset \mathbb{R}_{\geq 0} \times \mathbb{N}$ is defined as

$$\mathbb{E} = \bigcup_{j=0}^{J-1} \left([t_j, t_{j+1}] \times \{j\} \right), \tag{2.16}$$

for some finite sequence $0 = t_0 \leq t_1 \leq \cdots \leq t_J$, with the last interval (if existent) possibly in the form $([t_{J-1}, T) \times \{J\})$ with T finite or $T = +\infty$. On each hybrid time domain there is a natural ordering of points: $(t, j) \preceq (t', j')$ if $t \leq t'$ and $j \leq j'$.

A hybrid arc is a function $\phi : \mathbb{E} \to \mathbb{R}^n$, where dom ξ is a hybrid time domain, and for each fixed $j \in \mathbb{N}$, the function $t \to \xi(t, j)$ is a locally absolutely continuous function on the interval $I_j = \{t : (t, j) \in \mathbb{E}\}$. A hybrid arc ϕ is a solution to the hybrid system $\mathcal{H}$ if

- $\phi(0,0) \in \overline{\mathcal{F}} \cup \mathcal{J}$, where $\overline{\mathcal{F}}$ denotes the closure of $\mathcal{F}$,
- for all $j \in \mathbb{N}$ such that I_j has nonempty interior

$$\begin{aligned} &\phi(t,j) \in \mathcal{C} \text{ for all } t \in I_j^\circ, \\ &\dot{\phi}(t,j) \in \mathbf{F}(\phi(t,j)) \text{ for almost all } t \in I_j, \end{aligned} \tag{2.17}$$

- for all $(t,j) \in \text{ dom } \phi$ such that $(t, j+1) \in \text{ dom } \phi$,

$$\begin{aligned} &\phi(t,j) \in \mathcal{J}, \\ &\phi(t,j+1) \in \mathbf{J}(\phi(t,j)), \end{aligned} \tag{2.18}$$

A solution ξ to $\mathcal{H}$ is *maximal* if it cannot be extended by flowing nor jumping, and it is *complete* if its domain dom ϕ is unbounded. We denote $\mathcal{S}_\mathcal{H}$ as the set of all *maximal* solutions ϕ to $\mathcal{H}$. One can proof existence of nontrivial solutions for the given hybrid system $\mathcal{H}$ by verifying the hybrid basic conditions [Goebel et al., 2012, Assumption 6.5] which are stated below:

Assumption 2.1 (Hybrid basic conditions) *:*

1. *$\mathcal{F}$ and $\mathcal{J}$ are closed subsets of $\mathbb{R}^n$;*
2. *$\mathbf{F}$ is outer semicontinuous and locally bounded relative to $\mathcal{F}$, $\mathcal{F} \subset$ dom $\mathbf{F}$, and $\mathbf{F}(\xi)$ is convex for every $\xi \in \mathcal{F}$;*
3. *$\mathbf{J}$ is outer semicontinuous and locally bounded relative to $\mathcal{J}$, and $\mathcal{J} \subset$ dom $\mathbf{J}$.*

2.5 Preliminary lemmas

Next, we provide a few lemmas that describe some properties of the sets with positive reach, which will be used later.

Lemma 2.1 *Let $\mathcal{A} \subset \mathbb{R}^n$ be a closed convex set and $\mathbf{q} \in \mathbb{R}^n \backslash \mathcal{A}$. Then the vector $(\mathbf{q} - \Pi(\mathbf{q}, \mathcal{A}))$ is normal to $\mathcal{D}_r(\mathcal{A})$ at $\Pi(\mathbf{q}, \mathcal{D}_r(\mathcal{A}))$ and the hyperplane $\mathcal{P}(\Pi(\mathbf{q}, \mathcal{D}_r(\mathcal{A})), (\mathbf{q} - \Pi(\mathbf{q}, \mathcal{A})))$ is a supporting hyperplane to $\mathcal{D}_r(\mathcal{A})$ at $\Pi(\mathbf{q}, \mathcal{D}_r(\mathcal{A}))$ for $r \in [0, d(\mathbf{q}, \mathcal{A})]$.*

Proof See Appendix A.1.

Lemma 2.1 provides a property of the projection (2.3) such that given a closed convex set $\mathcal{A}$ and a point $\mathbf{q} \in \mathbb{R}^n$ outside the set $\mathcal{A}$, the vector joining the projection of $\mathbf{q}$ on $\mathcal{A}$ with the point $\mathbf{q}$ is always normal to the dilated versions of the set $\mathcal{A}$, $\mathcal{D}_r(\mathcal{A})$ where $r \in [0, d(\mathbf{q}, \mathcal{A})]$.

Lemma 2.2 *Given a closed set $\mathcal{A} \subset \mathbb{R}^n$, we define the set $\mathcal{G} = (\mathcal{A} \oplus \mathcal{B}_\alpha^\circ(\mathbf{0}))^c$. If **reach**$(\mathcal{A}) \geq \alpha$, then **reach**$(\mathcal{G}) \geq \alpha$.*

Proof See Appendix A.2.

According to Lemma 2.2, if a closed set $\mathcal{A}$ has reach greater than or equal to a non-negative scalar α, then the complement of its dilation with the open Euclidean ball of radius α also has reach greater than or equal to α.

Lemma 2.3 *Consider a closed set* $\mathcal{A} \subset \mathbb{R}^n$ *and scalars* $\alpha \geq \beta \geq 0$. *If* $\boldsymbol{reach}(\mathcal{A}) \geq \alpha$, *then* $\boldsymbol{reach}(\mathcal{D}_\beta(\mathcal{A})) \geq \alpha - \beta$.

Proof See Appendix A.3.

According to Lemma 2.3, if a closed set $\mathcal{A}$, with reach greater than or equal to a non-negative scalar α, is dilated by some distance β less than or equal to α, then reach of the dilated set is greater than or equal to $\alpha - \beta$.

Chapter 3

Autonomous Navigation in Planar Environments with Convex Obstacles

3.1 Introduction

In this chapter, we deal with the autonomous robot navigation problem in environments with arbitrarily-shaped convex obstacles. One of the widely explored techniques in this context is the NF-based approach which is directly applicable to sphere world environments [Koditschek and Rimon, 1992], [Verginis and Dimarogonas, 2021] or environments that contain sufficiently curved obstacles [Filippidis and Kyriakopoulos, 2012]. To make it applicable in environments with more general convex and star-shaped obstacles, one can make use of diffeomorphic mappings provided in [Koditschek and Rimon, 1992], [Li and Tanner, 2018], to transform a given environment into a sphere world. However, in order to perform these diffeomorphic mappings, the robot must have global knowledge about the environment, which makes the NF-based mobile robot navigation schemes less attractive in practical applications. In [Arslan and Koditschek, 2019], the authors proposed a purely reactive power diagram-based approach for robots operating in environments cluttered with unknown but sufficiently separated and strongly convex obstacles while ensuring almost global asymptotic stabilization of the target location. This approach has been extended in [Vasilopoulos and Koditschek, 2018], for partially known non-convex environments, wherein it is assumed that the robot has the geometrical information of the non-convex obstacles but not their locations in the workspace. However, using the continuous time-invariant approaches discussed above, one can at best guarantee almost global asymptotic stability [Koditschek and Rimon, 1990]. In [Sanfelice et al., 2006] and [Casau et al., 2019], hybrid control techniques are used to ensure robust global asymptotic stabilization of a target location in $\mathbb{R}^2$, while avoiding collision with a single spherical obstacle. The approach in [Sanfelice et al., 2006] has been extended in [Poveda et al., 2018] to steer a group of planar robots in formation towards the source of an unknown but measurable signal, while avoiding a single obstacle. In [Braun et al., 2018], the authors proposed a hybrid control law to globally asymptotically stabilize a class of linear

systems while avoiding neighbourhoods of unsafe isolated points. In other works such as [Matveev et al., 2011], [Berkane et al., 2021a], the proposed hybrid control techniques allow the robot to operate either in the *obstacle-avoidance* mode when it is in close proximity of an obstacle or in the *move-to-target* mode when it is away from the obstacles. The strategies used in these research works are similar to the point robot path planning algorithms referred to as the bug algorithms [Lumelsky and Stepanov, 1986]. For some special obstacle arrangements, the robot retraces a previously followed path instead of converging to the predefined target location, in which case these algorithms terminate the path planning process establishing the failure to converge to the target location due to the presence of a closed trajectory around the target location. The authors in [Matveev et al., 2011], [Berkane et al., 2021a], overcame these special scenarios by restricting the inter-obstacle arrangements.

In this chapter, we propose a hybrid controller that allows to steer a holonomic robot, modelled as a single integrator, to reach a predefined target location while avoiding convex obstacles in two-dimensional environments. The proposed controller, enjoying global asymptotic stability guarantees, operates in the *move-to-target* mode when the robot is away from the obstacles and in the *obstacle-avoidance* mode when it is in close proximity to an obstacle. The main contributions of the proposed research work are as follows:

1. *Global asymptotic stability:* The proposed autonomous navigation solution provides global asymptotic stability guarantees for robots operating in two-dimensional environments with convex obstacles of arbitrary shapes. Note that the few existing results in the literature achieving such strong stability results are of hybrid type and are restricted to elliptically-shaped convex obstacles [Berkane et al., 2021a].

2. *Arbitrarily-shaped convex obstacles:* The proposed hybrid feedback controller is applicable to environments consisting of convex obstacles with arbitrary shapes. Compared to this, the recently developed separating hyperplane-based approach is restricted to smooth obstacles which satisfy some curvature conditions [Arslan and Koditschek, 2019, Assumption 2]. Similarly, in [Berkane et al., 2021a], the obstacles are assumed to be ellipsoidal.

3. *Arbitrary inter-obstacle arrangements:* There are no restrictions on the inter-obstacle arrangements such as those in [Matveev et al., 2011, Assumption 10], [Berkane et al., 2021a, Theorem 2], except for the widely used mild ones stated in Assumption 1, *i.e.*, the robot can pass in between any two obstacles while maintaining a positive distance.

4. *Continuous vector field:* The proposed hybrid controller generates continuous velocity input trajectories as long as the robot is initialized away from the boundaries of the unsafe regions. This is a very interesting feature for practical implementations that distinguishes our approach with respect to the hybrid approach of [Berkane et al., 2021a].

5. *Applicable in a priori unknown environments:* The proposed obstacle avoidance

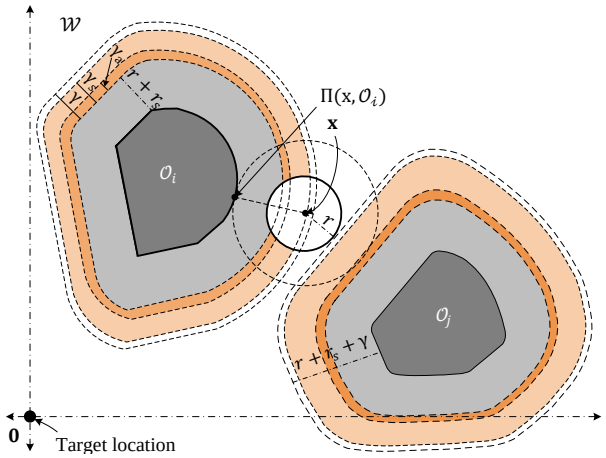

Figure 3.1: Workspace $\mathcal{W}$ with two convex obstacles separated by the distance greater than or equal to $2(r_a + \gamma)$. The $\gamma-$neighbourhood of dilated obstacles is further partitioned into three region such that $\gamma > \gamma_s > \gamma_a > 0$.

approach can be implemented using only range scanners (*e.g.,* LiDAR) without *a priori* global knowledge of the environment (sensor-based technique).

3.2 Problem formulation

We consider a disk-shaped robot with radius $r \geq 0$, operating in a two dimensional Euclidean space $\mathcal{W} \subseteq \mathbb{R}^2$ as shown in Fig. 3.1. The workspace contains a finite number of compact convex obstacles $\mathcal{O}_i \subset \mathcal{W}, i \in \{1, \ldots, b\} := \mathbb{I}$, where $b \in \mathbb{N}$ is the total number of obstacles. The task is to reach a predefined target location from any obstacle-free region while avoiding collisions. Without loss of generality, consider the origin $\mathbf{0}$ as the target location. Throughout this chapter we make the following feasibility assumption.

Assumption 3.1 *The minimum separation between any pair of obstacles is greater than* $2r$ *i.e., for all* $i, j \in \mathbb{I}, i \neq j$*, one has* $d(\mathcal{O}_i, \mathcal{O}_j) := \min_{\mathbf{p}\in\mathcal{O}_i, \mathbf{q}\in\mathcal{O}_j} \|\mathbf{p} - \mathbf{q}\| > 2r$.

According to Assumption 3.1 and the compactness of the obstacles, there exists a minimum separating distance between any pair of obstacles $\bar{r} = \min_{i,j\in\mathbb{I}, i\neq j} d(\mathcal{O}_i, \mathcal{O}_j) > 2r$. Moreover, for collision-free navigation we require $d(\mathbf{0}, \mathcal{O}_\mathcal{W}) - r > 0$, where $\mathcal{O}_\mathcal{W} := \bigcup_{i\in\mathbb{I}} \mathcal{O}_i$. We define a positive real $\bar{r}_s$ as

$$\bar{r}_s = \min \left\{ \frac{\bar{r}}{2} - r, d(\mathbf{0}, \mathcal{O}_\mathcal{W}) - r \right\}. \tag{3.1}$$

We then pick an arbitrarily small value $r_s \in (0, \bar{r}_s)$ as the minimum distance that the robot should maintain with respect to any obstacle.

The obstacle-free workspace is then defined as

$$\mathcal{W}_0 := \mathcal{W} \backslash \bigcup_{i\in\mathbb{I}} \mathcal{O}_i^\circ.$$

Given $y \geq 0$, an eroded version of the obstacle-free workspace, $\mathcal{W}_y$ is defined as

$$\mathcal{W}_y := \mathcal{W} \backslash \bigcup_{i \in \mathbb{I}} \left(\mathcal{D}_y(\mathcal{O}_i^\circ) \right) \subset \mathcal{W}_0. \tag{3.2}$$

Hence, $\mathcal{W}_{r_a}$ with $r_a = r + r_s$ is a free workspace with respect to the center of the robot *i.e.*, $\mathbf{x} \in \mathcal{W}_{r_a} \iff \mathcal{B}_{r_a}(\mathbf{x}) \subset \mathcal{W}_0$. The robot is governed by a single integrator dynamics

$$\dot{\mathbf{x}} = \mathbf{u}, \tag{3.3}$$

where $\mathbf{u} \in \mathbb{R}^2$ is the control input. Given a target location in the interior of the obstacle-free workspace *i.e.*, $\mathbf{0} \in \left(\mathcal{W}_{r_a}\right)^\circ$, we aim to design a feedback control law such that:

1. the obstacle-free space $\mathcal{W}_{r_a}$ is forward invariant,
2. the target location $\mathbf{x} = \mathbf{0}$ is a globally asymptotically stable equilibrium for the closed-loop system.

3.3 Hybrid control for obstacle avoidance

In the proposed scheme, similar to [Berkane et al., 2021a], depending upon the value of a mode indicator variable $m \in \{-1, 0, 1\} := \mathbb{M}$, the robot operates in two different modes, namely the *move-to-target* mode ($m = 0$) when it is away from the obstacles and the *obstacle-avoidance* mode ($m \in \{-1, 1\}$) when it is in the close proximity of any obstacle. In the *move-to-target* mode, the robot moves straight towards the target whereas during the *obstacle-avoidance* mode the robot moves around the nearest obstacle, either in the clockwise direction ($m = 1$) or in the counter-clockwise direction ($m = -1$). We allow the robot to exit the *obstacle-avoidance* mode whenever it can move straight towards the target without reducing its proximity from the nearest obstacle. We ensure that when the robot switches between the two modes, the velocity vector remains continuous.

Now, notice that, if the robot were to arbitrarily choose between the clockwise and counter-clockwise motions when it switches from the *move-to-target* mode to the *obstacle-avoidance* mode, then for some inter-obstacle arrangements the robot might get trapped in a closed trajectory around the target location. To avoid this situation, we propose a switching strategy which allows the robot to decide between the clockwise motion and the counter-clockwise motion based on its location and a line segment joining its initial location and the target location. When the robot operates in the *obstacle-avoidance* mode, it always attempts to go towards this line, which in turn ensures that the robot does not get trapped in a closed trajectory around the target and eventually converges to it. The results presented in this Chapter have been published in [Sawant et al., 2023a] and [Sawant et al., 2022a].

3.3.1 Hybrid control law

The proposed hybrid control law is given as

$$\mathbf{u}(\mathbf{x}, m) = -\kappa\sigma(\mathbf{x}, m)\mathbf{x} + \kappa[1 - \sigma(\mathbf{x}, m)]\mathbf{v}(\mathbf{x}, m), \tag{3.4a}$$

$$\underbrace{\dot{m} = 0,}_{(\mathbf{x},m)\in\mathcal{F}_{\mathcal{W}}} \qquad \underbrace{m^{+} = \mathbf{L}(\mathbf{x}, m),}_{(\mathbf{x},m)\in\mathcal{J}_{\mathcal{W}}} \tag{3.4b}$$

where $\kappa > 0$, and $\mathbf{x} \in \mathcal{W}_{r_a}$ is the location of the center of the robot. The discrete variable $m \in \mathbb{M}$ is the mode indicator. The update law $\mathbf{L}(\mathbf{x}, m) \in \mathbb{M}$ in (3.4b) will be provided later in Section 3.3.3. The flow set $\mathcal{F}_{\mathcal{W}}$ and the jump set $\mathcal{J}_{\mathcal{W}}$ will be defined later in Section 3.3.2. Next, we provide the construction of the vector $\mathbf{v}(\mathbf{x}, m) \in \mathbb{R}^2$ along with the scalar function $\sigma(\mathbf{x}, m) \in [0, 1]$, used in (3.4a).

The vector $\mathbf{v}(\mathbf{x}, m) \in \mathbb{R}^2$ is defined as

$$\mathbf{v}(\mathbf{x}, m) = \begin{bmatrix} 0 & m \\ -m & 0 \end{bmatrix} \frac{\mathbf{x} - \Pi(\mathbf{x}, \mathcal{O}_{\mathcal{W}})}{\|\mathbf{x} - \Pi(\mathbf{x}, \mathcal{O}_{\mathcal{W}})\|} \|\mathbf{x}\|, \tag{3.5}$$

where $\Pi(\mathbf{x}, \mathcal{O}_{\mathcal{W}})$, defined in Section 2.2.1, is the closest point on the boundary of the obstacle-occupied workspace from the robot's center. It should be noted that, if the center of the robot is within the $(r_a + \gamma_{ad})-$neighbourhood of any obstacle, let us say $\mathcal{O}_k, k \in \mathbb{I}$, where $\gamma_{ad} \in (0, \bar{r}_s - r_s)$, then the projection $\Pi(\mathbf{x}, \mathcal{O}_{\mathcal{W}})$ is unique and equals $\Pi(\mathbf{x}, \mathcal{O}_k)$. In this case, the rotational vector $\mathbf{v}(\mathbf{x}, m)$ allows the robot to revolve around the obstacle $\mathcal{O}_k$. The direction of the rotation depends on the value of the mode indicator variable. When $m = 1$ the robot moves in the clockwise direction, whereas if $m = -1$ it moves in the counter-clockwise direction with respect to the boundary of the obstacle $\mathcal{O}_k$.

The scalar function $\sigma : \mathcal{W}_{r_a} \times \mathbb{M} \to [0, 1]$ defined as

$$\sigma(\mathbf{x}, m) = 1 + m^2 \big[\eta(\varrho(\mathbf{x})) - 1\big], \tag{3.6}$$

allows for a continuous transition between the stabilizing vector $-\mathbf{x}$ and the rotational vector $\mathbf{v}(\mathbf{x}, m)$ whenever the robot operates in the *obstacle-avoidance* mode *i.e.*, $m \in \{-1, 1\}$, depending on its proximity with respect to the boundary of the set $\mathcal{O}_{\mathcal{W}}$. In (3.6), the scalar function $\varrho(\mathbf{x})$ evaluates the proximity of the robot with the unsafe region $\mathcal{O}_{\mathcal{W}}$, and is given by

$$\varrho(\mathbf{x}) = d(\mathbf{x}, \mathcal{O}_{\mathcal{W}}) - r_a. \tag{3.7}$$

According to (3.6), whenever $m \in \{-1, 1\}$, the value of $\sigma(\mathbf{x}, m)$ equals to the value of a non-decreasing continuous scalar function $\eta : \mathbb{R} \to [0, 1]$, defined as

$$\eta(\varrho(\mathbf{x})) = \begin{cases} 1, & \varrho(\mathbf{x}) \geq \gamma_s, \\ \frac{\varrho(\mathbf{x}) - \gamma_a}{\gamma_s - \gamma_a}, & \gamma_a \leq \varrho(\mathbf{x}) \leq \gamma_s, \\ 0, & \varrho(\mathbf{x}) \leq \gamma_a, \end{cases} \tag{3.8}$$

where $0 < \gamma_a < \gamma_s < \gamma$. The scalar function η is constructed such that the influence of the stabilizing control vector in (3.4a) decreases and the contribution from the rotational control vector increases, as the robot approaches the γ_a-neighbourhood of the obstacle-occupied workspace $\mathcal{O}_{\mathcal{W}}$. Next, we provide a geometric construction of the flow set $\mathcal{F}_{\mathcal{W}}$ and the jump set $\mathcal{J}_{\mathcal{W}}$, used in (3.4b).

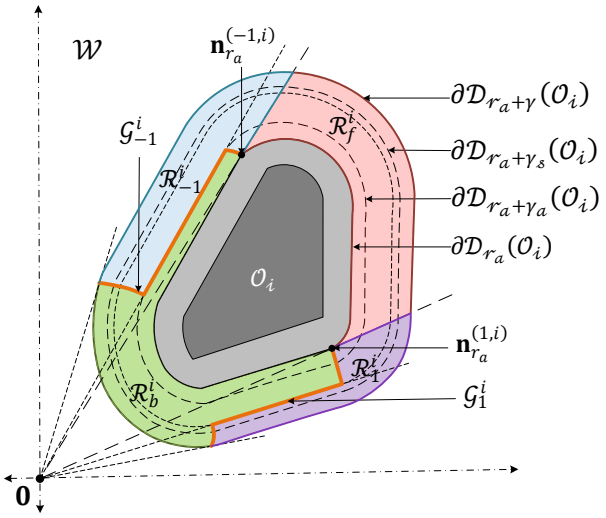

Figure 3.2: Partitions of the local neighbourhood of obstacle $\mathcal{O}_i,\ i \in \mathbb{I}$ based on the location of the target.

3.3.2 Geometric construction of the flow and jump sets

We define an $\gamma-$neighbourhood around the dilated obstacle $\mathcal{D}_{r_a}(\mathcal{O}_i), i \in \mathbb{I}$, where $\gamma \in (0, \bar{r}_s - r_s)$.[1] For an obstacle $\mathcal{O}_i, i \in \mathbb{I}$, the compact tubular neighbourhood $\mathcal{N}_\gamma(\mathcal{D}_{r_a}(\mathcal{O}_i)) := \mathcal{D}_{r_a+\gamma}(\mathcal{O}_i) \backslash \big(\mathcal{D}_{r_a}(\mathcal{O}_i)\big)^\circ$ is partitioned into several sub-regions, as shown in Fig. 3.2, which then will be used to construct the jump and the flow sets used in (3.4).

Back region

$\mathcal{R}_b^i$ is defined as

$$\mathcal{R}_b^i = \{\mathbf{q} \in \mathcal{N}_\gamma(\mathcal{D}_{r_a}(\mathcal{O}_i)) | \mathbf{q}^\intercal(\mathbf{q} - \Pi(\mathbf{q}, \mathcal{O}_i)) \leq 0\}. \tag{3.9}$$

The back region $\mathcal{R}_b^i$ is a closed connected subset of the region $\mathcal{N}_\gamma(\mathcal{D}_{r_a}(\mathcal{O}_i))$ such that for all $\mathbf{q} \in \mathcal{R}_b^i$ the angle measured from the vector $\mathbf{q}$ to the vector $\mathbf{q} - \Pi(\mathbf{q}, \mathcal{O}_i)$ satisfies $\psi(\mathbf{q}, (\mathbf{q} - \Pi(\mathbf{q}, \mathcal{O}_i))) \in [\frac{\pi}{2}, \frac{3\pi}{2}]$.

Gates

$\mathcal{G}_m^i,\ m \in \{-1, 1\}$, defined as

$$\mathcal{G}_m^i = \left\{ \mathbf{q} \in \mathcal{N}_\gamma(\mathcal{D}_{r_a}(\mathcal{O}_i)) | \psi(\mathbf{q}, (\mathbf{q} - \Pi(\mathbf{q}, \mathcal{O}_i))) = \frac{-m\pi}{2} \right\}, \tag{3.10}$$

are the regions where the vectors $\mathbf{q}$ and $(\mathbf{q} - \Pi(\mathbf{q}, \mathcal{O}_i))$ are orthogonal to each other. In Proposition 3.1, it is shown that, while operating in the *obstacle-avoidance* mode, away

[1] Note that the value of the parameter γ can be small. Since this parameter adds a safety margin around the robot's body, one can choose a sufficiently small value while compensating for the measurement noise.

from the boundary of the respective obstacle's unsafe region, if the robot switches to the *move-to-target* mode in the gate region, then the control input trajectories remain continuous.

Front region

$\mathcal{R}_f^i$ is defined as

$$\mathcal{R}_f^i = \{\mathbf{q} \in \mathcal{N}_\gamma(\mathcal{D}_{r_a}(\mathcal{O}_i)) | \mathcal{L}_s(\mathbf{q}, \mathbf{0}) \cap (\mathcal{D}_{r_a}(\mathcal{O}_i))^\circ \neq \emptyset\}. \tag{3.11}$$

If the robot, located in the front region $\mathcal{R}_f^i$, moves straight towards the origin, it will eventually enter in the unsafe region related to obstacle $\mathcal{O}_i$. To avoid this, in this region the robot should switch to the *obstacle-avoidance* mode.

Side regions

$\mathcal{R}_m^i$, $m \in \{-1, 1\}$, are constructed as

$$\begin{aligned} \mathcal{R}_1^i &= \{\mathbf{q} \in \mathcal{N}_\gamma(\mathcal{D}_{r_a}(\mathcal{O}_i)) \backslash \big(\mathcal{R}_b^i \cup \mathcal{R}_f^i\big) | \psi(\mathbf{q}, \mathbf{q} - \Pi(\mathbf{q}, \mathcal{O}_i)) \in [-\pi/2, 0]\}, \\ \mathcal{R}_{-1}^i &= \{\mathbf{q} \in \mathcal{N}_\gamma(\mathcal{D}_{r_a}(\mathcal{O}_i)) \backslash \big(\mathcal{R}_b^i \cup \mathcal{R}_f^i\big) | \psi(\mathbf{q}, \mathbf{q} - \Pi(\mathbf{q}, \mathcal{O}_i)) \in [0, \pi/2]\}. \end{aligned} \tag{3.12}$$

Since the intersection of the interior of the conic hull [Boyd et al., 2004, Section 2.1.5] for the dilated obstacle $\mathcal{D}_{r_a}(\mathcal{O}_i)$, having its vertex at the origin, with the side regions is empty, for $\mathbf{x} \in \mathcal{R}_m^i, m \in \{-1, 1\}$, the robot can move straight towards the target location, see Fig. 3.2.

Remark 3.1 *For an arbitrary compact convex obstacle $\mathcal{O}_i, i \in \mathbb{I}$, the projection of a point $\mathbf{q} \notin \mathcal{O}_i$ onto the obstacle $\mathcal{O}_i$ i.e., $\Pi(\mathbf{q}, \mathcal{O}_i)$ is continuous with respect to $\mathbf{q}$. As a result, the respective back region $\mathcal{R}_b^i$ defined in (3.9), is a compact connected subset of the $\gamma-$neighbourhood of the obstacle $\mathcal{O}_i$. Hence, one has for all $\mathbf{q} \in \mathcal{N}_\gamma(\mathcal{D}_{r_a}(\mathcal{O}_i)) \backslash \mathcal{R}_b^i$*

$$\mathbf{q}^\intercal(\mathbf{q} - \Pi(\mathbf{q}, \mathcal{O}_i)) > 0. \tag{3.13}$$

This concludes the partitioning of the $\gamma-$neighbourhood of the dilated obstacle $\mathcal{D}_{r_a}(\mathcal{O}_i)$ for some $i \in \mathbb{I}$. Similar regions are defined for all remaining obstacles. Next, we utilize these regions to define the flow and the jump sets for each mode of operation.

Flow and jump sets (*move-to-target* mode)

In this mode, the robot moves straight towards the origin. Consider Fig. 3.3 for a visual representation. As discussed earlier, the robot moving straight towards the origin should switch to the *obstacle-avoidance* mode whenever it enters $\mathcal{R}_f^i$, $\forall i \in \mathbb{I}$, otherwise it will collide with obstacle $\mathcal{O}_i$. Hence, we define the jump set $\mathcal{J}_0^i$ for each obstacle $i \in \mathbb{I}$ as

$$\mathcal{J}_0^i := \mathcal{D}_{r_a+\gamma_s}(\mathcal{O}_i) \cap \bar{\mathcal{R}}_f^i, \tag{3.14}$$

where $\gamma_s \in (0, \gamma)$.

However, if the center of the robot is located in the back or side regions of an obstacle $\mathcal{O}_i, i \in \mathbb{I}$, the robot can navigate safely with respect to obstacle $\mathcal{O}_i$ towards the target in the *move-to-target* mode. Hence, the flow set of the *move-to-target* mode $\mathcal{F}_0^i$ for each obstacle $\mathcal{O}_i, i \in \mathbb{I}$, defined as

$$\mathcal{F}_0^i := \left(\mathcal{W}_{r_a} \backslash \left(\mathcal{D}_{r_a+\gamma_s}(\mathcal{O}_i)\right)^\circ\right) \cup \mathcal{R}_{-1}^i \cup \mathcal{R}_1^i \cup \mathcal{R}_b^i, \tag{3.15}$$

includes the union of the back and side regions of the respective obstacle. Inspired by [Berkane et al., 2021a, (17)], taking all obstacles into consideration, the flow and jump sets for the *move-to-target* mode $m = 0$ are defined as

$$\mathcal{F}_0 := \bigcap_{i \in \mathbb{I}} \mathcal{F}_0^i, \quad \mathcal{J}_0 := \bigcup_{i \in \mathbb{I}} \mathcal{J}_0^i. \tag{3.16}$$

Next, we define the flow and jump sets for the *obstacle-avoidance* mode.

Flow and jump sets (*obstacle-avoidance* mode)

This mode is activated only if the robot enters in the $\gamma-$neighbourhood of some obstacle $\mathcal{O}_i,\ i \in \mathbb{I}$, which according to Assumption 3.1 can only be valid for at most one obstacle at any given time. We now consider the construction of the flow and jump sets for the *obstacle-avoidance* mode ($m \in \{-1, 1\}$) with a specific obstacle $\mathcal{O}_i$, as shown in Fig. 3.3. Here the mode indicator variable $m = -1$ and $m = 1$, prompts the robot to move in the counter-clockwise and clockwise directions with respect to the obstacle's boundary $\partial\mathcal{O}_i$, respectively. Hence for $m \in \{-1, 1\}$ the flow sets are constructed as follows:

$$\mathcal{F}_m^i := \mathcal{R}_m^i \cup \overline{\mathcal{E}\mathcal{R}_f^i \backslash \mathcal{R}_b^i}, \tag{3.17}$$

where the set $\mathcal{E}\mathcal{R}_f^i$ is defined as

$$\mathcal{E}\mathcal{R}_f^i = \{\mathbf{q} \in \mathcal{N}_\gamma(\mathcal{D}_{r_a}(\mathcal{O}_i)) | \mathcal{L}_s(\mathbf{q}, \mathbf{0}) \cap (\mathcal{D}_{r_a+\gamma_a}(\mathcal{O}_i))^\circ \neq \emptyset\}. \tag{3.18}$$

where $\gamma_a \in (0, \gamma_s)$. The jump set $\mathcal{J}_m^i$ of the respective mode, which includes the relative complement of the set $\mathcal{W}_{r_a}$ with respect to the interior of the flow set $\left(\mathcal{F}_m^i\right)^\circ$, is defined as

$$\mathcal{J}_m^i := (\mathcal{W}_{r_a} \backslash (\mathcal{D}_{r_a+\gamma}(\mathcal{O}_i))^\circ) \cup \mathcal{R}_b^i \cup \left(\mathcal{R}_{-m}^i \backslash \mathcal{E}\mathcal{R}_f^i\right). \tag{3.19}$$

Finally, taking all the obstacles into consideration, the flow and jump sets for the *obstacle-avoidance* mode are defined as

$$\mathcal{F}_m := \bigcup_{i \in \mathbb{I}} \mathcal{F}_m^i, \quad \mathcal{J}_m := \bigcap_{i \in \mathbb{I}} \mathcal{J}_m^i, \tag{3.20}$$

where $m \in \{-1, 1\}$. Finally the flow set $\mathcal{F}_\mathcal{W}$ and the jump set $\mathcal{J}_\mathcal{W}$ in (3.4a) are defined as

$$\mathcal{F}_\mathcal{W} := \bigcup_{m \in \mathbb{M}} (\mathcal{F}_m \times \{m\}),\ \mathcal{J}_\mathcal{W} := \bigcup_{m \in \mathbb{M}} (\mathcal{J}_m \times \{m\}), \tag{3.21}$$

with $\mathcal{F}_m, \mathcal{J}_m$ defined in (3.16) for $m = 0$ and in (3.20) for $m \in \{-1, 1\}$. Next, we provide the formalism for the update law $\mathbf{L}$ used in (3.4b).

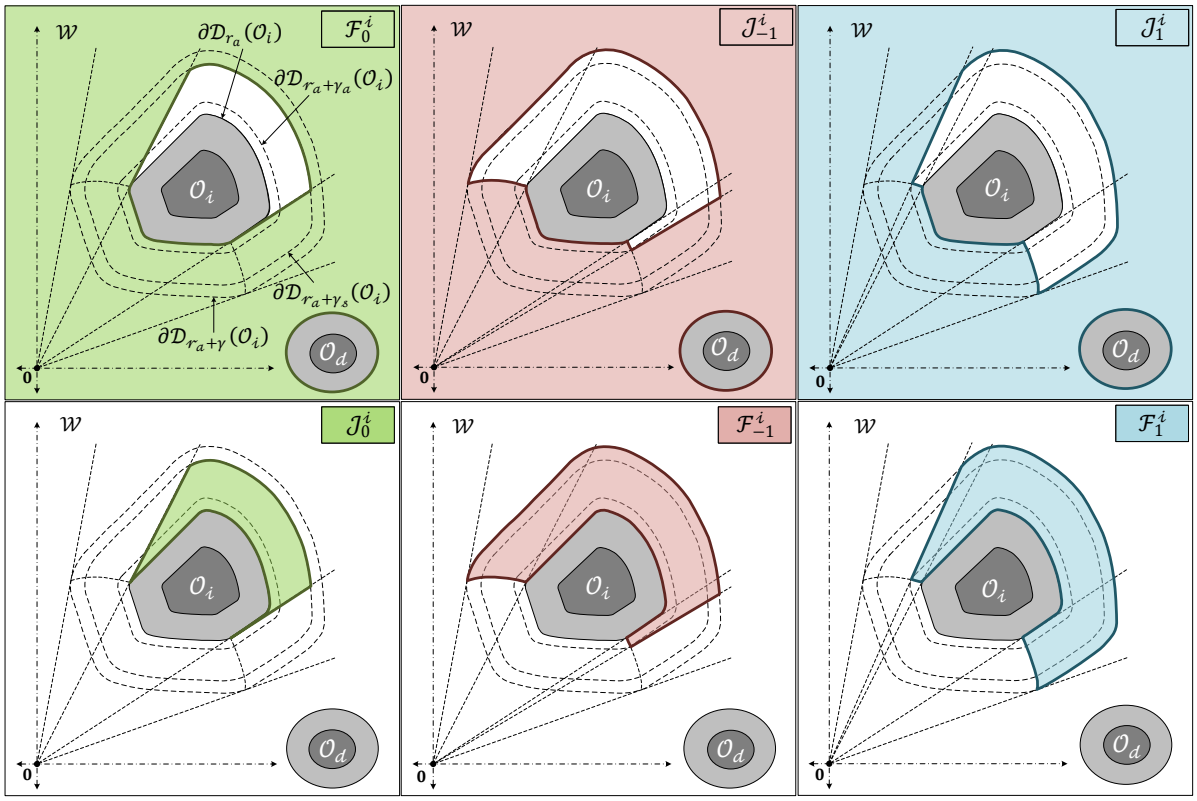

Figure 3.3: Geometric representations of the flow and jump sets for different modes of operation related to obstacle $\mathcal{O}_i$, $i \in \mathbb{I}$. The left figures ($m = 0$) illustrate the case where the robot operates in the *move-to-target* mode and moves straight toward the target location. The middle figures ($m = -1$) illustrate the case where the robot, operating in the *obstacle-avoidance* mode, moves in the counter-clockwise direction with respect to $\partial\mathcal{O}_i$. The right figures ($m = 1$) illustrate the case where the robot, operating in the *obstacle-avoidance* mode, moves in the clockwise direction with respect to $\partial\mathcal{O}_i$.

3.3.3 Mode selection map $\mathbf{L}(\mathbf{x}, m)$

The update law $\mathbf{L}(\mathbf{x}, m)$, used in (3.4b), allows the robot to update the value of the mode indicator variable $m \in \mathbb{M}$ when the state $(\mathbf{x}, m)$ belongs to the jump set $\mathcal{J}_{\mathcal{W}}$, which is defined in (3.21), is given as

$$\mathbf{L}(\mathbf{x}, m) = \begin{cases} 0, & (\mathbf{x}, m) \in \mathcal{J}_m \times \{-1, 1\}, \\ \mathbf{M}(\mathbf{x}), & (\mathbf{x}, m) \in \mathcal{J}_0 \times \{0\}. \end{cases} \tag{3.22}$$

When the robot enters in the jump set of the *obstacle-avoidance* mode, the value of the mode indicator variable switches to 0. The mapping $\mathbf{M}$, which is based on the current location of the center of the robot $\mathbf{x}$ with respect to the hyperplane $\mathcal{P}(\mathbf{0}, \mathbf{s})$ is defined as

$$\mathbf{M}(\mathbf{x}) := \begin{cases} \{-1\}, & \mathbf{x}^\intercal \mathbf{s} < 0, \\ \{-1, 1\}, & \mathbf{x}^\intercal \mathbf{s} = 0, \\ \{1\}, & \mathbf{x}^\intercal \mathbf{s} > 0, \end{cases} \tag{3.23}$$

where $\mathbf{s} \in \mathbb{R}^2 \backslash \{\mathbf{0}\}$ is an arbitrary non-zero constant vector. The switching strategy in (3.23), allows the robot to choose between the clockwise and counter-clockwise motions based on its current location whenever the state $(\mathbf{x}, m)$ belongs to the jump set of the *move-to-target* mode, $\mathcal{J}_0 \times \{0\}$. This strategy is crucial to establish global asymptotic convergence of the robot towards the target location, irrespective of the arrangements of the obstacles as it is going to be stated later in Theorem 3.1.

It is shown that if, at some point in time, the center of the robot does not belong to the half-line $\mathcal{L}_>(\mathbf{0}, \nu_{-1}(\mathbf{s}))$, then it will never enter the half-line $\mathcal{L}_>(\mathbf{0}, \nu_{-1}(\mathbf{s}))$ for all future times under the control law (3.4), where $\nu_z(\mathbf{p}) := \begin{bmatrix} 0 & z \\ -z & 0 \end{bmatrix} \mathbf{p}$, with $\mathbf{p} \in \mathbb{R}^2$ and $z \in \{-1, 1\}$. This ensures that our algorithm will never generate a closed trajectory around the target location. Moreover, the robot cannot move indefinitely in either $\mathcal{P}_>(\mathbf{0}, \mathbf{s})$ or $\mathcal{P}_<(\mathbf{0}, \mathbf{s})$ *i.e.*, during the motion it will either directly converge to the origin or intersect the half-line $\mathcal{L}_>(\mathbf{0}, \nu_1(\mathbf{s}))$, and with every consecutive intersection with this half-line, the robot gets closer to the origin. This concludes the definition of the update law $\mathbf{L}$ in (3.4b).

Control design summary: The proposed hybrid feedback control law can be summarized as follows:

- **Parameters selection**: the target location is set at the origin with $\mathbf{0} \in \mathcal{W}_{r_a}^\circ$. The state variables $\mathbf{x}$ and m are initialized such that $\mathbf{x}(0,0) \in \mathcal{W}_{r_a}$ and $m \in \mathbb{M}$. The gain parameter κ is set to a positive value. The scalar parameter γ, used in the construction of the flow set $\mathcal{F}_\mathcal{W}$ and the jump set $\mathcal{J}_\mathcal{W}$, is selected such that $\gamma \in (0, \bar{r}_s - r_s)$, where $\bar{r}_s$ is defined in (3.1). The parameters γ_a and γ_s are set to satisfy $0 < \gamma_a < \gamma_s < \gamma$.

- ***Move-to-target* mode** $m = 0$: this mode is activated when $\mathbf{x} \in \mathcal{F}_0$ and $m = 0$. As per (3.4a) and (3.6), the control input is given by $\mathbf{u}(\mathbf{x}, m) = -\kappa \mathbf{x}$, causing $\mathbf{x}$ to evolve along the line segment $\mathcal{L}_s(\mathbf{0}, \mathbf{x})$ towards the origin. If, at some instance of time, $(\mathbf{x}, m) \in \mathcal{J}_0 \times \{0\}$, the mode indicator variable m is updated using (3.22), and the control input switches to the *obstacle-avoidance* mode.

- ***Obstacle-avoidance* mode** $m \in \{-1, 1\}$: this mode is activated when $(\mathbf{x}, m) \in \mathcal{F}_m \times \{m\}$ for some $m \in \{-1, 1\}$. As per (3.4a) and (3.6), the control input is given by $\mathbf{u}(\mathbf{x}, m) = \kappa \eta(\rho(\mathbf{x})) \mathbf{v}(\mathbf{x}, m)$, causing $\mathbf{x}$ to evolve in the $\gamma-$neighborhood of the nearest modified obstacle until $(\mathbf{x}, m) \in \mathcal{J}_m \times \{m\}$, where $m \in \{-1, 1\}$. When $(\mathbf{x}, m) \in \mathcal{J}_m \times \{m\}$ with $m \in \{-1, 1\}$, the control input switches to the *move-to-target* mode by setting $m = 0$, as per (3.22).

This concludes the design of the proposed hybrid controller.

3.4 Forward invariance and stability analysis

As noted earlier, the robot operating with the proposed hybrid control law avoids one obstacle at a time. In general, while moving in the workspace, the robot might encounter more than one obstacle. To model this change of obstacle to be avoided, we introduce a

discrete variable $k \in \mathbb{I}$, which corresponds to the index of the obstacle being avoided by the robot while operating in the *obstacle-avoidance* mode. The hybrid evolution of the state k is given as

$$\underbrace{\dot{k} = 0,}_{\xi \in \mathcal{F}} \qquad \underbrace{k^+ = \mathbf{K}(\xi),}_{\xi \in \mathcal{J}} \tag{3.24}$$

where

$$\xi := (\mathbf{x}, m, k) \in \mathcal{W}_{r_a} \times \mathbb{M} \times \mathbb{I} =: \mathcal{K}, \tag{3.25}$$

is the composite state vector. The flow set $\mathcal{F}$ and the jump set $\mathcal{J}$ are defined as

$$\mathcal{F} = \mathcal{F}_{\mathcal{W}} \times \mathbb{I}, \qquad \mathcal{J} = \mathcal{J}_{\mathcal{W}} \times \mathbb{I}. \tag{3.26}$$

The update law for the state $k \in \mathbb{I}$, denoted as $\mathbf{K}(\xi)$, is designed to change the value of the variable k to the index of the closest obstacle whenever the robot encounters the jump set of the *move-to-target* mode. Otherwise, the value remains unchanged. Hence, $\mathbf{K}(\xi)$ is given as

$$\mathbf{K}(\xi) = \begin{cases} k', & \xi \in \mathcal{J}_0^{k'} \times \{0\} \times \mathbb{I}, \\ k, & \xi \in \mathcal{J}_m \times \{m\} \times \mathbb{I}, m \in \{-1, 1\}. \end{cases} \tag{3.27}$$

The hybrid closed-loop system, resulting from the control law (3.4b) and auxiliary state hybrid dynamics (3.24), is given by

$$\underbrace{\begin{aligned} \dot{\mathbf{x}} &= \mathbf{u}(\xi) \\ \dot{m} &= 0 \\ \dot{k} &= 0 \end{aligned}}_{\dot{\xi} = \mathbf{F}(\xi),\ \xi \in \mathcal{F},} \qquad \underbrace{\begin{aligned} \mathbf{x}^+ &= \mathbf{x} \\ m^+ &\in \mathbf{L}(\xi) \\ k^+ &\in \mathbf{K}(\xi) \end{aligned}}_{\xi^+ = \mathbf{J}(\xi),\ \xi \in \mathcal{J},} \tag{3.28}$$

where $\mathbf{u}(\xi)$ is defined in (3.4a), and the update laws $\mathbf{L}(\xi)$ and $\mathbf{K}(\xi)$ are provided in (3.22)-(3.23) and (3.27), respectively. The definitions of the flow set $\mathcal{F}$ and the jump set $\mathcal{J}$ are provided in (3.21), (3.26). In the next section, we analyze the hybrid closed-loop system (3.28) in terms of the forward invariance of the obstacle-free state space $\mathcal{K}$ along with the stability properties of the target set $\mathcal{A}$, which is defined as

$$\mathcal{A} := \{\mathbf{0}\} \times \mathbb{M} \times \mathbb{I}. \tag{3.29}$$

Next, we analyze the forward invariance of the obstacle-free workspace, which then will be followed by the convergence analysis. First, we show that the hybrid closed-loop system (3.28) satisfies the hybrid basic conditions, as stated in Assumption 2.1, which allows us to invoke some useful results on hybrid systems in our proofs.

Lemma 3.1 *The hybrid closed-loop system* (3.28) *with the data* $(\mathcal{F}, \mathbf{F}, \mathcal{J}, \mathbf{J})$ *satisfies the hybrid basic conditions stated in Assumption 2.1.*

Proof See Appendix B.1.

For safe autonomous navigation, the robot should belong to the obstacle-free workspace $\mathcal{W}_0$ for all time *i.e.*, the state $\mathbf{x}$ must always evolve within the robot-centered free workspace $\mathcal{W}_{r_a}$, regardless of the variables k and m. This is equivalent to showing that the set $\mathcal{K}$, defined in (3.25), is forward invariant with respect to the hybrid closed-loop system (3.28). This is stated in the next Lemma.

Lemma 3.2 (Safety) *Under Assumption 3.1, for the obstacle-free set $\mathcal{K}$, defined in (3.25), and the hybrid closed-loop system (3.28), the set $\mathcal{K}$ is forward invariant.*

Proof See Appendix B.2.

The proposed switching strategy between the *move-to-target* mode and the *obstacle-avoidance* mode is similar to the strategies used in the sensor-based path planning algorithms for a point robot, referred to as bug algorithms [Ng and Bräunl, 2007]. As discussed earlier, in [Matveev et al., 2011], [Berkane et al., 2021a], the authors imposed restrictions on the inter-obstacle arrangements to avoid closed trajectories around the target location. In the proposed approach, non-existence of closed trajectories, around the target location, is guaranteed by design without imposing any restrictions on the inter-obstacle arrangements except for the ones stated in Assumption 3.1. The next lemma shows that the robot operating with the proposed hybrid controller (3.4b), in environments satisfying Assumption 3.1, does not get stuck in any closed trajectory around the target location.

Lemma 3.3 *Consider the hybrid closed-loop system (3.28) and let Assumption 3.1 hold. If $\xi(t_0, j_0) \in \mathcal{W}_{r_a} \backslash \mathcal{L}_{>}(\mathbf{0}, \nu_{-1}(\mathbf{s})) \times \{0\} \times \mathbb{I}$ at some $(t_0, j_0) \in \operatorname{dom} \xi$, then $\xi(t, j) \notin \mathcal{L}_{>}(\mathbf{0}, \nu_{-1}(\mathbf{s})) \times \mathbb{M} \times \mathbb{I}$ for all $(t, j) \succeq (t_0, j_0)$.*

Proof See Appendix B.3.

Lemma 3.3 shows that if the robot, operating in the obstacle-free workspace $\mathcal{W}_{r_a}$, with the *move-to-target* mode, does not belong to the half-line $\mathcal{L}_{>}(\mathbf{0}, \nu_{-1}(\mathbf{s}))$, see Fig. B.3, at some time (t_0, j_0), then it can never intersect the half-line $\mathcal{L}_{>}(\mathbf{0}, \nu_{-1}(\mathbf{s}))$ for all $(t, j) \succeq (t_0, j_0)$. An example is provided in Fig. B.3, showing that the robot's trajectory, initialized at $\mathbf{x}_2$, does not intersect the half-line $\mathcal{L}_{>}(\mathbf{0}, \nu_{-1}(\mathbf{s}))$ represented in red. The main reason behind this behaviour is the switching strategy (3.23) for the mode indicator variable when the solution enters in the *obstacle-avoidance* mode, which assigns the direction of motion that always steers the robot away from the half-line $\mathcal{L}_{>}(\mathbf{0}, \nu_{-1}(\mathbf{s}))$. This feature ensures that the robot cannot revolve around the target location. Next, we provide one of our main results which establishes the fact that for all initial conditions in the obstacle-free set $\mathcal{K}$, the proposed hybrid controller not only ensures safe navigation but also guarantees global asymptotic convergence to the predefined target location at the origin.

We define the Lebesgue measure zero set $\mathcal{Z}_0 := \mathcal{M}_0 \times \mathbb{M} \times \mathbb{I}$ such that

$$\mathcal{M}_0 := \bigcup_{i \in \mathbb{I}} (\partial \mathcal{D}_{r_a}(\mathcal{O}_i) \cap \mathcal{J}_0^i), \tag{3.30}$$

is the intersection of the boundaries of the unsafe region and the *move-to-target* mode jump set. The intersection of the *move-to-target* mode jump set $\mathcal{J}_0 \times \{0\} \times \mathbb{I}$ and the *obstacle-avoidance* mode jump set $\mathcal{J}_m \times \{m\} \times \mathbb{I}, m \in \{-1, 1\}$, is not empty, for $\mathbf{x} \in \mathcal{M} := \bigcup_{i \in \mathbb{I}} \{\mathbf{n}_{r_a}^{(-1,i)}, \mathbf{n}_{r_a}^{(1,i)}\}$, where

$$\mathbf{n}_y^{(m,i)} = \underset{\mathbf{q} \in \partial \mathcal{D}_y(\mathcal{O}_i) \cap \mathcal{G}_m^i}{\arg\max} \|\mathbf{q}\|. \tag{3.31}$$

Note that $\mathbf{n}_y^{(m,i)}$ is the farthest point from the origin, which belongs to the boundary of the dilated obstacle $\mathcal{D}_y(\mathcal{O}_i)$ such that $\psi(\mathbf{q}, \mathbf{q} - \Pi(\mathbf{q}, \mathcal{O}_i))$ is $-m\pi/2$. For example, see points $\mathbf{n}_{r_a}^{(m,i)}, m \in \{-1, 1\}$, depicted in Fig. 3.2. As stated next in Theorem 3.1, the solution will reach the Zeno set $\mathcal{M} \times \mathbb{M} \times \mathbb{I} =: \mathcal{Z}$ when it is initialized in the Lebesgue measure zero set $\mathcal{Z}_0$.

Theorem 3.1 *Consider the hybrid closed-loop system* (3.28) *and let Assumption 3.1 hold. Then,*

i) the obstacle-free set $\mathcal{K}$ is forward invariant,

ii) the set $\mathcal{A}$ is almost globally asymptotically stable,

iii) the solutions will converge to $\mathcal{A}$ from all initial conditions except from the set of Lebesgue measure zero $\mathcal{Z}_0$ where the solutions may stay jumping in $\mathcal{Z}$ (Zeno behavior),

Proof See Appendix B.5.

It is worth pointing out that the almost global stability result established in Theorem 3.1 is not due to the existence of undesired saddle points as in [Koditschek and Rimon, 1990], but due to the potential existence of a Zeno behaviour [Goebel et al., 2012]. In fact, if the robot is initialized in $\mathcal{M}_0$, which consists of all the inner boundaries of the front regions, it may not converge to the target and instead will converge to some isolated points where it will experience a Zeno behaviour by switching indefinitely between the two modes of operation. This behaviour is obtained only if the jumps are prioritized over the flows in the implementation.

Remark 3.2 *It is possible to avoid the Zeno behaviour by prioritizing flows over jumps, however this arrangement does not always satisfy the useful structural and robustness properties of the set of solutions guaranteed by the hybrid basic conditions [Goebel et al., 2012, Assumption 6.5]. Another practical way (different from prioritizing the flows over jumps), that helps in avoiding the Zeno behaviour, consists in introducing a small enough time period $\tau > 0$ (dwell time) between consecutive jumps. This will force the solution ξ, after switching once, to leave the set $\mathcal{M}$ through the flow. The hybrid basic conditions are in this case preserved.*

Remark 3.3 (Continuous input) *The continuous scalar function σ, as described in (3.6), helps to guarantee the continuity of the control input vector when transitioning from the move-to-target mode to the obstacle-avoidance mode. On the other hand, the control law switches from the obstacle-avoidance mode to the move-to-target mode at the gate region. This ensures that the obstacle-avoidance control vector $\kappa\mathbf{v}(\mathbf{x}, m)$ and the stabilization control vector $-\kappa\mathbf{x}$ are equivalent at the location where the control law switches back to the move-to-target mode, thereby helping to guarantee the continuity of the control input. This interesting feature of the proposed hybrid control law (3.4b) is formalized in Proposition 3.1.*

Proposition 3.1 *Consider the closed-loop system (3.3) and let Assumption 3.1 hold. If $\xi(t_0, j_0) \in \mathcal{K}\backslash\mathcal{Z}_0$, for some $(t_0, j_0) \in$ dom ξ, then the control input trajectories $\mathbf{u}(\xi(t, j))$, generated according to (3.4b), are continuous $\forall (t, j) \succeq (t_0, j_0)$.*

Proof See Appendix B.6.

According to Proposition 3.1, if the solution is in the set $\mathcal{K}\backslash\mathcal{Z}_0$ at some time $(t_0, j_0) \in$ dom ξ during the evolution, then the proposed hybrid feedback control law (3.4b) ensures that continuous control input trajectories are generated for all subsequent times $(t, j) \succeq (t_0, j_0)$. This concludes the stability analysis of the hybrid closed-loop system (3.28). Next, we provide a procedure to implement the proposed hybrid feedback controller (3.4b) for safe autonomous navigation of a mobile robot operating in *a priori* known and unknown environments.

3.5 Sensor-based implementation procedure

Without loss of generality, we assume that the target location is at the origin, and we set $m(0, 0) = 0$. The non-zero vector $\mathbf{s}$, used in (3.23), can be selected such that $\mathbf{x}(0, 0) \in \mathcal{L}_{>}(\nu_1(\mathbf{s}))$. Then the robot can implement the proposed hybrid control law (3.4), using Algorithm 1. Since the parameters $\gamma > \gamma_s > \gamma_a > 0$ can be tuned offline, Algorithm 1 should be implemented excluding the steps highlighted in blue color. The blue colored steps are essential for the sensor-based implementation in an *a priori* unknown environment.

In the case where the environment is *a priori* unknown, we choose a sufficiently small value of the parameter $\gamma \in (0, \bar{r}_s - r_s)$, which ensures that the target location is at a distance greater than $r_a + \gamma$ from the unsafe region. We assume that the robot is equipped with a range-bearing sensor with angular scanning range of 360° and sensing radius $R_s > r_a + \gamma$. Due to the limited sensing radius, the robot can only detect a subset of the obstacles $\mathbb{I}_{\mathbf{x}} \subseteq \mathbb{I}$, defined as

$$\mathbb{I}_{\mathbf{x}} = \{i \in \mathbb{I} | d(\mathbf{x}, \mathcal{O}_i) \leq R_s\}. \tag{3.32}$$

Based on the local sensing information, we provide a procedure that allows to identify whether the state $(\mathbf{x}, m)$ belongs to the jump set $\mathcal{J}_{\mathcal{W}}$ (3.21) or not, when $m(0, 0) = 0$, which is summarized in Algorithm 2. Similar to [Arslan and Koditschek, 2019; Berkane,

Algorithm 1 General implementation of the proposed hybrid control law (3.4).

Set target location at the origin $\mathbf{0}$.
Initialize $\mathbf{x}(0,0) \in \mathcal{W}_{r_a}$, $m(0,0) = 0$, $\gamma \in (0, \bar{r}_s - r_s)$. Pick $\mathbf{s} \in \mathbb{R}^2 \backslash \{\mathbf{0}\}$, used in (3.23), such that $\mathbf{x}(0,0) \in \mathcal{L}_{\geq}(\mathbf{0}, \nu_1(\mathbf{s}))$.
Measure $\mathbf{x}$.
if $m = 0$, **then**
  Implement Algorithm 2.
  if $(\mathbf{x}, m) \in \mathcal{J}_0 \times \{0\}$, **then**
    Set $\gamma_s = d(\mathbf{x}, \mathcal{O}_{\mathcal{W}}) - r_a$.
    Select $\gamma_a = (0, \gamma_s)$.
    Update $m \leftarrow \mathbf{L}(\mathbf{x}, m)$ using (3.22), (3.23).
  end if
end if
if $m \in \{-1, 1\}$, **then**
  Implement Algorithm 2.
  if $(\mathbf{x}, m) \in \mathcal{J}_m \times \{m\}$, **then**
    Update $m \leftarrow \mathbf{L}(\mathbf{x}, m)$ using (3.22), (3.23).
  end if
end if
Execute $\mathbf{u}(\mathbf{x}, m)$ (3.4), used in (4.29).
Go to step 3.

2021], the range-bearing sensor is modeled using a polar curve $r_g(\mathbf{x}, \theta) : \mathcal{W}_{r_a} \times [-\pi, \pi] \to [0, R_s]$,

$$r_g(\mathbf{x}, \theta) = \min \left\{ R_s, \min_{\substack{\mathbf{y} \in \partial \mathcal{O}_{\mathcal{W}} \\ \text{atan2}(\mathbf{y} - \mathbf{x}) = \theta}} \|\mathbf{x} - \mathbf{y}\| \right\}, \tag{3.33}$$

which represents the distance between the center of the robot and the boundary of the unsafe region $\partial \mathcal{O}_{\mathcal{W}}$, measured by the sensor, in the direction defined by the angle θ. Given the location of the center of the robot $\mathbf{x}$, along with the bearing angle θ, the mapping $\lambda(\mathbf{x}, \theta) : \mathcal{W}_{r_a} \times [-\pi, \pi] \to \mathcal{W}_0$, given by

$$\lambda(\mathbf{x}, \theta) = \mathbf{x} + r_g(\mathbf{x}, \theta)[\cos\theta, \sin\theta]^\intercal, \tag{3.34}$$

evaluates the Cartesian coordinates of the detected point.

The robot should identify the minimum distance from the set $\mathcal{O}_{\mathcal{W}}$,

$$d(\mathbf{x}, \mathcal{O}_{\mathcal{W}}) = \min_{\theta \in [-\pi, \pi]} r_g(\mathbf{x}, \theta). \tag{3.35}$$

If $d(\mathbf{x}, \mathcal{O}_{\mathcal{W}})$ is greater than or equal to $r_a + \gamma$, then, according to (3.14), (3.16) and (3.21), the state $(\mathbf{x}, m) \notin \mathcal{J}_0 \times \{0\}$, *i.e.*, the robot should continue to operate in the

move-to-target mode. On the other hand, if $d(\mathbf{x}, \mathcal{O}_{\mathcal{W}}) \in [r_a, r_a + \gamma]$, which, according to Assumption 3.1, can be true for only one obstacle, let us say $k \in \mathbb{I}_{\mathbf{x}}$, then the robot should identify whether the state $\mathbf{x}$ belongs to the back region of the respective obstacle $\mathcal{R}_b^k$ or not. The robot should locate the projection of its center onto the obstacle $\mathcal{O}_k$ *i.e.*, $\Pi(\mathbf{x}, \mathcal{O}_k)$, which is unique and given by

$$\Pi(\mathbf{x}, \mathcal{O}_k) = \lambda(\mathbf{x}, \theta^*), \tag{3.36}$$

where

$$\theta^* = \underset{\theta \in [-\pi, \pi]}{\operatorname{argmin}} r_g(\mathbf{x}, \theta). \tag{3.37}$$

Then, the robot should verify the following condition:

$$\mathbf{x}^\intercal (\mathbf{x} - \Pi(\mathbf{x}, \mathcal{O}_k)) \leq 0. \tag{3.38}$$

The satisfaction of (3.38) implies that the state $\mathbf{x}$ belongs to the back region of the obstacle $\mathcal{O}_k$, and, according to (3.14), (3.16) and (3.21), $(\mathbf{x}, m) \notin \mathcal{J}_0 \times \{0\}$ implying that the robot can continue to operate in the *move-to-target* mode. Otherwise, if (3.38) is not satisfied, the robot should further investigate the possibility of collision while operating in the *move-to-target* mode.

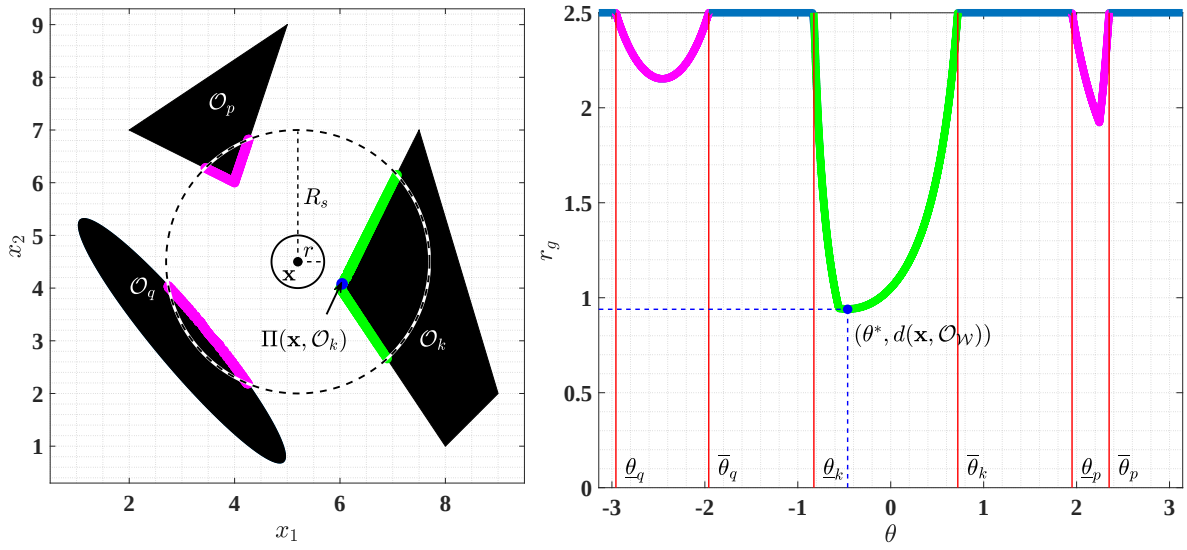

Figure 3.4: The left figure shows a robot, with radius $r = 0.5m$, using a range-bearing sensor to locate the partial boundary of the obstacles within the sensing range $R_s = 2.5m$, wherein observed boundary of the nearest obstacle is shown in green and the observed boundaries of the remaining obstacles are represented by the blue colored curves. The right figure displays the range measurements obtained with a sensor located at $\mathbf{x}$ for $\theta \in [-\pi, \pi]$. Similar colors have been used to represent the correlation between the points on the boundary of the observed obstacles (left figure) and the rang/bearing measurements (right figure).

Next, the robot should identify the boundary curve $\eth\mathcal{O}_k \subset \partial\mathcal{O}_k$, which is a set of points which belongs to the boundary of the obstacle $\mathcal{O}_k$ and are in the line-of-sight of

the center of the robot. Figure 3.4 illustrates the measurements obtained via a range-bearing sensor when the robot is located in the obstacle-free space. Since the obstacles are disjoint with a minimum separation greater than $2r$ as per Assumption 3.1, the range-bearing measurement graph, shown in Fig. 3.4, consists of convex curves, one for each of the obstacles present within the sensing region $\mathcal{B}_{R_s}(\mathbf{x})$.

For each obstacle $\mathcal{O}_i, i \in \mathbb{I}_{\mathbf{x}}$, the robot can identify $\underline{\theta}_i, \overline{\theta}_i \in [-\pi, \pi]$ such that the measurements related to the obstacle $\mathcal{O}_i, i \in \mathbb{I}_{\mathbf{x}}$, lie within the angular range of $\left[\underline{\theta}_i, \overline{\theta}_i\right]$, as shown in Fig. 3.4. Since the measurements are acquired in the line-of-sight format, there cannot be any overlap between the angular intervals related to any two obstacles i.e., $\left[\underline{\theta}_i, \overline{\theta}_i\right] \cap \left[\underline{\theta}_j, \overline{\theta}_j\right] = \emptyset, i, j \in \mathbb{I}_{\mathbf{x}}, i \neq j$. The robot should then identify $\left[\underline{\theta}_k, \overline{\theta}_k\right]$ for the obstacle $\mathcal{O}_k$ where

$$k = \left\{ i \in \mathbb{I}_{\mathbf{x}} | \theta^* \in \left[\underline{\theta}_i, \overline{\theta}_i\right] \right\}, \tag{3.39}$$

then the set $\eth\mathcal{O}_k$ can be defined as

$$\eth\mathcal{O}_k = \left\{ \lambda(\mathbf{x}, \theta) \in \mathcal{W}_0 | \theta \in \left[\underline{\theta}_k, \overline{\theta}_k\right] \right\}. \tag{3.40}$$

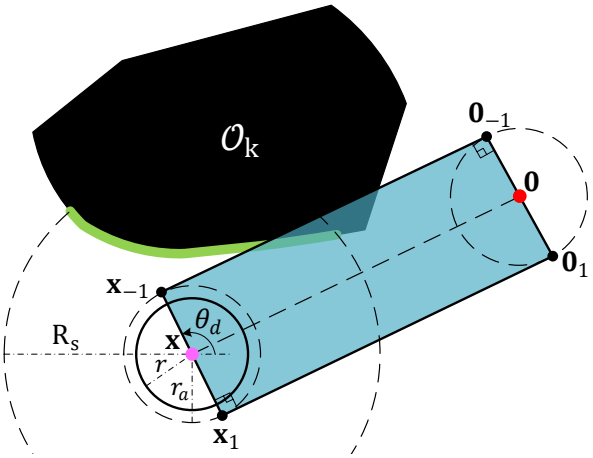

Figure 3.5: Construction of the rectangle $\square(\mathbf{x})$, used in (3.42), based on the location of the robot and the target location at the origin.

The robot should then construct a rectangle $\square(\mathbf{x})$ with its vertices located at the points $\mathbf{x}_{-1}, \mathbf{x}_1, \mathbf{0}_{-1}$ and $\mathbf{0}_1$, as shown in Fig. 3.5, defined as

$$\begin{bmatrix} \mathbf{x}_z \\ \mathbf{0}_z \end{bmatrix} = \begin{bmatrix} \mathbf{x} \\ \mathbf{0} \end{bmatrix} + z r_a \begin{bmatrix} \mathbf{I} \\ \mathbf{I} \end{bmatrix} \begin{bmatrix} \cos\theta_d \\ \sin\theta_d \end{bmatrix}, z \in \{-1, 1\}, \tag{3.41}$$

where $\mathbf{I}$ is a 2×2 identity matrix, and $\theta_d = \pi/2 + \text{atan2}(\mathbf{x})$. It is straightforward to notice that, the robot can continue to navigate in the *move-to-target* mode, safely with respect to partial obstacle boundary $\eth\mathcal{O}_k$, if and only if the following condition holds true:

$$\eth\mathcal{O}_k \cap \square(\mathbf{x}) = \emptyset. \tag{3.42}$$

If the above condition is not satisfied at some (t, j), as illustrated in Fig. 3.5, then the robot can conclude that continuing to move in the *move-to-target* mode will result in a

collision with obstacle $\mathcal{O}_k$ *i.e.*, $(\mathbf{x}(t,j), m(t,j)) \in \mathcal{J}_0 \times \{0\}$, and that now it should operate in the *obstacle-avoidance* mode. At this instant, the robot should set $\gamma_s = d(\mathbf{x}, \mathcal{O}_\mathcal{W}) - r_a$ and $\gamma_a = p\gamma_s, p \in (0,1)$. Finally, as the robot starts operating in the *obstacle-avoidance* mode, it should continuously verify (3.38) to identify whether it has entered the back region of obstacle $\mathcal{O}_k$. Satisfaction of (3.38), according to (3.14), (3.20) and (3.21), implies that the state $(\mathbf{x}, m)$ belongs to the jump set of the *obstacle-avoidance* mode.

Remark 3.4 *The proposed hybrid control law* (3.4) *requires the state* $(\mathbf{x}, m)$ *and the projection of* $\mathbf{x}$ *on the nearest obstacle. Additionally, it also requires knowledge of all positions along the visible boundary of the nearest obstacle when the robot enters the* γ*-neighborhood of that obstacle. This additional information is crucial to determine whether the state* $(\mathbf{x}, m)$ *belongs to the jump set of the move-to-target mode or not.*

3.6 Simulation results

In this section, we present simulation results for a robot navigating in *a priori* unknown environments. In both simulations discussed below, the robot is assumed to be equipped with a range-bearing sensor (*e.g.* LiDAR) with angular scanning range of 360° and sensing radius $R_s = 1.5m$. The angular resolution of the sensor is chosen to be 0.5°. The simulations are performed in MATLAB 2020a.

In the first simulation scenario, we consider an environment with 6 convex obstacles, as shown in Fig. 3.6. The robot with radius $r = 0.3m$ is initialized at $[-22, 0]^\intercal$. The target is located at the origin. The minimum safety distance $r_s = 0.1m$. We set $\gamma = 0.35m$ and choose the location of the vector $\mathbf{s}$, used in (3.23), to be $[0, -1]^\intercal$. We set the gain value κ, used in (3.4), to be 0.2. Fig. 3.6 illustrates the motion of the robot towards the target location while avoiding obstacles. Whenever the robot enters in the $\gamma-$neighbourhood of any obstacle, it identifies the points on the boundary of that respective obstacle, which are in the line-of-sight of the center of the robot, to investigate the collision possibilities while operating in the *move-to-target* mode, as shown by the green curve in Fig. 3.6 for obstacle $\mathcal{O}_2$ and $\mathcal{O}_4$. Then by verifying the condition in (3.42), the robot chooses either to stay in the *move-to-target* mode or switch to the *obstacle-avoidance* mode. When the robot operates in the *obstacle-avoidance* mode, it only needs to identify the closest point on the nearest obstacle, as depicted with the pink dot in Fig. 3.6, which is used in the rotational control vector $\mathbf{v}(\mathbf{x}, m)$ (3.5). The complete simulation video can be found at https://youtu.be/llRrbGfvGBA.

In the second simulation scenario, and as shown in Fig. 3.7, we consider an environment consisting of convex obstacles with smooth and non-smooth boundaries, and apply the proposed hybrid controller (3.4) for a point robot navigation initialized at 14 different locations in the obstacle-free workspace. The safety distance $r_s = 0.15$, and the value of the variable $\gamma = 0.5$. We set the gain value κ, used in (3.4), to be 0.2. For each initialization, the vector $\mathbf{s}$, used in (3.23), is selected such that the initial location of the robot belongs to the half-line $\mathcal{L}_{\geq}(\mathbf{0}, \nu_1(\mathbf{s}))$. It can be noticed that the point robot intersects with the half-line $\mathcal{L}_{>}(\mathbf{0}, \nu_1(\mathbf{s}))$ and with each consecutive intersections it moves closer to

Algorithm 2 Sensor-based identification of the jump set.

Measure $d(\mathbf{x}, \mathcal{O}_{\mathcal{W}})$ defined in (3.35).
if $m = 0$, **then**
  if $d(\mathbf{x}, \mathcal{O}_{\mathcal{W}}) \leq r_a + \gamma$, **then**
    Identify $\mathcal{O}_k, k \in \mathbb{I}$ using (3.37), (3.39).
    Locate $\Pi(\mathbf{x}, \mathcal{O}_k)$ defined in (3.36).
    if $\mathbf{x}^\intercal(\mathbf{x} - \Pi(\mathbf{x}, \mathcal{O}_k)) > 0$, see (3.38), **then**
      Identify $\eth\mathcal{O}_k$ using (3.40).
      Construct $\square(\mathbf{x})$ using (3.41).
      if $\eth\mathcal{O}_k \cap \square(\mathbf{x}) \neq \emptyset$, see (3.42), **then**
        $(\mathbf{x}, m) \in \mathcal{J}_0 \times \{0\}$.
      else
        $(\mathbf{x}, m) \notin \mathcal{J}_0 \times \{0\}$.
      end if
    else
      $(\mathbf{x}, m) \notin \mathcal{J}_0 \times \{0\}$.
    end if
  else
    $(\mathbf{x}, m) \notin \mathcal{J}_0 \times \{0\}$.
  end if
end if
if $m \in \{-1, 1\}$, **then**
  if $d(\mathbf{x}, \mathcal{O}_{\mathcal{W}}) \leq r_a + \gamma$, **then**
    Identify $\mathcal{O}_k, k \in \mathbb{I}$ using (3.37), (3.39).
    Locate $\Pi(\mathbf{x}, \mathcal{O}_k)$ defined in (3.36).
    if $\mathbf{x}^\intercal(\mathbf{x} - \Pi(\mathbf{x}, \mathcal{O}_k)) \leq 0$, see (3.38), **then**
      $(\mathbf{x}, m) \in \mathcal{J}_m \times \{m\}$.
    end if
  else
    $(\mathbf{x}, m) \in \mathcal{J}_m \times \{m\}$.
  end if
end if

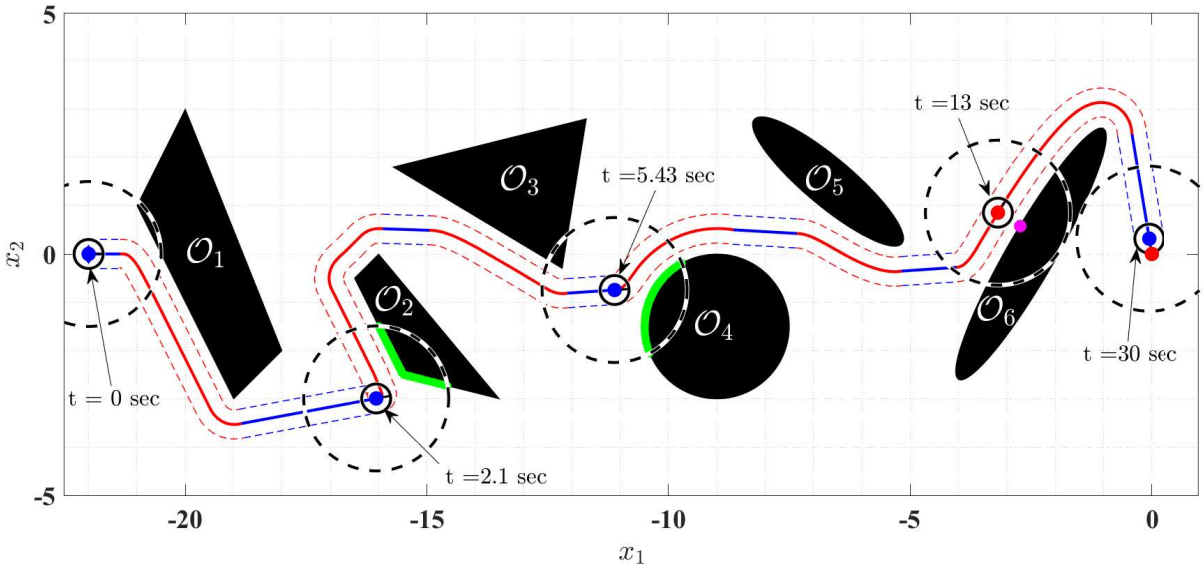

Figure 3.6: Robot safely navigating towards the target (red dot), along with three intermediate locations along the path.

the target location at the origin while ensuring obstacle avoidance, as shown in Fig. 3.7. The complete simulation video can be found at https://youtu.be/_AwDqNY06rU.

Notice that when the robot operates in the *move-to-target* mode, in addition to its own location and the target location, it only requires its distance from the nearby obstacles. When it operates in the *obstacle-avoidance* mode, it further requires the closest point on the obstacle-occupied workspace $\mathcal{O}_{\mathcal{W}}$. The robot needs to identify all the points on the closest obstacle which are in the line-of-sight of the center of the robot only when it operates in the *move-to-target* mode inside the $\gamma-$neighbourhood of any obstacle so that it can evaluate the possibility of collision and switch to the *obstacle-avoidance* mode, as stated in Remark 3.4.

The proposed hybrid feedback algorithm has been designed with some robustness to noise properties through the additional safety layers around the obstacles and the overlaps between the flow and jump sets. For example, for a range-bearing sensor with measurement error of $\pm\delta$, one should ensure that the separation between the $\gamma-$safety layer and the γ_s-safety layer should be greater than δ. Similarly, to ensure collision free motion while operating in the *obstacle-avoidance* mode, the γ_a-safety layer should be larger than δ, see Fig. 3.2 for the construction of these layers.

The simulation results given in Fig. 3.8 show the effectiveness of our proposed algorithm implemented with noisy sensor data. We consider an environment similar to the one shown in Fig. 3.6. The robot radius is $0.3m$ and the minimum safety distance is $r_s = 0.1m$. We set $\gamma = 0.35m$ and choose the gain $\kappa = 0.2$. The range measurements are affected by a Gaussian noise of 0 mean and $50mm$ standard deviation. Figure 3.8 shows the trajectory of the robot, initialized at $[-22, 0]^\intercal$, converging to the target location at the origin. Figure 3.9 indicates that even in the presence of measurement noise, the robot maintains a safe distance from the obstacle-occupied workspace.

We next provide a comparison with the separating hyperplane approach recently

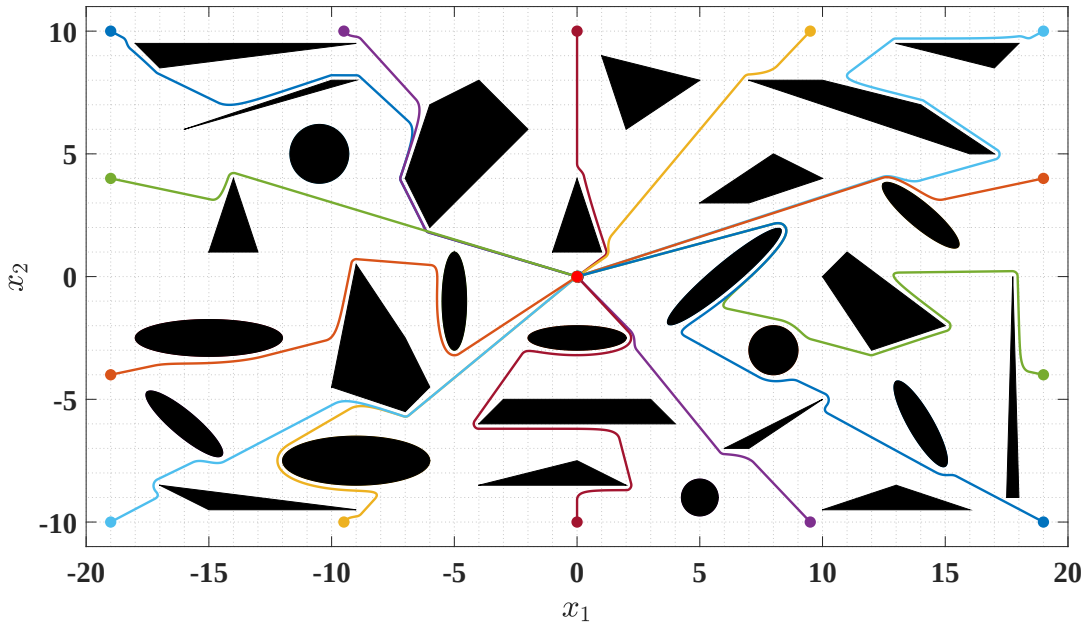

Figure 3.7: Robot trajectories starting from different locations.

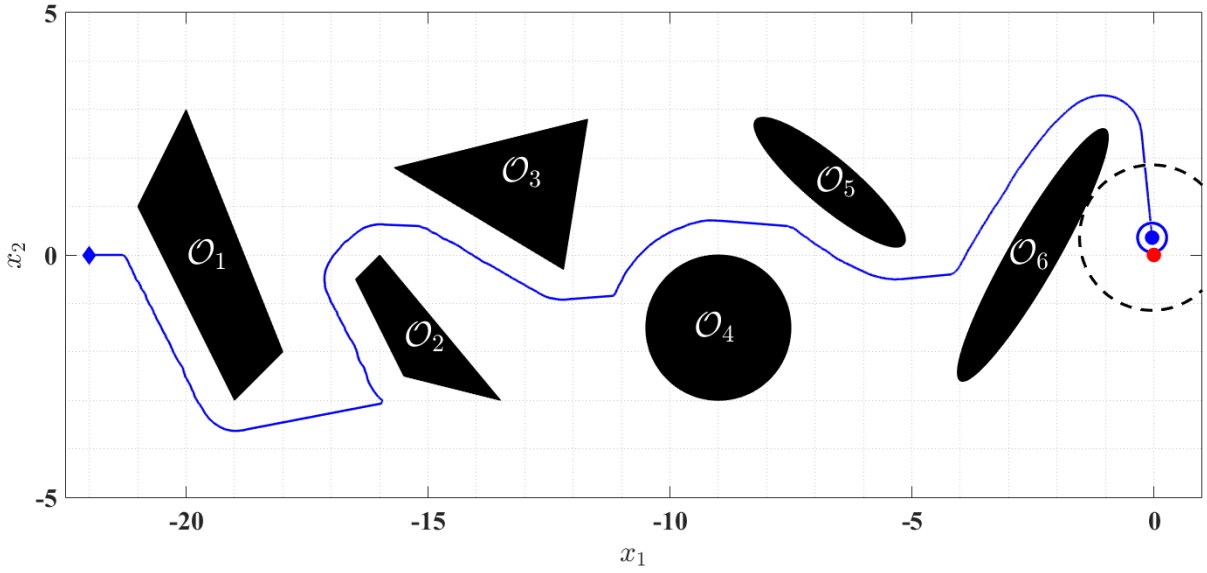

Figure 3.8: Trajectory of a robot, equipped with a range-bearing sensor, converging safely to the target location at the origin. The sensor measurements are affected by a Gaussian noise of 0 mean and $50mm$ standard deviation.

developed in [Arslan and Koditschek, 2019]. Similar to our approach, this approach can be implemented in *a priori* unknown environments using the information obtained via a range-bearing sensor mounted on the robot. Contrary to our approach, this approach only works for convex obstacles that satisfy the curvature condition [Arslan and Koditschek, 2019, Assumption 2]. When this assumption is not satisfied, the separating hyperplane approach generates stable undesired equilibria. Some of the differences between our

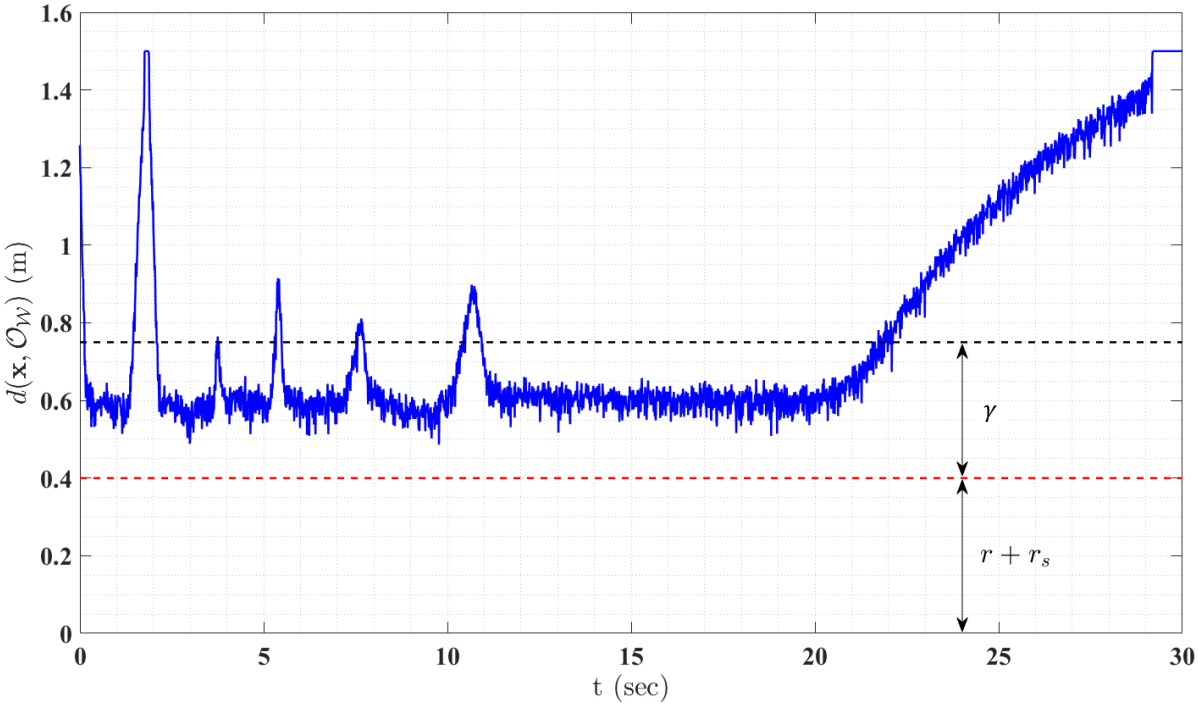

Figure 3.9: Distance of the center of the robot from the boundary of the obstacle occupied workspace as the robot converges to the target location.

approach and the separating hyperplane approach are given below.

In the separating hyperplane-based navigation approach, the robot has to construct a local obstacle-free region by first identifying the lines joining the closest point on each obstacle (within the sensing range) with its location, and then constructing the hyperplanes perpendicular to these lines that separate the robot's body from the obstacles. Then, at each control update step, it has to locate the projection of the target location onto the boundary of the local obstacle-free region. Compared to this approach, in our proposed sensor-based hybrid feedback approach, the robot only requires the closest point on the nearest obstacle when it operates in the *obstacle-avoidance* mode. It only needs to identify all the points on the closest obstacle, which are in the line-of-sight of the center of the robot only when it operates in the *move-to-target* mode inside the $\gamma-$neighbourhood of that obstacle, to evaluate the possibility of collision and switch to the *obstacle-avoidance* mode, if necessary, as stated in Remark 3.4.

When the environment consists of obstacles that do not satisfy the obstacle curvature condition [Arslan and Koditschek, 2019, Assumption 2], the separating hyperplane approach generates undesired stable equilibria as shown in Fig. 3.10(left). On the other hand, our proposed hybrid feedback approach always guarantees convergence to the target location regardless of the shape and size of the convex obstacles as shown in Fig. 3.10(right).

If the workspace satisfies the obstacle curvature condition [Arslan and Koditschek, 2019, Assumption 2], then for almost all initial locations, the robot trajectories obtained using the separating hyperplane approach converge asymptotically to the target location,

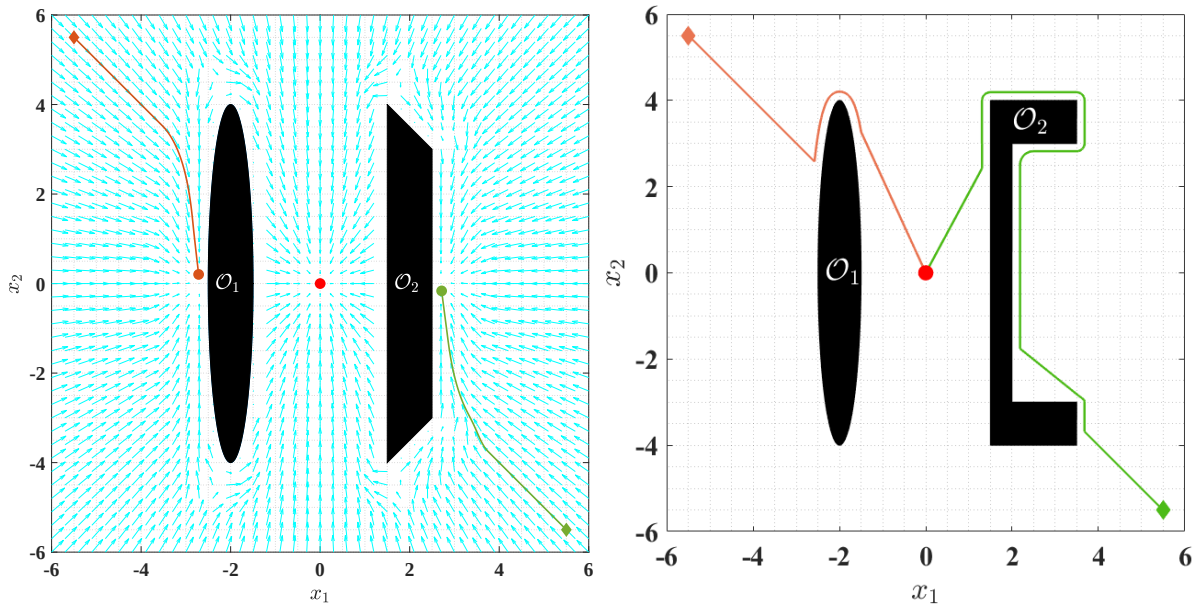

Figure 3.10: The left figure represents the robot trajectories obtained using the sensor-based separating hyperplane approach [Arslan and Koditschek, 2019] showing the presence of stable undesired equilibria. The right figure presents the robot trajectories converging to the target location under the proposed hybrid navigation scheme.

while strictly decreasing the Euclidean distance from the robot to the target location [Arslan and Koditschek, 2019, Theorem 3], see Fig. 3.11(left). This feature is advantageous compared to our approach. In fact, when the robot operates using our approach, it may travel away from the target when operating in the *obstacle-avoidance* mode, as seen in Fig. 3.11(right) for the robot trajectory initialized at $[-7.5, -10.5]^T$, around the obstacle $\mathcal{O}_1$.

3.7 Conclusions

In this chapter, we proposed a hybrid feedback controller for safe autonomous navigation in two-dimensional environments with arbitrary convex obstacles. The obstacles can have nonsmooth boundaries and large sizes and can be placed arbitrarily provided that some mild disjointedness requirements are satisfied as per Assumption 1. The proposed hybrid feedback controller guarantees almost global asymptotic stability of the target location in the obstacle-free workspace, as stated in Theorem 3.1. The mode-switching strategy along with the geometric construction of the flow and jump sets ensures the continuity of the control input, which is one of the interesting practical features of the proposed hybrid control scheme. Since the obstacle avoidance part of the control law depends on the projection of the center of the robot on the nearest obstacle, the proposed hybrid control scheme can be applied in a priori unknown environments, as discussed in Section VI.

We require obstacles to be sufficiently separated such that the robot can pass in

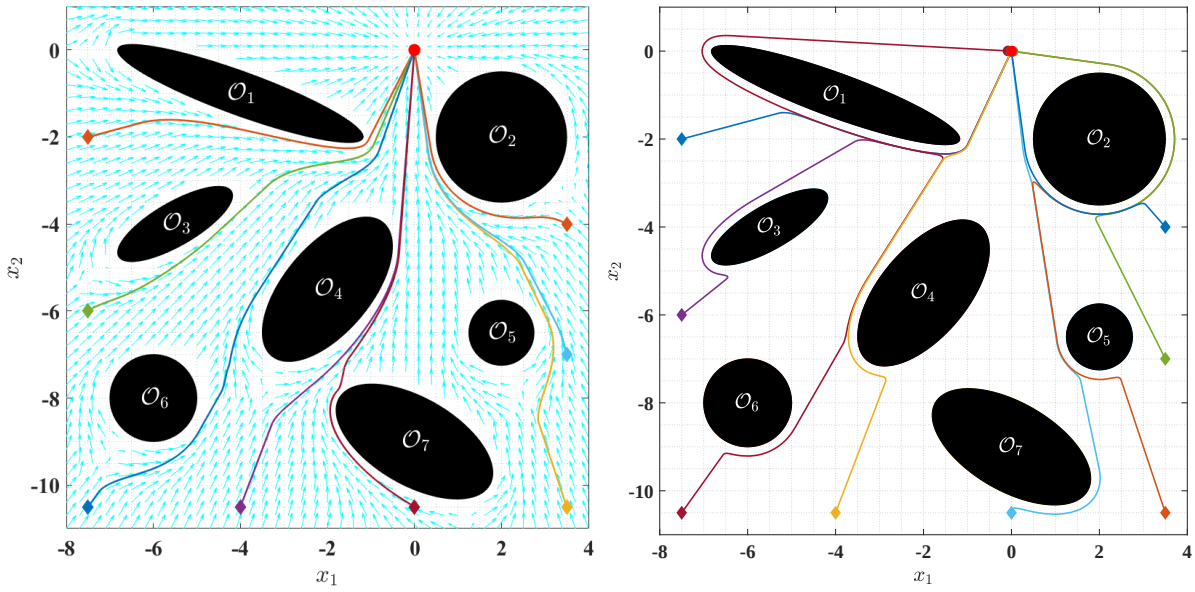

Figure 3.11: The left figure shows the robot trajectories obtained using the hyperplane approach [Arslan and Koditschek, 2019]. The right figure shows the robot trajectories obtained using our proposed sensor-based hybrid feedback approach.

between any pair of obstacles, as stated in Assumption 3.1. As a result, by carefully selecting the parameter γ^1, the robot tackles one obstacle at a time. However, in most of the realistic environments, wherein obstacles may have non-convex shapes, the satisfaction of Assumption 3.1 is not always guaranteed. One of the main reasons that restricts the direct application of the proposed hybrid feedback controller to environments that do not satisfy Assumption 3.1 is the presence of multiple closest points from the center of the robot to the obstacle-occupied workspace in the close proximity of the unsafe region. For example, consider Fig. 3.12 (left) which depicts an environment that satisfies Assumption 3.1. There exists $\alpha-$neighborhood around the obstacles, where $\alpha > r_a$ such that for any location $\mathbf{x} \in \mathcal{D}_\alpha(\mathcal{O}_\mathcal{W})$ the projection of the center of the robot on the obstacle-occupied workspace is unique. On the other hand, consider Fig. 3.12 (right) which depicts an environment that does not satisfy Assumption 3.1. For any location on the line segment $\mathcal{L}_s(\mathbf{x}_1, \mathbf{x}_2)$ there exist two closest points on the obstacle. Since the rotational control vector $\mathbf{v}(\mathbf{x}, \mathbf{m})$, defined in (3.5), requires a unique projection $\Pi(\mathbf{x}, \mathcal{O}_\mathcal{W})$, the proposed hybrid feedback controller (3.4) is not applicable for the environment in Fig. 3.12 (right).

To address this issue, in the next chapter, we propose an instrumental workspace transformation operator which allows us to extend the applicability of the proposed hybrid feedback control law (3.4) to two-dimensional environments with arbitrarily shaped non-convex obstacles.

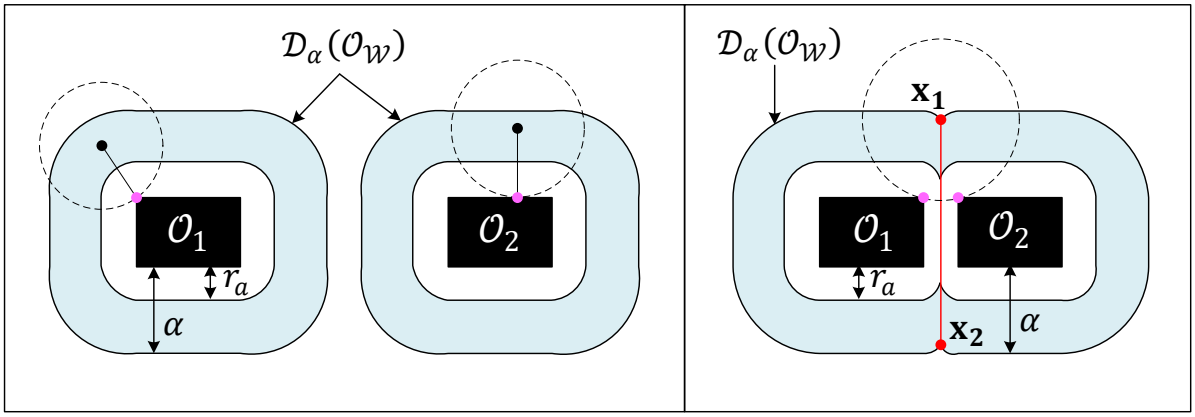

Figure 3.12: The left figure illustrates an obstacle-occupied workspace $\mathcal{O}_\mathcal{W} = \mathcal{O}_1 \cup \mathcal{O}_2$ that satisfies Assumption 3.1. The right figure depicts an obstacle-occpuied workspace that does not satisfy Assumption 3.1

Chapter 4

Autonomous Navigation in Planar Environments with Non-Convex Obstacles

4.1 Introduction

In this chapter, we propose an instrumental workspace transformation operator which allows us to extend the applicability of the hybrid feedback control law proposed in Chapter 3 to environments with arbitrarily-shaped non-convex obstacles. As discussed earlier, the NF-based approaches [Koditschek and Rimon, 1992], [Filippidis and Kyriakopoulos, 2012], [Verginis and Dimarogonas, 2021], which with proper parameter tuning provide almost global convergence to the target location, can be directly applied to the sphere worlds and the point worlds. To extend the applicability of the NF approach to environments containing more general convex and star-shaped obstacles, one can employ diffeomorphic mappings developed in [Koditschek and Rimon, 1992] and [Li and Tanner, 2018]. However, the application of these diffeomorphic mappings requires a global knowledge of the environment. The NF-based approach was extended in [Paternain et al., 2017] to environments containing curved obstacles. The authors established sufficient conditions on the curvature of the obstacles' boundaries to guarantee almost global convergence to a neighborhood of the *a priori* unknown target location. This approach is applicable to convex, smooth and sufficiently curved obstacles. In [Arslan and Koditschek, 2019], a reactive power diagram-based approach was introduced for robots navigating in *a priori* unknown environments. This approach guarantees almost global asymptotic stabilization of the target location, provided that the obstacles are sufficiently separated and strongly convex. This approach was further extended in [Vasilopoulos and Koditschek, 2018] to handle partially known non-convex obstacles, where it is assumed that the robot has the geometrical information about the non-convex obstacles but lacks knowledge of their precise locations within the workspace. However, due to the topological obstruction induced by the motion space in the presence of obstacles for any continuous time-invariant vector fields [Koditschek and Rimon, 1990], the above-mentioned approaches provide at best almost global convergence guarantees.

In [Braun et al., 2020], the authors proposed a hybrid control law to globally asymptotically stabilize a class of linear systems while avoiding neighbourhoods of unsafe points. In [Matveev et al., 2011] and [Berkane et al., 2021a], hybrid control techniques were employed to enable the robot to operate in the *obstacle-avoidance* mode when in close proximity to an obstacle or in the *move-to-target* mode when located away from obstacles. These strategies bear resemblance to bug algorithms [Lumelsky and Stepanov, 1986], which are commonly used for point robot path planning. In [Berkane et al., 2021a, Definition 2], the proposed hybrid controller is applicable in *a priori* known $n-$dimensional environments with sufficiently disjoint elliptical obstacles. On the other hand, in [Matveev et al., 2011, Assumption 10], the obstacles are assumed to be smooth and sufficiently separated from each other. In [Loizou et al., 2003], the authors proposed a discontinuous feedback control law for autonomous robot navigation in partially known two-dimensional environments. When a known obstacle is encountered, the control vector aligns with the negative gradient of the Navigation Function. However, when close to an unknown obstacle, the robot moves along its boundary, relying on the local curvature information of the obstacle. This method is limited to point robots and, similar to [Matveev et al., 2011], assumes smooth obstacle boundaries without sharp edges.

In this chapter, we consider the autonomous robot navigation problem in a two-dimensional space with arbitrarily-shaped non-convex obstacles which can be in close proximity with each other. Unlike [Arslan and Koditschek, 2019], [Berkane et al., 2021a] and [Sawant et al., 2023a], wherein the robot is allowed to pass between any pair of obstacles, we require the existence of a safe path joining the initial and the target location, as stated in Assumption 4.1. The main contributions of this chapter are as follows:

1) *Asymptotic stability:* The proposed autonomous navigation solution ensures asymptotic stability of the target location for the robot operating in planar environments with arbitrary non-convex obstacles.

2) *Arbitrarily-shaped obstacles:* There are no restrictions on the shape of the non-convex obstacles such as those mentioned in [Paternain et al., 2017], [Arslan and Koditschek, 2019], [Berkane et al., 2021a], and their proximity with respect to each other *e.g.*, see [Matveev et al., 2011, Assumption 10], [Berkane et al., 2021a, Definition 2], except for the mild feasibility assumptions 4.1 and 4.2.

3) *Applicable in a priori unknown environments:* The proposed obstacle avoidance approach can be implemented using only range scanners (*e.g.*, LiDAR) without an *a priori* global knowledge of the environment which satisfies Assumption 4.1.

The results presented in this chapter have been published in [Sawant et al., 2022b] and [Sawant et al., 2023b].

4.2 Problem formulation

We consider a disk-shaped robot operating in a two dimensional, compact, arbitrarily-shaped (possibly non-convex) subset of the Euclidean space $\mathcal{W} \subset \mathbb{R}^2$. The workspace is cluttered with a finite number of compact, pairwise disjoint obstacles $\mathcal{O}_i \subset \mathcal{W}, i \in$

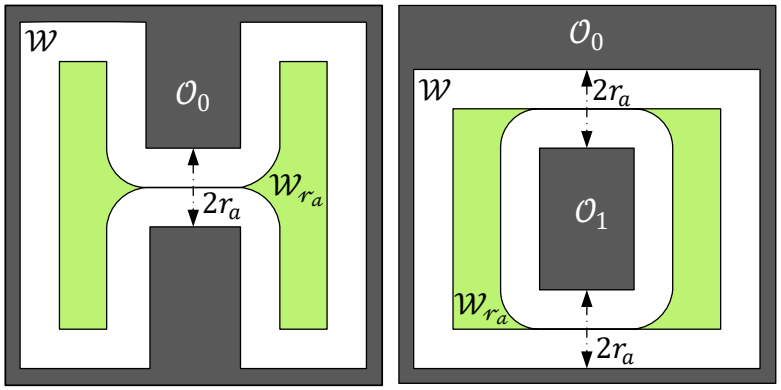

Figure 4.1: Two examples of workspaces that do not satisfy Assumption 4.1.

$\{1, \ldots, b\}, b \in \mathbb{N}$. We define obstacle $\mathcal{O}_0 := (\mathcal{W}^\circ)^c$ as the complement of the interior of the workspace. The robot is governed by single integrator dynamics

$$\dot{\mathbf{x}} = \mathbf{u}, \tag{4.1}$$

where $\mathbf{x}$ is the location of the center of the robot and $\mathbf{u} \in \mathbb{R}^2$ is the control input. The task is to reach a predefined obstacle-free target location from any obstacle-free region while avoiding collisions. Without loss of generality, consider the origin $\mathbf{0}$ as the target location.

We define the obstacle-occupied workspace as $\mathcal{O}_\mathcal{W} := \bigcup_{i \in \mathbb{I}} \mathcal{O}_i$, where the set $\mathbb{I} := \{0, 1, ..., b\}$, contains indices corresponding to the disjoint obstacles. The obstacle-free workspace is denoted by $\mathcal{W}_0$, where, given $y \geq 0$, the $y-$eroded version of the obstacle-free workspace *i.e.*, $\mathcal{W}_y$ is defined as

$$\mathcal{W}_y := \mathbb{R}^2 \setminus \mathcal{D}_y(\mathcal{O}_\mathcal{W}^\circ) \subset \mathcal{W}_0. \tag{4.2}$$

Let $r > 0$ be the radius of the robot and $r_s > 0$ be the minimum distance that the robot should maintain with respect to any obstacle for safe navigation. Hence, $\mathcal{W}_{r_a}$, with $r_a = r + r_s$, is a free workspace with respect to the center of the robot *i.e.*, $\mathbf{x} \in \mathcal{W}_{r_a} \iff \mathcal{B}_{r_a}(\mathbf{x}) \subset \mathcal{W}_0$. Since the obstacles can be non-convex and can be in close proximity with each other, to maintain the feasibility of the robot navigation, we make the following assumption:

Assumption 4.1 *The interior of the obstacle-free workspace w.r.t. the center of the robot, namely $\mathcal{W}_{r_a}^\circ$, is pathwise connected, and $\mathbf{0} \in \mathcal{W}_{r_a}^\circ$.*

According to Assumption 4.1, from any location in the set $\mathcal{W}_{r_a}$, there exists at least one feasible path to the target location. We require the origin to be in the interior of the set $\mathcal{W}_{r_a}$ to ensure its stability, as discussed later in Theorem 4.1. Since we require the interior of the set $\mathcal{W}_{r_a}$ to be pathwise connected, the environments, such as the ones showed in Fig. 4.1, which do not satisfy Assumption 4.1, are invalid.

The obstacle-avoidance strategy, which will be detailed later in Section 4.4, requires a unique closest point on the obstacle-occupied workspace from the robot's center. This

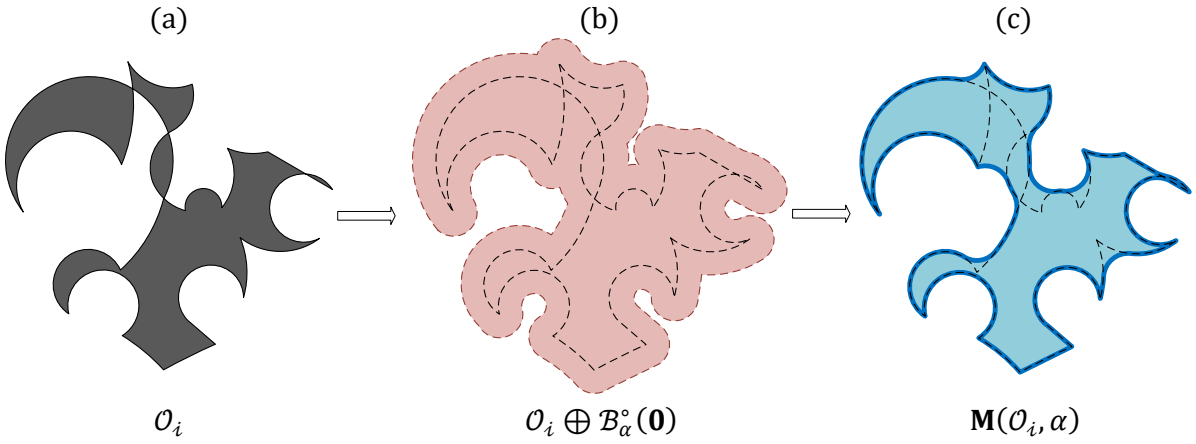

Figure 4.2: (a) The original obstacle $\mathcal{O}_i \subset \mathbb{R}^2$. (b) Dilation of obstacle $\mathcal{O}_i$ by a structuring element $\mathcal{B}^\circ_\alpha(\mathbf{0}), \alpha > 0$. (c) Erosion of the dilated obstacle $\mathcal{O}_i \oplus \mathcal{B}^\circ_\alpha(\mathbf{0})$ by the same structuring element $\mathcal{B}^\circ_\alpha(\mathbf{0})$.

condition is not always satisfied in the case of non-convex and closely positioned obstacles. Constructing convex hulls around the non-convex obstacles is conservative solution since it makes much of the obstacle-free workspace non-available for navigation. Therefore, in Section 4.3, we will introduce an obstacle reshaping technique that generates a modified obstacle-occupied workspace $\mathcal{O}^M_{\mathcal{W}}$, in a less conservative manner (without necessarily convexifying the obstacles), in a way that ensures uniqueness of the closest point on $\mathcal{O}^M_{\mathcal{W}}$ from the robot's center.

Similar to $\mathcal{W}_y$ in (4.2), the $y-$eroded modified obstacle-free workspace, which is denoted by $\mathcal{V}_y$, is defined as

$$\mathcal{V}_y := \mathbb{R}^2 \setminus \mathcal{D}_y(\mathcal{O}^M_{\mathcal{W}})^\circ, \tag{4.3}$$

where $y \geq 0$. Hence, the set $\mathcal{V}_{r_a}$ denotes the modified obstacle-free workspace with respect to the center of the robot. We construct $\mathcal{O}^M_{\mathcal{W}}$ such that the modified obstacle-free workspace $\mathcal{V}_{r_a}$ is a subset of the original obstacle-free workspace $\mathcal{W}_{r_a}$, as stated with more details later in Remark 4.6.

Given a target location in the interior of the obstacle-free workspace, *i.e.*, $\mathbf{0} \in (\mathcal{W}_{r_a})^\circ$, as stated in Assumption 4.1, we aim to design a hybrid feedback control law such that:

1. the set $\mathcal{V}_{r_a}$ is forward invariant.

2. the target location $\mathbf{x} = 0$ is globally asymptotically stable.

As it is going to be shown later, the obstacle reshaping procedure guarantees that if the target location belongs to $(\mathcal{W}_{r_a})^\circ$ then it also belongs to $\mathcal{V}_{r_a}$.

The design process can be summarized as follows:

1. the proposed hybrid navigation scheme involves two modes of operation for the robot: *move-to-target* and *obstacle-avoidance*. The design of the obstacle avoidance strategy requires a unique projection onto the unsafe region within its close proximity. However, ensuring this uniqueness can be challenging in cases where

obstacles have arbitrary shapes and are in close proximity to one another. Hence, before implementing the hybrid navigation scheme, we first transform the obstacle-occupied workspace using an obstacle-reshaping operator, as discussed later in Section 4.3, to obtain the modified obstacle-occupied workspace. This operator transforms the obstacle-occupied workspace and guarantees the uniqueness of the projection of robot's center onto the modified obstacle-occupied workspace in its α-neighbourhood, where the parameter α is chosen as per Lemma 4.3.

2. when the center of the robot is outside the α-neighbourhood of the modified obstacle-occupied workspace or the nearest disjoint modified obstacle does not intersect with its straight path to the target location, the robot moves straight towards the target in the *move-to-target* mode.

3. when the center of the robot enters the $\alpha-$neighbourhood of the modified obstacle that is obstructing its straight path towards the target location, the robot switches to the *obstacle-avoidance* mode.

4. in the *obstacle-avoidance* mode, to avoid collision, the robot moves parallel to the boundary of the nearest modified obstacle until it reaches the location at which the following two conditions are satisfied: 1) the robot is closer to the target location than the location where it entered in the *obstacle-avoidance* mode; 2) the straight path towards the target from that location does not intersect with the nearest disjoint modified obstacle. At this location, the robot switches back to the *move-to-target* mode.

5. later in Lemma 4.4, we show that the target location belongs to the modified obstacle-free workspace, and from any location away from the interior of the modified obstacle-occupied workspace, there exists a feasible path towards the target location. Hence, with a consecutive implementation of steps $2-4$ for the environment with modified obstacle-occupied workspace, we guarantee asymptotic convergence of the center of the robot to the target location.

In the next section, we provide the transformation that modifies the obstacle-occupied workspace $\mathcal{O}_{\mathcal{W}}$ which satisfies Assumption 4.1, such that the robot always has a unique closest point on the modified obstacle-occupied workspace inside its $\alpha-$neighbourhood.

4.3 Obstacle reshaping

Given an obstacle-occupied workspace $\mathcal{O}_{\mathcal{W}}$ that satisfies Assumption 4.1, the objective of the obstacle-reshaping task is to obtain a modified obstacle-occupied workspace $\mathcal{O}^M_{\mathcal{W}}$ such that every location less than $\alpha-$distance away from the set $\mathcal{O}^M_{\mathcal{W}}$ has a unique closest point on the set. The choice of the parameter α is crucial for the successful implementation of the proposed navigation scheme, as stated later in Lemma 4.3. For now, we assume that $\alpha > 0$ such that the $\alpha-$eroded obstacle-free workspace $\mathcal{W}_\alpha$ is not an empty set. The obstacle-reshaping operator $\mathbf{M}$ is defined as

$$\mathbf{M}(\mathcal{O}_{\mathcal{W}}, \alpha) = (\mathcal{O}_{\mathcal{W}} \oplus \mathcal{B}^\circ_\alpha(\mathbf{0})) \ominus \mathcal{B}^\circ_\alpha(\mathbf{0}) =: \mathcal{O}^M_{\mathcal{W}}. \tag{4.4}$$

The operator $\mathbf{M}$ first dilates the obstacle-occupied workspace $\mathcal{O}_{\mathcal{W}}$ using the open Euclidean ball of radius α centered at the origin as the structuring element, and then erodes the dilated set using the same structuring element, resulting in the modified obstacle-occupied workspace $\mathcal{O}_{\mathcal{W}}^{M}$. This process is similar to the *closing* operator commonly used in the field of mathematical morphology [Haralick et al., 1987]. Note that the proposed modification scheme is applicable to $n-$dimensional environments. Next, we discuss some of the features of the obstacle-reshaping operator $\mathbf{M}$.

Remark 4.1 *Consider the modified obstacle-occupied workspace $\mathcal{O}_{\mathcal{W}}^{M}$ obtained after applying the operator $\mathbf{M}$ on the obstacle-occupied workspace $\mathcal{O}_{\mathcal{W}}$ with $\alpha > 0$. Some of the features of the obstacle-reshaping operator $\mathbf{M}$, as stated in [Serra, 1986, Table 1], are as follows:*
Idempotent: *the application of the transformation $\mathbf{M}$ to a modified obstacle $\mathcal{O}_{\mathcal{W}}^{M}$ with the same structuring element (the open Euclidean ball $\mathcal{B}_{\alpha}^{\circ}(\mathbf{0})$), does not change the set $\mathcal{O}_{\mathcal{W}}^{M}$ i.e.,*

$$\mathbf{M}(\mathbf{M}(\mathcal{O}_{\mathcal{W}}, \alpha), \alpha) = \mathbf{M}(\mathcal{O}_{\mathcal{W}}, \alpha) = \mathcal{O}_{\mathcal{W}}^{M}. \tag{4.5}$$

Extensive: *the modified set always contains the original set i.e., $\mathcal{O}_{\mathcal{W}} \subset \mathcal{O}_{\mathcal{W}}^{M}$.*
Increasing: *for any subset $\mathcal{A} \subset \mathcal{O}_{\mathcal{W}}$, the modified set $\mathcal{A}^{M}$ always belongs to the modified set $\mathcal{O}_{\mathcal{W}}^{M}$ i.e., $\mathcal{A}^{M} \subset \mathcal{O}_{\mathcal{W}}^{M}$.*

Notice that, by duality of dilation and erosion [Haralick et al., 1987, Theorem 25], the dilation of a set, with an open Euclidean ball centered at the origin as the structuring element, is equivalent to the erosion of the complement of that set with the same structuring element. This allows us to provide alternative representations of the proposed obstacle-reshaping operator, as stated in the next remark.

Remark 4.2 *The $\alpha-$eroded obstacle-free workspace $\mathcal{W}_{\alpha}$, defined according to (4.2), is equivalent to the complement of the set obtained after dilating the obstacle-occupied workspace $\mathcal{O}_{\mathcal{W}}$ with the open Euclidean ball of radius α centered at the origin $\mathcal{B}_{\alpha}^{\circ}(\mathbf{0})$ i.e., $\mathcal{W}_{\alpha} = (\mathcal{O}_{\mathcal{W}} \oplus \mathcal{B}_{\alpha}^{\circ}(\mathbf{0}))^{c}$. Therefore, by duality of dilation and erosion [Haralick et al., 1987, Theorem 25], the modified obstacle-occupied workspace is equivalent to the complement of the set obtained after dilating $\mathcal{W}_{\alpha}$ by the open Euclidean ball of radius α centered at the origin $\mathcal{B}_{\alpha}^{\circ}(\mathbf{0})$. In other words,*

$$\mathbf{M}(\mathcal{O}_{\mathcal{W}}, \alpha) = (\mathcal{W}_{\alpha} \oplus \mathcal{B}_{\alpha}^{\circ}(\mathbf{0}))^{c} = \mathcal{W}_{\alpha}^{c} \ominus \mathcal{B}_{\alpha}^{\circ}(\mathbf{0}). \tag{4.6}$$

The operator $\mathbf{M}$ does not guarantee a unique projection onto the modified obstacle from every point in its $\alpha-$neighbourhood. To illustrate this fact, we consider an environment with two obstacles $\mathcal{O}_{\mathcal{W}} = \mathcal{O}_i \cup \mathcal{O}_j$ such that $d(\mathcal{O}_i, \mathcal{O}_j) < 2\alpha$, as shown in Fig. 4.3. In Fig. 4.3b, one can see that the operation $\mathbf{M}(\mathcal{O}_{\mathcal{W}}, \alpha)$ has fused these obstacles into a single set, represented in black. However, depending on the arrangement of the obstacles, it may happen that even though $d(\mathcal{O}_i, \mathcal{O}_j) < 2\alpha$, the modified obstacle-occupied workspace $\mathcal{O}_{\mathcal{W}}^{M}$ contains two disjoint modified obstacles which are less than 2α distance apart from each other, as shown in Fig. 4.3a. In this case, it is possible to find a location

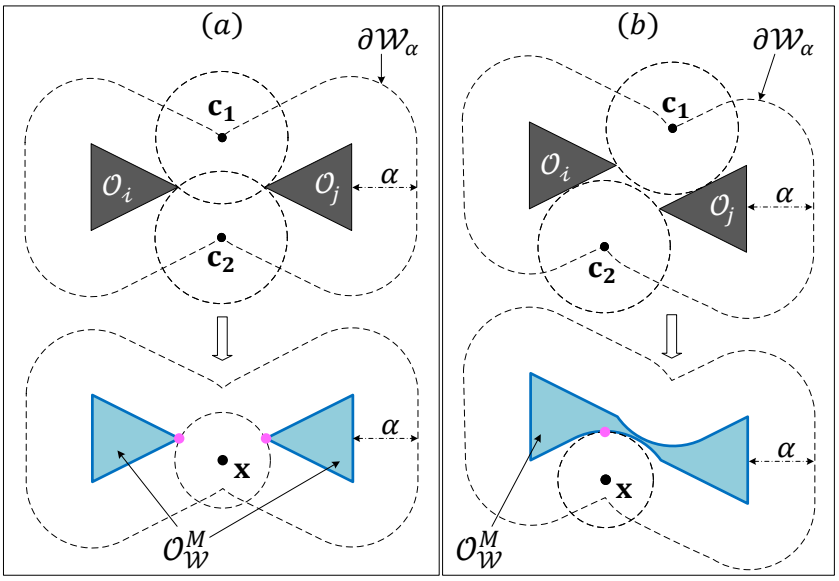

Figure 4.3: Workspace with two obstacles $\mathcal{O}_\mathcal{W} = \mathcal{O}_i \cup \mathcal{O}_j$ such that $d(\mathcal{O}_i, \mathcal{O}_j) < 2\alpha$. Left figure shows that the set $\mathcal{O}_\mathcal{W}^M$ is not a connected set. Right figure shows that the set $\mathcal{O}_\mathcal{W}^M$ is a connected set.

$\mathbf{x}$ less than α distance away from the set $\mathcal{O}_\mathcal{W}^M$ which has multiple closest points on the set $\mathcal{O}_\mathcal{W}^M$, as shown in Fig. 4.3a.

Observe that in Fig. 4.3a, the open Euclidean balls of radius α centered at the locations $\mathbf{c}_1$ and $\mathbf{c}_2$ intersect each other. Hence, when the set $\mathcal{O}_\mathcal{W} \oplus \mathcal{B}_\alpha^\circ(\mathbf{0})$ is eroded to obtain the modified obstacle-occupied workspace (4.4), two disjoint modified obstacles are obtained, even though $d(\mathcal{O}_i, \mathcal{O}_j) < 2\alpha$. As a result, at the location $\mathbf{x}$ inside the $\alpha-$dilated modified obstacle, one can get multiple projections, as shown in Fig. 4.3a.

To guarantee a unique projection onto the modified obstacle from all locations inside its $\alpha-$neighbourhood, we require the following assumption on the obstacle-occupied workspace:

Assumption 4.2 *For all* $\mathbf{x} \in \partial\mathcal{W}_\alpha$ *and for every* $\mathbf{n} \in \mathbf{N}_{\mathcal{W}_\alpha}(\mathbf{x})$ *with* $\|\mathbf{n}\| = 1$, *the intersection* $\mathcal{B}_\alpha^\circ(\mathbf{x} + \alpha\mathbf{n}) \cap \mathcal{W}_\alpha$ *is an empty set, where* $\alpha > 0$ *such that* $\mathcal{W}_\alpha \neq \emptyset$.

According to Assumption 4.2, for all $\mathbf{x}$ on the boundary of the $\alpha-$eroded obstacle-free workspace $\mathcal{W}_\alpha$ and for every unit normal vector $\mathbf{n}$ to $\mathcal{W}_\alpha$ at $\mathbf{x}$, the open Euclidean ball $\mathcal{B}_\alpha(\mathbf{x} + \alpha\mathbf{n})$ does not intersect with the set $\mathcal{W}_\alpha$. Figure 4.4a shows a two-dimensional workspace that does not satisfy Assumption 4.2, whereas the inter-obstacle arrangement shown in Fig. 4.4b satisfies Assumption 4.2.

Unlike [Arslan and Koditschek, 2019, Assumprtion 1], [Verginis and Dimarogonas, 2021, Assumprtion 2], and [Berkane et al., 2021a, Section V-C3], Assumption 4.2 does not impose restrictions on the minimum separation between any pair of obstacles and allows obstacles to be non-convex. In fact, if one assumes (as in the above mentioned references) that the obstacles are convex and the minimum separation between any pair of obstacles is greater than $2r_a$, then Assumption 4.2 along with Assumption 4.1 are satisfied, as stated later in Proposition 4.1.

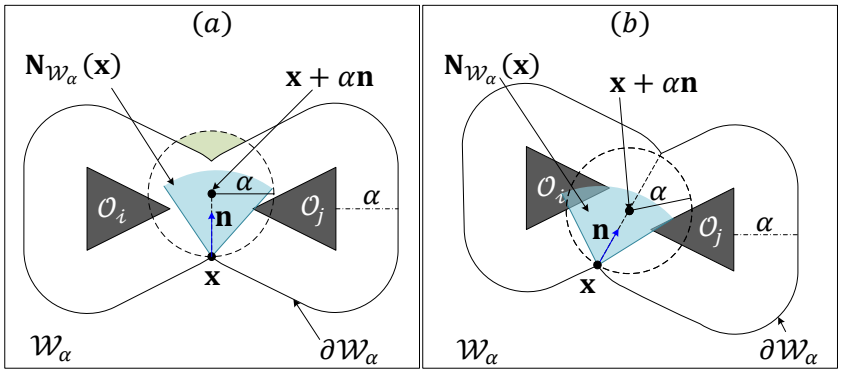

Figure 4.4: Workspace with two obstacle $\mathcal{O}_\mathcal{W} = \mathcal{O}_i \cup \mathcal{O}_j$ such that $d(\mathcal{O}_i, \mathcal{O}_j) < 2\alpha$. (a) $\mathcal{O}_\mathcal{W}$ does not satisfy Assumption 4.2. (b) $\mathcal{O}_\mathcal{W}$ satisfies Assumption 4.2.

Next, we show that if the obstacle-occupied workspace $\mathcal{O}_\mathcal{W}$ satisfies Assumptions 4.1 and 4.2, then from any location in the $\alpha-$neighbourhood of the modified obstacle-occupied workspace $\mathcal{O}^M_\mathcal{W}$, obtained using (4.4), the projection onto this modified obstacle-occupied workspace is always unique.

Lemma 4.1 *Under Assumption 4.2, for all locations* $\mathbf{x}$ *less than* α *distance away from the modified obstacle-occupied workspace, there is a unique closest point from* $\mathbf{x}$ *to the set* $\mathcal{O}^M_\mathcal{W}$ *i.e.,* $\forall \mathbf{x} \in \mathcal{D}_\alpha((\mathcal{O}^M_\mathcal{W})^\circ)$, $\boldsymbol{card}(\mathcal{PJ}(\mathbf{x}, \mathcal{O}^M_\mathcal{W})) = 1$.

Proof See Appendix C.1.

Notice that in Fig. 4.3b, even though initially the obstacles were disjoint, the obstacle-reshaping operator combined them into one pathwise connected set. In fact, for the obstacle-occupied workspace that satisfies Assumption 4.2, if two obstacles are less than 2α distance apart, then the modified obstacle set obtained for the union of these two obstacles is a connected set. Next, we elaborate on this feature of the proposed obstacle-reshaping operator.

For each obstacle $\mathcal{O}_i, i \in \mathbb{I}$, we define the following set:

$$\mathcal{O}_{i,\alpha} = \bigcup_{k \in \mathbb{I}_{i,\alpha}} \bigcup_{j \in \mathbb{I}_{k,\alpha}} \mathcal{O}_j, \tag{4.7}$$

where, for $k \in \mathbb{I}$, the set $\mathbb{I}_{k,\alpha}$, which is defined as

$$\mathbb{I}_{k,\alpha} = \{j \in \mathbb{I} | d(\mathcal{O}_k, \mathcal{O}_j) < 2\alpha\}, \tag{4.8}$$

contains the indices corresponding to obstacles that are at distances less than 2α from obstacle $\mathcal{O}_k$. According to (4.7) and (4.8), the distance between any proper subset of the obstacle set $\mathcal{O}_{i,\alpha}$ and its relative complement with respect to the same set, is always less than 2α. In other words, if $\mathcal{O}_\mathbb{C} \subset \mathcal{O}_{i,\alpha}$ and $\mathcal{O}_\mathbb{D} = \mathcal{O}_{i,\alpha} \setminus \mathcal{O}_\mathbb{C}$, then the distance $d(\mathcal{O}_\mathbb{C}, \mathcal{O}_\mathbb{D}) < 2\alpha$. If $\mathcal{O}_j \subset \mathcal{O}_{i,\alpha}, j \in \mathbb{I} \setminus \{i\}$, then $\mathcal{O}_{i,\alpha} = \mathcal{O}_{j,\alpha}$. Next, we show that the modified obstacle-occupied set $\mathcal{O}^M_{i,\alpha}$, for any $i \in \mathbb{I}$, is a connected set.

Lemma 4.2 *Under Assumption 4.2, the modified obstacle-occupied set* $\mathcal{O}_{i,\alpha}^{M}$*, for any* $i \in \mathbb{I}$*, is a connected set.*

Proof See Appendix C.2

According to Lemma 4.2, if the modified obstacle-occupied workspace contains two disjoint modified obstacles, then the distance between these two modified obstacles will always be greater than or equal to 2α.

Remark 4.3 *When the obstacle is non-convex, the modified obstacle obtained using the operator* $\mathbf{M}$*, defined in (4.4), always occupies less workspace as opposed to the convex hull [Boyd et al., 2004, Section 2.1.4] of the same obstacle. Although, one obtains a unique projection onto the convex hull of a given obstacle within its* $\alpha-$*neighbourhood, the use of the convex hull renders most of the obstacle-free workspace unavailable for the robot's navigation, as shown in Fig. 4.5. Moreover, if a given obstacle* $\mathcal{O}_i$ *is convex, then the modified obstacle* $\mathcal{O}_i^M$ *obtained using (4.4) for any* $\alpha > 0$ *is equal to the original obstacle* $\mathcal{O}_i$ *i.e.,* $\mathcal{O}_i^M = \mathcal{O}_i$*.*

Since, as per Lemma 4.1, from any location less than α distance away from the modified obstacle-occupied workspace $\mathcal{O}_{\mathcal{W}}^{M}$, the projection on the set $\mathcal{O}_{\mathcal{W}}^{M}$ is unique, one can roll up an Euclidean ball of radius at most α on the boundary $\partial\mathcal{O}_{\mathcal{W}}^{M}$, as stated in [Thäle, 2008, Definition 11]. This motivates an alternative procedure to obtain the boundary of the modified obstacle-occupied workspace when the obstacle-occupied workspace $\mathcal{O}_{\mathcal{W}}$ is two-dimensional, by having a virtual ring of radius α rolling on the boundary of the set $\mathcal{O}_{\mathcal{W}}$, as stated in the next remark.

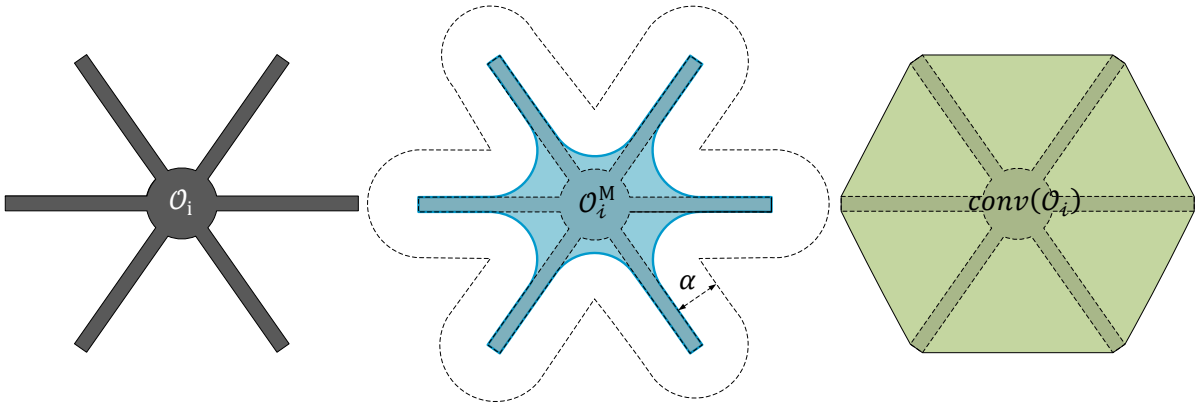

Figure 4.5: Left figure shows the original obstacle $\mathcal{O}_i \subset \mathbb{R}^2$. Middle figure shows the modified obstacle $\mathcal{O}_i^M = \mathbf{M}(\mathcal{O}_i, \alpha)$ obtained using (4.4). Right figure shows the convex hull $\text{conv}(\mathcal{O}_i)$ for the obstacle $\mathcal{O}_i$.

Remark 4.4 *Given an obstacle-occupied workspace* $\mathcal{O}_{\mathcal{W}} \subset \mathbb{R}^2$*, satisfying Assumptions 4.1 and 4.2, one can construct the modified obstacle* $\mathcal{O}_{i,\alpha}^{M} = \mathbf{M}(\mathcal{O}_{i,\alpha}, \alpha)$*, where* $i \in \mathbb{I}$*, by rotating a virtual ring, of radius* α *and center* $\mathbf{c}$*, around the set* $\mathcal{O}_{i,\alpha}$*, just touching the set*

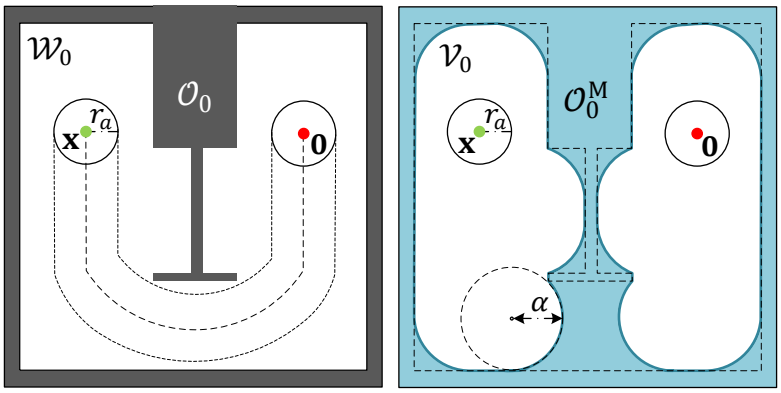

Figure 4.6: The left figure shows an original workspace where a feasible path exists from location $\mathbf{x}$ to the origin. The right figure shows the modified workspace obtained using (4.4) with some $\alpha > r_a$, where there is no feasible path from the location $\mathbf{x}$ to the origin.

$\mathcal{O}_{i,\alpha}$, while ensuring that the ring does not intersect with the interior of that set, as shown in Fig. 4.7. Then, based on the number of projections of the location $\mathbf{c}$ on the obstacle set $\mathcal{O}_{i,\alpha}$ i.e., $\mathbf{card}(\mathcal{PJ}(\mathbf{c}, \mathcal{O}_{i,\alpha}))$, we construct the boundary of the modified obstacle set $\partial\mathcal{O}_{i,\alpha}^M$ as follows:

- *If the ring $\partial\mathcal{B}_\alpha(\mathbf{c})$ is touching the set $\mathcal{O}_{i,\alpha}$ at a single location, then include that location in the set $\partial\mathcal{O}_{i,\alpha}^M$. That is, if $\mathbf{card}(\mathcal{PJ}(\mathbf{c}, \mathcal{O}_{i,\alpha})) = 1$, then $\Pi(\mathbf{c}, \mathcal{O}_{i,\alpha}) \in \partial\mathcal{O}_{i,\alpha}^M$.*
- *If the ring $\partial\mathcal{B}_\alpha(\mathbf{c})$ is simultaneously touching the set $\mathcal{O}_{i,\alpha}$ at more than one location, then include in the set $\partial\mathcal{O}_{i,\alpha}^M$ the part of the ring $\partial\mathcal{B}_\alpha(\mathbf{c})$ which intersects the conic hull of the set $\mathcal{PJ}(\mathbf{c}, \mathcal{O}_{i,\alpha})$ with its vertex at $\mathbf{c}$. That is, if $\mathbf{card}(\mathcal{PJ}(\mathbf{c}, \mathcal{O}_{i,\alpha})) > 1$, then $\mathcal{Y}(\mathbf{c}) \subset \partial\mathcal{O}_{i,\alpha}^M$, where the set $\mathcal{Y}(\mathbf{c})$ is given by*

$$\mathcal{Y}(\mathbf{c}) = \mathcal{CH}(\mathbf{c}, \mathcal{PJ}(\mathbf{c}, \mathcal{O}_{i,\alpha})) \cap \partial\mathcal{B}_\alpha(\mathbf{c}). \tag{4.9}$$

We consider the modified obstacle-occupied workspace $\mathcal{O}_{\mathcal{W}}^M \subset \mathcal{W}$ to be the region that the robot should avoid. The set $\mathcal{V}_{r_a}$, defined in (4.3), represents the modified obstacle-free workspace for the center of the robot. We require the set $\mathcal{V}_{r_a}$ to be a pathwise connected set. However, the pathwise connectedness of the set $\mathcal{V}_{r_a}$ mainly depends on the value of the parameter α. For example, see Fig. 4.6 in which the set $\mathcal{V}_{r_a}$ is not connected due to improper selection of the parameter α. To that end, we require the following lemma:

Lemma 4.3 *Under Assumption 4.1, there exists $\bar{\alpha} > r_a$ such that for all $\alpha \in (r_a, \bar{\alpha}]$ the following conditions are satisfied:*

1. *the $\alpha-$eroded obstacle-free workspace $\mathcal{W}_\alpha$ is a pathwise connected set,*
2. *the distance between the origin and the set $\mathcal{W}_\alpha$ is less than $\alpha - r_a$.*

Proof See Appendix C.3.

Next, we show that if we choose the parameter α, which is used in (4.4) and (4.3) to obtain the set $\mathcal{V}_{r_a}$, as per Lemma 4.3, then the set $\mathcal{V}_{r_a}$ is pathwise connected and the origin belongs to its interior.

Lemma 4.4 *If the parameter α, which is used in (4.4), is chosen as per Lemma 4.3, then the modified obstacle-free workspace $\mathcal{V}_{r_a}$ is pathwise connected and $\mathbf{0} \in \mathcal{V}_{r_a}^{\circ}$.*

Proof See Appendix C.4

This concludes the discussion on the formulation and features of the obstacle-reshaping operator $\mathbf{M}$ (4.4), which is applicable to $n-$dimensional Euclidean subsets of $\mathbb{R}^n$. Next, we provide the hybrid control design for the robot operating in a planar workspace *i.e.*, $\mathcal{W} \subset \mathbb{R}^2$.

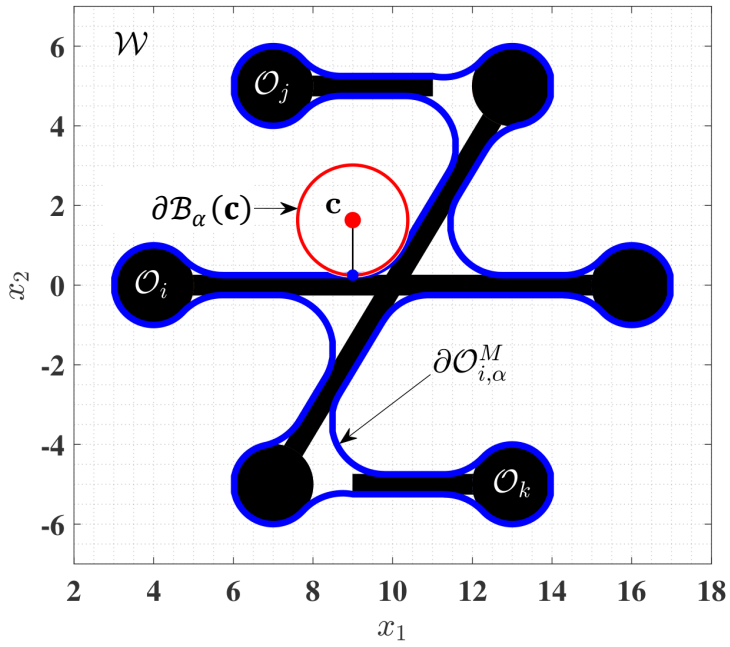

Figure 4.7: An obstacle-occupied workspace $\mathcal{O}_\mathcal{W}$ with three obstacles $\mathcal{O}_i, \mathcal{O}_j$ and $\mathcal{O}_k$, and the boundary of the modified obstacle $\mathcal{O}_{i,\alpha}^M$ obtained using a virtual ring with radius α, where $\mathcal{O}_{i,\alpha} = \mathcal{O}_i \cup \mathcal{O}_j \cup \mathcal{O}_k$, see (4.7). A video can be seen here https://youtu.be/mylrTOtYOSY

.

4.4 Hybrid control for obstacle avoidance

We consider planar environments that satisfy Assumptions 4.1 and 4.2. The proposed obstacle-avoidance strategy requires a unique closest point on the nearest obstacle from

the center of the robot. To achieve this, we first modify the obstacles using the obstacle-reshaping operator (4.4). This modification guarantees that, for all locations in the $\alpha-$neighbourhood of the modified obstacles, there will be a unique closest point on the nearest modified obstacle from the robot's center, as stated in Lemma 4.1. In the proposed scheme, similar to [Berkane et al., 2021a], depending upon the value of the mode indicator $m \in \{-1, 0, 1\} =: \mathbb{M}$, the robot operates in two different modes, namely the *move-to-target* mode ($m = 0$) when it is away from the modified obstacles and the *obstacle-avoidance* mode ($m \in \{-1, 1\}$) when it is in the vicinity of an modified obstacle. In the *move-to-target* mode, the robot moves straight towards the target, whereas during the *obstacle-avoidance* mode the robot moves around the nearest modified obstacle, either in the clockwise direction ($m = 1$) or in the counter-clockwise direction ($m = -1$). We utilize a vector joining the center of the robot and its projection on the modified obstacle-occupied workspace to select between the modes and assign the direction of motion while operating in the *obstacle-avoidance* mode.

4.4.1 Hybrid control design

The proposed hybrid control $\mathbf{u}(\mathbf{x}, \mathbf{h}, m)$ is given by

$$\mathbf{u}(\xi) = -\kappa_s(1 - m^2)\mathbf{x} + \kappa_r m^2 \mathbf{v}(\mathbf{x}, m), \tag{4.10a}$$

$$\underbrace{\begin{matrix}\dot{\mathbf{h}} = \mathbf{0} \\ \dot{m} = 0\end{matrix}}_{\xi \in \mathcal{F}}, \quad \underbrace{\begin{bmatrix}\mathbf{h}^+ \\ m^+\end{bmatrix} \in \mathbf{L}(\xi)}_{\xi \in \mathcal{J}}, \tag{4.10b}$$

where $\kappa_s > 0$, $\kappa_r > 0$ and $\xi = (\mathbf{x}, \mathbf{h}, m) \in \mathcal{V}_{r_a} \times \mathcal{V}_{r_a} \times \mathbb{M} =: \mathcal{K}$, is the composite state vector. In (4.10a), $\mathbf{x} \in \mathcal{V}_{r_a}$ is the location of the center of the robot. The state $\mathbf{h} \in \mathcal{V}_{r_a}$, referred to as a *hit point*, is the location of the center of the robot when it enters in the *obstacle-avoidance* mode. The discrete variable $m \in \mathbb{M}$ is the mode indicator. The update law $\mathbf{L}(\xi)$, used in (4.10b), which allows the robot to switch between the modes, is discussed in Section 4.4.3. The symbols $\mathcal{F}$ and $\mathcal{J}$ denote the flow and jump sets related to different modes of operations, respectively, whose constructions are provided in Section 4.4.2. Next, we provide the design of the vector $\mathbf{v}(\mathbf{x}, m) \in \mathbb{R}^2$, used in (4.10a).

The vector $\mathbf{v}(\mathbf{x}, m)$ is defined as

$$\mathbf{v}(\mathbf{x}, m) = \begin{bmatrix} 0 & m \\ -m & 0 \end{bmatrix} \frac{\mathbf{x} - \Pi(\mathbf{x}, \mathcal{O}_{\mathcal{W}}^M)}{\|\mathbf{x} - \Pi(\mathbf{x}, \mathcal{O}_{\mathcal{W}}^M)\|}, \tag{4.11}$$

where $\Pi(\mathbf{x}, \mathcal{O}_{\mathcal{W}}^M)$ is the point on the modified obstacle-occupied workspace $\mathcal{O}_{\mathcal{W}}^M$ which is closest to the center of the robot $\mathbf{x}$, as defined in Section 2.2.1. As per Lemma 4.1, if the center of the robot $\mathbf{x}$ is inside the $\alpha-$neighbourhood of the set $\mathcal{O}_{\mathcal{W}}^M$, then $\Pi(\mathbf{x}, \mathcal{O}_{\mathcal{W}}^M)$ is unique. When the robot operates in the *obstacle-avoidance* mode, the vector $\mathbf{v}(\mathbf{x}, m)$ allows it to move around the nearest obstacle either in the clockwise direction ($m = 1$) or in the counter-clockwise direction ($m = -1$). Next, we discuss the design of the flow set $\mathcal{F}$ and the jump set $\mathcal{J}$, used in (4.10).

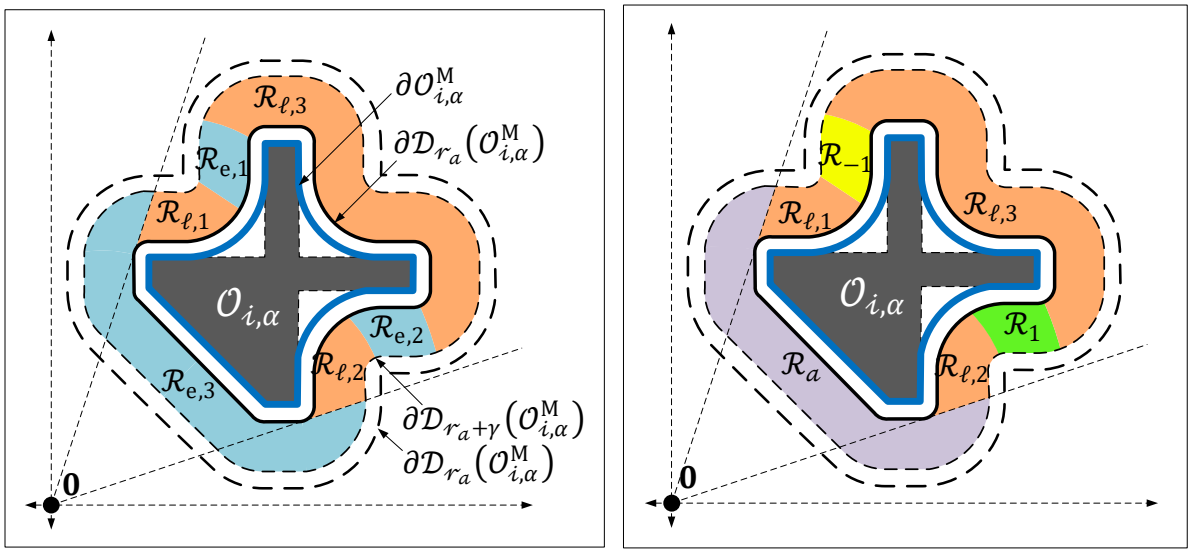

Figure 4.8: The left figure shows the partitioning of the region $\mathcal{N}_\gamma(\mathcal{D}_{r_a}(\mathcal{O}^M_i))$ into the *landing* region $\mathcal{R}_l = \mathcal{R}_{l,1} \cup \mathcal{R}_{l,2} \cup \mathcal{R}_{l,3}$, and the *exit* region $\mathcal{R}_e = \mathcal{R}_{e,1} \cup \mathcal{R}_{e,2} \cup \mathcal{R}_{e,3}$, using (4.12) and (4.14). The right figure shows the partitioning of the *exit* region into three sub-regions namely the *always exit* region $\mathcal{R}_a$, the *clockwise exit* region $\mathcal{R}_1$, and the *counter-clockwise exit* region $\mathcal{R}_{-1}$, using (4.15), (4.17) and (4.18), respectively.

4.4.2 Geometric construction of the flow and jump sets

When the robot operates in the *move-to-target* mode, in the modified free workspace, its velocity is directed towards the target location. If any connected modified obstacle $\mathcal{O}^M_{i,\alpha}, i \in \mathbb{I}$, is on the line segment joining the robot's location with the target location $\mathcal{L}_s(\mathbf{x}, \mathbf{0})$, then the robot, operating in the *move-to-target* mode, will enter the $\alpha-$neighbourhood of that modified obstacle (*i.e.*, $d(\mathbf{x}, \mathcal{O}^M_{i,\alpha}) \leq \alpha$) from the *landing* region $\mathcal{R}_l$, as depicted in Fig. 4.8. The parameter α is chosen as per Lemma 4.3. The *landing* region is defined as

$$\mathcal{R}_l := \bigcup_{i \in \mathbb{I}} \mathcal{R}^i_l, \tag{4.12}$$

where, for each $i \in \mathbb{I}$, the set $\mathcal{R}^i_l$ is given by

$$\begin{aligned} \mathcal{R}^i_l := \{\mathbf{x} \in \mathcal{N}_\gamma(\mathcal{D}_{r_a}(\mathcal{O}^M_{i,\alpha})) | \mathbf{x}^\intercal(\mathbf{x} - \Pi(\mathbf{x}, \mathcal{O}^M_{i,\alpha})) \geq 0, \\ \mathcal{L}_s(\mathbf{x}, \mathbf{0}) \cap \left(\mathcal{D}_{r_a}(\mathcal{O}^M_{i,\alpha})\right)^\circ \neq \emptyset\}, \end{aligned} \tag{4.13}$$

where $\gamma \in (0, \alpha - r_a)$. Given a set $\mathcal{A} \subset \mathbb{R}^n$ and a scalar $r > 0$, the $r-$neighbourhood of the set $\mathcal{A}$ is denoted by $\mathcal{N}_r(\mathcal{A}) = \mathcal{D}_r(\mathcal{A}) \setminus (\mathcal{A})^\circ$.

Notice that for a connected modified obstacle $\mathcal{O}^M_{i,\alpha}, i \in \mathbb{I}$, the *landing* region $\mathcal{R}^i_l$, defined in (4.13), is the intersection of the following two regions:

1. the region where the line segment $\mathcal{L}_s(\mathbf{x}, \mathbf{0})$, which joins the center of the robot and the target location, intersects with the interior of the r_a-dilated connected modified obstacle $\mathcal{D}^\circ_{r_a}(\mathcal{O}^M_{i,\alpha})$. Hence, if the robot moves straight towards the target in this region, it will eventually collide with the modified obstacle $\mathcal{O}^M_{i,\alpha}$.

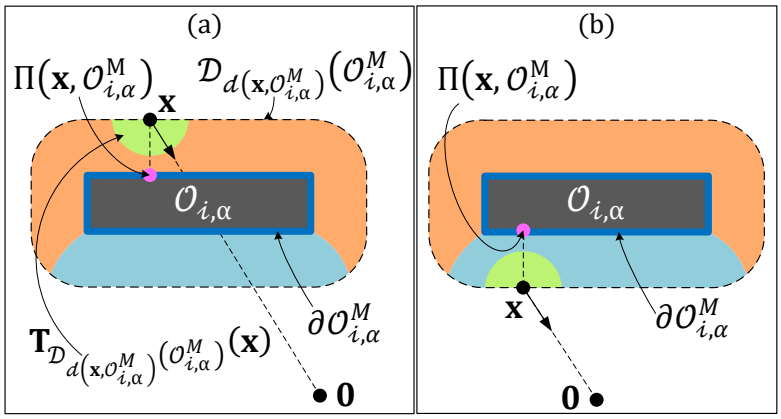

Figure 4.9: Partitions of the neighbourhood of the modified obstacle $\mathcal{O}^M_{i,\alpha}$ based on the value of the inner product between the two vectors $-\mathbf{x}$ and $\mathbf{x}-\Pi(\mathbf{x}, \mathcal{O}^M_{i,\alpha})$ and the tangent cone to the set $\mathcal{D}_{d(\mathbf{x},\mathcal{O}^M_{i,\alpha})}(\mathcal{O}^M_{i,\alpha})$ at $\mathbf{x}$. (a) The vector $-\mathbf{x}$ is pointing inside the tangent cone. (b) The vector $-\mathbf{x}$ is pointing outside the tangent cone.

2. the region where the inner product between the vectors $\mathbf{x}$ and $\mathbf{x} - \Pi(\mathbf{x}, \mathcal{O}^M_{i,\alpha})$ is non-negative, as shown in Fig. 4.9. Notice that, when the robot moves straight towards the target in this region, its distance from the modified obstacle $\mathcal{O}^M_{i,\alpha}$ *i.e.*, $d(\mathbf{x}, \mathcal{O}^M_{i,\alpha})$ does not increase. To understand this fact, observe that if for any $\mathbf{x} \in \mathcal{N}_\gamma(\mathcal{D}_{r_a}(\mathcal{O}^M_{i,\alpha}))$, $\mathbf{x}^\intercal(\mathbf{x} - \Pi(\mathbf{x}, \mathcal{O}^M_{i,\alpha})) \geq 0$, then $-\mathbf{x} \in \mathbf{T}_{\mathcal{D}_{d(\mathbf{x},\mathcal{O}^M_{i,\alpha})}(\mathcal{O}^M_{i,\alpha})}(\mathbf{x}) = \mathcal{P}_{\leq}(\mathbf{0}, \mathbf{x} - \Pi(\mathbf{x}, \mathcal{O}^M_{i,\alpha}))$ *i.e.*, the robot, moving straight towards the target in this region, does not leave the region $\mathcal{D}_{d(\mathbf{x},\mathcal{O}^M_{i,\alpha})}(\mathcal{O}^M_{i,\alpha})$. The notation $\mathbf{T}_{\mathcal{D}_{d(\mathbf{x},\mathcal{O}^M_{i,\alpha})}(\mathcal{O}^M_{i,\alpha})}(\mathbf{x})$ denotes the tangent cone to the set $\mathcal{D}_{d(\mathbf{x},\mathcal{O}^M_{i,\alpha})}(\mathcal{O}^M_{i,\alpha})$ at $\mathbf{x}$.

According to (4.13), due to the intersection of the above-mentioned two regions, the *landing* region $\mathcal{R}^i_l$ excludes a set of locations from the region $\mathcal{N}_\gamma(\mathcal{D}_{r_a}(\mathcal{O}^M_{i,\alpha}))$, for which the inner product between the vectors $\mathbf{x}$ and $\mathbf{x} - \Pi(\mathbf{x}, \mathcal{O}^M_{\mathcal{W}})$ is negative and the line segment $\mathcal{L}_s(\mathbf{x}, \mathbf{0})$ intersects with the interior of the set $\mathcal{D}_{r_a}(\mathcal{O}^M_{i,\alpha})$, for example see the regions $\mathcal{R}_{e,1}$ and $\mathcal{R}_{e,2}$ in Fig. 4.8. Even though the robot does not have a line-of-sight towards the target location, as long as it moves straight towards the target in these regions, its distance from the modified obstacle $\mathcal{O}^M_{i,\alpha}$ *i.e.*, $d(\mathbf{x}, \mathcal{O}^M_{i,\alpha})$ increases. To understand this fact, observe that if for any $\mathbf{x} \in \mathcal{N}_\gamma(\mathcal{D}_{r_a}(\mathcal{O}^M_{i,\alpha}))$, $\mathbf{x}^\intercal(\mathbf{x} - \Pi(\mathbf{x}, \mathcal{O}^M_{i,\alpha}))$ is negative, then $-\mathbf{x} \notin \mathbf{T}_{\mathcal{D}_{d(\mathbf{x},\mathcal{O}^M_{i,\alpha})}(\mathcal{O}^M_{i,\alpha})}(\mathbf{x}) = \mathcal{P}_{\leq}(\mathbf{0}, \mathbf{x} - \Pi(\mathbf{x}, \mathcal{O}^M_{i,\alpha}))$ *i.e.*, the robot, moving straight towards the target in this region, does not enter the region $\mathcal{D}_{d(\mathbf{x},\mathcal{O}^M_{i,\alpha})}(\mathcal{O}^M_{i,\alpha})$. Due to this property, we include these locations in the region called an *exit* region, wherein the robot can operate in the *move-to-target* mode, as discussed next.

When the robot operates in the *obstacle-avoidance* mode in the $\gamma-$ neighbourhood of the modified obstacle-occupied workspace, it will switch to the *move-to-target* mode from the *exit* region, which is defined as follows:

$$\mathcal{R}_e := \overline{\mathcal{N}_\gamma(\mathcal{D}_{r_a}(\mathcal{O}^M_{\mathcal{W}})) \setminus \mathcal{R}_l}. \tag{4.14}$$

According to (4.12), (4.13) and (4.14), the *exit* region is a combination of following two regions:

1. the region where the inner product $\mathbf{x}^\intercal(\mathbf{x} - \Pi(\mathbf{x}, \mathcal{O}_{\mathcal{W}}^M))$ is non-positive. As discussed earlier, when the robot moves straight towards the target in this region, its distance from the unsafe region does not decrease.

2. the region where the inner product $\mathbf{x}^\intercal(\mathbf{x} - \Pi(\mathbf{x}, \mathcal{O}_{\mathcal{W}}^M))$ is positive and the line segment $\mathcal{L}_s(\mathbf{x}, \mathbf{0})$, which joins the robot's location and the target location, does not intersect with the nearest modified obstacle. Hence, the robot can move straight towards the target and safely leave the $\alpha-$neighbourhood of this connected modified obstacle.

As shown in Fig. 4.8 (left), for a modified non-convex obstacle $\mathcal{O}_{i,\alpha}^M, i \in \mathbb{I}$, the *exit* region is not a connected set. Consider a situation, wherein the robot is moving in the clockwise direction with respect to the set $\mathcal{O}_{i,\alpha}^M$ in the *landing* region $\mathcal{R}_{l,1}$. If the robot were to start moving straight towards the target after entering the *exit* region $\mathcal{R}_{e,1}$, it will re-enter the region $\mathcal{R}_{l,1}$, resulting in multiple simultaneous switching instances. Similar situation can occur for the robot moving in the *counter-clockwise* direction with respect to the set $\mathcal{O}_{i,\alpha}^M$ in the *landing* region $\mathcal{R}_{l,2}$, if it moves straight towards the target after entering the *exit* region $\mathcal{R}_{e,2}$. On the other hand, if the robot enters in the region $\mathcal{R}_{e,3}$, then, irrespective of the direction of motion around the obstacle, it can safely move straight towards the target and leave the $\gamma-$neighbourhood of the modified obstacle $\mathcal{O}_{i,\alpha}^M$.

Hence, as shown in Fig. 4.8 (right), based on the angle between the vectors $\mathbf{x}$ and $\mathbf{x} - \Pi(\mathbf{x}, \mathcal{O}_{\mathcal{W}}^M)$, and the presence of a line-of-sight to the target location with respect to the nearest disjoint modified obstacle, we divide the *exit* region $\mathcal{R}_e$ into three sub-regions $\mathcal{R}_a$, $\mathcal{R}_1$ and $\mathcal{R}_{-1}$, referred to as the *always exit* region, the *clockwise exit* region and the *counter-clockwise exit* region, respectively, as follows:

The *always exit* region $\mathcal{R}_a$ is defined as

$$\mathcal{R}_a := \bigcup_{i \in \mathbb{I}} \mathcal{R}_a^i, \tag{4.15}$$

where, for each $i \in \mathbb{I}$, the set $\mathcal{R}_a^i$, which is given by

$$\mathcal{R}_a^i := \{\mathbf{x} \in \mathcal{R}_e | \mathcal{L}_s(\mathbf{x}, \mathbf{0}) \cap \left(\mathcal{D}_{r_a}(\mathcal{O}_{i,\alpha}^M)\right)^\circ = \emptyset\}, \tag{4.16}$$

contains the locations from the exit region $\mathcal{R}_e$ such that the line segments joining them to the origin do not intersect with the interior of the r_a-dilated modified obstacle $\mathcal{D}_{r_a}(\mathcal{O}_{i,\alpha}^M)$.

The *clockwise exit* region $\mathcal{R}_1$ is defined as

$$\mathcal{R}_1 := \left\{\mathbf{x} \in \mathcal{R}_e \setminus \mathcal{R}_a | \psi(\mathbf{x}, \mathbf{x} - \Pi(\mathbf{x}, \mathcal{O}_{\mathcal{W}}^M)) \in [\pi, 2\pi]\right\}, \tag{4.17}$$

and the *counter-clockwise exit* region $\mathcal{R}_{-1}$ is defined as

$$\mathcal{R}_{-1} := \left\{\mathbf{x} \in \mathcal{R}_e \setminus \mathcal{R}_a | \psi(\mathbf{x}, \mathbf{x} - \Pi(\mathbf{x}, \mathcal{O}_{\mathcal{W}}^M)) \in [0, \pi]\right\} \tag{4.18}$$

where, given two vectors $\mathbf{p}, \mathbf{q} \in \mathbb{R}^2$, the notation $\psi(\mathbf{p}, \mathbf{q})$ indicates the angle measured from $\mathbf{p}$ to $\mathbf{q}$. The angle measured in the counter-clockwise direction is considered positive, and vice versa.

While moving in the clockwise direction around the modified obstacle, the robot is allowed to move straight towards the target only if its center is in the region $\mathcal{R}_1 \cup \mathcal{R}_a$. Whereas, the robot moving in the counter-clockwise direction around the modified obstacle should move straight towards the target only if its center is in the region $\mathcal{R}_{-1} \cup \mathcal{R}_a$. Next, we provide the geometric constructions of the flow set $\mathcal{F}$ and the jump set $\mathcal{J}$, used in (4.10).

Flow and jump sets (move-to-target mode)

As discussed earlier, if the robot, which is moving straight towards the target, is on a collision path towards a connected modified obstacle $\mathcal{O}^M_{i,\alpha}$, for some $i \in \mathbb{I}$, then it will enter the $\gamma-$neighbourhood of this modified obstacle through the *landing* region. Hence, the jump set of the *move-to-target* mode for the state $\mathbf{x}$ is defined as

$$\mathcal{J}_0^{\mathcal{W}} := \mathcal{N}_{\gamma_s}(\mathcal{D}_{r_a}(\mathcal{O}^M_{\mathcal{W}})) \cap \mathcal{R}_l, \tag{4.19}$$

where $\gamma_s \in (0, \gamma)$. For robustness purposes (with respect to noise), we introduce a hysteresis region by allowing the robot, operating in the *move-to-target* mode inside the $\gamma-$neighbourhood of the set $\mathcal{O}^M_{\mathcal{W}}$, to move closer to the set $\mathcal{O}^M_{\mathcal{W}}$ before switching to the *obstacle-avoidance* mode.

The flow set of the *move-to-target* mode for the state $\mathbf{x}$ is then defined as

$$\mathcal{F}_0^{\mathcal{W}} := \left(\mathcal{W} \setminus \left(\mathcal{D}_{r_a+\gamma_s}(\mathcal{O}^M_{\mathcal{W}})\right)^\circ\right) \cup \mathcal{R}_e. \tag{4.20}$$

Notice that the union of the jump set (4.19) and the flow set (4.20) exactly covers the modified robot-centred obstacle-free workspace $\mathcal{V}_{r_a}$ (4.3). Refer to Fig. 4.11 for the representation of the flow and jump sets related to the obstacle-occupied workspace $\mathcal{O}^M_{\mathcal{W}}$. Next, we provide the construction of the flow and jump sets for the *obstacle-avoidance* mode.

Flow and jump sets (*obstacle-avoidance* mode)

The robot operates in the *obstacle-avoidance* mode only in the $\gamma-$neighbourhood of the modified obstacle-occupied workspace $\mathcal{O}^M_{\mathcal{W}}$. The mode indicator variable $m = 1$ and $m = -1$ prompts the robot to move either in the clockwise direction or in the counter-clockwise direction with respect to the nearest boundary of the set $\mathcal{O}^M_{\mathcal{W}}$, respectively. As discussed earlier, for some $m \in \{-1, 1\}$, the robot should exit the *obstacle-avoidance* mode and switch to the *move-to-target* mode only if its center belongs to the exit region $\mathcal{R}_m \cup \mathcal{R}_a$.

To that end, we make use of the *hit point* $\mathbf{h}$ (*i.e.*, the location of the center of the robot when it switched from the *move-to-target* mode to the current *obstacle-avoidance* mode) to define the jump set of the *obstacle-avoidance* mode $\mathcal{J}_m^{\mathcal{W}}$ for the state $\mathbf{x}$ as follows:

$$\mathcal{J}_m^{\mathcal{W}} := \left(\mathcal{W} \setminus (\mathcal{D}_{r_a+\gamma}(\mathcal{O}^M_{\mathcal{W}}))^\circ\right) \cup \mathcal{E}\mathcal{R}^{\mathbf{h}}_m \cup \mathcal{B}_\delta(\mathbf{0}), \tag{4.21}$$

where $m \in \{-1, 1\}$ and the parameter $\delta \in (0, d(\mathbf{0}, \mathcal{O}^M_{\mathcal{W}}) - r_a)$. Note that, according to Lemma 4.4, the target location $\mathbf{0} \in \mathcal{V}^\circ_{r_a}$. As a result, the distance $d(\mathbf{0}, \mathcal{O}^M_{\mathcal{W}}) > r_a$, which

guarantees the existence of the parameter δ. In (4.21), the inclusion of the set $\mathcal{B}_\delta(\mathbf{0})$ in the set $\mathcal{J}_m^{\mathcal{W}}$ allows us to ensure the stability of the origin, as stated later in Theorem 4.1.

For some $m \in \{-1, 1\}$ and the *hit point* $\mathbf{h} \in \mathcal{V}_{r_a}$, the set $\mathcal{ER}_m^{\mathbf{h}}$ is given by

$$\mathcal{ER}_m^{\mathbf{h}} := \{\mathbf{x} \in \overline{\mathcal{R}_m \cup \mathcal{R}_a} \big| \|\mathbf{h}\| - \|\mathbf{x}\| \geq \epsilon\}, \tag{4.22}$$

where $\epsilon \in (0, \bar{\epsilon}]$, with $\bar{\epsilon} > 0$. This set contains all locations $\mathbf{x}$ from the *exit* region $\mathcal{R}_m \cup \mathcal{R}_a$ for which the target location $\mathbf{0}$ is at least ϵ units closer to $\mathbf{x}$ than to the current *hit point* $\mathbf{h}$.

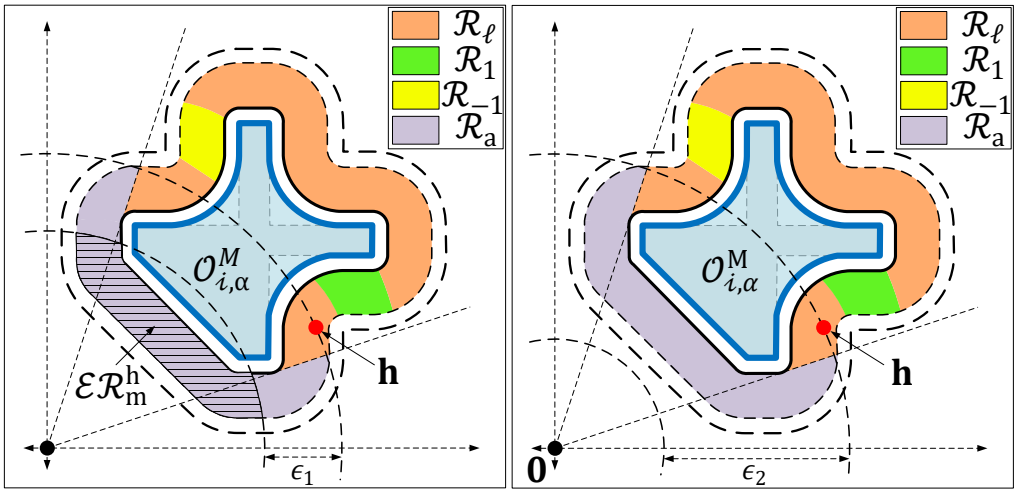

Figure 4.10: Effects of ϵ, used in (4.22), on the construction of the sets $\mathcal{ER}_m^{\mathbf{h}}$, for $m \in \{-1, 1\}$ and a *hit point* $\mathbf{h} \in \mathcal{J}_0^{\mathcal{W}}$. The left figure shows that when $\epsilon = \epsilon_1$, the sets $\mathcal{ER}_m^{\mathbf{h}}, m \in \{-1, 1\}$, are non-empty. The right figure shows that when $\epsilon = \epsilon_2$, the sets $\mathcal{ER}_m^{\mathbf{h}}, m \in \{-1, 1\}$, are empty.

Since, according to Lemma 4.4, the target location belongs to the interior of the modified obstacle-free workspace w.r.t. the center of the robot *i.e.*, $\mathbf{0} \in (\mathcal{V}_{r_a})^\circ$, the existence of a positive scalar $\bar{\epsilon}$ can be guaranteed. However, if one selects a very high value for ϵ, then for some connected modified obstacles $\mathcal{O}_{i,\alpha}^M, i \in \mathbb{I}$, the set $\mathcal{ER}_m^{\mathbf{h}} \cap \mathcal{N}_\gamma(\mathcal{D}_{r_a}(\mathcal{O}_{i,\alpha}^M))$ will become empty, as shown in Fig. 4.10, and the robot might get stuck (indefinitely) in the *obstacle-avoidance* mode in the vicinity of those modified obstacles. Therefore, in the next lemma, we provide an upper bound on the value of $\bar{\epsilon}$.

Lemma 4.5 *Under Assumptions 4.1 and 4.2, we consider a connected modified obstacle* $\mathcal{O}_{i,\alpha}^M, i \in \mathbb{I}$. *If* $\bar{\epsilon} \in (0, \epsilon_h]$, *where*

$$\epsilon_h = \sqrt{(d(\mathbf{0}, \mathcal{O}_{\mathcal{W}}^M)^2 - r_a^2)} - \left(d(\mathbf{0}, \mathcal{O}_{\mathcal{W}}^M) - r_a\right), \tag{4.23}$$

then, for every $\mathbf{h} \in \mathcal{J}_0^{\mathcal{W}}$ *with* $d(\mathbf{h}, \mathcal{O}_{i,\alpha}^M) = \beta \in [r_a, r_a + \gamma]$, *and any location* $\mathbf{p} \in \mathcal{PJ}(\mathbf{0}, \partial\mathcal{D}_\beta(\mathcal{O}_{i,\alpha}^M))$, *the set* $\mathcal{H}_{\mathbf{p}} := \mathcal{B}_\delta(\mathbf{p}) \cap \mathcal{N}_\gamma(\mathcal{D}_{r_a}(\mathcal{O}_{i,\alpha}^M)) \subset \mathcal{ER}_m^{\mathbf{h}}$, *for some* $m \in \{-1, 1\}$ *and* $\delta = \min\{\beta - r_a, d(\mathbf{0}, \mathcal{O}_{\mathcal{W}}^M) - r_a\}$, *where the set* $\mathcal{ER}_m^{\mathbf{h}}$ *is defined in* (4.22).

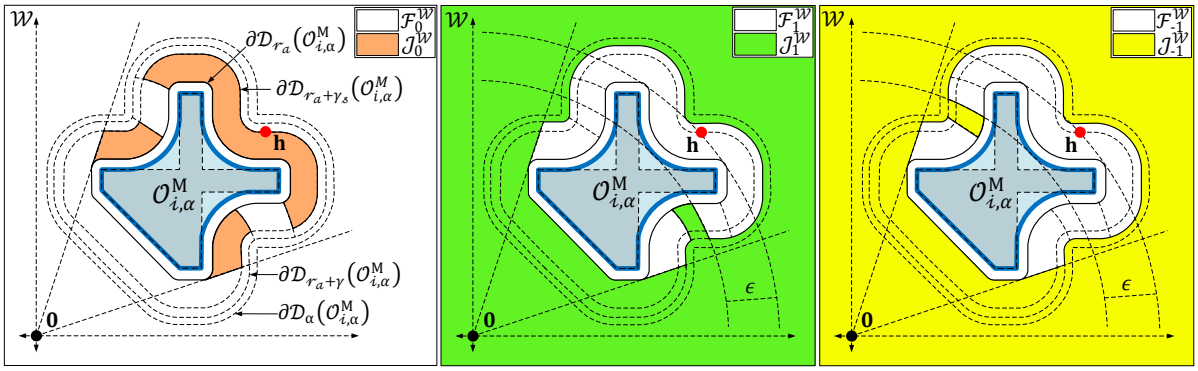

Figure 4.11: Flow and jump sets $\mathcal{F}_m^{\mathcal{W}}$, $\mathcal{J}_m^{\mathcal{W}}$, related to the set $\mathcal{O}_{i,\alpha}$ shown in Fig. 4.8. The left figure ($m = 0$) illustrates the case where the robot operates in the *move-to-target* mode and moves straight toward the target location. The middle figure ($m = 1$) illustrates the case where the robot, operating in the *obstacle-avoidance* mode, moves in the clockwise direction with respect to $\partial\mathcal{O}_{i,\alpha}^{M}$. The right figure ($m = -1$) illustrates the case where the robot, operating in the *obstacle-avoidance* mode, moves in the counter-clockwise direction with respect to $\partial\mathcal{O}_{i,\alpha}^{M}$.

Proof See Appendix C.5.

According to Lemma 4.5, if the *hit point* belongs to the jump set of the *move-to-target* mode associated with a connected modified obstacle $\mathcal{O}_{i,\alpha}^{M}$ and $\epsilon \in (0, \bar{\epsilon}]$, where $\bar{\epsilon}$ is chosen as per Lemma 4.5, then the set $\mathcal{ER}_m^{\mathbf{h}} \cap \mathcal{N}_\gamma(\mathcal{D}_{r_a}(\mathcal{O}_{i,\alpha}^{M}))$ is non-empty. Hence, we initialize the robot in the *move-to-target* mode so that the *hit point* will always belong to the jump set of the *move-to-target* mode, as stated later in Theorem 4.1.

According to (4.21) and (4.22), while operating in the *obstacle-avoidance* mode with some $m \in \{-1, 1\}$, the robot can switch to the *move-to-target* mode when its center belongs to the *exit* region $\mathcal{R}_m \cup \mathcal{R}_a$ and the target location $\mathbf{0}$ is at least ϵ units closer to $\mathbf{x}$ than to the current *hit point* $\mathbf{h}$. This creates a hysteresis region and ensures Zeno-free switching between the modes. This switching strategy is inspired by [Kamon et al., 1998], which allows us to establish convergence properties of the target location, as discussed later in Theorem 4.1.

We then define the flow set of the *obstacle-avoidance* mode $\mathcal{F}_m^{\mathcal{W}}$ for the state $\mathbf{x}$ as follows:

$$\mathcal{F}_m^{\mathcal{W}} := \mathcal{R}_l \cup \overline{\mathcal{R}_{-m}} \cup \overline{\mathcal{R}_m \cup \mathcal{R}_a \setminus \mathcal{ER}_m^{\mathbf{h}}}, \tag{4.24}$$

where $m \in \{-1, 1\}$. Notice that the union of the jump set (4.21) and the flow set (4.24) exactly covers the modified robot-centred free workspace $\mathcal{V}_{r_a}$ (4.3). Refer to Fig. 4.11 for the representation of the flow and jump sets related to the modified obstacle-occupied workspace $\mathcal{O}_{\mathcal{W}}^{M}$.

Finally, the flow set $\mathcal{F}$ and the jump set $\mathcal{J}$, used in (4.10), are defined as

$$\mathcal{F} := \bigcup_{m \in \mathbb{M}} \mathcal{F}_m, \quad \mathcal{J} := \bigcup_{m \in \mathbb{M}} \mathcal{J}_m, \tag{4.25}$$

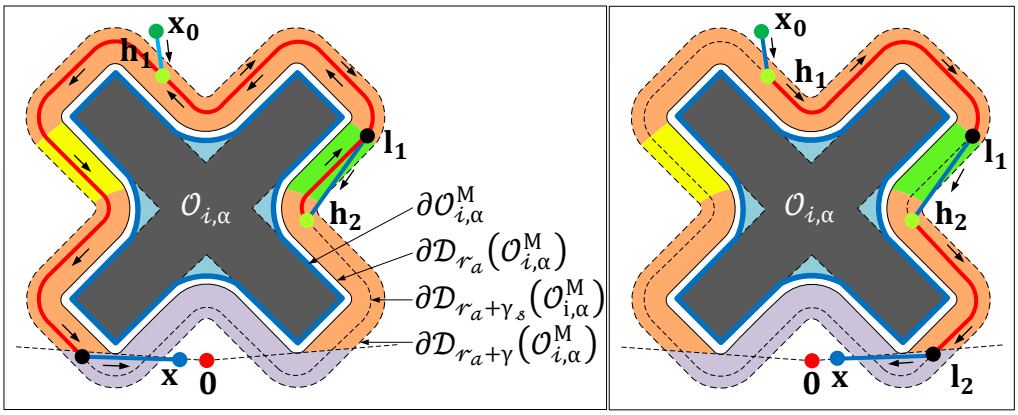

Figure 4.12: The left figure illustrates a case in which the robot, operating in the *obstacle-avoidance* mode, moves initially in the clockwise direction from $\mathbf{h}_1$ to $\mathbf{l}_1$, and then in the counter-clockwise direction from $\mathbf{h}_2$ to $\mathbf{l}_2$ with respect to the nearest point on the modified obstacle $\mathcal{O}^M_{i,\alpha}$. The right figure illustrates a case in which the robot, operating in the *obstacle-avoidance* mode, moves in the clockwise direction with respect to the nearest point on the modified obstacle $\mathcal{O}^M_{i,\alpha}$.

where for $m \in \mathbb{M}$, the sets $\mathcal{F}_m$ and $\mathcal{J}_m$ are given by

$$\mathcal{F}_m := \mathcal{F}^{\mathcal{W}}_m \times \mathcal{V}_{r_a} \times \{m\}, \quad \mathcal{J}_m := \mathcal{J}^{\mathcal{W}}_m \times \mathcal{V}_{r_a} \times \{m\}, \tag{4.26}$$

with $\mathcal{F}^{\mathcal{W}}_m, \mathcal{J}^{\mathcal{W}}_m$ defined in (4.20), (4.19) for $m = 0$ and in (4.24), (4.21) for $m \in \{-1, 1\}$.

Remark 4.5 *Let us look at the case where the robot is moving in the $\gamma-$neighbourhood of a connected modified obstacle $\mathcal{O}^M_{i,\alpha}$, for some $i \in \mathbb{I}$. If the robot needs to switch between the modes of operation multiple times before leaving the $\gamma-$neighbourhood of the modified obstacle $\mathcal{O}^M_{i,\alpha}$, then it should move in the same direction in the obstacle-avoidance mode i.e., either in the clockwise direction or in the counter-clockwise direction, to avoid retracing the previously travelled path, as shown in Fig. 4.12b. In fact, if the robot does not maintain the same direction of motion in the obstacle-avoidance mode, while operating in the $\gamma-$neighbourhood of the connected modified obstacle $\mathcal{O}^M_{i,\alpha}$, then it will retraces the previously travelled path, as shown in Fig. 4.12a.*

Next, we provide the update law $\mathbf{L}(\mathbf{x}, \mathbf{h}, m)$, used in (4.10b).

4.4.3 Update law $\mathbf{L}(\mathbf{x}, \mathbf{h}, m)$

The update law $\mathbf{L}(\xi)$, used in (4.10b), updates the value of the *hit point* $\mathbf{h}$ and the mode indicator m when the state $(\mathbf{x}, \mathbf{h}, m)$ belongs to the jump set $\mathcal{J}$ which is defined in (4.25) and (4.26). When the robot, operating in the *move-to-target* mode, enters in the jump set $\mathcal{J}_0$, which is defined according to (4.19) and (4.26), the update law $\mathbf{L}(\mathbf{x}, \mathbf{h}, 0)$ is given as

$$\mathbf{L}(\mathbf{x}, \mathbf{h}, 0) = \left\{ \begin{bmatrix} \mathbf{x} \\ z \end{bmatrix} \middle| z \in \{-1, 1\} \right\}. \tag{4.27}$$

Notice that, when the robot switches from the *move-to-target* mode to the *obstacle-avoidance* mode, the coordinates of the *hit point* gets updated to the current value of $\mathbf{x}$.

On the other hand, when the robot operating in the *obstacle-avoidance* mode, enters in the jump set $\mathcal{J}_m, m \in \{-1, 1\}$, defined in (4.21) and (4.26), the update law $\mathbf{L}(\mathbf{x}, \mathbf{h}, m), m \in \{-1, 1\}$, is given by

$$\mathbf{L}(\mathbf{x}, \mathbf{h}, m) = \begin{bmatrix} \mathbf{h} \\ 0 \end{bmatrix}. \tag{4.28}$$

When the robot switches from the *obstacle-avoidance* mode to the *move-to-target mode*, the value of the *hit point* remains unchanged.

Control design summary: The proposed hybrid feedback control law can be summarized as follows:

- **Parameters selection**: the target location is set at the origin with $\mathbf{0} \in \mathcal{W}_{r_a}^{\circ}$. The parameter α is set such that $\alpha > r_a$ and it satisfies the conditions in Lemma 4.3. The gain parameters κ_s and κ_r are set to positive values. The parameter $\bar{\epsilon}$, used in (4.22), is chosen as per Lemma 4.5. The scalar parameter γ, used in the construction of the flow set $\mathcal{F}$ and the jump set $\mathcal{J}$, is selected such that $\gamma \in (0, \alpha - r_a)$, and the parameter γ_s is set to satisfy $0 < \gamma_s < \gamma$.

- **Obstacle modification**: the obstacle reshaping operator (4.4) is used to obtain the modified obstacle-occupied workspace $\mathcal{O}_{\mathcal{W}}^{M}$. The state vector is initialized in the set $\mathcal{K}$ *i.e.*, $\xi(0, 0) \in \mathcal{K}$.

- ***Move-to-target* mode** $m = 0$: this mode is activated when $\xi \in \mathcal{F}_0$. As per (4.10a), the control input is given by $\mathbf{u}(\xi) = -\kappa_s \mathbf{x}$, causing $\mathbf{x}$ to evolve along the line segment $\mathcal{L}_s(\mathbf{0}, \mathbf{x})$ towards the origin. If, at some instance of time, ξ enters in the jump set $\mathcal{J}_0$ of the *move-to-target* mode, the state variables $(\mathbf{h}, m)$ are updated using (4.27), and the control input switches to the *obstacle-avoidance* mode.

- ***Obstacle-avoidance* mode** $m \in \{-1, 1\}$: this mode is activated when $\xi \in \mathcal{F}_m$ for some $m \in \{-1, 1\}$. As per (4.10a), the control input is given by $\mathbf{u}(\xi) = \kappa_r \mathbf{v}(\mathbf{x}, m)$, causing $\mathbf{x}$ to evolve in the $\gamma-$neighborhood of the nearest modified obstacle until the state ξ enters in the jump set $\mathcal{J}_m$, $m \in \{-1, 1\}$. When $\xi \in \mathcal{J}_m$, $m \in \{-1, 1\}$, the control input switches to the *move-to-target* mode by setting $m = 0$, as per (4.28).

This concludes the design of the proposed hybrid feedback controller (4.10).

4.5 Stability analysis

The hybrid closed-loop system resulting from the hybrid control law (4.10) is given by

$$\underbrace{\begin{aligned} \dot{\mathbf{x}} &= \mathbf{u}(\xi) \\ \dot{\mathbf{h}} &= \mathbf{0} \\ \dot{m} &= 0 \end{aligned}}_{\dot{\xi} = \mathbf{F}(\xi), \xi \in \mathcal{F},} \qquad \underbrace{\begin{aligned} \mathbf{x}^+ &= \mathbf{x} \\ \begin{bmatrix} \mathbf{h}^+ \\ m^+ \end{bmatrix} &\in \mathbf{L}(\xi) \end{aligned}}_{\xi^+ \in \mathbf{J}(\xi), \xi \in \mathcal{J},} \tag{4.29}$$

where $\mathbf{u}(\xi)$ is defined in (4.10a), and the update law $\mathbf{L}(\xi)$ is provided in (4.27), (4.28). The definitions of the flow set $\mathcal{F}$ and the jump set $\mathcal{J}$ are provided in (4.25), (4.26). Next, we analyze the hybrid closed-loop system (4.29) in terms of the forward invariance of the obstacle-free state space $\mathcal{K} := \mathcal{V}_{r_a} \times \mathcal{V}_{r_a} \times \mathbb{M}$ along with the stability properties of the target set $\mathcal{A}$, which is defined as

$$\mathcal{A} := \{\mathbf{0}\} \times \mathcal{V}_{r_a} \times \mathbb{M}. \tag{4.30}$$

We analyze the forward invariance of the modified obstacle-free workspace, which then will be followed by the convergence analysis.

First, we show that the hybrid closed-loop system (4.29) satisfies the hybrid basic conditions, as stated in Assumption 2.1, which guarantees the well-posedness of the hybrid closed-loop system.

Lemma 4.6 *The hybrid closed-loop system* (4.29) *with the data* $(\mathcal{F}, \mathbf{F}, \mathcal{J}, \mathbf{J})$ *satisfies the hybrid basic conditions stated in Assumption 2.1.*

Proof See Appendix C.6.

For safe autonomous navigation, the state $\mathbf{x}$ must always evolve within the set $\mathcal{V}_{r_a}$ (4.3). This is equivalent to having the set $\mathcal{K} := \mathcal{V}_{r_a} \times \mathcal{V}_{r_a} \times \mathbb{M}$ forward invariant for the hybrid closed-loop system (4.29). This is stated in the next Lemma.

Lemma 4.7 *Under Assumptions 4.1 and 4.2, for the hybrid closed-loop system* (4.29), *the obstacle-free set* $\mathcal{K} := \mathcal{V}_{r_a} \times \mathcal{V}_{r_a} \times \mathbb{M}$ *is forward invariant.*

Proof See Appendix C.7.

Next, we show that if the robot is initialized in the *move-to-target* mode, at any location in $\mathcal{V}_{r_a}$ and the parameter $\bar{\epsilon}$, used in (4.22), is chosen as per Lemma 4.5, then it will safely and asymptotically converge to the target location at the origin.

Theorem 4.1 *Consider the hybrid closed-loop system* (4.29) *and let Assumption 4.1 holds true. Also, let Assumption 4.2 hold true for the parameter* α *chosen as per Lemma 4.3. If the parameter* $\bar{\epsilon}$, *used in* (4.22), *is chosen as per Lemma 4.5, then*

i) the obstacle-free set $\mathcal{K}$ *is forward invariant,*

ii) the set $\mathcal{A}$ *is stable and attractive from all initial conditions* $\xi(0,0) \in \mathcal{V}_{r_a} \times \mathcal{V}_{r_a} \times \{0\}$,

iii) the number of jumps is finite.

Proof See Appendix C.8.

According to Theorem 4.1, we initialize the robot in the *move-to-target* mode to ensure that when it switches to the *obstacle-avoidance* mode, the *hit point* $\mathbf{h}$ belongs to the set $\mathcal{J}_0^{\mathcal{W}}$. This allows us to establish an upper bound on the value of the parameter $\bar{\epsilon}$ as given in Lemma 4.5, which is crucial to ensure that the robot, which moving in the *obstacle-avoidance* mode always enters in the *move-to-target* mode, and to guarantee convergence of the robot to the target location.

Remark 4.6 *Theorem 4.1 guarantees global asymptotic stability of the target location in the modified set $\mathcal{V}_{r_a}$ and not in the original set $\mathcal{W}_{r_a}$. Since the obstacle reshaping operator* $\mathbf{M}$ *is extensive, as stated in Remark 4.1, the set $\mathcal{V}_{r_a}$ is a subset of the original set $\mathcal{W}_{r_a}$ i.e., $\mathcal{V}_{r_a} \subset \mathcal{W}_{r_a}$. Interestingly, if one chooses the value of the parameter α close to r_a, then the region occupied by the set $\mathcal{V}_{r_a}$ approaches the original set $\mathcal{W}_{r_a}$. In other words, if $\mathcal{V}^1_{r_a}$ and $\mathcal{V}^2_{r_a}$ are two modified sets obtained for two different values of the parameter α_1 and α_2, respectively, using (4.4) and (4.3), where $\alpha_1, \alpha_2 \in (r_a, \bar{\alpha}]$, $\alpha_1 > \alpha_2$ and $\bar{\alpha}$ defined as per Lemma 4.3, then the set $\mathcal{V}^1_{r_a} \subset \mathcal{V}^2_{r_a} \subset \mathcal{W}_{r_a}$. Hence, by selecting a smaller value of the parameter α one can implement the proposed hybrid feedback controller (4.10) in a larger area.*

Unlike [Arslan and Koditschek, 2019, Assumprtion 1], [Verginis and Dimarogonas, 2021, Assumprtion 2], and [Berkane et al., 2021a, Section V-C3], Assumptions 4.1 and 4.2 do not impose restrictions on the minimum separation between any pair of obstacles and allow obstacles to be non-convex. In particular, Assumptions 4.1 and 4.2 are satisfied in the case of environments with convex obstacles where the minimum separation between any pair of obstacles is greater than $2r_a$, as discussed next.

Proposition 4.1 *Let the workspace $\mathcal{W}$ be a compact, convex subset of $\mathbb{R}^2$. Let the obstacles $\mathcal{O}_i, i \in \mathbb{I} \setminus \{0\}$, be compact and convex, $d(\mathcal{O}_i, \mathcal{O}_j) > 2r_a, \forall i, j \in \mathbb{I}, i \neq j$, and $\mathbf{0} \in \mathcal{W}^\circ_{r_a}$. Then Assumptions 4.1 and 4.2 hold true for all $\alpha \in (r_a, \bar{\alpha}]$, where the parameter $\bar{\alpha}$ is defined as*

$$\bar{\alpha} = \min_{i,j \in \mathbb{I}, i \neq j} d(\mathcal{O}_i, \mathcal{O}_j)/2. \tag{4.31}$$

Proof See Appendix C.9.

The workspace that satisfies the conditions (commonly used in the literature) in Proposition 4.1, also satisfies Assumptions 4.1 and 4.2. Notice that, since the internal obstacles are convex, if one chooses $\alpha \in (0, \bar{\alpha}]$, which is used in (4.4), where $\bar{\alpha}$ is defined in (4.31), then the shapes of the internal convex obstacles remains unchanged in the modified obstacle-occupied workspace. Hence, for any $\alpha \in (r_a, \bar{\alpha}]$, the set of locations that do not belong to the modified obstacle-free workspace $\mathcal{V}_{r_a}$ always belong to the $\alpha-$neighborhood of the boundary of the workspace *i.e.*, the set $\mathcal{W}_{r_a} \setminus \mathcal{V}_{r_a} \subset \mathcal{D}_\alpha(\mathcal{O}_0)$, where $\mathcal{O}_0 = (\mathcal{W}^\circ)^c$.

However, since the workspace $\mathcal{W}$ is convex, if the robot is initialized in the *move-to-target* mode, in the set $\mathcal{W}_{r_a} \setminus \mathcal{V}_{r_a}$, it will initially move straight towards the target and enter the set $\mathcal{V}_{r_a}$. Then, according to Lemma 4.7, the robot will continue to move inside the set $\mathcal{V}_{r_a}$ and according to Theorem 4.1, will asymptotically converge to the target location. Next, we provide procedural steps to implement the proposed hybrid feedback controller (4.10) for safe autonomous navigation in *a priori* known and *a priori* unknown environments.

4.6 Sensor-based implementation procedure

We choose the origin as the target location. We initialize the center of the robot in the interior of the set $\mathcal{W}_{r_a}$ and assume that the value of parameter α, defined in Lemma 4.3, is *a priori* known. The robot is initialized in the *move-to-target* mode *i.e.*, $m(0,0) = 0$, as stated in Theorem 4.1, and the *hit point* is initialized at the initial location of the robot. We choose $\epsilon \in (0, \bar{\epsilon}]$, where $\bar{\epsilon}$ is selected as per Lemma 4.5. The obstacles can have arbitrary shapes and can be in close proximity with each other as long as Assumptions 4.1 and 4.2 are satisfied.

Notice that the robot can have multiple closest points in the proximity of non-convex obstacles, in which case, the obstacle avoidance term $\mathbf{v}(\mathbf{x}, m)$, defined in (4.11), is not viable, since it requires a unique closest point. Moreover, in an unknown environment, the modified obstacle-occupied workspace cannot be obtained in advance. Therefore, motivated by the method described in Remark 4.4, a virtual ring $\partial\mathcal{B}_{v_r}(\mathbf{c})$ is constructed whenever the robot enters the *obstacle-avoidance* mode, as described in Section 4.6.1. One should ensure that the robot's body is always enclosed by the ring, that the ring does not intersect with the interior of the obstacle-occupied workspace, and that the ring moves along with the robot in the *obstacle-avoidance* mode. Using this ring, the robot can then anticipate the possibility of multiple projections of its center onto the obstacle-occupied workspace and locally modify the obstacle-occupied workspace to ensure that the projection of its center onto the modified workspace is always unique, as discussed later in Section 4.6.2.

Note that if the robot is initialized on the boundary of the obstacle-occupied workspace such that its center has multiple closest points on the obstacle-occupied workspace, then one cannot construct a virtual ring with a radius greater than r_a that not only encloses the robot's body but also does not intersect with the interior of the obstacle-occupied workspace. Consequently, one should initialize the robot in the interior of the obstacle-free workspace.

For safe navigation in *a priori* unknown environments, we assume that the robot is equipped with a range-bearing sensor with angular scanning range of 360° and sensing radius $R_s > 2\alpha$. Similar to [Sawant et al., 2023a] and [Berkane, 2021], the range-bearing sensor is modeled using a polar curve $r_g(\mathbf{x}, \theta) : \mathcal{W}_{r_a} \times [-\pi, \pi] \to [0, R_s]$, which is defined as

$$r_g(\mathbf{x}, \theta) = \min \left\{ R_s, \quad \min_{\substack{\mathbf{y} \in \partial\mathcal{O}_{\mathcal{W}} \\ \text{atan2v}(\mathbf{y}-\mathbf{x}) = \theta}} \|\mathbf{x} - \mathbf{y}\| \right\}. \tag{4.32}$$

where $\text{atan2v}(\mathbf{q}) = \text{atan2}(q_2, q_1), \mathbf{q} = [q_1, q_2]^\intercal$. The function $r_g(\mathbf{x}, \theta)$ provides the distance between the center of the robot $\mathbf{x}$ and the boundary of the unsafe region $\partial\mathcal{O}_{\mathcal{W}}$, measured by the sensor, in the direction defined by the angle θ. Given the location $\mathbf{x}$, along with the bearing angle θ, the mapping $\lambda(\mathbf{x}, \theta) : \mathcal{W}_{r_a} \times [-\pi, \pi] \to \mathcal{W}_0$, which is given by

$$\lambda(\mathbf{x}, \theta) = \mathbf{x} + r_g(\mathbf{x}, \theta)[\cos(\theta), \sin(\theta)]^\intercal, \tag{4.33}$$

evaluates the Cartesian coordinates of the detected point.

Using (4.32) and (4.33), the distance between the center of the robot $\mathbf{x} \in \mathcal{W}_{r_a}$ and the unsafe region $\mathcal{O}_{\mathcal{W}}$ *i.e.,* $d(\mathbf{x}, \mathcal{O}_{\mathcal{W}})$ is calculated as follows:

$$d(\mathbf{x}, \mathcal{O}_{\mathcal{W}}) = r_g(\mathbf{x}, \theta), \tag{4.34}$$

where $\theta \in \Theta$. The set Θ, which is defined as

$$\Theta = \left\{ \theta_p \in [-\pi, \pi] \middle| \theta_p = \underset{\theta \in [-\pi, \pi]}{\arg\min}\ r_g(\mathbf{x}, \theta) \right\}, \tag{4.35}$$

contains bearing angles such that the range measurement (4.32) in the directions defined by these bearing angles gives the smallest value when compared to the values obtained in any other directions. Then, the set of projections of the location $\mathbf{x}$ onto the unsafe regions *i.e.,* $\mathcal{PJ}(\mathbf{x}, \mathcal{O}_{\mathcal{W}})$ is given by

$$\mathcal{PJ}(\mathbf{x}, \mathcal{O}_{\mathcal{W}}) = \{\lambda(\mathbf{x}, \theta) | \forall \theta \in \Theta\}. \tag{4.36}$$

For a given location of the robot $\mathbf{x}$, the set $\partial\mathcal{O}$, which is defined as

$$\partial\mathcal{O} = \{\lambda(\mathbf{x}, \theta), \theta \in [-\pi, \pi] | r_g(\mathbf{x}, \theta) < R_s\}, \tag{4.37}$$

contains the locations in the sensing region that belong to the boundary of the unsafe region. The robot moving straight towards the target will collide with the obstacle-occupied workspace if the following condition holds true:

$$\partial\mathcal{O} \cap \square(\mathbf{x}, \mathbf{0}) \neq \emptyset, \tag{4.38}$$

where the notation $\square(\mathbf{x}, \mathbf{0})$ represents a rectangle, as shown in Fig. 4.13, with its vertices located at $\mathbf{x}_1, \mathbf{x}_{-1}, \mathbf{0}_1$ and $\mathbf{0}_{-1}$, which are evaluated as

$$\begin{bmatrix} \mathbf{x}_z \\ \mathbf{0}_z \end{bmatrix} = \begin{bmatrix} \mathbf{x} \\ \mathbf{0} \end{bmatrix} + z r_a \begin{bmatrix} \mathbf{I} \\ \mathbf{I} \end{bmatrix} \begin{bmatrix} \cos\theta_d \\ \sin\theta_d \end{bmatrix}, z \in \{-1, 1\}, \tag{4.39}$$

where $\mathbf{I}$ is a 2×2 identity matrix, and $\theta_d = \pi/2 + \text{atan2v}(\mathbf{x})$ The robot moving in the *move-to-target* mode can infer the possibility of collision with the unsafe region by verifying the condition in (4.38). Next, we provide a procedure, summarized in Algorithm 2, which allows the robot to identify whether the state $(\mathbf{x}, \mathbf{h}, m)$ belongs to the jump set or not.

4.6.1 Switching to the *obstacle-avoidance* mode

Since the robot is initialized in the *move-to-target* mode, it will initially move towards the target, under the influence of the stabilizing control vector $-\kappa_s \mathbf{x}, \kappa_s > 0$. Suppose, there exists an obstacle-occupied workspace $\mathcal{O}_{\mathcal{W}}$ such that the line segment $\mathcal{L}_s(\mathbf{x}, \mathbf{0})$ intersects with the *landing region i.e.,* $\mathcal{L}_s(\mathbf{x}, \mathbf{0}) \cap \mathcal{R}_l \neq \emptyset$. This can be identified by evaluating the inner product between the vectors $\mathbf{x}$ and $\mathbf{x} - \Pi(\mathbf{x}, \mathcal{O}_{\mathcal{W}})$, according to (4.13) and (4.36), and by verifying the condition given in (4.38). Eventually, the robot moving straight

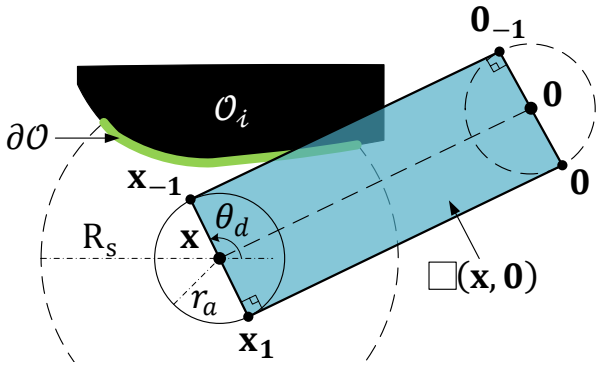

Figure 4.13: Construction of the rectangle $\square(\mathbf{x}, \mathbf{0})$ based on the location of the robot and the target location at the origin.

towards the target will enter the $\beta-$neighbourhood of the obstacle-occupied workspace, where $\beta \in (r_a, \alpha)$, *i.e.,* $d(\mathbf{x}, \mathcal{O}_\mathcal{W}) = \beta$ such that one of the following two cases holds:

Case A: there is a unique projection of the robot's center onto the obstacle-occupied workspace *i.e.*, $\mathbf{card}(\mathcal{PJ}(\mathbf{x}, \mathcal{O}_\mathcal{W})) = \mathbf{1}$.

Case B: there are more than one projections of the robot's center onto the obstacle-occupied workspace *i.e.*, $\mathbf{card}(\mathcal{PJ}(\mathbf{x}, \mathcal{O}_\mathcal{W})) > \mathbf{1}$, and $-\mathbf{x} \in \mathcal{CH}(\mathbf{x}, \mathcal{PJ}(\mathbf{x}, \mathcal{O}_\mathcal{W}))$.

First, we consider case A. Since $\mathcal{L}_s(\mathbf{x}, \mathbf{0}) \cap \mathcal{R}_l \neq \emptyset$, the robot has to switch to the *obstacle-avoidance* mode. However, before that, it needs to construct a virtual ring $\partial\mathcal{B}_{v_r}(\mathbf{c})$ to locally modify the obstacle-occupied workspace to ensure the uniqueness of the projection of its center onto the unsafe region. We locate the center of the virtual ring $\partial\mathcal{B}_{v_r}(\mathbf{c})$ *i.e.*, $\mathbf{c}$ using the following formula:

$$\mathbf{c} = \Pi(\mathbf{x}, \mathcal{O}_\mathcal{W}) + (r_a + \gamma)\frac{\mathbf{x} - \Pi(\mathbf{x}, \mathcal{O}_\mathcal{W})}{\|\mathbf{x} - \Pi(\mathbf{x}, \mathcal{O}_\mathcal{W})\|}, \tag{4.40}$$

where $\gamma \in (\beta - r_a, \alpha - r_a)$ such that $\mathrm{card}(\mathcal{PJ}(\mathbf{c}, \mathcal{O}_\mathcal{W})) = 1$ and $\Pi(\mathbf{c}, \mathcal{O}_\mathcal{W}) = \Pi(\mathbf{x}, \mathcal{O}_\mathcal{W})$. Then, the radius v_r of the virtual ring $\partial\mathcal{B}_{v_r}(\mathbf{c})$ is set to $r_a + \gamma$. The robot then sets $\gamma_s = \beta - r_a$, and enters in the *obstacle-avoidance* mode *i.e.*, switches m to $+1$ or -1. At this instance, we assign the current location as the *hit point* $\mathbf{h}$, as per (4.27). Case A is illustrated in Fig. 4.14a.

Now, we consider case B. We set $\mathbf{c}$ to be the current location of the robot's center *i.e.*, $\mathbf{c} = \mathbf{x}$, and $v_r = \beta$. Since the robot has multiple projections on the obstacle-occupied workspace $\mathcal{O}_\mathcal{W}$, it indicates the presence of a non-convex obstacle in its immediate neighbourhood, as shown in Fig. 4.14b. Hence, to ensure the uniqueness of the projection of the center of the robot onto the unsafe region, we augment the boundary of the obstacle-occupied workspace with a curve $\mathcal{Y}$, which is defined as

$$\mathcal{Y} = \partial\mathcal{B}_{v_r}(\mathbf{c}) \cap \mathcal{CH}(\mathbf{c}, \mathcal{PJ}(\mathbf{c}, \mathcal{O}_\mathcal{W})). \tag{4.41}$$

The curve $\mathcal{Y}$ is the section of the virtual ring $\partial\mathcal{B}_{v_r}(\mathbf{c})$ that belongs to the conic hull $\mathcal{CH}(\mathbf{c}, \mathcal{PJ}(\mathbf{c}, \mathcal{O}_\mathcal{W}))$. Notice that the curve $\mathcal{Y}$ belongs to the boundary of the modified obstacle $\mathbf{M}(\mathcal{O}_\mathcal{W}, v_r)$, as per Remark 4.4. We treat this curve as a part of the boundary of the unsafe region *i.e.*, $\partial\mathcal{O}_\mathcal{W} \leftarrow \partial\mathcal{O}_\mathcal{W} \cup \mathcal{Y}$.

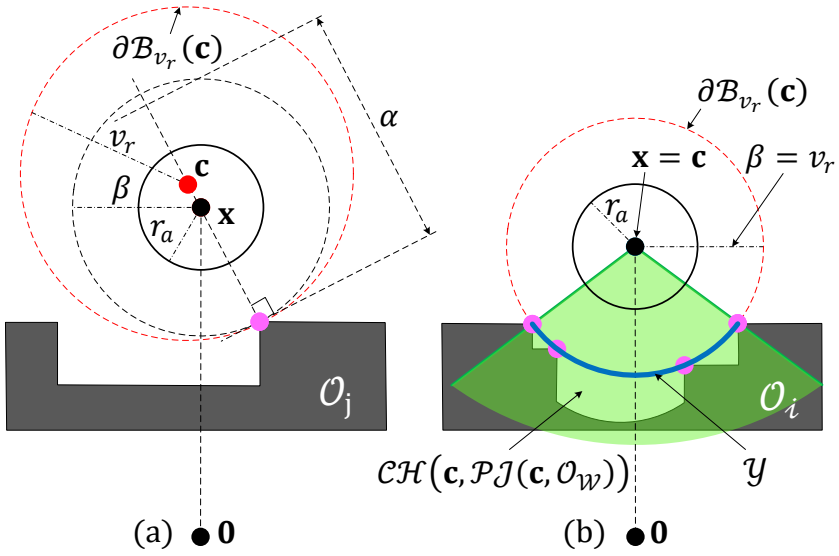

Figure 4.14: Illustration of two possible situations that can occur when the robot, while operating in the *move-to-target* mode, enters in the $\beta-$neighbourhood of obstacles $\mathcal{O}_\mathcal{W}$, for some $\beta \in (r_a, \alpha)$. (a) When $\mathbf{card}(\mathcal{PJ}(\mathbf{x}, \mathcal{O}_\mathcal{W})) = 1$. (b) When $\mathbf{card}(\mathcal{PJ}(\mathbf{x}, \mathcal{O}_\mathcal{W})) > 1$.

The robot has not yet switched to the *obstacle-avoidance* mode, and is moving straight towards the target inside the previously constructed virtual ring $\partial\mathcal{B}_{v_r}(\mathbf{c})$, along the line segment $\mathcal{L}_s(\mathbf{c}, \mathbf{0})$. Since $\mathcal{B}_{r_a}(\mathbf{x}) \subset \mathcal{B}_{v_r}(\mathbf{c})$, after moving straight towards the target, the robot will have unique projection on the curve $\mathcal{Y}$ and hence on the unsafe region $\mathcal{O}_\mathcal{W}$. Then the robot will switch to the *obstacle-avoidance* mode, according to case A.

4.6.2 Moving in the *obstacle-avoidance* mode

We use a virtual ring $\partial\mathcal{B}_{v_r}(\mathbf{c})$ to ensure a unique projection in the obstacle-avoidance mode. This ring anticipates multiple projections and enables local modification of the obstacle-occupied workspace to maintain uniqueness of the projection of the robot's center.

Note that when the robot switches from the *move-to-target* mode to the *obstacle-avoidance* mode, it is enclosed by the virtual ring *i.e.*, $\mathcal{B}_{r_a}(\mathbf{x}) \subset \mathcal{B}_{v_r}(\mathbf{c})$. Hence, if the virtual ring $\partial\mathcal{B}_{v_r}(\mathbf{c})$ touches the obstacle-occupied workspace $\mathcal{O}_\mathcal{W}$ at only one location *i.e.*, $\mathbf{card}(\mathcal{PJ}(\mathbf{c}, \mathcal{O}_\mathcal{W})) = 1$, then $\Pi(\mathbf{x}, \mathcal{O}_\mathcal{W}) = \Pi(\mathbf{c}, \mathcal{O}_\mathcal{W})$. Then, the robot can successfully implement the rotational control vector $\mathbf{v}(\mathbf{x}, m)$. To ensure that the robot's body is always enclosed by the virtual ring, we update the location of the center $\mathbf{c}$ as follows:

$$\mathbf{c} = \Pi(\mathbf{x}, \mathcal{O}_\mathcal{W}) + v_r \frac{\mathbf{x} - \Pi(\mathbf{x}, \mathcal{O}_\mathcal{W})}{\|\mathbf{x} - \Pi(\mathbf{x}, \mathcal{O}_\mathcal{W})\|}, \tag{4.42}$$

where v_r is defined when the robot switches from the *move-to-target* mode to the current *obstacle-avoidance* mode, as discussed in Section 4.6.1.

When the virtual ring touches the obstacle-occupied workspace at multiple locations, it indicates the presence of a non-convex obstacle in the immediate neighbourhood of the

robot, as shown in Fig. 4.15. In this case, the robot should use the projection of its center onto the part of the ring that intersects with the conic hull $\mathcal{CH}(\mathbf{c}, \mathcal{PJ}(\mathbf{c}, \mathcal{O}_\mathcal{W}))$ *i.e.,* onto the set $\mathcal{Y}$, defined in (4.41), as the closest point. Note that since $\mathcal{B}_{r_a}(\mathbf{x}) \subset \mathcal{B}_{v_r}(\mathbf{c})$, the projection $\Pi(\mathbf{x}, \mathcal{Y})$, which is used to implement the rotational control vector $\mathbf{v}(\mathbf{x}, m)$, is unique.

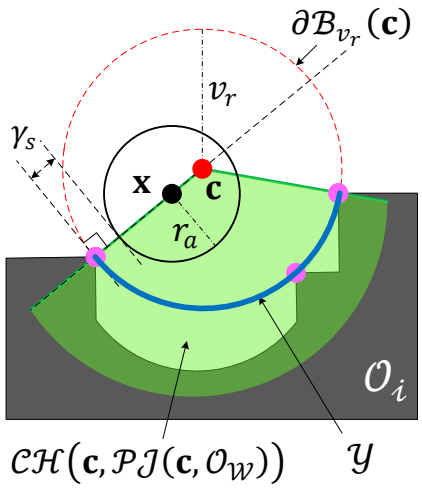

Figure 4.15: A scenario in which, for the robot operating in the *obstacle-avoidance* mode, the virtual ring $\partial\mathcal{B}_{v_r}(\mathbf{c})$ encounters more than one intersection point with the obstacle-occupied workspace $\mathcal{O}_\mathcal{W}$ *i.e.,* $\mathbf{card}(\mathcal{PJ}(\mathbf{c}, \mathcal{O}_\mathcal{W})) > 1$.

4.6.3 Switching to the *move-to-target* mode

When the robot, operating in the *obstacle-avoidance* mode, with some $m \in \{-1, 1\}$, reaches the location $\mathbf{x}$, which is ϵ units closer to the target location than the current *hit point* $\mathbf{h}$, and belongs to the *exit* region $\mathcal{R}_m \cup \mathcal{R}_a$, defined in (4.15), (4.17) and (4.18), it switches to the *move-to-target* mode by setting $m = 0$.

4.7 Simulation results

In this section, we present simulation results for a robot navigating in *a priori* unknown environments. In simulations discussed below, the robot is assumed to be equipped with a range-bearing sensor (*e.g.,* LiDAR) with an angular scanning range of 360° and sensing radius $R_s = 3m$. The angular resolution of the sensor is chosen to be 1°. The simulations are performed in MATLAB 2020a.

In the first simulation scenario, we consider an unbounded workspace *i.e.,* $\mathcal{O}_0 = \emptyset$, with 3 non-convex obstacles, as shown in Fig. 4.16. The robot with radius $r = 0.3m$ is initialized at $[-16, 4]^\intercal$. The target is located at the origin. The minimum safety distance $r_s = 0.1m$. The parameter $\alpha = 0.8m$ is known *a priori*, as per Lemma 4.3. We set the gain values κ_s and κ_r, used in (4.10), to be 0.5 and 2, respectively. The parameter ϵ,

Algorithm 3 General implementation of the proposed hybrid control law (4.10).

1: **Set** target location at the origin $\mathbf{0}$.
2: **Initialize** $\mathbf{x}(0,0) \in \mathcal{W}_{r_a}$, $\mathbf{h}(0,0) = \mathbf{x}(0,0)$ and $m(0,0) = 0$. Choose $\bar{\epsilon}$ according to Lemma 4.5, and initialize $\epsilon \in (0, \bar{\epsilon}]$. Select $\alpha > 0$ according to Lemma 4.3, and choose $\beta \in (r_a, \alpha)$.
3: **Measure** $\mathbf{x}$.
4: **if** $m = 0$, **then**
5: **Implement** Algorithm 4.
6: **if** $\xi \in \mathcal{J}_0$, **then**
7: **Update** $(\mathbf{h}, m) \leftarrow \mathbf{L}(\mathbf{x}, \mathbf{h}, m)$ using (4.27).
8: **end if**
9: **end if**
10: **if** $m \in \{-1, 1\}$, **then**
11: **Implement** Algorithm 4.
12: **if** $\xi \in \mathcal{J}_m$, **then**
13: **Update** $(\mathbf{h}, m) \leftarrow \mathbf{L}(\mathbf{x}, \mathbf{h}, m)$ using (4.28).
14: **end if**
15: **end if**
16: **if** $m \in \{-1, 1\}$, **then**
17: **Measure** $\Pi(\mathbf{x}, \mathcal{O}_{\mathcal{W}})$ using (4.36).
18: **Locate** $\mathbf{c}$ using (4.42).
19: **if** $\mathbf{card}(\mathcal{PJ}(\mathbf{c}, \mathcal{O}_{\mathcal{W}})) > 1$, **then**
20: **Construct** $\mathcal{Y}$ using (4.41).
21: **Assign** $\partial\mathcal{O}_{\mathcal{W}} \leftarrow \partial\mathcal{O}_{\mathcal{W}} \cup \mathcal{Y}$.
22: **end if**
23: **end if**
24: **Execute** $\mathbf{u}(\mathbf{x}, \mathbf{h}, m)$ (4.10), used in (4.29).
25: **Go to** step 3.

Algorithm 4 Sensor-based identification of the jump set.

Measure $d(\mathbf{x}, \mathcal{O}_\mathcal{W})$ (4.34), and $\mathcal{PJ}(\mathbf{x}, \mathcal{O}_\mathcal{W})$ (4.36).
if $m = 0$, **then**
  if $d(\mathbf{x}, \mathcal{O}_\mathcal{W}) \leq \beta$ **then**
    if **card**$(\mathcal{PJ}(\mathbf{x}, \mathcal{O}_\mathcal{W})) = 1$, **then**
      if $\mathbf{x}^\intercal(\mathbf{x} - \Pi(\mathbf{x}, \mathcal{O}_\mathcal{W})) \geq 0$, **then**
        Identify $\partial\mathcal{O}$ using (4.38).
        Construct $\square(\mathbf{x}, \mathbf{0})$ using (4.39).
        if $\partial\mathcal{O} \cap \square(\mathbf{x}, \mathbf{0}) \neq \emptyset$ **then**
          $\xi \in \mathcal{J}_0$.
          Set $\gamma_s = \beta - r_a$.
          Choose $\gamma \in (\gamma_s, \alpha - r_a)$.
          Set $v_r = r_a + \gamma$.
          Locate $\mathbf{c}$ using (4.40).
        end if
      end if
    else
      if $-\mathbf{x} \in \mathcal{CH}(\mathbf{x}, \mathcal{PJ}(\mathbf{x}, \mathcal{O}_\mathcal{W}))$, **then**
        Set $\mathbf{c} = \mathbf{x}$ and $v_r = \beta$.
        Construct $\mathcal{Y}$ using (4.41).
        Assign $\partial\mathcal{O}_\mathcal{W} \leftarrow \partial\mathcal{O}_\mathcal{W} \cup \mathcal{Y}$.
      end if
    end if
  end if
end if
if $m \in \{-1, 1\}$ **then**
  if $d(\mathbf{x}, \mathcal{O}_\mathcal{W}) < r_a + \alpha$, **then**
    if $\mathbf{x} \in \mathcal{R}_m \cup \mathcal{R}_a$, defined in (4.15), (4.17) and (4.18), **then**
      if $\|\mathbf{x}\| \leq \|\mathbf{h}\| - \epsilon$, **then**
        $\xi \in \mathcal{J}_m$.
      end if
    end if
  else
    $\xi \in \mathcal{J}_m$.
  end if
end if

which is essential for the design of the jump set of the *obstacle-avoidance* mode as given in (4.21) and (4.22), is set to be $0.1m$.

The robot's motion in the *move-to-target* mode is represented by the black-coloured curves, whereas the red-coloured curves depict its motion in the *obstacle-avoidance* mode. The locations $\mathbf{h}_1$ to $\mathbf{h}_6$ are the *hit points* where the robot switches from the *move-to-target* mode to the *obstacle-avoidance* mode. Notice that the location of each *hit point* is closer to the target location than the previous one, which ensures global convergence of the robot to the target location, as stated in Theorem 4.1. Since the robot moves parallel to the boundary of the unsafe region in the *obstacle-avoidance* mode, it maintains a safe distance from the unsafe region, as shown in Fig. 4.17. To avoid multiple projections onto the unsafe region, while operating in the *obstacle-avoidance* mode, the robot constructs a virtual ring, as explained in Section 4.3, and moves along its boundaries around the obstacles $\mathcal{O}_1$ and $\mathcal{O}_2$. The complete simulation video can be found at https://youtu.be/tRRUQNjLtGU.

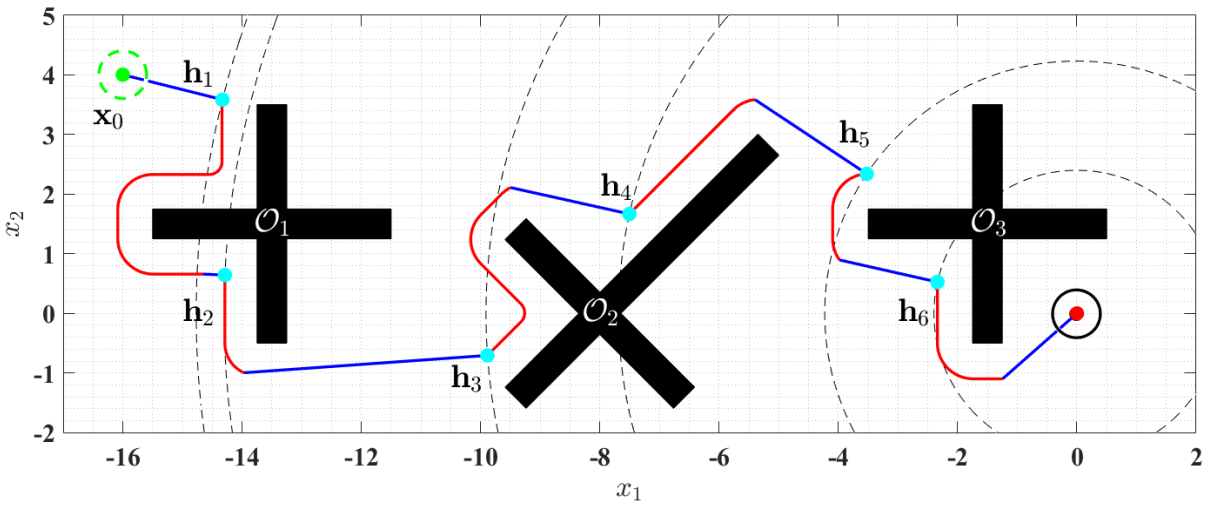

Figure 4.16: Trajectory of a robot, initialized at $\mathbf{x}_0$, safely converging to the target location at the origin, while avoiding non-convex obstacles.

In the next simulation scenario, as shown in Fig. 4.18, we consider an environment consisting of arbitrarily-shaped non-convex obstacles, and apply the proposed hybrid controller (4.10) for a point robot navigation initialized at 10 different locations in the obstacle-free workspace. The target is located at the origin. The minimum safety distance $r_s = 0.1m$ and the parameter $\alpha = 0.5m$. We set the gains κ_s and κ_r, used in (4.10a), to be 0.25 and 2, respectively. The parameter ϵ is set to be $0.05m$.

Since the environment is *a priori* unknown and contains non-convex obstacles, the robot maintains the same direction of motion when it moves in the *obstacle-avoidance* mode to avoid retracing the previously travelled path, as discussed in remark 4.5. This does not necessarily result in the robot trajectories with the shortest lengths. The complete simulation video can be found at https://youtu.be/OtHt-oQPg68.

Next, we consider an environment with unsafe region $\mathcal{O}_\mathcal{W}$, consisting of 2 non-convex obstacles $\mathcal{O}_1$ and $\mathcal{O}_2$, that does not satisfy Assumption 4.2, as shown in Fig. 4.19. The

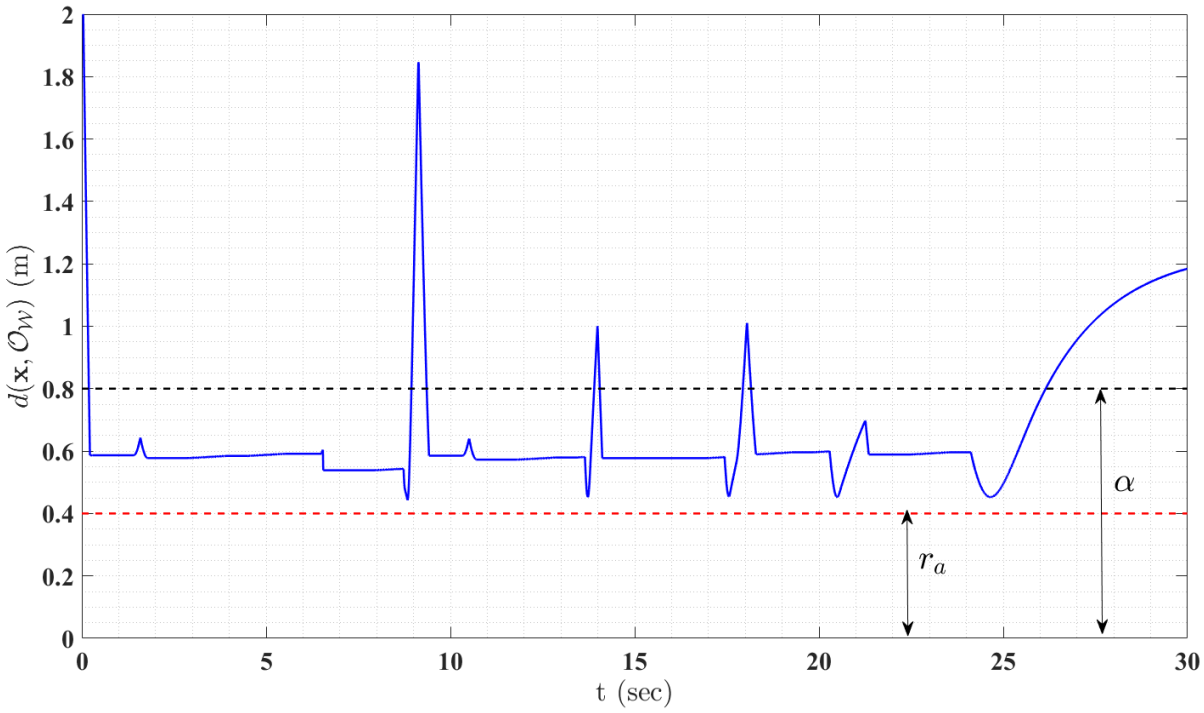

Figure 4.17: Distance of the robot's center from the boundary of the obstacle-occupied workspace for the simulation results shown in Fig. 4.16.

robot with radius $r = 0.3m$ is initialized at $[-6, 3]^\intercal$. The target is located at the origin. The minimum safety distance $r_s = 0.1m$. The parameter $\alpha = 1m$ is known *a priori*, as per Lemma 4.3. We set the gain values κ_s and κ_r, used in (4.10), to be 0.5 and 2, respectively. The parameter ϵ, used in (4.22), is set to be $0.1m$.

Notice that even though the distance between the obstacles $\mathcal{O}_1$ and $\mathcal{O}_2$ is less than 2α, the modified obstacle-occupied workspace $\mathcal{O}_W^M$, obtained using (4.4), is not connected. However, using the virtual ring construction mentioned in Section 4.6.2, the robot maintains the uniqueness of its projection and moves safely across the gap in the *obstacle-avoidance* mode, as shown in Fig. 4.19. The complete simulation video can be found at https://youtu.be/T4xzo01_mkc.

4.7.1 Gazebo simulation

The next simulation is performed using the Turtlebot3 Burger model in Gazebo. The simulation runs on a computer, equipped with 4 GB RAM, running Ubuntu 20.04 with the ROS Noetic distribution installed, which we refer to as *Computer 1*. The proposed hybrid controller is run in Matlab R2020a on another computer running Windows 10, equipped with an Intel(R) i5-5200U CPU with a clock speed of 2.20 GHz and 12 GB RAM, referred to as *Computer 2*.

The Turtlebot is equipped with a two-dimensional LiDAR scanner with a sensing range of 1m. The angular scanning range and angular resolution are set to 360 degrees and 1 degree, respectively. The sensor measurements are assumed to be affected by

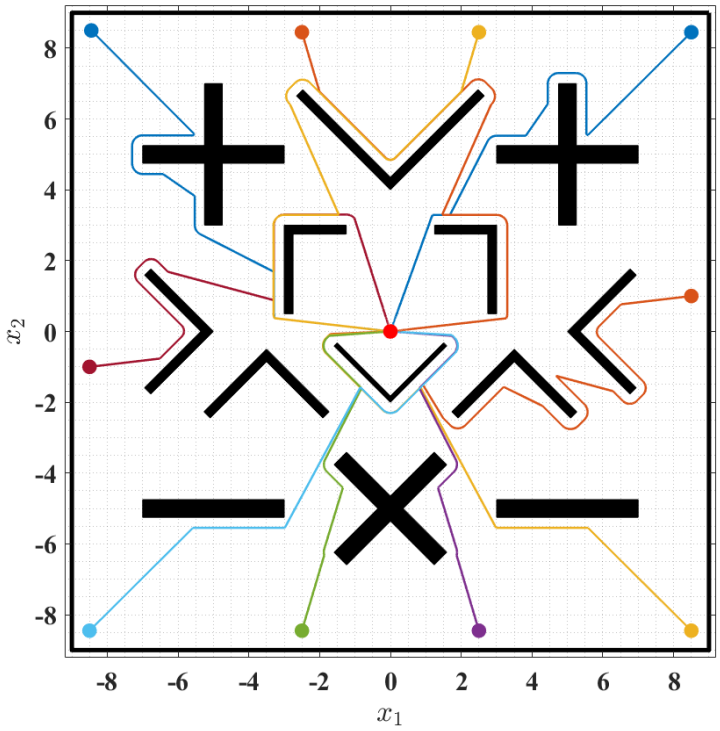

Figure 4.18: Robot trajectories starting from different locations

Gaussian noise with zero mean and a standard deviation of 0.01 m. The maximum bounds on the linear velocity and angular velocity, denoted as $\nu_{\max}$ and $\omega_{\max}$ respectively, are set to 0.15 m/s and 2.84 rad/s. The LiDAR scanning rate is set to 5 Hz.

At each iteration, the LiDAR measurements and pose information are sent from *Computer 1* to *Computer 2*. The control commands are then sent from *Computer 2* to *Computer 1*. The execution time of the proposed hybrid controller is approximately 5 ms. The sensor-based implementation of the proposed hybrid navigation algorithm only requires the measurements acquired via a range-bearing sensor. Since the size of the acquired sensor data is independent of the surrounding environment, the code execution time will remain approximately the same regardless of changes in the environment.

The Turtlebot can be represented with the following nonholonomic model:

$$\begin{aligned} \dot{x}_1 &= \nu \cos\theta, \\ \dot{x}_2 &= \nu \sin\theta, \\ \dot{\theta} &= \omega, \end{aligned} \tag{4.43}$$

where $\mathbf{x} = [x_1, x_2]^\intercal$ is the location of the center of the robot and $\theta \in [-\pi, \pi)$ is the heading direction. The scalar control variables ν and ω represent the linear and angular velocities, respectively.

In practical applications, due to the discrete implementation of the control law designed for a point-mass robot, the nonholonomic Turtlebot (when operating in the

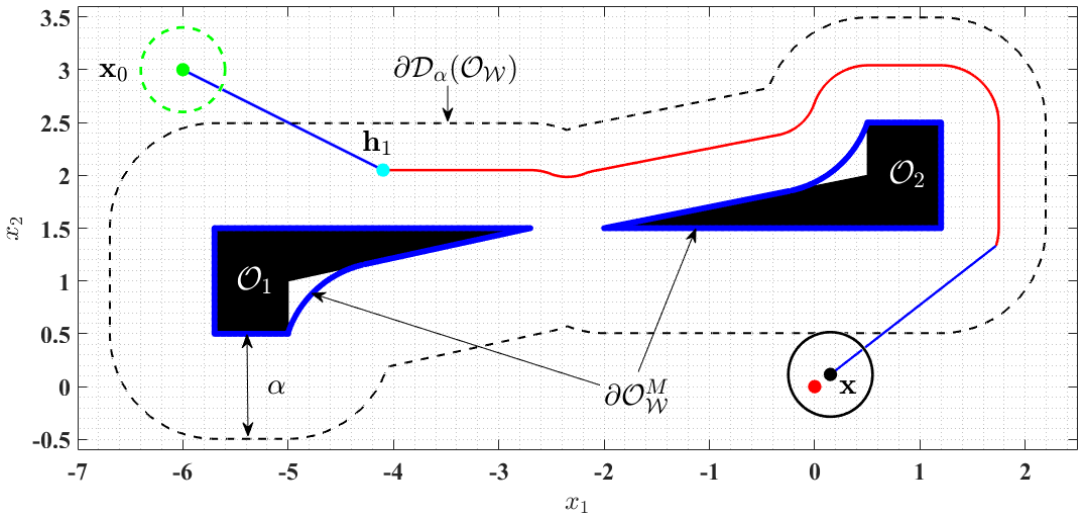

Figure 4.19: Robot safely navigating towards the target (red dot) in an environment that does not satisfy Assumption 4.2

obstacle-avoidance mode) may get very close to the obstacle or exit the α-neighborhood of the obstacle before getting closer to the target location than the current *hit point*. To avoid this situation, we introduce some minor modifications to the proposed hybrid control law to ensure that the Turtlebot stays inside the α-neighborhood of the nearest obstacle when operating in the *obstacle-avoidance* mode. We replace the vector $\mathbf{v}(\mathbf{x}, m)$, used in (4.10a), with a modified vector $\mathbf{v}_{mod}(\mathbf{x}, m)$, which is defined as

$$\mathbf{v}_d(\mathbf{x}, m) = \begin{bmatrix} \lambda(\varrho(\mathbf{x})) & m(1-\lambda(\varrho(\mathbf{x}))^2) \\ -m(1-\lambda(\varrho(\mathbf{x}))^2) & \lambda(\varrho(\mathbf{x})) \end{bmatrix} \mathbf{f}(\mathbf{x}, m), \tag{4.44}$$

where the vector-valued function $\mathbf{f}(\mathbf{x}, m)$ is given by

$$\mathbf{f}(\mathbf{x}, m) = \frac{\mathbf{x} - \Pi(\mathbf{x}, \mathcal{O}_\mathcal{W}^M)}{\|\mathbf{x} - \Pi(\mathbf{x}, \mathcal{O}_\mathcal{W}^M)\|}. \tag{4.45}$$

The scalar-valued function $\lambda(\varrho(\mathbf{x}))$ is evaluated as

$$\lambda(\varrho(\mathbf{x})) = \begin{cases} \frac{0.25\eta - \varrho(\mathbf{x})}{0.25\eta}, & 0 \leq \varrho(\mathbf{x}) \leq 0.25\eta, \\ 0, & 0.25\eta \leq \varrho(\mathbf{x}) \leq 0.75\eta, \\ \frac{0.75\eta - \varrho(\mathbf{x})}{0.25\eta}, & 0.75\eta \leq \varrho(\mathbf{x}) \leq \eta, \end{cases} \tag{4.46}$$

where $\eta = \alpha - r_a$ and $\varrho(\mathbf{x}) = d(\mathbf{x}, \mathcal{O}_\mathcal{W}^M) - r_a$. The continuous scalar-valued function $\lambda(\varrho(\mathbf{x})) \in [-1, 1]$, for all $\varrho(\mathbf{x}) \in [0, \eta]$.

Notice that when $\lambda(\varrho(\mathbf{x})) = 0$, the vector $\mathbf{v}_d(\mathbf{x}, m)$ equals to the vector $\mathbf{v}(\mathbf{x}, m)$, used in (4.10a). When the Turtlebot, while operating in the *obstacle-avoidance* mode, moves closer to the boundary of the modified obstacle-occupied workspace *i.e.,* $\varrho(\mathbf{x}) \to 0$, $\lambda(\varrho(\mathbf{x})) \to 1$. As a result, the vector $\mathbf{v}_d(\mathbf{x}, m) \to \mathbf{f}(\mathbf{x}, m)$ and the Turtlebot is steered away from the unsafe region. On the other hand, if the center of the Turtlebot

moves closer to the boundary of the $\alpha-$neighbourhood of the modified obstacle-occupied workspace *i.e.,* $\varrho(\mathbf{x}) \to \eta$, $\lambda(\varrho(\mathbf{x})) \to -1$. Due to this, the vector $\mathbf{v}_d(\mathbf{x}, m) \to -\mathbf{f}(\mathbf{x}, m)$ and the Turtlebot is steered back inside the $\alpha-$neighbourhood of the modified obstacle-occupied workspace.

Finally, given the modified hybrid control law $\mathbf{u}_{mod}$, obtained by replacing $\mathbf{v}(\mathbf{x}, m)$ by $\mathbf{v}_{mod}(\mathbf{x}, m)$ in (4.10a), the linear velocity ν and the angular velocity ω to be applied to the Turtlebot are obtained as follows:

$$\nu = \kappa_\nu \min\left\{\|\mathbf{u}_{mod}\| \cos^{2n}\left(\frac{\theta - \theta_d}{2}\right), \nu_{\max}\right\}, \tag{4.47}$$

$$\omega = -\kappa_\omega \omega_{\max} \sin(\theta - \theta_d), \tag{4.48}$$

where $n > 1$, $\kappa_\nu > 0$ and $\kappa_\omega > 0$. The angle θ represents the heading direction of the robot. The desired heading direction is denoted by θ_d, which is evaluated as $\theta_d = \text{atan2v}(\mathbf{u}_{\text{mod}})$. The expression $\frac{1+\cos(\theta-\theta_d)}{2}$ in (4.47) reduces the linear velocity of the Turtlebot based on the disparity between its current heading direction θ and the desired heading direction θ_d.

We set the gains κ_s, κ_r, used in (4.10a), and κ_ν, κ_ω, used in (4.47) and (4.48), to 1. The minimum safety distance $r_s = 0.03$ m and the parameter $\alpha = 0.3$ m. Additionally, the parameter ϵ, used in (4.22), is set to 0.15 m. The target location is set to the origin, represented by the light green dot, as shown in Fig. 4.20. In Fig. 4.20a, the left figure shows the workspace setup in Gazebo with the initial location of the Turtlebot, and the right figure shows the LiDAR sensor measurements. The desired heading direction is denoted by the blue arrow, while the red arrow represents the current heading direction of the Turtlebot. The Turtlebot and the target location are connected via a dotted red line. When the Turtlebot moves straight towards the target location, it eventually enters the $\alpha-$neighbourhood of the unsafe region and switches to the *obstacle-avoidance* mode. In the *obstacle-avoidance* mode, it constructs a virtual ring represented using the red dotted circle, as shown in Fig. 4.20b. When the nearby obstacle workspace is convex in nature, the projection of the center of the Turtlebot onto this workspace matches the intersection point between the virtual ring and the nearby obstacle, which is represented by the magenta coloured dot. In Fig. 4.20b, the blue-dotted curve is a partial boundary of the circle with its center at the origin and a radius of $\|\mathbf{h}\| - \epsilon$, where $\mathbf{h}$ is the current location of the *hit point*. According to (4.21), (4.22) and (4.26), the Turtlebot can switch back to the *move-to-target* mode only if it is inside this circle. When the nearby unsafe region is non-convex in nature, the virtual ring, which is larger in size compared to the robot's body, will have multiple intersections with the obstacles, as shown in Fig. 4.20c. This prompts the Turtlebot to project on the boundary of the virtual ring instead of the obstacle-occupied workspace to maintain the uniqueness of the projection. In other words, boundary of the virtual ring acts as the boundary of the modified obstacle, as discussed in Remark 4.4. Finally, in Fig. 4.20d we can see the Turtlebot approaching towards the target location at the origin. The complete simulation video can be found at https://youtu.be/ZNeiS5qE00k.

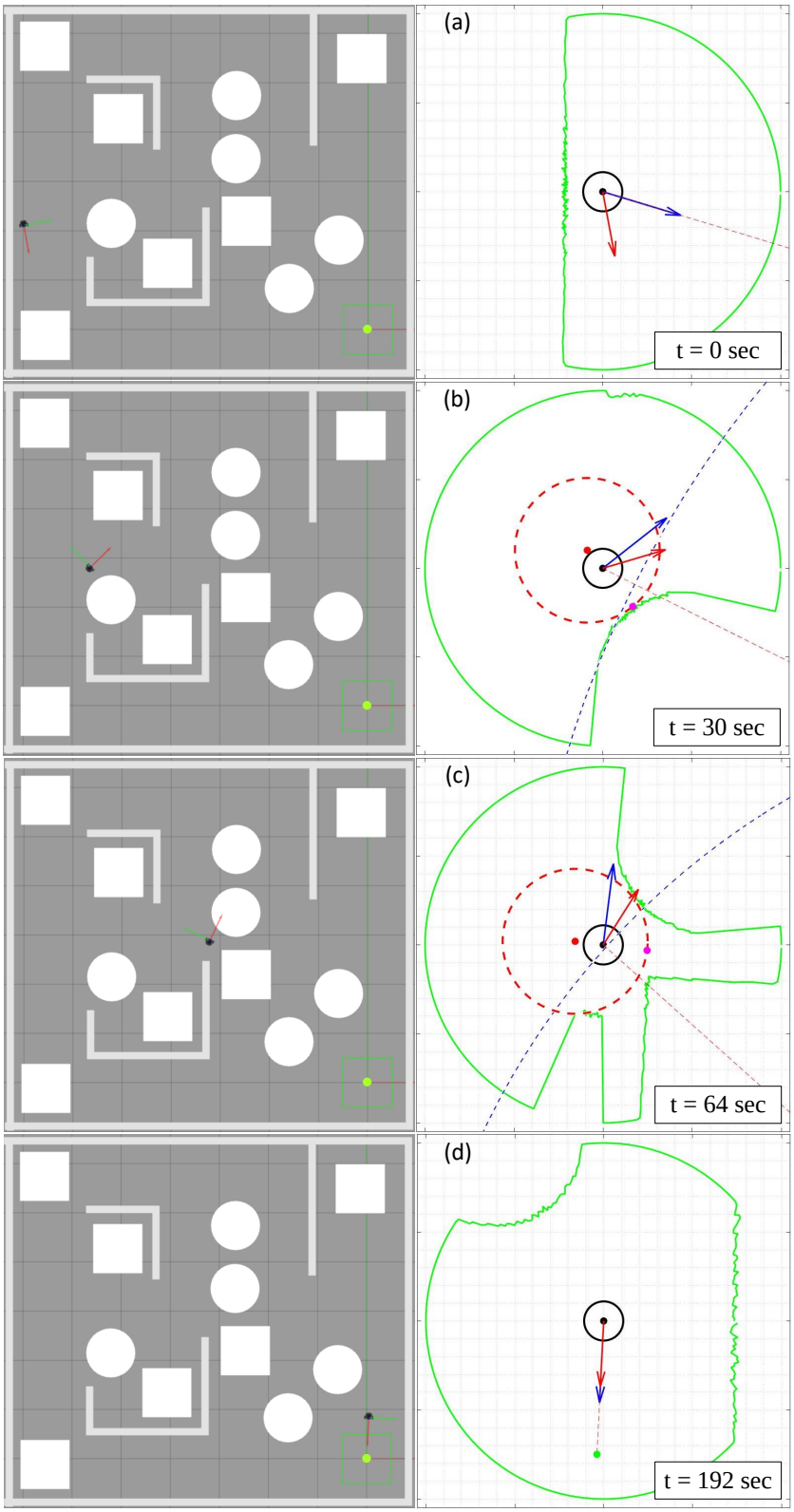

Figure 4.20: Autonomous navigation of the Turtlebot in non-convex environment.

4.8 Conclusions

In this chapter, we proposed a hybrid feedback controller for safe autonomous navigation in two-dimensional environments with arbitrary-shaped obstacles (possibly non-convex). The obstacles can have non-smooth boundaries and large sizes and can be placed arbitrarily close to each other provided the feasibility requirements stated in Assumptions 4.1 and 4.2 are satisfied. The proposed hybrid controller relies on an instrumental transformation that virtually modifies the obstacles' shapes such that the uniqueness of the projection of the robot's center onto the closest obstacle is guaranteed; a feature that helps in the design of our *obstacle-avoidance* strategy. The obstacle avoidance component of the control law (4.11) utilizes the projection of the robot's center onto the nearest obstacle. Hence, it is possible to apply the proposed hybrid control scheme in *a priori* unknown environments, as discussed in Section 4.6.

It should be noted that the autonomous navigation schemes proposed in Chapters 3 and 4 are applicable only to two-dimensional environments. Consequently, when the robot enters the *obstacle-avoidance* mode, it can move either in a clockwise direction or in a counter-clockwise direction with respect to the nearest obstacle's boundary. Since obstacles are compact, this ensures that the robot will eventually reach a location from which the line segment joining the center of the robot to the target location does not intersect with the nearest obstacle.

Chapter 5

Autonomous Navigation in Environments with Three-dimensional Convex Obstacles

5.1 Introduction

This chapter deals with the problem of autonomous robot navigation in three-dimensional environments with arbitrarily-shaped convex obstacles. One of the widely explored techniques in this regard is the Navigation Function (NF) approach [Koditschek and Rimon, 1990], which guarantees almost[1] global convergence of the robot to a target location in sphere words. To apply the NF approach in environments with general convex and star-shaped obstacles, diffeomorphic mappings from [Koditschek and Rimon, 1992] and [Li and Tanner, 2018] can be used assuming global knowledge of the environment. The NF-based approach has been extended in [Paternain et al., 2017] to environments containing convex obstacles with smooth boundaries. The authors established sufficient conditions on the curvature of the obstacles' boundaries to guarantee almost global convergence to a neighborhood of the *a priori* unknown target location. However, it is assumed that the shapes of the obstacles avoided by the robot are known.

In [Berkane, 2021], the authors proposed a feedback controller based on Nagumo's theorem [Blanchini et al., 2008, Theorem 4.7], for autonomous navigation in environments with general convex obstacles. The forward invariance of the obstacle-free space is ensured by projecting the *ideal* velocity control vector (pointing to the target) onto the tangent cone at the boundary of the obstacle whenever it points to the obstacle. In [Reis et al., 2020], a control barrier function-based approach was used for robot navigation in an environment with a single spherical obstacle.

In [Arslan and Koditschek, 2019], the authors proposed a separating hyperplane-based autonomous navigation algorithm for autonomous navigating in environments with convex obstacles with smooth boundaries. This approach was extended in [Vasilopoulos and Koditschek, 2018] to handle partially known environments with non-convex obsta-

[1] Almost global convergence here refers to the convergence from all initial conditions except a set of zero Lebesgue measure.

cles, where it is assumed that the robot possesses geometrical information about the non-convex obstacles but lacks knowledge of their precise locations in the workspace. However, due to the topological obstruction to global asymptotic stability, with continuous time-invariant vector fields, in sphere words [Koditschek and Rimon, 1990], the above-mentioned approaches provide at best almost global asymptotic stability guarantees.

In [Berkane et al., 2021a], hybrid control techniques were employed to achieve global stabilization of the target location in environments with sufficiently separated ellipsoidal obstacles. In [Matveev et al., 2011], the authors proposed a hybrid autonomous navigation technique for a nonholonomic robot operating in environments with non-convex obstacles under some restrictions on the inter-obstacle arrangements. In [Loizou et al., 2003], the authors proposed a discontinuous feedback control law for autonomous robot navigation in partially known two-dimensional environments. When a known obstacle is encountered, the control vector aligns with the negative gradient of the navigation function. When close to an unknown obstacle, the robot moves along its boundary, relying on the local curvature information of the obstacle. Similar to [Matveev et al., 2011], this approach is applicable in two-dimensional environments and assumes smooth obstacle boundaries without sharp edges. In our earlier work [Sawant et al., 2023a], we proposed a hybrid feedback control strategy for autonomous robot navigation in two-dimensional environments with arbitrarily-shaped convex obstacles.

In this chapter, we propose a hybrid control strategy, endowed with global asymptotic stability guarantees, for autonomous robot navigation in three-dimensional environments containing arbitrarily-shaped convex obstacles. We also propose a sensor based version of our approach for autonomous navigation in *a priori* unknown three-dimensional environments with arbitrarily-shaped convex obstacles.

The main contributions of this chapter are as follows:

1. *Global asymptotic stability:* the proposed autonomous navigation algorithm ensures global asymptotic stability of the target location for the robot operating in three-dimensional environments with convex obstacles.

2. *Arbitrarily-shaped three-dimensional obstacles:* the proposed hybrid feedback controller is applicable to environments consisting of three-dimensional convex obstacles with arbitrary shapes. Compared to this work, the research work [Arslan and Koditschek, 2019] is restricted to convex obstacles with smooth boundaries, which satisfy some curvature condition. Similarly, in [Berkane et al., 2021a], the obstacles are assumed to ellipsoids.

3. *Arbitrary interobstacle arrangements:* there are no restrictions on the interobstacle arrangement such as those in [Matveev et al., 2011, Assumption 10], [Berkane et al., 2021a, Theorem 2], except for the widely used mild feasibility Assumption 5.1, the robot can pass in between any two obstacles while maintaining a positive distance.

4. *Applicable in a priori unknown environments:* the proposed autonomous navigation algorithm can be implemented using range scanners (*e.g.,* LiDAR) and/or vision sensors without *a priori* global knowledge of the environment.

The results presented in this chapter have been published in [Sawant et al., 2024].

5.2 Problem formulation

We consider a spherical robot with radius $r \geq 0$ operating in a convex, three-dimensional Euclidean space $\mathcal{W} \subseteq \mathbb{R}^3$. The workspace $\mathcal{W}$ is cluttered with finite number of compact, convex obstacles $\mathcal{O}_i \subset \mathcal{W}, i \in \{1, \ldots, b\}, b \in \mathbb{N}$. We define obstacle $\mathcal{O}_0 := (\mathcal{W}^\circ)^c$ as the complement of the interior of the workspace. Collectively, the obstacle-occupied workspace is denoted by $\mathcal{O}_\mathcal{W} = \bigcup_{i \in \mathbb{I}} \mathcal{O}_i$, where $\mathbb{I} = \{0, \ldots, b\}$. We make the following workspace feasibility assumption:

Assumption 5.1 *The minimum separation between any pair of obstacles should be greater than $2r$ i.e., for all $i, j \in \mathbb{I}, i \neq j$, one has*

$$d(\mathcal{O}_i, \mathcal{O}_j) := \min_{\mathbf{p} \in \mathcal{O}_i, \mathbf{q} \in \mathcal{O}_j} \|\mathbf{p} - \mathbf{q}\| > 2r. \tag{5.1}$$

According to Assumption 5.1 and the compactness of the obstacles, there exists a minimum separating distance between any pair of obstacles $\bar{r} = \min_{i,j \in \mathbb{I}, i \neq j} d(\mathcal{O}_i, \mathcal{O}_j) > 2r$. Moreover, for collision-free navigation we require $d(\mathbf{0}, \mathcal{O}_\mathcal{W}) - r > 0$. We define a positive real $\bar{r}_s$ as

$$\bar{r}_s = \min \left\{ \frac{\bar{r}}{2} - r, d(\mathbf{0}, \mathcal{O}_\mathcal{W}) - r \right\}. \tag{5.2}$$

We then pick an arbitrarily small value $r_s \in (0, \bar{r}_s)$ as the minimum distance that the robot should maintain with respect to any obstacle.

The obstacle-free workspace is then defined as $\mathcal{W}_0 := \mathcal{W} \setminus \mathcal{O}_\mathcal{W}$. Given $y \geq 0$, a $y-$eroded obstacle-free workspace, $\mathcal{W}_y$ is defined as

$$\mathcal{W}_y := \mathcal{W} \setminus \bigcup_{i \in \mathbb{I}} \mathcal{D}_y^\circ(\mathcal{O}_i) \subseteq \mathcal{W}_0. \tag{5.3}$$

Hence, $\mathcal{W}_{r_a}$ with $r_a = r + r_s$ is the obstacle-free workspace with respect to the center of the robot *i.e.*, $\mathbf{x} \in \mathcal{W}_{r_a} \iff \mathcal{B}_{r_a}(\mathbf{x}) \subset \mathcal{W}_0$.

The robot is governed by a single integrator dynamics

$$\dot{\mathbf{x}} = \mathbf{u}, \tag{5.4}$$

where $\mathbf{u} \in \mathbb{R}^3$ is the control input. The task is to design a feedback control law $\mathbf{u}$ such that:

1. **Safety**: the robot-centered obstacle-free workspace $\mathcal{W}_{r_a}$ is forward invariant,
2. **Global Asymptotic Stability**: The target location $\mathbf{x} = \mathbf{0} \in \mathcal{W}_{r_a}^\circ$ is globally asymptotically stable for the closed-loop system.

5.3 Hybrid control for obstacle avoidance

In the proposed scheme, the robot operates in two modes based on the value of a mode indicator variable $m \in \mathbb{M} := \{0, 1\}$. The *move-to-target* mode ($m = 0$) is adopted when the robot is away from the obstacles and the the *obstacle-avoidance* mode ($m = 1$) is adopted when the robot is close to an obstacle obstructing its motion towards the target location. In the *move-to-target* mode, the robot moves straight towards the target location. In the *obstacle-avoidance* mode, the robot navigates around the obstacle while staying withing its $\gamma-$neighborhood, where $\gamma \in (0, \bar{r}_s - r_s)$. When the robot operates in the *obstacle-avoidance* mode, the robot's center has a unique closest point on the nearest obstacle. Furthermore, to prevent the robot from getting trapped in a loop around an obstacle, the proposed obstacle-avoidance strategy confines the robot's center to a hyperplane that passes through the target location. This ensures that the robot will eventually reach a position where the nearest obstacle does not intersect with the line segment joining the center of the robot and the target location.

5.3.1 Hybrid control design

The proposed hybrid control $\mathbf{u}(\mathbf{x}, \mathbf{h}, \mathbf{a}, m, s)$ is given as

$$\mathbf{u}(\xi) = -\kappa_s(1-m)\mathbf{x} + \kappa_r m \mathbf{v}(\mathbf{x}, \mathbf{a}), \tag{5.5a}$$

$$\underbrace{\begin{aligned} \dot{\mathbf{h}} &= \mathbf{0}, \\ \dot{\mathbf{a}} &= 0, \\ \dot{m} &= 0 \\ \dot{s} &= 1, \end{aligned}}_{(\mathbf{x},\mathbf{h},\mathbf{a},m,s)\in\mathcal{F}} \qquad \underbrace{\begin{bmatrix} \mathbf{h}^+ \\ \mathbf{a}^+ \\ m^+ \\ s^+ \end{bmatrix} \in \mathbf{L}(\mathbf{x}, \mathbf{h}, \mathbf{a}, m, s),}_{(\mathbf{x},\mathbf{h},\mathbf{a},m,s)\in\mathcal{J}} \tag{5.5b}$$

where $\kappa_s > 0$, $\kappa_r > 0$, and $\xi = (\mathbf{x}, \mathbf{h}, \mathbf{a}, m, s) \in \mathcal{K} := \mathcal{W}_{r_a} \times \mathcal{W}_{r_a} \times \mathbb{S}^2 \times \mathbb{M} \times \mathbb{R}_{\geq 0}$. The variable $\mathbf{h}$ denotes the *hit point*, which is the location where the robot switches from the *move-to-target* mode to the *obstacle-avoidance* mode. The vector $\mathbf{a} \in \mathbb{S}^2$ is instrumental for the construction of the avoidance control vector $\mathbf{v}(\mathbf{x}, \mathbf{a})$, used in (5.5a). The scalar variable $s \in \mathbb{R}_{\geq 0}$ allows the robot to switch from the *obstacle-avoidance* mode to the *move-to-target* mode when initially in the *obstacle-avoidance* mode. Details of this switching process are provided later in Section 5.3.2. The sets $\mathcal{F}$ and $\mathcal{J}$ are the flow and jump sets related to different modes of operation, respectively, whose constructions are provided in Section 5.3.2. The update law $\mathbf{L}$, which allows the robot to update the values of the variables $\mathbf{h}$, $\mathbf{a}$, m and s based on the current location of the robot with respect to the nearest obstacle and the target location, will be designed later in Section 5.3.3. Next, we provide the design of the vector $\mathbf{v}(\mathbf{x}, \mathbf{a}) \in \mathbb{R}^3$.

The vector $\mathbf{v}(\mathbf{x}, \mathbf{a})$, used in (5.5a), is defined as

$$\mathbf{v}(\mathbf{x}, \mathbf{a}) = \big[\eta(\mathbf{x})\mathbf{I} + (1 - |\eta(\mathbf{x})|)\mathbf{R}(\mathbf{a})\big]\mathbf{P}(\mathbf{a})\mathbf{x}_\pi \tag{5.6}$$

where $\mathbf{I} \in \mathbb{R}^{3\times 3}$ is the identity matrix and $\mathbf{x}_\pi := \mathbf{x} - \Pi(\mathbf{x}, \mathcal{O}_\mathcal{W})$. The operator $\Pi(\mathbf{x}, \mathcal{O}_\mathcal{W})$ provides the closest point on the obstacle-occupied workspace from the location of the

center of the robot $\mathbf{x}$, as defined in Section 2.2.1. Notice that, since the obstacles $\mathcal{O}_i, i \in \mathbb{I} \setminus \{0\}$ are convex and the parameter $\gamma \in (0, \bar{r}_s - r_s)$, according to (5.2), the robot will have a unique closest point to the obstacles whenever its center is in the $(r_a + \gamma)-$neighborhood of these obstacles. On the other hand, there may be some locations in the $(r_a + \gamma)-$neighborhood of the obstacle $\mathcal{O}_0 = (\mathcal{W}^\circ)^c$ for which the uniqueness of the closest point from robot's center to the obstacle $\mathcal{O}_0$ cannot be guaranteed. However, as discussed later in Remark 5.1, the design of the flow sets and jump sets guarantees that the obstacle-avoidance control vector $\mathbf{v}(\mathbf{x}, \mathbf{a})$ is never activated in the region $\mathcal{N}_{r_a+\gamma}(\mathcal{O}_0)$.

The rotation matrix $\mathbf{R}(\mathbf{a}) := \mathcal{R}(\frac{\pi}{2}, \mathbf{a}) \in \mathsf{SO}(3)$, with $\mathcal{R}(\theta, \mathbf{a})$ being the rotation by an angle θ about the unit vector $\mathbf{a}$, defined as follows:

$$\mathcal{R}(\theta, \mathbf{a}) := \mathbf{I}_3 + \sin(\theta)\mathbf{a}^\times + (1 - \cos(\theta))(\mathbf{a}^\times)^2,$$

which, for $\theta = \frac{\pi}{2}$, leads to

$$\mathbf{R}(\mathbf{a}) = \mathbf{a}\mathbf{a}^\top + \mathbf{a}^\times,$$

where we used the fact that $(\mathbf{a}^\times)^2 = \mathbf{a}\mathbf{a}^\top - \mathbf{I}_3$, with $\mathbf{a}^\times$ being the skew-symmetric matrix associated to the unit vector $\mathbf{a} = [a_1 \ a_2 \ a_3]^\top$, defined according to (2.1).

The matrix $\mathbf{P}(\mathbf{a}) \in \mathbb{R}^{3\times 3}$, which is used in (5.6), is given by

$$\mathbf{P}(\mathbf{a}) := \mathbf{I}_3 - \frac{\mathbf{a}\mathbf{a}^\intercal}{\|\mathbf{a}\|^2}. \tag{5.7}$$

For any vector $\mathbf{x} \in \mathbb{R}^3$, the vector $\mathbf{P}(\mathbf{a})\mathbf{x}$ corresponds to the projection of $\mathbf{x}$ onto the hyperplane orthogonal to $\mathbf{a}$. As discussed later in Section 5.3.3, the coordinates of the unit vector $\mathbf{a}$ are updated when the robot switches from the *move-to-target* mode to the *obstacle-avoidance* mode according to the update law $\mathbf{L}(\xi)$, whose design is provided later in Section 5.3.3.

Finally, the scalar function $\eta(\mathbf{x}) \in [0, 1]$ is given by

$$\eta(\mathbf{x}) = \begin{cases} -1, & d(\mathbf{x}, \mathcal{O}_\mathcal{W}) - r_a \geq \gamma_s, \\ 1 - \frac{d(\mathbf{x}, \mathcal{O}_\mathcal{W}) - r_a - \gamma_a}{0.5(\gamma_s - \gamma_a)}, & \gamma_a \leq d(\mathbf{x}, \mathcal{O}_\mathcal{W}) - r_a \leq \gamma_s, \\ 1, & d(\mathbf{x}, \mathcal{O}_\mathcal{W}) - r_a \leq \gamma_a, \end{cases} \tag{5.8}$$

where $0 < \gamma_a < \gamma_s < \gamma$. The scalar function η is designed to ensure that the center of the robot remains inside the $\gamma-$neighborhood of the r_a-dilated obstacle-occupied workspace $\mathcal{N}_\gamma(\mathcal{D}_{r_a}(\mathcal{O}_\mathcal{W}))$ when it operates in the *obstacle-avoidance* mode in the set $\mathcal{N}_\gamma(\mathcal{D}_{r_a}(\mathcal{O}_\mathcal{W}))$. This feature allows for the design of the jump set of the *obstacle-avoidance* mode, as discussed later in Section 5.3.2, and ensures convergence to the target location, as stated later in Theorem 5.1. Next, we provide the construction of the flow set $\mathcal{F}$ and the jump set $\mathcal{J}$ used in (5.5).

5.3.2 Geometric construction of the flow and jump sets

When the robot operates in the *move-to-target* mode, its velocity is directed towards the target location. Hence, if the path joining the robot's location and the target is

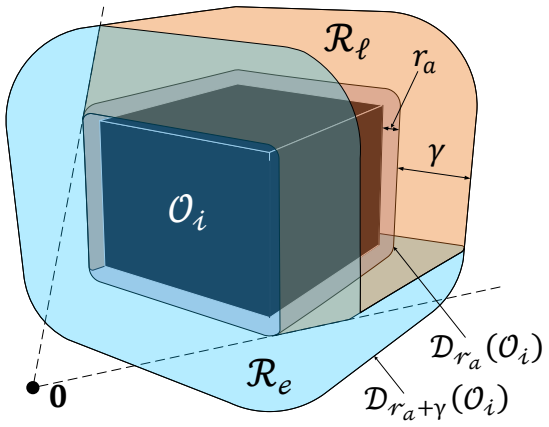

Figure 5.1: Geometrical representation of the *landing* region and the *exit* region.

obstructed by an obstacle, let's say $\mathcal{O}_i$ for some $i \in \mathbb{I}$ *i.e.*, $\mathcal{L}_s(\mathbf{x}, \mathbf{0}) \cap \mathcal{D}^\circ_{r_a}(\mathcal{O}_i) \neq \emptyset$, then the center of the robot enters the $(r_a + \gamma)-$neighbourhood of the obstacle $\mathcal{O}_i$ through the *landing* region $\mathcal{R}^i_l$, which is defined as

$$\mathcal{R}^i_l := \left\{ \mathbf{x} \in \mathcal{N}_\gamma(\mathcal{D}_{r_a}(\mathcal{O}_i)) | \mathcal{L}_s(\mathbf{x}, \mathbf{0}) \cap \mathcal{D}^\circ_{r_a}(\mathcal{O}_i) \neq \emptyset \right\}. \tag{5.9}$$

The union of the *landing* regions over all obstacles is defined as

$$\mathcal{R}_l := \bigcup_{i \in \mathbb{I}} \mathcal{R}^i_l. \tag{5.10}$$

Next, we define an *exit* region $\mathcal{R}_e$ as the part of the $\gamma-$neighborhood of the r_a-dilated obstacles that do not belong the *landing* region. The exit region $\mathcal{R}_e$ is defined as

$$\mathcal{R}_e = \mathcal{N}_\gamma(\mathcal{D}_{r_a}(\mathcal{O}_\mathcal{W})) \setminus \mathcal{R}_l. \tag{5.11}$$

Note that when the robot's center at $\mathbf{x}$ belongs to the *exit* region, the line segment connecting its location to the target location $\mathcal{L}_s(\mathbf{x}, \mathbf{0})$ does not intersect with the interior of the nearest r_a-dilated obstacle. Hence, the robot should move straight towards the target location only if it is in the *exit* region. Next, we provide the geometric construction of the flow set $\mathcal{F}$ and the jump set $\mathcal{J}$, used in (5.5).

Flow and jump sets (*move-to-target* mode)

When the robot operating in the *move-to-target* mode, enters in the *landing* region $\mathcal{R}_l$ (5.10), it should switch to the *obstacle-avoidance* mode to avoid collision. Hence, the jump set of the *move-to-target* mode for the state $\mathbf{x}$ is defined as

$$\mathcal{J}^\mathcal{W}_0 := \overline{\mathcal{N}_{\gamma_s}(\mathcal{D}_{r_a}(\mathcal{O}_\mathcal{W})) \cap \mathcal{R}_l}, \tag{5.12}$$

where $\gamma_s \in (0, \gamma)$. For robustness purposes (with respect to noise), we introduce a hysteresis region by allowing the robot, operating in the *move-to-target* mode inside the $(r_a + \gamma)-$neighbourhood of the set $\mathcal{O}_\mathcal{W}$, to move closer to the set $\mathcal{O}_\mathcal{W}$ before switching to the *obstacle-avoidance* mode.

The flow set of the *move-to-target* mode for the state $\mathbf{x}$ is then defined as

$$\mathcal{F}_0^{\mathcal{W}} := \left(\mathcal{W} \setminus (\mathcal{D}^{\circ}_{r_a+\gamma_s}(\mathcal{O}_{\mathcal{W}}))\right) \cup \mathcal{R}_e. \tag{5.13}$$

Notice that the union of the jump set $\mathcal{J}_0^{\mathcal{W}}$ and the flow set $\mathcal{F}_0^{\mathcal{W}}$ covers the robot-centered obstacle-free workspace $\mathcal{W}_{r_a}$.

The overall flow and the jump set $\mathcal{F}_0$ and $\mathcal{J}_0$, for the *move-to-target* mode are given by

$$\begin{aligned} \mathcal{F}_0 &:= \{\xi \in \mathcal{K} | \mathbf{x} \in \mathcal{F}_0^{\mathcal{W}}, m = 0\}, \\ \mathcal{J}_0 &:= \{\xi \in \mathcal{K} | \mathbf{x} \in \mathcal{J}_0^{\mathcal{W}}, m = 0\}. \end{aligned} \tag{5.14}$$

Flow and jump sets (*obstacle-avoidance* mode)

The robot operates in the *obstacle-avoidance* mode inside the $\gamma-$neighbourhood of the obstacle-occupied workspace. Since the robot can safely move straight towards the target location and exit the $\gamma-$neighborhood of the nearest obstacle, whenever it is in the *exit* region (5.11), it should switch back to the *move-to-target* mode only if it is in the *exit* region. To that end, we make use of the *hit point* $\mathbf{h}$ (*i.e.*, the location of the center of the robot when it switched from the *move-to-target* mode to the current *obstacle-avoidance* mode) to define the jump set of the *obstacle-avoidance* mode $\mathcal{J}_1^{\mathcal{W}}$ for the state $\mathbf{x}$ as follows:

$$\mathcal{J}_1^{\mathcal{W}} := \left(\mathcal{W} \setminus \mathcal{D}^{\circ}_{r_a+\gamma}(\mathcal{O}_{\mathcal{W}})\right) \cup \mathcal{ER}^{\mathbf{h}} \cup \mathcal{N}_{\gamma}(\mathcal{D}_{r_a}(\mathcal{O}_0)). \tag{5.15}$$

For a *hit point* $\mathbf{h} \in \mathcal{W}_{r_a}$, the set $\mathcal{ER}^{\mathbf{h}}$ is given by

$$\mathcal{ER}^{\mathbf{h}} := \{\mathbf{x} \in \mathcal{R}_e \big| \|\mathbf{h}\| - \|\mathbf{x}\| \geq \epsilon\}, \tag{5.16}$$

with $\epsilon \in (0, \bar{\epsilon}]$ where $\bar{\epsilon}$ is a sufficiently small positive scalar. The set $\mathcal{ER}^{\mathbf{h}}$ contains the locations from the *exit* region $\mathcal{R}_e$ which are at least ϵ units closer to the target location than the current *hit point* $\mathbf{h}$. Since the obstacles are compact and convex, and the target location $\mathbf{0}$ is within the interior of the obstacle-free workspace $\mathcal{W}_{r_a}$, it is possible to guarantee the existence of the parameter $\bar{\epsilon}$ such that the intersection set $\mathcal{ER}^{\mathbf{h}} \cap \mathcal{N}_{\gamma}(\mathcal{D}_{r_a}(\mathcal{O}_i))$ is non-empty for every $\mathbf{h} \in \mathcal{J}_0^{\mathcal{W}} \cap \mathcal{N}_{\gamma}(\mathcal{D}_{r_a}(\mathcal{O}_i))$ for each $i \in \mathbb{I}$, as stated in the following lemma:

Lemma 5.1 *Let Assumption 5.1 hold. Then, for any location* $\mathbf{h} \in \mathcal{J}_0^{\mathcal{W}} \cap \mathcal{N}_{\gamma}(\mathcal{D}_{r_a}(\mathcal{O}_i))$, *there exists* $\bar{\epsilon} > 0$ *such that for any* $\epsilon \in (0, \bar{\epsilon}]$ *the set* $\mathcal{ER}^{\mathbf{h}} \cap \mathcal{N}_{\gamma}(\mathcal{D}_{r_a}(\mathcal{O}_i)) \neq \emptyset$, *where the set* $\mathcal{ER}^{\mathbf{h}}$ *is defined in* (5.16).

Proof See Appendix D.1.

According to (5.15) and (5.16), the robot operating in the *obstacle-avoidance* mode, can switch to the *move-to-target* mode only when its center belongs to the *exit* region $\mathcal{R}_e$ and the target location $\mathbf{0}$ is at least ϵ units closer to $\mathbf{x}$ than the current *hit point* $\mathbf{h}$.

The flow set of the *obstacle-avoidance* mode for the state $\mathbf{x}$ *i.e.*, $\mathcal{F}_1^{\mathcal{W}}$ is defined as follows:

$$\mathcal{F}_1^{\mathcal{W}} := \overline{\mathcal{N}_{\gamma}(\mathcal{D}_{r_a}(\mathcal{O}_{\mathcal{W}})) \setminus (\mathcal{ER}^{\mathbf{h}} \cup \mathcal{N}_{\gamma}(\mathcal{D}_{r_a}(\mathcal{O}_0)))}. \tag{5.17}$$

Notice that the union of the jump set (5.15) and the flow set (5.17) exactly covers the robot-centered obstacle-fee workspace $\mathcal{W}_{r_a}$.

Remark 5.1 *Given that the workspace $\mathcal{W}$ is both convex and compact, there may exist some locations $\mathbf{x} \in \mathcal{N}_\gamma(\mathcal{D}_{r_a}(\mathcal{O}_0))$ from which the nearest point to the robot's center on the obstacle $\mathcal{O}_0 = (\mathcal{W}^\circ)^c$ is not unique. This scenario prevents the implementation of the obstacle-avoidance term $\mathbf{v}(\mathbf{x}, \mathbf{a})$ in the control law, at such locations. However, by excluding the set $\mathcal{N}_\gamma(\mathcal{D}_{r_a}(\mathcal{O}_0))$ from the set $\mathcal{F}_1^{\mathcal{W}}$, as defined in (5.17), it is ensured that the obstacle-avoidance mode is never activated within the set $\mathcal{N}_\gamma(\mathcal{D}_{r_a}(\mathcal{O}_0))$.*

The overall flow and jump sets $\mathcal{F}_1$ and $\mathcal{J}_1$, for the *obstacle-avoidance* mode are given by

$$\begin{aligned} \mathcal{F}_1 &:= \{\xi \in \mathcal{K} | \mathbf{x} \in \mathcal{F}_1^{\mathcal{W}}, m = 1, s \neq s_0\}, \\ \mathcal{J}_1 &:= \mathcal{J}_{\mathbf{x}} \cup \mathcal{J}_s, \end{aligned} \tag{5.18}$$

where $\mathcal{J}_{\mathbf{x}} := \{\xi \in \mathcal{K} | m = 1, \mathbf{x} \in \mathcal{J}_1^{\mathcal{W}}\}$ and $\mathcal{J}_s := \{\xi \in \mathcal{K} | m = 1, s = s_0\}$ with $s_0 \in \mathbb{R}_{\geq 0}$ being the initial value of the state s, *i.e.*, $s(0, 0) = s_0$.

Remark 5.2 *The definition of sets in (5.18) enables the control to immediately switch to the move-to-target mode if it is initialized in the obstacle-avoidance mode (i.e., $\xi(0, 0) \in \mathcal{J}_1$). This ensures that the hit point $\mathbf{h}$ always belongs to the set $\mathcal{J}_0^{\mathcal{W}}$ before the robot starts moving in the obstacle-avoidance mode, thus guaranteeing the existence of the parameter $\bar{\epsilon}$, as stated in Lemma 5.1.*

Finally, the overall flow and jump sets $\mathcal{F}$ and $\mathcal{J}$, used in (5.5), are defined as

$$\mathcal{F} := \bigcup_{m \in \mathbb{M}} \mathcal{F}_m, \quad \mathcal{J} := \bigcup_{m \in \mathbb{M}} \mathcal{J}_m, \tag{5.19}$$

where $\mathcal{F}_0, \mathcal{J}_0$ defined in (5.14) for $m = 0$ and in (5.18) for $m = 1$. Next, we provide the update law $\mathbf{L}(\mathbf{x}, \mathbf{h}, \mathbf{a}, m, s)$ used in (5.5b).

5.3.3 Update law $\mathbf{L}(\mathbf{x}, \mathbf{h}, \mathbf{a}, m)$

The update law $\mathbf{L}(\xi)$, used in (5.5b), updates the value of the *hit point* $\mathbf{h}$, the unit vector $\mathbf{a}$, the mode indicator m and the variable s when the state $(\mathbf{x}, \mathbf{h}, \mathbf{a}, m, s)$ belongs to the jump set $\mathcal{J}$ defined in (5.19) and is given by

$$\mathbf{L}(\xi) = \begin{cases} \mathbf{L}_0(\xi), & \xi \in \mathcal{J}_0, \\ \mathbf{L}_1(\xi), & \xi \in \mathcal{J}_1. \end{cases} \tag{5.20}$$

When the state ξ enters in the jump set $\mathcal{J}_0$ (5.14), the update law $\mathbf{L}_0(\mathbf{x}, \mathbf{h}, \mathbf{a}, 0, s)$ is given as

$$\mathbf{L}_0(\mathbf{x}, \mathbf{h}, \mathbf{a}, 0, s) = \begin{bmatrix} \mathbf{x} \\ \mathbf{A}(\mathbf{x}) \\ 1 \\ s + 1 \end{bmatrix}, \tag{5.21}$$

Given $\mathbf{x} \in \mathcal{N}_\gamma(\mathcal{D}_{r_a}(\mathcal{O}_{\mathcal{W}}))$, the set-valued mapping $\mathbf{A} : \mathbb{R}^3 \rightrightarrows \mathbb{S}^2$ is defined as

$$\mathbf{A}(\mathbf{x}) = \begin{cases} \mathbf{q} \in \mathcal{P}^\perp(\mathbf{x}), & \mathbf{x}^\times \mathbf{x}_\pi = \mathbf{0}, \\ \mathbf{q} \in \frac{\mathbf{x}^\times \mathbf{x}_\pi}{\|\mathbf{x}^\times \mathbf{x}_\pi\|}, & \mathbf{x}^\times \mathbf{x}_\pi \neq \mathbf{0}, \end{cases} \tag{5.22}$$

where for any $\mathbf{p} \in \mathbb{R}^3$, the set $\mathcal{P}^{\perp}(\mathbf{p})$, which is defined as

$$\mathcal{P}^{\perp}(\mathbf{p}) := \{\mathbf{q} \in \mathbb{S}^2 | \mathbf{q}^{\intercal}\mathbf{p} = 0\}, \tag{5.23}$$

contains unit vectors that are perpendicular to the vector $\mathbf{p}$.

According to (5.21), when the robot switches from the *move-to-target* mode to the *obstacle-avoidance* mode, the coordinates of the *hit point* $\mathbf{h}$ get updated to the current value of $\mathbf{x}$. Moreover, according to (5.22), the unit vector $\mathbf{a}$ is updated such that it is perpendicular to the vector $\mathbf{h}$ and the resulting hyperplane $\mathcal{P}(\mathbf{h}, \mathbf{a})$ intersects with the interior of the nearest r_a-dilated obstacle. Since the target location $\mathbf{0} \in \mathcal{P}(\mathbf{h}, \mathbf{a})$ and the *hit point* $\mathbf{h} \in \mathcal{J}_0^{\mathcal{W}}$, the hyperplane intersects with both the *landing region* $\mathcal{R}_l$ and the *exit* region $\mathcal{R}_e$ associated with the nearest obstacle. This feature is then used to ensure that the robot, operating in the *obstacle-avoidance* mode, always enters in the *move-to-target* mode. This allows one to ensure global convergence to the target location, as stated later in Theorem 5.1.

When the state ξ enters in the jump set $\mathcal{J}_1$, defined in (5.18), the update law $\mathbf{L}_1(\mathbf{x}, \mathbf{h}, \mathbf{a}, 1, s)$ is given by

$$\mathbf{L}_1(\mathbf{x}, \mathbf{h}, \mathbf{a}, 1, s) = \begin{bmatrix} \mathbf{h} \\ \mathbf{a} \\ 0 \\ s+1 \end{bmatrix}. \tag{5.24}$$

According to (5.24), when the robot switches from the *obstacle-avoidance* mode to the *move-to-target* mode, the coordinates of the *hit point* $\mathbf{h}$ and the unit vector $\mathbf{a}$ remain unchanged.

Remark 5.3 *Since the parameter $\gamma \in (r_s, \bar{r}_s - r_s)$, where $\bar{r}_s$ is defined in (5.2), the $(r_a + \gamma)-$dilated obstacles $\mathcal{D}_{r_a+\gamma}(\mathcal{O}_i)$, $\forall i \in \mathbb{I}$, are disjoint, and the target location $\mathbf{0} \in \mathcal{W}_{r_a+\gamma}^{\circ}$. Furthermore, according to (5.17), the flow set of the obstacle-avoidance mode associated with the state $\mathbf{x}$, denoted as $\mathcal{F}_1^{\mathcal{W}}$, is contained within the region $\mathcal{N}_{\gamma}(\mathcal{D}_{r_a}(\mathcal{O}_{\mathcal{W}}))$. Hence, the proposed control law enables the robot to avoid one obstacle at a time.*

Control design summary: The proposed hybrid feedback control law can be summarized as follows:

- **Parameters selection**: the target location is set at the origin with $\mathbf{0} \in \mathcal{W}_{r_a}^{\circ}$, and $\xi(0, 0) \in \mathcal{K}$. The gain parameters κ_s and κ_r are set to positive values, and sufficiently small positive value is chosen for $\bar{\epsilon}$, used in (5.16). The scalar parameter γ, used in the construction of the flow set $\mathcal{F}$ and the jump set $\mathcal{J}$, is selected such that $\gamma \in (0, \bar{r}_s - r_s)$, where $\bar{r}_s$ is defined in (5.2). The parameters γ_a and γ_s are set to satisfy $0 < \gamma_a < \gamma_s < \gamma$.

- ***Move-to-target* mode** $m = 0$: this mode is activated when $\xi \in \mathcal{F}_0$. As per (5.5a), the control input is given by $\mathbf{u}(\xi) = -\kappa_s \mathbf{x}$, causing $\mathbf{x}$ to evolve along the line segment $\mathcal{L}_s(\mathbf{0}, \mathbf{x})$ towards the origin. If, at some instance of time, ξ enters in the jump set $\mathcal{J}_0$ of the *move-to-target* mode, the state variables $(\mathbf{h}, \mathbf{a}, m, s)$ are updated using (5.21), and the control input switches to the *obstacle-avoidance* mode.

- ***Obstacle-avoidance* mode** $m = 1$: this mode is activated when $\xi \in \mathcal{F}_1$. As per (5.5a), the control input is given by $\mathbf{u}(\xi) = \kappa_r \mathbf{v}(\mathbf{x}, \mathbf{a})$, causing $\mathbf{x}$ to evolve in the $\gamma-$neighborhood of the nearest obstacle along the hyperplane $\mathcal{P}(\mathbf{h}, \mathbf{a})$ until the state ξ enters in the jump set $\mathcal{J}_1$ of the *obstacle-avoidance* mode. When $\xi \in \mathcal{J}_1$, the state variables (m, s) are updated using (5.24), and the control input switches to the *move-to-target* mode.

This concludes the design of the proposed hybrid feedback controller (5.5). Next, we analyze the safety, stability and convergence properties of the proposed hybrid feedback controller.

5.4 Stability analysis

The hybrid closed-loop system resulting from the hybrid feedback control law (5.5) is given by

$$\underbrace{\begin{aligned}\dot{\mathbf{x}} &= \mathbf{u}(\xi)\\ \dot{\mathbf{h}} &= \mathbf{0}\\ \dot{\mathbf{a}} &= \mathbf{0}\\ \dot{m} &= 0\\ \dot{s} &= 1\end{aligned}}_{\dot{\xi}=\mathbf{F}(\xi),\ \xi\in\mathcal{F},} \qquad \underbrace{\begin{aligned}\mathbf{x}^+ &= \mathbf{x}\\ \begin{bmatrix}\mathbf{h}^+\\ \mathbf{a}^+\\ m^+\\ s^+\end{bmatrix} &\in \mathbf{L}(\xi)\end{aligned}}_{\xi^+\in\mathbf{J}(\xi),\ \xi\in\mathcal{J},} \tag{5.25}$$

where $\mathbf{u}(\xi)$ is defined in (5.5a), and the update law $\mathbf{L}(\xi)$ is provided in (5.20). Definitions of the flow set $\mathcal{F}$ and the jump set $\mathcal{J}$ are provided in (5.19). Next, we analyze the hybrid closed-loop system (5.25) in terms of forward invariance of the obstacle-free state space $\mathcal{K}$, along with the stability properties of the target set

$$\mathcal{A} := \{\xi \in \mathcal{K} | \mathbf{x} = \mathbf{0}\}. \tag{5.26}$$

The next lemma shows that the hybrid closed-loop system (5.25) satisfies the hybrid basic conditions, as stated in Assumption 2.1, which guarantees the well-posedness of the hybrid closed-loop system.

Lemma 5.2 *The hybrid closed-loop system* (5.25) *with data* $(\mathcal{F}, \mathbf{F}, \mathcal{J}, \mathbf{J})$ *satisfies the hybrid basic conditions stated in Assumption 2.1.*

Proof See Appendix D.2.

For safe autonomous navigation, the state $\mathbf{x}$ must always evolve within the obstacle-free workspace $\mathcal{W}_{r_a}$, defined in (5.3). This is equivalent to having the set $\mathcal{K}$ forward invariant for the hybrid closed-loop system (5.25). This is stated in the next Lemma.

Lemma 5.3 *Under Assumption 5.1, for the hybrid closed-loop system* (5.25)*, the obstacle-free set* $\mathcal{K} := \mathcal{W}_{r_a} \times \mathcal{W}_{r_a} \times \mathbb{S}^2 \times \mathbb{M} \times \mathbb{R}_{\geq 0}$ *is forward invariant.*

Proof See Appendix D.3.

Next, we provide one of our main results which establishes the fact that for all initial conditions in the obstacle-free set $\mathcal{K}$, the proposed hybrid controller not only ensures safe navigation but also guarantees global asymptotic stability of the target location at the origin.

Theorem 5.1 *Under Assumption 5.1, for the hybrid closed-loop system (4.29), the following holds true:*

i) the obstacle-free set $\mathcal{K}$ is forward invariant,

ii) the target set $\mathcal{A}$ is globally asymptotically stable over the set $\mathcal{K}$,

iii) the number of jumps is finite.

Proof See Appendix D.4.

5.5 Application to sphere worlds

Obviously, the hybrid feedback controller (5.5), which is designed for safe autonomous navigation in 3-D environments with arbitrary convex obstacles, is applicable in sphere words *i.e.,* environments with spherical obstacles. However, in this section, we will take advantage of the simplified geometry of the obstacles to redesign the control law (5.5) in way that ensures a monotonic decrease of the distance between the robot and the target location–a feature that is not guaranteed with the control law (5.5) in environments with arbitrary convex obstacles.

Let us consider environments with spherical obstacles as defined in [Koditschek and Rimon, 1990]. The workspace $\mathcal{W} := \mathcal{B}_{r_0}(\mathbf{c}_0)$ is a compact sphere with radius $r_0 \in \mathbb{R}_{>0}$ and center $\mathbf{c}_0 \in \mathbb{R}^3$. In addition, the workspace $\mathcal{W}$ contains disjoint, compact spherical obstacles $\mathcal{O}_i := \mathcal{B}_{r_i}(\mathbf{c}_i), i \in \mathbb{I} \setminus \{0\}$, where $r_i \in \mathbb{R}_{\geq 0}$ and $\mathbf{c}_i \in \mathcal{W}$ represent the radius and the center of obstacle $\mathcal{O}_i$. Similar to [Koditschek and Rimon, 1990], the workspace $\mathcal{W}$ satisfies Assumption 5.1.

Taking advantage of the spherical geometry of the obstacles, we will modify the obstacle-avoidance control vector $\mathbf{v}(\mathbf{x}, \mathbf{a})$ in (5.6), to ensure that in the *obstacle-avoidance* mode, the inner product between the modified velocity control vector and the vector $\mathbf{x}$ remains non-positive. This will ensure that the distance, between the target location and the robot, monotonically decreases when the robot operates according to the proposed hybrid feedback controller (5.5) with modifications, as stated later in Theorem 5.2.

When the control law switches from the *move-to-target* mode to the *obstacle-avoidance* mode, the unit vector $\mathbf{a}$ is updated using (5.22) such that the hyperplane $\mathcal{P}(\mathbf{0}, \mathbf{a})$ intersects the current *hit point* $\mathbf{h}$ and the interior of the nearest r_a-dilated obstacle $\mathcal{D}^{\circ}_{r_a}(\mathcal{O}_i)$. Since obstacle $\mathcal{O}_i$ is a sphere, it can be shown that the hyperplane $\mathcal{P}(\mathbf{0}, \mathbf{a})$ passes through the center $\mathbf{c}_i$ of obstacle $\mathcal{O}_i$. This ensures that for all $\mathbf{x} \in \mathcal{N}_\gamma(\mathcal{D}_{r_a}(\mathcal{O}_i)) \cap \mathcal{P}(\mathbf{0}, \mathbf{a})$, $\Pi(\mathbf{x}, \mathcal{O}_\mathcal{W}) = \Pi(\mathbf{x}, \mathcal{O}_i) \in \mathcal{P}(\mathbf{0}, \mathbf{a})$. As a result, if $\mathbf{h} \in \partial\mathcal{D}_\beta(\mathcal{O}_i)$ for $\beta \in [r_a, r_a + \gamma]$,

and $\mathbf{x}(t_0, j_0) \in \partial\mathcal{D}_\beta(\mathcal{O}_i) \cap \mathcal{P}(\mathbf{h}, \mathbf{a})$ for some $(t_0, j_0) \in$ dom ξ, where $\mathbf{a} = \mathbf{A}(\mathbf{h})$, then under the control input $\mathbf{u}(\xi) = \mathbf{v}_s(\mathbf{x}, \mathbf{a})$, where

$$\mathbf{v}_s(\mathbf{x}, \mathbf{a}) = \mathbf{R}(\mathbf{a})\mathbf{x}_\pi, \tag{5.27}$$

one has $\mathbf{x}(t, j) \in \partial\mathcal{D}_\beta(\mathcal{O}_i) \cap \mathcal{P}(\mathbf{0}, \mathbf{a})$ for all time $(t, j) \succeq (t_0, j_0)$, ensuring robot's safety, as stated later in Theorem 5.2

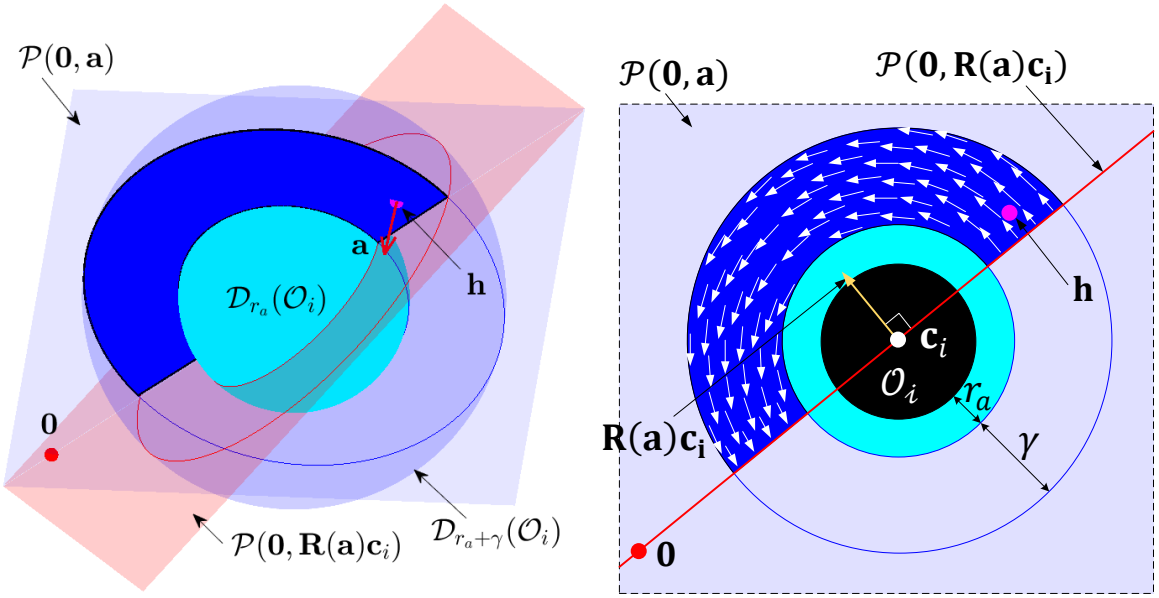

Figure 5.2: The left figure depicts the set $\mathcal{N}_\gamma(\mathcal{D}_{r_a}(\mathcal{O}_i)) \cap \mathcal{P}(\mathbf{h}, \mathbf{a}) \cap \mathcal{P}_{\geq}(\mathbf{0}, \mathbf{R}(\mathbf{a})\mathbf{c}_i)$, shaded in a dark blue color. The right figure shows the direction of the modified obstacle-avoidance control vector, $\mathbf{v}_s(\mathbf{x}, \mathbf{a})$, at $\mathbf{x} \in \mathcal{N}_\gamma(\mathcal{D}_{r_a}(\mathcal{O}_i)) \cap \mathcal{P}(\mathbf{h}, \mathbf{a}) \cap \mathcal{P}_{\geq}(\mathbf{0}, \mathbf{R}(\mathbf{a})\mathbf{c}_i)$.

Now, for a given $\mathbf{h} \in \mathcal{N}_\gamma(\mathcal{D}_{r_a}(\mathcal{O}_i))$, consider the hyperplane $\mathcal{P}(\mathbf{0}, \mathbf{R}(\mathbf{a})\mathbf{c}_i)$, where $\mathbf{a} = \mathbf{A}(\mathbf{h})$ and $\mathbf{c}_i$ is the center of obstacle $\mathcal{O}_i$. Notice that, for all $\mathbf{x}$ in the set $\mathcal{N}_\gamma(\mathcal{D}_{r_a}(\mathcal{O}_i)) \cap \mathcal{P}(\mathbf{h}, \mathbf{a}) \cap \mathcal{P}_{\geq}(\mathbf{0}, \mathbf{R}(\mathbf{a})\mathbf{c}_i)$, which is depicted in Fig. 5.2, the inner product between the modified obstacle-avoidance control term $\mathbf{v}(\mathbf{x}, \mathbf{a})$ and the vector $\mathbf{x}$ is always non-positive. This allows one to show that if one has $\mathbf{h} \in \mathcal{N}_\gamma(\mathcal{D}_{r_a}(\mathcal{O}_i))$, $\mathbf{a} = \mathbf{A}(\mathbf{h})$ and $\mathbf{x} \in \mathcal{N}_\gamma(\mathcal{D}_{r_a}(\mathcal{O}_i)) \cap \mathcal{P}(\mathbf{h}, \mathbf{a}) \cap \mathcal{P}_{\geq}(\mathbf{0}, \mathbf{R}(\mathbf{a})\mathbf{c}_i)$, then the control input vector $\mathbf{u}(\xi) = \mathbf{v}_s(\mathbf{x}, \mathbf{a})$ will ensure monotonic decrease of the distance $\|\mathbf{x}\|$ as long as the state $\mathbf{x}$ remains in the set $\mathcal{P}_{\geq}(\mathbf{0}, \mathbf{R}(\mathbf{a})\mathbf{c}_i)$, as stated later in Theorem 5.2.

Next, motivated by the preceding discussion, we modify the proposed hybrid feedback control law (5.5) using the modified obstacle-avoidance control vector $\mathbf{v}_s(\mathbf{x}, \mathbf{a})$, defined in (5.27), as follows:

- the modified hybrid control input vector $\mathbf{u}_s(\xi)$, which is obtained by replacing the obstacle-avoidance control vector $\mathbf{v}(\mathbf{x}, \mathbf{a})$ with the modified obstacle-avoidance control vector $\mathbf{v}_s(\mathbf{x}, \mathbf{a})$ in (5.5a), is given as

$$\mathbf{u}_s(\xi) = -\kappa_s(1 - m)\mathbf{x} + \kappa_r m\mathbf{v}_s(\mathbf{x}, \mathbf{a}), \tag{5.28}$$

  where $\kappa_s > 0$ and $\kappa_r > 0$.

The hybrid closed-loop system resulting from the modified hybrid feedback control law is given by

$$\underbrace{\begin{aligned}\dot{\mathbf{x}} &= \mathbf{u}_s(\xi)\\ \dot{\mathbf{h}} &= \mathbf{0}\\ \dot{\mathbf{a}} &= \mathbf{0}\\ \dot{m} &= 0\\ \dot{s} &= 1\end{aligned}}_{\dot{\xi}=\mathbf{F}_s(\xi),\xi\in\mathcal{F},} \qquad \underbrace{\begin{aligned}\mathbf{x}^+ &= \mathbf{x}\\ \begin{bmatrix}\mathbf{h}^+\\ \mathbf{a}^+\\ m^+\\ s^+\end{bmatrix} &\in \mathbf{L}(\xi)\end{aligned}}_{\xi^+\in\mathbf{J}(\xi),\xi\in\mathcal{J},} \tag{5.29}$$

where the control input vector $\mathbf{u}_s$ is defined in (5.28) and the update law $\mathbf{L}(\xi)$ is given in (5.20).

The next lemma shows that the hybrid closed-loop system (5.29) with the data $(\mathcal{F}, \mathbf{F}_s, \mathcal{J}, \mathbf{J})$ satisfies the hybrid basic conditions, as stated in Assumption 2.1.

Lemma 5.4 *The hybrid closed-loop system* (5.29) *with data* $(\mathcal{F}, \mathbf{F}_s, \mathcal{J}, \mathbf{J})$ *satisfies the hybrid basic conditions stated in Assumption 2.1.*

The proof of Lemma 5.4 is similar to the proof of Lemma 5.2, therefore, it is omitted.

Next, we demonstrate that for the robot operating in a sphere world, which satisfies Assumption 5.1, the modified proposed hybrid feedback controller ensures safe navigation. It also guarantees global asymptotic stability of the target location at the origin, with a monotonic decrease of the distance between the robot's center and the target location.

Theorem 5.2 *Under Assumption 5.1, for the hybrid closed-loop system* (5.29)*, the following holds true:*

i) the obstacle-free set $\mathcal{K}$ is forward invariant,

ii) the target set $\mathcal{A}$ is globally asymptotically stable over the set $\mathcal{K}$,

iii) the number of jumps is finite.

iv) $\|\mathbf{x}(t,j)\| \leq \|\mathbf{x}(t_0,j_0)\|$, for all $(t,j) \succeq (t_0,j_0) \in$ dom ξ.

Proof See Appendix D.5.

5.6 Implementation procedure

We consider a workspace with convex obstacles that satisfies Assumption 5.1 with some $\bar{r}_s > 0$, as discussed in Section 5.2. The target location is set at the origin within the interior of the obstacle-free workspace $\mathcal{W}_{r_a}^{\circ}$. The center of the robot is initialized in the obstacle-free workspace $\mathcal{W}_{r_a}$. The variables $\mathbf{h}, \mathbf{a}, m$ and s are initialized in the sets $\mathcal{W}_{r_a}, \mathbb{S}^2, \mathbb{M}$ and $\mathbb{R}_{\geq 0}$, respectively. The parameter $\gamma \in (0, \bar{r}_s - r_s)$ enables the algorithm to avoid one obstacle at a time, as discussed in Remark 5.3. The parameters γ_a and γ_s are set to satisfy $0 < \gamma_a < \gamma_s < \gamma$. A sufficiently small value for $\bar{\epsilon}$ is selected as stated

in Lemma 5.1, and the parameter $\epsilon \in (0, \bar{\epsilon}]$. We set a sensing radius $R_s > r_a + \gamma$ such that the robot can detect the boundary of the obstacles within its line-of-sight inside the region $\mathcal{B}_{R_s}(\mathbf{x})$.

When the control input is initialized in the *move-to-target* mode, according to (5.5a), it steers the robot straight towards the origin. The robot should constantly measure the distance between its center and the surrounding obstacles to identify whether the state ξ has entered in the jump set $\mathcal{J}_0$ of the *move-to-target* mode. To do this, the robot needs to identify the set $\partial\mathcal{O}$ which contains the locations from the boundary of the surrounding obstacles that are less than R_s units away from the center of the robot and have clear line-of-sight to the center of the robot, where $R_s > r_a + \gamma$ represents sensing radius. In other words, the set $\partial\mathcal{O}$ is defined as

$$\partial\mathcal{O} = \{\mathbf{p} \in \partial\mathcal{O}_{\mathcal{W}} | \|\mathbf{x} - \mathbf{p}\| \leq R_s, \mathcal{L}_s(\mathbf{x}, \mathbf{p}) \cap \mathcal{D}^{\circ}_{r_a}(\mathcal{O}_{\mathcal{W}}) = \emptyset\}. \tag{5.30}$$

Then, one can obtain the distance between the robot's center and the surrounding obstacles by evaluating $d(\mathbf{x}, \partial\mathcal{O})$ according to Section 2.2.1. If $d(\mathbf{x}, \partial\mathcal{O}) \leq r_a + \gamma_s$, the algorithm should identify whether the robot can move straight towards the target location without colliding with the nearest obstacle. In other words, the algorithm should evaluate whether the center of the robot belongs to the *landing* region $\mathcal{R}_l$, defined in (5.9), associated with the nearest obstacle. To that end, the algorithm identifies the set $\partial\mathcal{O}_c \subset \partial\mathcal{O}$ which contains the locations from the set $\partial\mathcal{O}$ that belong to the boundary of the closest obstacle. Let $\mathcal{O}_i$ for some $i \in \mathbb{I}$ be the closest obstacle to the center of the robot, then the set $\partial\mathcal{O}_c$ is defined as

$$\partial\mathcal{O}_c = \partial\mathcal{O}_i \cap \partial\mathcal{O}. \tag{5.31}$$

Once the set $\partial\mathcal{O}_c$ has been identified, one needs to determine whether the center of the robot $\mathbf{x}$ belongs to the *landing* region $\mathcal{R}_l$ by evaluating the intersection between the set $\partial\mathcal{O}_c$ and the set $\mathcal{D}^{\circ}_{r_a}(\mathcal{L}_s(\mathbf{x}, \mathbf{0}))$. If $\partial\mathcal{O}_c \cap \mathcal{D}^{\circ}_{r_a}(\mathcal{L}_s(\mathbf{x}, \mathbf{0})) \neq \emptyset$, then the center of the robot belongs to the *landing* region $\mathcal{R}_l$ and the state ξ has entered in the jump set of the *move-to-target* mode $\mathcal{J}_0$. Otherwise, the robot continues to operate in the *move-to-target* mode.

When the state ξ enters in the jump set of the *move-to-target* mode $\mathcal{J}_0$, the algorithm updates the state ξ as per (5.21) and (5.25), and the control input switches to the *obstacle-avoidance* mode. According to Lemma D.1, when the robot operates in the *obstacle-avoidance* mode, it stays inside the $\gamma-$neighborhood of the closest obstacle. As the robot operates in the *obstacle-avoidance* mode, the algorithm continuously evaluates the intersection $\partial\mathcal{O}_c \cap \mathcal{D}^{\circ}_{r_a}(\mathcal{L}_s(\mathbf{x}, \mathbf{0}))$ to check whether the center of the robot has entered in the *exit* region $\mathcal{R}_e$. If $\partial\mathcal{O}_c \cap \mathcal{D}^{\circ}_{r_a}(\mathcal{L}_s(\mathbf{x}, \mathbf{0})) = \emptyset$, then the center of the robot belongs to the exit region $\mathcal{R}_e$. If the robot's center in the *exit region* is ϵ units closer to the target location than the current *hit point* $\mathbf{h}$, it implies that the state ξ has entered in the jump set $\mathcal{J}_1$ of the *obstacle-avoidance* mode. Then the algorithm updates the value of the variables m and s as per (5.24) and the control input switches to the *move-to-target* mode.

Finally, if the control input is initialized in the *obstacle-avoidance* mode, according to (5.18), the state $\xi(0, 0)$ belongs to the jump set of the *obstacle-avoidance* mode $\mathcal{J}_1$.

As a result, according to (5.24) the algorithm updates the value of the variables $\mathbf{h}, \mathbf{a}, m$ and s, and switches the control input to the *move-to-target* mode.

The above-mentioned implementation procedure is summarised in Algorithm 5.

Algorithm 5 Implementation of the proposed hybrid control law (5.5) in *a priori* unknown environment.

Set target location at the origin $\mathbf{0}$.
Initialize $\mathbf{x}(0,0) \in \mathcal{W}_{r_a}$, $\mathbf{h}(0,0) \in \mathcal{W}_{r_a}$, $\mathbf{a}(0,0) \in \mathbb{S}^2$, $m(0,0) \in \mathbb{M}$ and $s(0,0) \in \mathbb{R}_{\geq 0}$. Choose sufficiently small value of $\bar{\epsilon}$ according to Lemma 5.1, and initialize $\epsilon \in (0, \bar{\epsilon}]$. Identify the parameter $\bar{r}_s$, as discussed in Section 5.2, and set parameters γ, γ_s and γ_a such that $0 < \gamma_a < \gamma_s < \gamma < \bar{r}_s - r_s$. Choose $R_s > r_a + \gamma$, used in (5.30).
Measure $\mathbf{x}$ and the set $\partial\mathcal{O}$ as defined in (5.30).
if $m = 0$, **then**
  if $d(\mathbf{x}, \partial\mathcal{O}) \leq r_a + \gamma_s$, **then**
    Identify the set $\partial\mathcal{O}_c \subset \partial\mathcal{O}$ as defined in (5.31).
    if $\partial\mathcal{O}_c \cap \mathcal{D}^{\circ}_{r_a}(\mathcal{L}_s(\mathbf{x}, \mathbf{0})) \neq \emptyset$, **then**
      Update $\xi \leftarrow \mathbf{J}(\xi)$ using (5.21) and (5.25).
    end if
  end if
end if
if $m = 1$, **then**
  if $s = s(0,0)$, **then**
    Update $\xi \leftarrow \mathbf{J}(\xi)$ using (5.24) and (5.25).
  else
    if $d(\mathbf{x}, \partial\mathcal{O}) \leq r_a + \gamma$, **then**
      Identify the set $\partial\mathcal{O}_c \subset \partial\mathcal{O}$ as defined in (5.31).
      if $\partial\mathcal{O}_c \cap \mathcal{D}^{\circ}_{r_a}(\mathcal{L}_s(\mathbf{x}, \mathbf{0})) = \emptyset$, **then**
        if $\|\mathbf{x}\| \leq \|\mathbf{h}\| - \epsilon$, **then**
          Update $\xi \leftarrow \mathbf{J}(\xi)$ using (5.24) and (5.25).
        end if
      end if
    else
      Update $\xi \leftarrow \mathbf{J}(\xi)$ using (5.24) and (5.25).
    end if
  end if
end if
Execute $\mathbf{F}(\xi)$ given (5.5), used in (5.25).
Go to step 3.

5.7 Simulation results

In the first simulation, we consider a single three-dimensional convex obstacle, as shown in Fig. 5.3. The initial location of the robot $\mathbf{x}(0,0)$ is represented by the green diamond

symbol, and the origin is selected as the target location. The radius of the robot $r = 0.15m$ and the safety distance $r_s = 0.1m$. The parameter $\gamma = 0.4m$ and the parameter ϵ, used in (5.16), is set to $0.1m$. The gains κ_s and κ_r, used in (5.5a), are set to 1 and 0.5, respectively. The sensing radius R_s, used in (5.30), is set to $1m$. The simulations are performed in MATLAB 2020a. In Fig. 5.3, the red-colored trajectory represents the motion of the robot in the *move-to-target* mode, whereas the black-colored trajectory represents the motion of the robot in the *obstacle-avoidance* mode. When the robot switches from the *move-to-target* mode to the *obstacle-avoidance* mode, the algorithm updates the coordinates of the *hit point* $\mathbf{h}$ and the unit vector $\mathbf{a}$ according to (5.21). Then, the robot moves in the $\gamma-$neighborhood of the nearest obstacle with its center in the hyperplane $\mathcal{P}(\mathbf{h}, \mathbf{a})$, as shown in Fig. 5.3. When the center of the robot enters in the jump set of the *obstacle-avoidance* mode, it switches back to the *move-to-target* mode and converges to the target location at the origin.

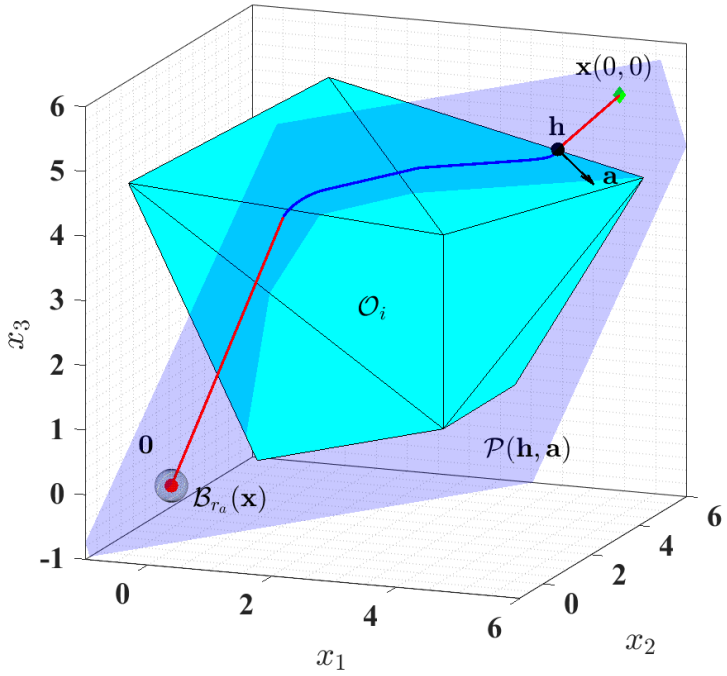

Figure 5.3: Trajectory of the robot safely converging to the origin.

We consider an unbounded workspace *i.e.*, obstacle $\mathcal{O}_0 = \emptyset$, with 2 three-dimensional, convex obstacles, as shown in Fig. 5.4. We apply the proposed hybrid feedback controller (5.5) for robot initialized at 8 different locations in the obstacle-free workspace. The target is located at the origin. The radius of the robot is set to $0.15m$. The minimum safety distance $r_s = 0.05m$ and the parameter $\gamma = 0.2m$. The gains κ_s and κ_r, used in (5.5a), are set to 0.5 and 1, respectively. The sensing radius R_s, used in (5.30), is set to $1m$. The parameter ϵ, used in (5.16), is set to 0.05m. From Fig. 5.4, it can be observed that the robot converges to the target location while simultaneously avoiding collisions with the obstacles. Fig. 5.5 shows that the center of the robot stays at least r_a meters away from the boundary of the obstacles. The complete simulation video can be found at https://youtu.be/67eDVXH1wbw.

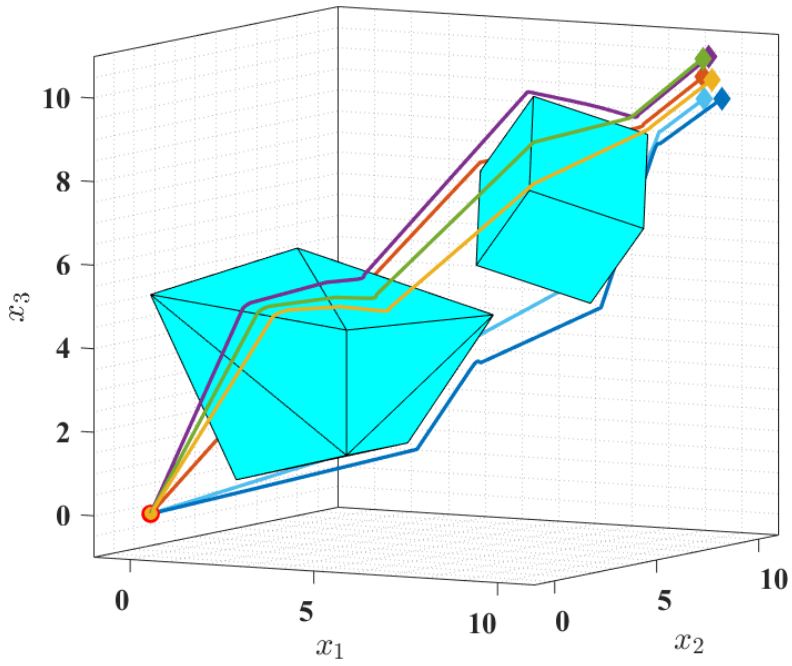

Figure 5.4: Robot trajectories starting from different locations.

In the next simulation scenario, as shown in Fig. 5.6, we consider 2 three-dimensional spherical obstacles and apply the proposed hybrid controller (5.5) with modifications mentioned in Section 5.5, for a point robot initialized at 8 different locations in the obstacle-free workspace. The safety distance is set to $0.15m$ and the parameter $\gamma = 0.15m$. The gains κ_s and κ_r, used in (5.5a), are set to 0.5. The sensing radius R_s, used in (5.30), is set to $1m$. The parameter ϵ, used in (4.22), is set to $0.05m$. Similar to the previous simulations, it can be observed from Fig. 5.7 that the robot converges asymptotically to the target location without colliding with the obstacles. Since the obstacles are spheres, the distance between the robot and target location monotonically decreases as the robot converges to the target location, as stated in Theorem 5.2 and as shown in Fig. 5.7(right).

5.8 Conclusions

In this chapter, we proposed a hybrid feedback controller for safe autonomous robot navigation in three-dimensional environments with arbitrarily-shaped convex obstacles. These obstacles may have nonsmooth boundaries, large sizes, and can be placed arbitrarily, provided they meet certain mild disjointedness requirements, as per Assumption 5.1. The proposed hybrid controller guarantees global asymptotic stability of the target location in the obstacle-free workspace. The obstacle-avoidance component of the control law relies on the projection of the robot's center onto the nearest obstacle, enabling applications in *a priori* unknown environments, as discussed in Section 5.6. In general, the proposed hybrid feedback control law generates non-smooth trajectories when switching between modes. Incorporating a smoothing mechanism in our proposed hybrid feedback

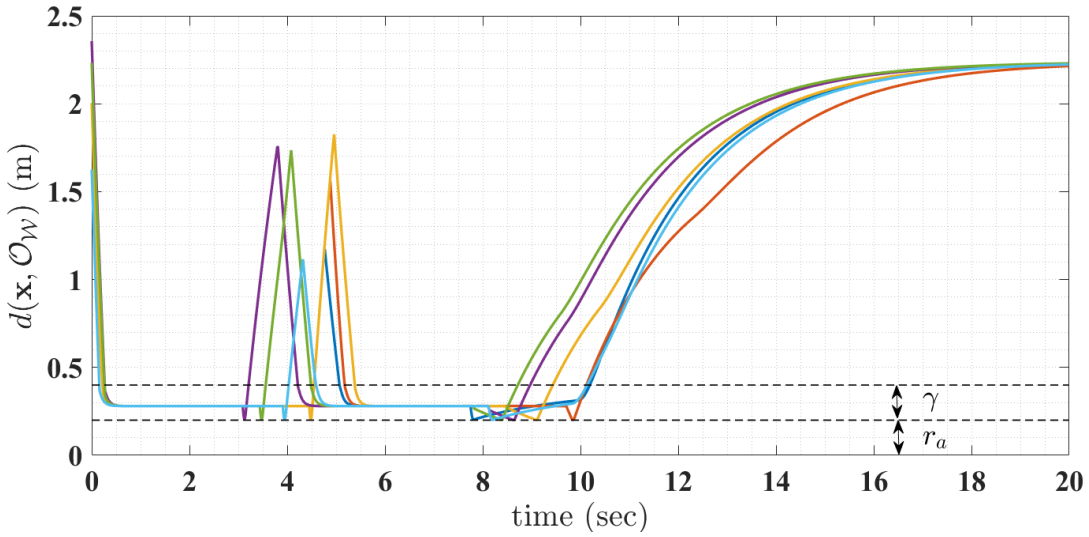

Figure 5.5: Distance of the center of the robot $\mathbf{x}$ from the boundary of the obstacle occupied workspace $\mathcal{O}_\mathcal{W}$.

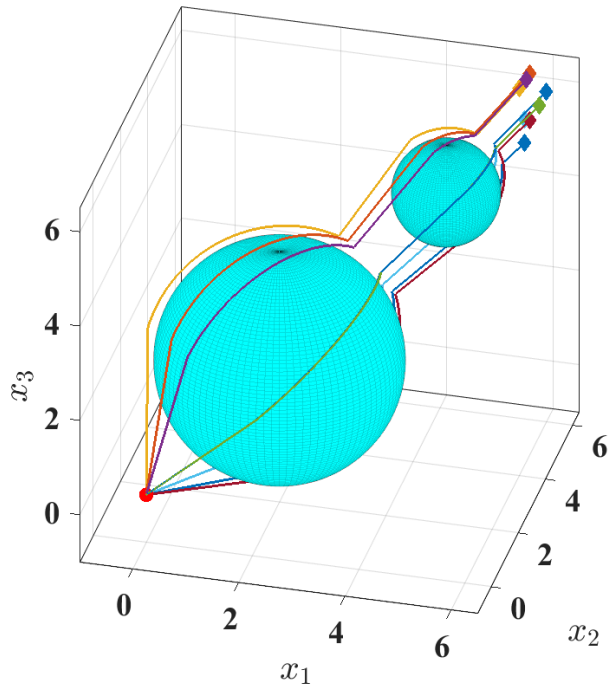

Figure 5.6: Robot trajectories safely navigating around spherical obstacles and converging to the target location at the origin.

would be an interesting practical extension.

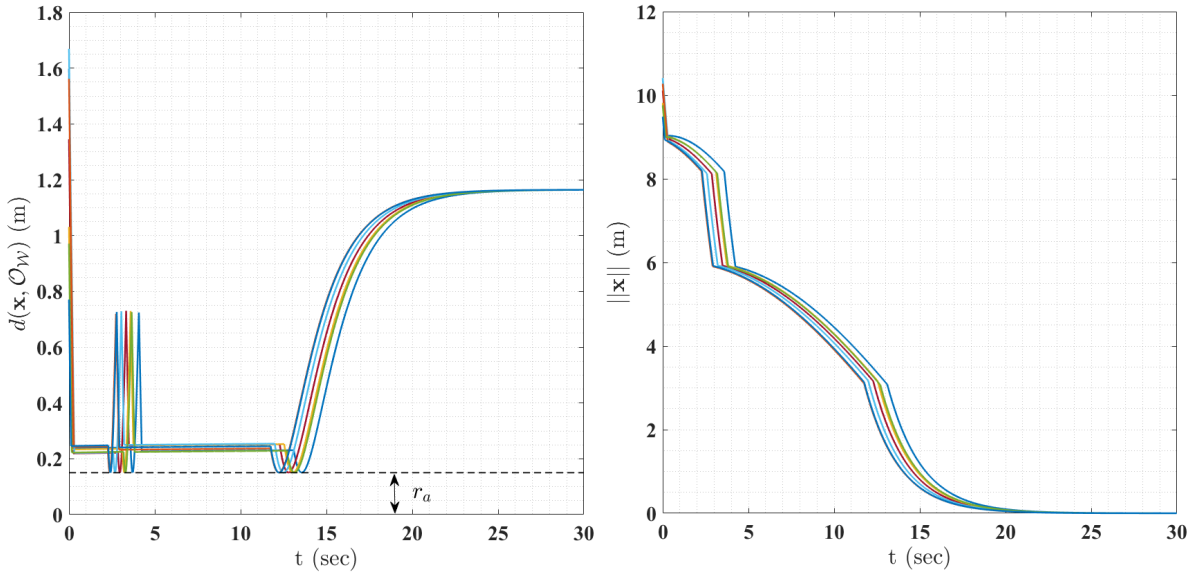

Figure 5.7: The left figure shows the change in the distance between the robot $\mathbf{x}$ and the boundary of the obstacle-occupied workspace $\mathcal{O}_{\mathcal{W}}$. The right figure shows monotonic decrease of the distance between the robot $\mathbf{x}$ and the target location at the origin.

Chapter 6

Conclusions

6.1 Summary

In this thesis, we utilized hybrid feedback control techniques to design autonomous robot navigation algorithms in obstacle-cluttered environments. In Chapter 3, we considered planar environments with arbitrarily-shaped convex obstacles. Unlike [Paternain et al., 2017], [Arslan and Koditschek, 2019] and [Berkane et al., 2021a], the obstacles are allowed to have non-smooth boundaries. The proposed autonomous navigation approach relies on an appropriately designed switching mechanism between the *move-to-target* mode and the *obstacle-avoidance* mode, resulting in safe navigation and global asymptotic stability of the target location. Additionally, it is shown that when the robot is initialized away from the obstacles boundaries, the proposed navigation approach generates continuous control inputs. A procedure for the implementation of the proposed hybrid feedback controller in *a priori* unknown environments is provided.

Chapter 4 deals with the problem of autonomous robot navigation in planar environments with arbitrarily-shaped obstacles, including non-convex obstacles. An instrumental obstacle reshaping operator, which guarantees the uniqueness of the closest point on the modified obstacles from the robot's center when it is near the modified obstacles, is proposed to facilitate the obstacle-avoidance mechanism design. Similar to Chapter 3, the proposed hybrid navigation approach relies on an appropriately designed switching mechanism between the *move-to-target* mode and the *obstacle-avoidance* mode. When initialized in the *move-to-target* mode, the proposed control scheme guarantees safe global convergence to the target location in the modified workspace. It is shown that the effect of the obstacle reshaping operator can be replicated with a virtual ring rolling along the obstacles' boundaries. A sensor-based implementation of the proposed navigation scheme in *a priori* unknown environments has been discussed in Section 4.6.

Chapter 5 is dedicated to the design of a hybrid feedback controller for safe autonomous robot navigation in three-dimensional environments with arbitrarily-shaped convex obstacles. When the robot is away from the obstacles, the control input operates in the *move-to-target* mode, steering the robot towards the target location. When the robot gets close to an obstacle and has no clear line-of-sight to the target location, the control switches to *obstacle-avoidance* mode, steering the robot along the hyperplane,

passing through the center of the robot and the target location, without moving far away from the obstacle. The proposed navigation scheme guarantees global asymptotic stability of the target location and forward invariance of the obstacle-free workspace. A procedure for the implementation of the proposed autonomous navigation controller, in *a priori* unknown three-dimensional environments, is also provided.

6.2 Perspective

The proposed solutions in this work constitute a good platform for several future extensions. The hybrid feedback controllers proposed in this dissertation are applicable to robots modeled as first order integrator with velocity input. However, the motion of mechanical systems is actually governed by second order dynamics with torque/force inputs. In [Arslan and Koditschek, 2017], the authors proposed a reference governor based approach to extend the single integrator based navigation controllers to second order dynamics, assuming that the robot is not very close to the obstacles boundaries. In [Verginis and Dimarogonas, 2021], the authors proposed an adaptive navigation function-based control design for robots with uncertain second order dynamics navigating in sphere worlds. Since the navigation function is allowed to grow unbounded near the obstacles boundaries, the control input in this region can grow unbounded. Moreover, this work has several restrictions in terms of the initial and final locations of the robots.
The development of autonomous navigation control strategies, endowed with safety and global asymptotic stability guarantees, for second order dynamical systems navigating in environments containing arbitrarily-shaped obstacles is a challenging open problem worth investigating.

Extending our developed framework to multi-robot autonomous navigation with collision and obstacle avoidance is an interesting future work. Most of the existing strategies for multi-robot navigation rely on the navigation function-based approach and they are applicable in obstacle-free environments, *e.g.,* [Dimarogonas et al., 2006], [Tanner and Boddu, 2012]. In [Roussos and Kyriakopoulos, 2013], the authors proposed an almost global priority-based multi-robot navigation approach in environments with circular obstacles. In [Verginis and Dimarogonas, 2021], with certain restrictions on the initial and final locations of the robots in environments with stationary spherical obstacles, the authors provided a leader-follower based approach for almost global convergence of the robots to their predefined target locations. To the best of the author's knowledge, the development of a globally convergent collision-free autonomous navigation algorithm for multi-robot systems, even in a known environment consisting of obstacles with complex geometries, is still an open problem.

Bibliography

Arslan, O. and Koditschek, D. E. (2016). Exact robot navigation using power diagrams. In *2016 IEEE International Conference on Robotics and Automation (ICRA)*, pp. 1–8. IEEE.

Arslan, O. and Koditschek, D. E. (2017). Smooth extensions of feedback motion planners via reference governors. In *2017 IEEE International Conference on Robotics and Automation (ICRA)*, pp. 4414–4421. IEEE.

Arslan, O. and Koditschek, D. E. (2019). Sensor-based reactive navigation in unknown convex sphere worlds. *The International Journal of Robotics Research*, 38(2-3):196–223.

Arslan, O., Pacelli, V., and Koditschek, D. E. (2017). Sensory steering for sampling-based motion planning. In *2017 IEEE/RSJ International Conference on Intelligent Robots and Systems (IROS)*, pp. 3708–3715. IEEE.

Aubin, J.-P., Bayen, A. M., and Saint-Pierre, P. (2011). *Viability theory: new directions*. Springer Science & Business Media.

Berkane, S. (2021). Navigation in unknown environments using safety velocity cones. In *2021 American Control Conference (ACC)*, pp. 2336–2341. IEEE.

Berkane, S., Bisoffi, A., and Dimarogonas, D. V. (2019). A hybrid controller for obstacle avoidance in an n-dimensional euclidean space. In *2019 18th European Control Conference (ECC)*, pp. 764–769. IEEE.

Berkane, S., Bisoffi, A., and Dimarogonas, D. V. (2021a). Obstacle avoidance via hybrid feedback. *IEEE Transactions on Automatic Control*, 67(1):512–519.

Berkane, S., Bisoffi, A., and Dimarogonas, D. V. (2021b). Obstacle avoidance via hybrid feedback. *arXiv preprint arXiv:2102.02883*.

Blanchini, F., Miani, S., et al. (2008). *Set-theoretic methods in control*, volume 78. Springer.

Boissonnat, J.-D. and Yvinec, M. (1998). *Algorithmic geometry*. Cambridge university press.

Boor, V., Overmars, M. H., and Van Der Stappen, A. F. (1999). The gaussian sampling strategy for probabilistic roadmap planners. In *Proceedings 1999 IEEE International Conference on Robotics and Automation (Cat. No. 99CH36288C)*, volume 2, pp. 1018–1023. IEEE.

Boyd, S., Boyd, S. P., and Vandenberghe, L. (2004). *Convex optimization*. Cambridge university press.

Braun, P., Kellett, C. M., and Zaccarian, L. (2018). Unsafe point avoidance in linear state feedback. In *2018 IEEE Conference on Decision and Control (CDC)*, pp. 2372–2377. IEEE.

Braun, P., Kellett, C. M., and Zaccarian, L. (2020). Explicit construction of stabilizing robust avoidance controllers for linear systems with drift. *IEEE Transactions on Automatic Control*, 66(2):595–610.

Brooks, R. A. and Lozano-Perez, T. (1985). A subdivision algorithm in configuration space for findpath with rotation. *IEEE Transactions on Systems, Man, and Cybernetics*, (2):224–233.

Casau, P., Cunha, R., Sanfelice, R. G., and Silvestre, C. (2019). Hybrid control for robust and global tracking on smooth manifolds. *IEEE Transactions on Automatic Control*, 65(5):1870–1885.

Chen, C., Li, C., and Tanner, H. G. (2020). Navigation functions with non-point destinations and moving obstacles. In *2020 American Control Conference (ACC)*, pp. 2532–2537. IEEE.

Choset, H., Lynch, K. M., Hutchinson, S., Kantor, G. A., and Burgard, W. (2005). *Principles of robot motion: theory, algorithms, and implementations*. MIT press.

Dimarogonas, D. V., Loizou, S. G., Kyriakopoulos, K. J., and Zavlanos, M. M. (2006). A feedback stabilization and collision avoidance scheme for multiple independent non-point agents. *Automatica*, 42(2):229–243.

Filippidis, I. and Kyriakopoulos, K. J. (2011). Adjustable navigation functions for unknown sphere worlds. In *2011 50th IEEE Conference on Decision and Control and European Control Conference*, pp. 4276–4281. IEEE.

Filippidis, I. and Kyriakopoulos, K. J. (2013). Navigation functions for focally admissible surfaces. In *2013 American Control Conference*, pp. 994–999. IEEE.

Filippidis, I. F. and Kyriakopoulos, K. J. (2012). Navigation functions for everywhere partially sufficiently curved worlds. In *2012 IEEE International Conference on Robotics and Automation*, pp. 2115–2120. IEEE.

Goebel, R., Sanfelice, R. G., and Teel, A. R. (2012). *Hybrid dynamical systems*. Princeton University Press.

Haralick, R. M., Sternberg, S. R., and Zhuang, X. (1987). Image analysis using mathematical morphology. *IEEE transactions on pattern analysis and machine intelligence*, (4):532–550.

Jain, N., Gupta, A. K., and Mathur, P. (2021). Autonomous drone using ros for surveillance and 3d mapping using satellite map. In *Proceedings of the Second International Conference on Information Management and Machine Intelligence: ICIMMI 2020*, pp. 255–266. Springer.

Kamon, I., Rimon, E., and Rivlin, E. (1998). Tangentbug: A range-sensor-based navigation algorithm. *The International Journal of Robotics Research*, 17(9):934–953.

Karaman, S. and Frazzoli, E. (2011). Sampling-based algorithms for optimal motion planning. *The international journal of robotics research*, 30(7):846–894.

Kavraki, L. E., Svestka, P., Latombe, J.-C., and Overmars, M. H. (1996). Probabilistic roadmaps for path planning in high-dimensional configuration spaces. *IEEE transactions on Robotics and Automation*, 12(4):566–580.

Khatib, O. (1986). Real-time obstacle avoidance for manipulators and mobile robots. In *Autonomous robot vehicles*, pp. 396–404. Springer.

Kim, J.-O. and Khosla, P. (1992). Real-time obstacle avoidance using harmonic potential functions.

Koditschek, D. and Rimon, E. (1992). Exact robot navigation using artificial potential functions. *IEEE Trans. Robot. Automat*, 8:501–518.

Koditschek, D. E. and Rimon, E. (1990). Robot navigation functions on manifolds with boundary. *Advances in applied mathematics*, 11(4):412–442.

Kumar, H., Paternain, S., and Ribeiro, A. (2022). Navigation of a quadratic potential with ellipsoidal obstacles. *Automatica*, 146:110643.

LaValle, S. (1998). Rapidly-exploring random trees: A new tool for path planning. *Research Report 9811*.

LaValle, S. M. (2006). *Planning algorithms*. Cambridge university press.

LaValle, S. M. and Kuffner Jr, J. J. (2001). Randomized kinodynamic planning. *The international journal of robotics research*, 20(5):378–400.

Leonard, J. J. and Bahr, A. (2016). Autonomous underwater vehicle navigation. *Springer handbook of ocean engineering*, pp. 341–358.

Li, C. and Tanner, H. G. (2018). Navigation functions with time-varying destination manifolds in star worlds. *IEEE Transactions on Robotics*, 35(1):35–48.

Lionis, G., Papageorgiou, X., and Kyriakopoulos, K. J. (2007). Locally computable navigation functions for sphere worlds. In *Proceedings 2007 IEEE International Conference on Robotics and Automation*, pp. 1998–2003. IEEE.

Loizou, S. G. (2011a). Closed form navigation functions based on harmonic potentials. In *2011 50th IEEE Conference on Decision and Control and European Control Conference*, pp. 6361–6366. IEEE.

Loizou, S. G. (2011b). The navigation transformation: Point worlds, time abstractions and towards tuning-free navigation. In *2011 19th Mediterranean Conference on Control & Automation (MED)*, pp. 303–308. IEEE.

Loizou, S. G. (2017). The navigation transformation. *IEEE Transactions on Robotics*, 33(6):1516–1523.

Loizou, S. G. and Rimon, E. D. (2021). Correct-by-construction navigation functions with application to sensor based robot navigation. *arXiv preprint arXiv:2103.04445*.

Loizou, S. G., Tanner, H. G., Kumar, V., and Kyriakopoulos, K. J. (2003). Closed loop motion planning and control for mobile robots in uncertain environments. In *IEEE 42nd Conference on Decision and Control*, volume 3, pp. 2926–2931. IEEE.

Lozano-Perez, T. (1987). A simple motion-planning algorithm for general robot manipulators. *IEEE Journal on Robotics and Automation*, 3(3):224–238.

Lozano-Perez, T. (1990). *Spatial planning: A configuration space approach*. Springer.

Lozano-Pérez, T. and Wesley, M. A. (1979). An algorithm for planning collision-free paths among polyhedral obstacles. *Communications of the ACM*, 22(10):560–570.

Lumelsky, V. and Stepanov, A. (1986). Dynamic path planning for a mobile automaton with limited information on the environment. *IEEE transactions on Automatic control*, 31(11):1058–1063.

Matveev, A. S., Teimoori, H., and Savkin, A. V. (2011). A method for guidance and control of an autonomous vehicle in problems of border patrolling and obstacle avoidance. *Automatica*, 47(3):515–524.

Mehndiratta, M., Kayacan, E., and Kayacan, E. (2018). A simple learning strategy for feedback linearization control of aerial package delivery robot. In *2018 IEEE conference on control technology and applications (CCTA)*, pp. 361–367. IEEE.

Nagumo, M. (1942). Über die lage der integralkurven gewöhnlicher differentialgleichungen. *Proceedings of the Physico-Mathematical Society of Japan. 3rd Series*, 24:551–559.

Ng, J. and Bräunl, T. (2007). Performance comparison of bug navigation algorithms. *Journal of Intelligent and Robotic Systems*, 50(1):73–84.

Paternain, S., Koditschek, D. E., and Ribeiro, A. (2017). Navigation functions for convex potentials in a space with convex obstacles. *IEEE Transactions on Automatic Control*, 63(9):2944–2959.

Poczter, S. L., Jankovic, L. M., et al. (2014). The google car: driving toward a better future? *Journal of Business Case Studies (JBCS)*, 10(1):7–14.

Poveda, J. I., Benosman, M., Teel, A. R., and Sanfelice, R. G. (2018). A hybrid adaptive feedback law for robust obstacle avoidance and coordination in multiple vehicle systems. In *2018 Annual American Control Conference (ACC)*, pp. 616–621. IEEE.

Rataj, J. and Zähle, M. (2019). *Curvature measures of singular sets*. Springer.

Reis, M. F., Aguiar, A. P., and Tabuada, P. (2020). Control barrier function-based quadratic programs introduce undesirable asymptotically stable equilibria. *IEEE Control Systems Letters*, 5(2):731–736.

Rockafellar, R. T. (1997). *Convex analysis*, volume 11. Princeton university press.

Roussos, G. and Kyriakopoulos, K. J. (2013). Decentralized and prioritized navigation and collision avoidance for multiple mobile robots. In *Distributed Autonomous Robotic Systems: The 10th International Symposium*, pp. 189–202. Springer.

Sanfelice, R. G. (2021). *Hybrid feedback control*. Princeton University Press.

Sanfelice, R. G., Messina, M. J., Tuna, S. E., and Teel, A. R. (2006). Robust hybrid controllers for continuous-time systems with applications to obstacle avoidance and regulation to disconnected set of points. In *2006 American Control Conference*, pp. 6–pp. IEEE.

Sanfelice, R. G. and Teel, A. R. (2010). Dynamical properties of hybrid systems simulators. *Automatica*, 46(2):239–248.

Sawant, M., Berkane, S., Polusin, I., and Tayebi, A. (2022a). Hybrid feedback for autonomous navigation in environments with arbitrary convex obstacles. *arXiv preprint arXiv:2111.09380*.

Sawant, M., Berkane, S., Polusin, I., and Tayebi, A. (2023a). Hybrid feedback for autonomous navigation in planar environments with convex obstacles. *IEEE Transaction on Automatic Control*, 68(12):7342–7357.

Sawant, M., Polushin, I., and Tayebi, A. (2024). Hybrid feedback for three-dimensional convex obstacle avoidance. *arXiv:2403.11279*.

Sawant, M., Tayebi, A., and Polushin, I. (2022b). Autonomous navigation in environments with arbitrary non-convex obstacles. In *2022 IEEE 61st Conference on Decision and Control (CDC)*, pp. 7208–7213.

Sawant, M., Tayebi, A., and Polushin, I. (2023b). Hybrid feedback control design for non-convex obstacle avoidance. *arXiv preprint arXiv:2304.10598*.

Serra, J. (1986). Introduction to mathematical morphology. *Computer vision, graphics, and image processing*, 35(3):283–305.

Sun, J. and Tanner, H. G. (2015). Constrained decision-making for low-count radiation detection by mobile sensors. *Autonomous Robots*, 39:519–536.

Tanioka, T., Osaka, K., Locsin, R., Yasuhara, Y., and Ito, H. (2017). Recommended design and direction of development for humanoid nursing robots perspective from nursing researchers. *Intelligent Control and Automation*, 8(2):96–110.

Tanner, H. G. and Boddu, A. (2012). Multiagent navigation functions revisited. *IEEE Transactions on Robotics*, 28(6):1346–1359.

Thäle, C. (2008). 50 years sets with positive reach–a survey. *Surveys in Mathematics and its Applications*, 3:123–165.

Vasilopoulos, V. and Koditschek, D. E. (2018). Reactive navigation in partially known non-convex environments. In *International Workshop on the Algorithmic Foundations of Robotics*, pp. 406–421. Springer.

Verginis, C. K. and Dimarogonas, D. V. (2021). Adaptive robot navigation with collision avoidance subject to 2nd-order uncertain dynamics. *Automatica*, 123:109303.

Vrohidis, C., Vlantis, P., Bechlioulis, C. P., and Kyriakopoulos, K. J. (2018). Prescribed time scale robot navigation. *IEEE Robotics and Automation Letters*, 3(2):1191–1198.

Willard, S. (2012). *General topology*. Courier Corporation.

Yeh, H.-Y., Thomas, S., Eppstein, D., and Amato, N. M. (2012). Uobprm: A uniformly distributed obstacle-based prm. In *2012 IEEE/RSJ International Conference on Intelligent Robots and Systems*, pp. 2655–2662. IEEE.

Appendix A

Proofs of Chapter 2

A.1 Proof of Lemma 2.1

We consider a closed convex set $\mathcal{A} \subset \mathbb{R}^n$ and $\mathbf{q} \in \mathbb{R}^n \backslash \mathcal{A}$. According to [Boyd et al., 2004, Section 8.1] the projection of $\mathbf{q}$ on the closed convex set $\mathcal{D}_r(\mathcal{A})$, $r \in [0, d(\mathbf{q}, \mathcal{A})]$, [Rockafellar, 1997, Theorem 3.1] in the sense of the Euclidean norm *i.e.*, $\Pi(\mathbf{q}, \mathcal{D}_r(\mathcal{A}))$ is unique. Since $\mathcal{B}_{d(\mathbf{q}, \mathcal{D}_r(\mathcal{A}))}(\mathbf{q})$ just touches the set $\mathcal{D}_r(\mathcal{A})$ at $\Pi(\mathbf{q}, \mathcal{D}_r(\mathcal{A}))$, the vector $\mathbf{q} - \Pi(\mathbf{q}, \mathcal{D}_r(\mathcal{A}))$ is normal to the set $\mathcal{D}_r(\mathcal{A})$ at $\Pi(\mathbf{q}, \mathcal{D}_r(\mathcal{A}))$. Hence, according to [Boyd et al., 2004, Section 2.5.2], the hyperplane $\mathcal{P}(\Pi(\mathbf{q}, \mathcal{D}_r(\mathcal{A})), \mathbf{q} - \Pi(\mathbf{q}, \mathcal{D}_r(\mathcal{A})))$ is a supporting hyperplane to the set $\mathcal{D}_r(\mathcal{A})$ at $\Pi(\mathbf{q}, \mathcal{D}_r(\mathcal{A}))$.

If we show that the points $\mathbf{q}, \Pi(\mathbf{q}, \mathcal{A})$ and $\Pi(\mathbf{q}, \mathcal{D}_r(\mathcal{A})), r \in (0, d(\mathbf{q}, \mathcal{A}))$, are collinear, then the proof is complete. We next consider $\mathcal{B}_r(\Pi(\mathbf{q}, \mathcal{A}))$ with $r \in [0, d(\mathbf{q}, \mathcal{A})]$. Let $\mathbf{p}$ be the projection of $\mathbf{q}$ on the set $\mathcal{B}_r(\Pi(\mathbf{q}, \mathcal{A}))$ *i.e.*, $\mathbf{p} = \Pi(\mathbf{q}, \mathcal{B}_r(\Pi(\mathbf{q}, \mathcal{A})))$. It is straightforward to notice that $\mathbf{p} \in \mathcal{L}_s(\mathbf{q}, \Pi(\mathbf{q}, \mathcal{A}))$. Hence $\mathbf{p} \in \partial\mathcal{D}_r(\mathcal{A})$, where the set $\mathcal{D}_r(\mathcal{A})$ is convex according to [Rockafellar, 1997, Theorem 3.1]. Moreover, $\mathbf{p} = \Pi(\mathbf{q}, \mathcal{D}_r(\mathcal{A}))$, otherwise $\exists \mathbf{p}_1 \in \big(\mathcal{L}_s(\mathbf{p}, \Pi(\mathbf{q}, \mathcal{D}_r(\mathcal{A})))\big)^\circ \subset \mathcal{D}_r(\mathcal{A})$ such that $\mathbf{p}_1 \in \big(\mathcal{B}_{\|\mathbf{q} - \Pi(\mathbf{q}, \mathcal{D}_r(\mathcal{A}))\|}(\mathbf{q})\big)^\circ$ which is a contradiction. Hence, the points $\mathbf{q}, \Pi(\mathbf{q}, \mathcal{D}_r(\mathcal{A}))$ with $r \in (0, d(\mathbf{q}, \mathcal{A}))$, and $\Pi(\mathbf{q}, \mathcal{A})$ are collinear.

A.2 Proof of Lemma 2.2

This proof is by contradiction. Let us assume that there exists $\mathbf{x} \in \mathbb{R}^n \setminus \mathcal{A}$ such that $d(\mathbf{x}, \mathcal{A}) = \beta$, where $\beta \in (0, \alpha)$. We further assume that $d(\mathbf{x}, \mathcal{G}) = \eta$ and the set $\mathcal{PJ}(\mathbf{x}, \mathcal{G})$ is not a singleton, where the closed set $\mathcal{G} = (\mathcal{A} \oplus \mathcal{B}^\circ_\alpha(\mathbf{0}))^c$.

Since we have $\mathbf{reach}(\mathcal{A}) \geq \alpha$, the set $\mathcal{PJ}(\mathbf{x}, \mathcal{A})$ is a singleton. As a result, according to [Rataj and Zähle, 2019, Lemma 4.5], it follows that $\frac{\mathbf{x} - \Pi(\mathbf{x}, \mathcal{A})}{\|\mathbf{x} - \Pi(\mathbf{x}, \mathcal{A})\|} \in \mathbf{N}_{\mathcal{A}}(\Pi(\mathbf{x}, \mathcal{A}))$, where $\mathbf{N}_{\mathcal{A}}(\Pi(\mathbf{x}, \mathcal{A}))$ denotes the normal cone to the set $\mathcal{A}$ at the point $\Pi(\mathbf{x}, \mathcal{A})$. Furthermore, according to [Rataj and Zähle, 2019, Lemma 4.5], for $\mathbf{q} = \Pi(\mathbf{x}, \mathcal{A}) + \alpha \frac{\mathbf{x} - \Pi(\mathbf{x}, \mathcal{A})}{\|\mathbf{x} - \Pi(\mathbf{x}, \mathcal{A})\|}$, the open Euclidean ball $\mathcal{B}^\circ_\alpha(\mathbf{q})$ does not intersect with the set $\mathcal{A}$ *i.e.*, $\mathcal{B}^\circ_\alpha(\mathbf{q}) \cap \mathcal{A} = \emptyset$. Hence, as the set $\partial\mathcal{G}$ contains all points in $\mathbb{R}^n$ that are exactly at α distance away from the set $\mathcal{A}$, one can conclude that $\mathbf{q} \in \partial\mathcal{G} \cap \mathcal{L}(\mathbf{x}, \Pi(\mathbf{x}, \mathcal{A}))$. Now, we consider two cases depending on the location of the point $\mathbf{q}$ on the line $\mathcal{L}(\mathbf{x}, \Pi(\mathbf{x}, \mathcal{A}))$ as follows:

Case 1: when $d(\mathbf{q}, \Pi(\mathbf{x}, \mathcal{A})) = \alpha \geq \beta + \eta$. Since $\alpha \geq \beta + \eta$, one has $\mathcal{B}_\eta(\mathbf{x}) \subset \mathcal{B}_\alpha(\Pi(\mathbf{x}, \mathcal{A})) \subset \mathcal{D}_\alpha(\mathcal{A})$. Additionally, as $\mathbf{card}(\mathcal{PJ}(\mathbf{x}, \partial\mathcal{G})) > 1$, there exist $\mathbf{p}_1 \in \mathcal{G}$ and $\mathbf{p}_2 \in \mathcal{G}$ such that $\{\mathbf{p}_1, \mathbf{p}_2\} \subset \partial\mathcal{B}_\eta(\mathbf{x}) \cap \partial\mathcal{G}$. Hence, there should be at least two points of contact between the sets $\partial\mathcal{B}_\eta(\mathbf{x})$ and $\partial\mathcal{B}_\alpha(\Pi(\mathbf{x}, \mathcal{A}))$. Since $\alpha \geq \beta + \eta$, the Euclidean ball $\mathcal{B}_\eta(\mathbf{x})$ can only touch the boundary of the Euclidean ball $\mathcal{B}_\alpha(\Pi(\mathbf{x}, \mathcal{A}))$ at no more that one point, resulting in a contradiction.

Case 2: when $d(\mathbf{q}, \Pi(\mathbf{x}, \mathcal{A})) = \alpha \in (\beta, \beta + \eta)$. Since $\mathbf{q} \in \partial\mathcal{G} \cap \mathcal{L}(\mathbf{x}, \Pi(\mathbf{x}, \mathcal{A}))$ and $\alpha \in (\beta, \beta+\eta)$, one has $\mathbf{q} \in \mathcal{B}^\circ_\eta(\mathbf{x})$. This implies that $d(\mathbf{x}, \mathcal{G}) < \eta$, which is a contradiction.

A.3 proof of Lemma 2.3

The cases where $\beta = 0$ and $\beta = \alpha$ are trivial. We analyze the case where $\beta \in (0, \alpha)$. This proof is by contradiction. Let us assume that there exists $\mathbf{x}$ such that $d(\mathbf{x}, \mathcal{A}) = \eta$, where $\eta \in (\beta, \alpha)$, and the set $\mathcal{PJ}(\mathbf{x}, \mathcal{D}_\beta(\mathcal{A}))$ is not a singleton. Therefore, there exist at least two distinct points $\mathbf{p}_1$ and $\mathbf{p}_2$ such that $\mathbf{p}_1, \mathbf{p}_2 \subset \partial\mathcal{D}_\beta(\mathcal{A}) \cap \mathcal{PJ}(\mathbf{x}, \mathcal{D}_\beta(\mathcal{A}))$.

Since $\mathbf{reach}(\mathcal{A}) \geq \alpha$, the points $\mathbf{p}_1$ and $\mathbf{p}_2$, which belong to the set $\partial\mathcal{D}_\beta(\mathcal{A})$, have unique projection on the set $\mathcal{A}$ and $d(\mathbf{p}_1, \Pi(\mathbf{p}_1, \mathcal{A})) = d(\mathbf{p}_2, \Pi(\mathbf{p}_2, \mathcal{A})) = \beta$. Moreover, as $\mathbf{x} \in \partial\mathcal{D}_\eta(\mathcal{A})$, one has $d(\mathbf{x}, \mathbf{p}_1) = d(\mathbf{x}, \mathbf{p}_2) = \eta - \beta$, and $d(\mathbf{x}, \mathcal{A}) = \eta$. Therefore, one has $d(\mathbf{x}, \Pi(\mathbf{p}_1, \mathcal{A})) = d(\mathbf{x}, \Pi(\mathbf{p}_2, \mathcal{A})) = \eta$. As a result, $\Pi(\mathbf{p}_1, \mathcal{A})$ and $\Pi(\mathbf{p}_2, \mathcal{A})$ belong to the set $\mathcal{PJ}(\mathbf{x}, \mathcal{A})$. Since $\eta \in (0, \alpha)$ and $\mathbf{reach}(\mathcal{A}) \geq \alpha$, it is clear that $\mathbf{card}(\mathcal{PJ}(\mathbf{x}, \mathcal{A})) = 1$. Hence, $\Pi(\mathbf{p}_1, \mathcal{A}) = \Pi(\mathbf{p}_2, \mathcal{A}) = \Pi(\mathbf{x}, \mathcal{A})$. This, by the application of triangular inequality, implies that $\mathbf{p}_1 = \mathbf{p}_2$, which is a contradiction.

Appendix B

Proofs of Chapter 3

B.1 Proof of Lemma 3.1

The flow set $\mathcal{F}$ and the jump set $\mathcal{J}$, defined in (3.21), (3.26), are closed subsets of $\mathbb{R}^2\times\mathbb{M}\times\mathbb{I}$. The flow map $\mathbf{F}$, given in (3.28), is continuous on $\mathcal{F}_0\times\{0\}\times\mathbb{I}$. In (3.28), due to the structure of the scalar function $\sigma(\xi)$ in (3.6)-(3.8), the rotational vector $\mathbf{v}(\xi)$, defined in (3.5), is active only within the γ_s-neighbourhood of any obstacle, which according to Assumption 3.1, is valid for at most one obstacle at a time, namely $\mathcal{O}_k$, $k\in\mathbb{I}$. Also, as $\mathcal{O}_k$ is convex, the projection of $\mathbf{x}$ on $\mathcal{O}_k$ *i.e.*, $\Pi(\mathbf{x},\mathcal{O}_k)$ is continuous with respect to $\mathbf{x}$. As a result, $\mathbf{F}$ is continuous on $\mathcal{F}_m\times\{m\}\times\mathbb{I}$, $m\in\{-1,1\}$. Hence $\mathbf{F}$ is continuous on $\mathcal{F}$. The jump map $\mathbf{J}$, defined in (3.28), is single-valued on $\mathcal{J}_m\times\{m\}\times\mathbb{I}$, $m\in\{-1,1\}$. Also, $\mathbf{J}$ has a closed graph relative to $\mathcal{J}_0\times\{0\}\times\mathbb{I}$ as $\mathbf{M}$, defined in (3.23), is allowed to be set-valued whenever $\mathbf{x}\in\mathcal{P}(\mathbf{0},\mathbf{s})$. Hence, according to [Goebel et al., 2012, Lemma 5.10], $\mathbf{J}$ is outer semi-continuous and locally bounded relative to $\mathcal{J}$.

B.2 Proof of Lemma 3.2

First, we prove that the union of the flow and jump sets covers exactly the obstacle-free state space $\mathcal{K}$. Inspired by [Berkane et al., 2021b, Appendix 11], for all $i\in\mathbb{I}$ and $m\in\{-1,1\}$, the satisfaction of the following equation:

$$\mathcal{F}_0\cup\mathcal{J}_0=\mathcal{F}_m^i\cup\mathcal{J}_m^i=\mathcal{W}_{r_a}, \tag{B.1}$$

along with (3.21) and (3.26) implies $\mathcal{F}\cup\mathcal{J}=\mathcal{W}_{r_a}\times\mathbb{M}\times\mathbb{I}=:\mathcal{K}$. Next we prove (B.1). It is clear that

$$\begin{aligned}\mathcal{F}_0\cup\mathcal{J}_0 &\overset{(3.16)}{=}\left(\bigcap_{i\in\mathbb{I}}\mathcal{F}_0^i\right)\cup\left(\bigcup_{i\in\mathbb{I}}\mathcal{J}_0^i\right)=\bigcap_{i\in\mathbb{I}}\left[\left(\mathcal{F}_0^i\cup\mathcal{J}_0^i\right)\cup\left(\bigcup_{i'\in\mathbb{I},i'\neq i}\left(\mathcal{F}_0^i\cup\mathcal{J}_0^{i'}\right)\right)\right]\\ &\overset{(3.14),(3.15)}{=}\bigcap_{i\in\mathbb{I}}\left(\mathcal{W}_{r_a}\cup\mathcal{F}_0^i\right)\overset{(3.15)}{=}\bigcap_{i\in\mathbb{I}}\mathcal{W}_{r_a}=\mathcal{W}_{r_a}.\end{aligned}$$

Similarly, for each $i\in\mathbb{I}$ and $m\in\{-1,1\}$, according to (3.17), (3.19), by construction $\mathcal{F}_m^i\cup\mathcal{J}_m^i=\mathcal{W}_{r_a}$.

Now, inspired by [Berkane et al., 2021b, Appendix 1], for the hybrid closed-loop system (3.28), with data $\mathcal{H} = (\mathcal{F}, \mathbf{F}, \mathcal{J}, \mathbf{J})$, define $\mathbf{S}_{\mathcal{H}}(\mathcal{K})$ as the set of all maximal solutions ξ to $\mathcal{H}$ with $\xi(0,0) \in \mathcal{K}$. Since $\mathcal{F} \cup \mathcal{J} = \mathcal{K}$, each $\xi \in \mathbf{S}_{\mathcal{H}}(\mathcal{K})$ has range rge $\xi \subset \mathcal{K}$. Additionally, if every maximal solution $\xi \in \mathbf{S}_{\mathcal{H}}(\mathcal{K})$ is complete, then the set $\mathcal{K}$ will be forward invariant [Sanfelice, 2021, Definition 3.13]. Since the hybrid closed-loop system (3.28) satisfies hybrid basic conditions, as stated in Lemma 3.1, one can use [Goebel et al., 2012, Proposition 6.10], to verify the following viability condition:

$$\mathbf{F}(\mathbf{x}, m, k) \cap \mathbf{T}_{\mathcal{F}}(\mathbf{x}, m, k) \neq \emptyset, \forall (\mathbf{x}, m, k) \in \mathcal{F} \backslash \mathcal{J}, \tag{B.2}$$

which will allow us to establish the completeness of the solution ξ to the hybrid closed-loop system (3.28). In (B.2), $\mathbf{T}_{\mathcal{F}}(\mathbf{x}, m, k)$ represents the tangent cone[1] to the set $\mathcal{F}$ at $(\mathbf{x}, m, k)$. Let $(\mathbf{x}, m, k) \in \mathcal{F} \backslash \mathcal{J}$, which implies by (3.21) that $(\mathbf{x}, k) \in (\mathcal{F}_m \backslash \mathcal{J}_m) \times \mathbb{I}$ for some $m \in \mathbb{M}$. We consider two cases corresponding to $m = 0$ and $m \in \{-1, 1\}$.

When $m = 0$, according to (3.16), there exists $k \in \mathbb{I}$ such that $\xi \in \mathcal{F}_0 \backslash \mathcal{J}_0 \times \{0\} \times \{k\}$. For $\mathbf{x} \in (\mathcal{F}_0)^\circ \backslash \mathcal{J}_0$, $\mathbf{T}_{\mathcal{F}}(\xi) = \mathbb{R}^2 \times \{0\} \times \{0\}$, and (B.2) holds. According to (3.14), (3.15) and (3.16), one has

$$\partial \mathcal{F}_0 \backslash \mathcal{J}_0 \in \bigcup_{k \in \mathbb{I}} \left(\partial \mathcal{D}_{r_a}(\mathcal{O}_k) \cap \mathcal{R}_b^k \right),$$

and for every $k \in \mathbb{I}$, according to Lemma 2.1, $\mathcal{P}(\Pi(\mathbf{x}, \mathcal{D}_{r_a}(\mathcal{O}_k)), \mathbf{x} - \Pi(\mathbf{x}, \mathcal{O}_k))$ is a supporting hyperplane to $\mathcal{D}_{r_a}(\mathcal{O}_k)$ at $\Pi(\mathbf{x}, \mathcal{D}_{r_a}(\mathcal{O}_k))$, hence $\forall \mathbf{x} \in \partial \mathcal{F}_0 \backslash \mathcal{J}_0$

$$\mathbf{T}_{\mathcal{F}}(\mathbf{x}, 0, k) = \mathcal{P}_{\geq}(\mathbf{0}, (\mathbf{x} - \Pi(\mathbf{x}, \mathcal{O}_k)) \times \{0\} \times \{0\}.$$

Also, for $m = 0$, $\mathbf{u}(\mathbf{x}, 0, k) = -\kappa \mathbf{x}$, $\kappa > 0$, (3.4a). Hence, according to (3.9), for $\mathbf{x} \in \partial \mathcal{D}_{r_a}(\mathcal{O}_k) \cap \mathcal{R}_b^k$, $\mathbf{u}^\intercal(\mathbf{x} - \Pi(\mathbf{x}, \mathcal{O}_k)) \geq 0$, hence $\mathbf{u}(\mathbf{x}, 0, k) \in \mathcal{P}_{\geq}(\mathbf{0}, (\mathbf{x} - \Pi(\mathbf{x}, \mathcal{O}_k))$, and (B.2) holds for $m = 0$.

When $m \in \{-1, 1\}$, according to (3.20), there exists $k \in \mathbb{I}$ such that $\mathbf{x} \in \mathcal{F}_m^k \backslash \mathcal{J}_m^k$. For $\mathbf{x} \in (\mathcal{F}_m^k)^\circ \backslash \mathcal{J}_m^k$, $\mathbf{T}_{\mathcal{F}_m}(\mathbf{x}) = \mathbb{R}^2$, so that $\mathbf{T}_{\mathcal{F}}(\xi) = \mathbb{R}^2 \times \{0\} \times \{0\}$, and (B.2) holds. According to (3.17), (3.19) and (3.20), one has

$$\partial \mathcal{F}_m^k \backslash \mathcal{J}_m^k \in \partial \mathcal{D}_{r_a}(\mathcal{O}_k),$$

and according to Lemma 2.1, $\mathcal{P}(\Pi(\mathbf{x}, \mathcal{D}_{r_a}(\mathcal{O}_k)), \mathbf{x} - \Pi(\mathbf{x}, \mathcal{O}_k))$ is a supporting hyperplane to $\mathcal{D}_{r_a}(\mathcal{O}_k)$ at $\Pi(\mathbf{x}, \mathcal{D}_{r_a}(\mathcal{O}_k))$, hence $\forall \mathbf{x} \in \partial \mathcal{F}_m^k \backslash \mathcal{J}_m^k$

$$\mathbf{T}_{\mathcal{F}}(\mathbf{x}, m, k) = \mathcal{P}_{\geq}(\mathbf{0}, (\mathbf{x} - \Pi(\mathbf{x}, \mathcal{O}_k)) \times \{0\} \times \{0\},$$

and according to (3.4a), $\mathbf{u}(\mathbf{x}, m, k) = \kappa \mathbf{v}(\mathbf{x}, m, k), \kappa > 0$. Since $\Pi(\mathbf{x}, \mathcal{O}_{\mathcal{W}})$ equals $\Pi(\mathbf{x}, \mathcal{O}_k)$, $\mathbf{v}(\mathbf{x}, k, m)^\intercal(\mathbf{x} - \Pi(\mathbf{x}, \mathcal{O}_k)) = 0$, and the condition in (B.2) holds true for $m = \{-1, 1\}$.

Hence, according to [Goebel et al., 2012, Proposition 6.10], since (B.2) holds for all $\xi \in \mathcal{F} \backslash \mathcal{J}$, there exists a nontrivial solution to $\mathcal{H}$ for each initial condition in $\mathcal{K}$. Finite escape time can only occur through flow. They can neither occur for $\mathbf{x}$ in the set $\mathcal{F}_{-1}^k \cup \mathcal{F}_1^k$, $k \in \mathbb{I}$, as these sets are bounded by definition (3.17)-(3.20), nor for $\mathbf{x}$ in the set $\mathcal{F}_0$ as

[1] The tangent cone to a set $\mathcal{K} \subset \mathbb{R}^n$ at a point $x \in \mathbb{R}^n$, denoted $\mathbf{T}_{\mathcal{K}}(x)$, is defined as in [Goebel et al., 2012, Def. 5.12 and Fig. 5.4].

this would make $\mathbf{x}^\intercal\mathbf{x}$ grow unbounded, and would contradict the fact that $\frac{d}{dt}(\mathbf{x}^\intercal\mathbf{x}) \leq 0$ in view of the definition of $\mathbf{u}(\mathbf{x}, 0, k)$. Therefore, all maximal solutions do not have finite escape times. Furthermore, according to (3.28), $\mathbf{x}^+ = \mathbf{x}$, and from the definition of the update laws in (3.22), (3.27), it follows immediately that $\mathbf{J}(\mathcal{J}) \subset \mathcal{K}$. Hence, solutions to the hybrid closed-loop system (3.28) cannot leave $\mathcal{K}$ through jump and, as per [Goebel et al., 2012, Proposition 6.10], all maximal solutions are complete.

B.3 Proof of Lemma 3.3

Let $\xi := (\mathbf{x}, m, k)$ be the solution to the hybrid closed-loop system (3.28). Notice that for the robot operating in the *move-to-target* mode ($m = 0$), if $\mathbf{x}(t_0, j_0) \notin \mathcal{L}_{>}(\mathbf{0}, \nu_{-1}(\mathbf{s}))$ at some $(t_0, j_0) \in$ dom ξ, then $\mathbf{x}(t, j) \notin \mathcal{L}_{>}(\mathbf{0}, \nu_{-1}(\mathbf{s})), \forall (t, j) \succeq (t_0, j_0)$, as long as it does not encounter any obstacle in the way, since $\mathcal{L}(\mathbf{0}, \mathbf{x}(t_0, j_0)) \cap \mathcal{L}_{>}(\mathbf{0}, \nu_{-1}(\mathbf{s})) = \emptyset$, where $\nu_z(\mathbf{p}) := \begin{bmatrix} 0 & z \\ -z & 0 \end{bmatrix} \mathbf{p}$, with $\mathbf{p} \in \mathbb{R}^2$ and $z \in \{-1, 1\}$. Hence, we investigate the case where the solution ξ evolves in the *obstacle-avoidance* mode ($m \in \{-1, 1\}$).

Lemma B.1 *Under Assumption 3.1, each maximal solution* $\mathbf{x}$ *to the flow-only system*

$$\dot{\mathbf{x}} = \mathbf{u}(\mathbf{x}, m, k), \ \mathbf{x} \in \mathcal{F}_m^k, \tag{B.3}$$

with $m \in \{-1, 1\}$ *and* $k \in \mathbb{I}$, *has* $T = sup_t$ *dom* $\mathbf{x} < +\infty$ *and* $\mathbf{x}(T) \in \mathcal{G}_m^k$.

Proof See Appendix B.4.

Lemma B.1 indicates that the solution $\mathbf{x}(t)$ to the flow-only system (B.3), evolving in the *obstacle-avoidance* flow set $\mathcal{F}_m^k$ related to some obstacle $\mathcal{O}_k, k \in \mathbb{I}$ with some $m \in \{-1, 1\}$, will enter in the gate region $\mathcal{G}_m^k$ in finite time. As $\mathcal{G}_m^k \times \{m\} \times \{k\} \subset \mathcal{J}_m \times \{-1, 1\} \times \mathbb{I}$, according to Lemma B.1, the solution ξ evolving in the *obstacle-avoidance* mode with some mode indicator $m \in \{-1, 1\}$, with respect to some obstacle $\mathcal{O}_k$, $k \in \mathbb{I}$, will ultimately enter in the *move-to-target* mode. Next, we introduce several notations to denote the instances where the solution ξ enters and leaves the *obstacle-avoidance* mode with respect to some obstacle $\mathcal{O}_k$, $k \in \mathbb{I}$.

Let $(t_{\mathcal{F}}^k, j_{\mathcal{F}}^k) \in$ dom ξ such that $\xi_{\mathcal{F}}^k = \xi(t_{\mathcal{F}}^k, j_{\mathcal{F}}^k) = (\mathbf{x}_{\mathcal{F}}^k, m, k) \in \mathcal{F}_m^k \times \{-1, 1\} \times \{k\}$ be the state at the instant when a solution ξ to the hybrid closed-loop system (3.28), earlier flowing in the *move-to-target* mode, enters in the flow set of the *obstacle-avoidance* mode related to obstacle $\mathcal{O}_k, k \in \mathbb{I}$, for some $m \in \{-1, 1\}$. Similarly, let $(t_{\mathcal{J}}^k, j_{\mathcal{J}}^k) \in$ dom ξ such that $\xi_{\mathcal{J}}^k = \xi(t_{\mathcal{J}}^k, j_{\mathcal{J}}^k) = (\mathbf{x}_{\mathcal{J}}^k, m, k) \in \mathcal{J}_m^k \times \{-1, 1\} \times \{k\}$ be the state at the instant when the solution ξ, earlier flowing in the *obstacle-avoidance* mode with respect to the obstacle $\mathcal{O}_k$, enters the jump set of the *obstacle-avoidance* mode associated with the respective obstacle.

We partition the obstacle-free state space $\mathcal{K}$ (3.25) into three subsets, based on the location of the vector $\mathbf{s} \in \mathbb{R}^2 \backslash \{\mathbf{0}\}$ used in the update law (3.23), as follows:

$$\mathcal{K} = \tilde{\mathcal{K}}_1(\mathbb{M}) \cup \tilde{\mathcal{K}}_{-1}(\mathbb{M}) \cup \tilde{\mathcal{K}}_0(\mathbb{M}), \tag{B.4}$$

where

$$\tilde{\mathcal{K}}_1(\{z\}) = (\mathcal{P}_>(\mathbf{0}, \mathbf{s}) \cap \mathcal{W}_{r_a}) \times \{z\} \times \mathbb{I},$$
$$\tilde{\mathcal{K}}_{-1}(\{z\}) = (\mathcal{P}_<(\mathbf{0}, \mathbf{s}) \cap \mathcal{W}_{r_a}) \times \{z\} \times \mathbb{I},$$
$$\tilde{\mathcal{K}}_0(\{z\}) = (\mathcal{P}(\mathbf{0}, \mathbf{s}) \cap \mathcal{W}_{r_a}) \times \{z\} \times \mathbb{I},$$

furthermore, let

$$\tilde{\mathcal{K}}_>(\{z\}) = \mathcal{L}_>(\mathbf{0}, \nu_1(\mathbf{s})) \times \{z\} \times \mathbb{I},$$
$$\tilde{\mathcal{K}}_<(\{z\}) = \mathcal{L}_>(\mathbf{0}, \nu_{-1}(\mathbf{s})) \times \{z\} \times \mathbb{I},$$

where $\{z\} \subseteq \mathbb{M}$, such that $\tilde{\mathcal{K}}_0(\mathbb{M}) = \mathcal{A} \cup \tilde{\mathcal{K}}_>(\mathbb{M}) \cup \tilde{\mathcal{K}}_<(\mathbb{M})$. Now, we proceed with the proof.

Given $\xi(t_0, j_0) \in \mathcal{W}_{r_a} \backslash \mathcal{L}_>(\mathbf{0}, \nu_{-1}(\mathbf{s})) \times \{0\} \times \mathbb{I}$, we further assume $\xi(t_0, j_0) \in \tilde{\mathcal{K}}_{m^*}(\{0\})$ for some $m^* \in \{-1, 1\}$ and that $\exists (t^k_{\mathcal{F}}, j^k_{\mathcal{F}} - 1) \succeq (t_0, j_0)$ such that $\xi(t^k_{\mathcal{F}}, j^k_{\mathcal{F}} - 1) \in \mathcal{J}_0 \times \{0\} \times \mathbb{I},\ k \in \mathbb{I}$. According to (3.22) and (3.23), $\xi(t^k_{\mathcal{F}}, j^k_{\mathcal{F}}) \in \mathcal{F}^k_{m^*} \times \{m^*\} \times \{k\}$. Then according to Lemma B.1, $\exists (t^k_{\mathcal{J}}, j^k_{\mathcal{J}}) \succ (t^k_{\mathcal{F}}, j^k_{\mathcal{F}})$ such that $\xi(t^k_{\mathcal{J}}, j^k_{\mathcal{J}} + 1) \in \mathcal{F}_0 \times \{0\} \times \mathbb{I}$. Now, in order to prove our claim, we show that

$$\mathbf{u}(\mathbf{x}(t, j), m^*, k) \in \mathcal{P}_{\geq}(\mathbf{0}, \nu_{m^*}(\mathbf{x}(t, j))), \tag{B.5}$$

for all $(t, j) \in ([t^k_{\mathcal{F}}, t^k_{\mathcal{J}}] \times [j^k_{\mathcal{F}}, j^k_{\mathcal{J}}])$. Since $\xi(t_0, j_0) \in \tilde{\mathcal{K}}_{m^*}(\{0\})$, one has $\mathcal{L}_>(\mathbf{0}, \nu_{-1}(\mathbf{s})) \cap \mathcal{P}_{\geq}(\mathbf{0}, \nu_{m^*}(\mathbf{x}^k_{\mathcal{F}})) = \emptyset$. The satisfaction of (B.5) ensures that the component $\mathbf{x}$ of the solution ξ always evolves towards the positive half-space generated by the hyperplane $\mathcal{P}(\mathbf{0}, \nu_{m^*}(\mathbf{x}(t, j)))$, as shown in Fig. B.1, such that

$$\xi(t, j) \notin \tilde{\mathcal{K}}_<(\mathbb{M}), \forall (t, j) \in ([t^k_{\mathcal{F}}, t^k_{\mathcal{J}}] \times [j^k_{\mathcal{F}}, j^k_{\mathcal{J}}]).$$

To that end, we analyze the behaviour of the solution $\xi(t, j)$, $\forall (t, j) \in ([t^k_{\mathcal{F}}, t^k_{\mathcal{J}}] \times [j^k_{\mathcal{F}}, j^k_{\mathcal{J}}])$. For $(t, j) \in ([t^k_{\mathcal{F}}, t^k_{\mathcal{J}}] \times [j^k_{\mathcal{F}}, j^k_{\mathcal{J}}])$, consider the flow-only system (B.3) for $\mathbf{x} \in \mathcal{F}^k_{m^*}$. According to (3.4a), the control input vector for the robot operating in the *obstacle-avoidance* mode is given by

$$\mathbf{u}(\mathbf{x}, m^*, k) = -\kappa\sigma(\xi)\mathbf{x} + \kappa[1 - \sigma(\xi)]\mathbf{v}(\mathbf{x}, m^*, k), \tag{B.6}$$

where $\kappa > 0$. Since $\mathbf{x}^\intercal \nu_{m^*}(\mathbf{x}) = 0$, $-\kappa\sigma(\xi)\mathbf{x} \in \mathcal{P}_{\geq}(\mathbf{0}, \nu_{m^*}(\mathbf{x}))$. Next, we consider the rotational vector $\kappa[1 - \sigma(\xi)]\mathbf{v}(\mathbf{x}, m^*, k), \kappa[1 - \sigma(\xi)] \geq 0$ such that

$$\begin{aligned} \mathbf{v}(\xi)^\intercal \nu_{m^*}(\mathbf{x}) &= \frac{\|\mathbf{x}\| \nu_{m^*}(\mathbf{x} - \Pi(\mathbf{x}, \mathcal{O}_k))^\intercal \nu_{m^*}(\mathbf{x})}{\|\mathbf{x} - \Pi(\mathbf{x}, \mathcal{O}_k)\|}, \\ &= \frac{\|\mathbf{x}\| (\mathbf{x} - \Pi(\mathbf{x}, \mathcal{O}_k))^\intercal \mathbf{x}}{\|\mathbf{x} - \Pi(\mathbf{x}, \mathcal{O}_k)\|}. \end{aligned} \tag{B.7}$$

According to Lemma B.1, the solution $\mathbf{x}$ will evolve within the set $\mathcal{F}^k_{m^*}$ for all $(t, j) \in ([t^k_{\mathcal{F}}, t^k_{\mathcal{J}}] \times [j^k_{\mathcal{F}}, j^k_{\mathcal{J}}])$, and at $(t^k_{\mathcal{J}}, j^k_{\mathcal{J}})$ will enter in the gate region $\mathcal{G}^k_{m^*}$. Hence, as per Remark 3.1 and (3.10), for all $(t, j) \in ([t^k_{\mathcal{F}}, t^k_{\mathcal{J}}] \times [j^k_{\mathcal{F}}, j^k_{\mathcal{J}}])$, one has

$$\mathbf{v}(\xi)^\intercal \nu_{m^*}(\mathbf{x}) = \frac{\|\mathbf{x}\| (\mathbf{x} - \Pi(\mathbf{x}, \mathcal{O}_k))^\intercal \mathbf{x}}{\|\mathbf{x} - \Pi(\mathbf{x}, \mathcal{O}_k)\|} \geq 0,$$

i.e., the vector $\kappa[1 - \sigma(\xi)]\mathbf{v}(\xi)$ in (B.6) belongs to the positive half-space $\mathcal{P}_{\geq}(\mathbf{0}, \nu_{m^*}(\mathbf{x}))$, and (B.5) is satisfied.

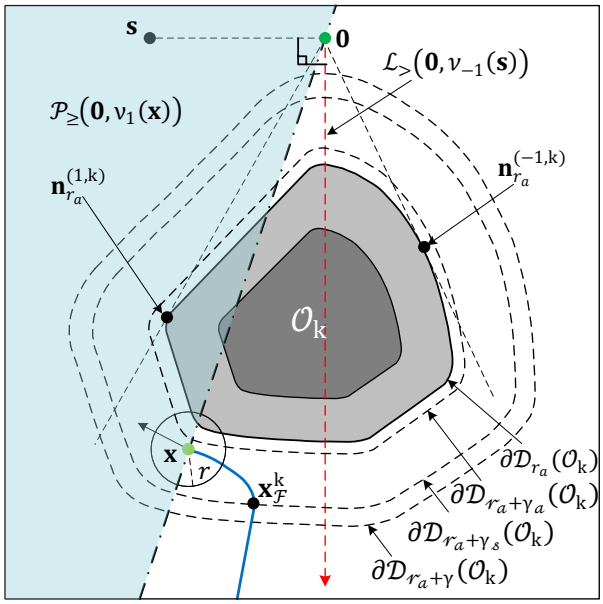

Figure B.1: Illustration of a robot trajectory (blue curve) not intersecting the half-line $\mathcal{L}_{>}(\mathbf{0}, \nu_{-1}(\mathbf{s}))$ (red line) while operating in the *obstacle-avoidance* mode in the flow set $\mathcal{F}_1^k \times \{1\} \times \{k\}$. The velocity vector at the current location of the robot (green dot) always points to the positive half-space $\mathcal{P}_{\geq}(\mathbf{0}, \nu_1(\mathbf{x}))$ (shaded blue region).

B.4 Proof of Lemma B.1

We consider the flow-only system (B.3) for the robot operating in the *obstacle-avoidance* mode with respect to some obstacle $\mathcal{O}_k, k \in \mathbb{I}$ *i.e.*, $\mathbf{x} \in \mathcal{F}_m^k$ and $m \in \{-1, 1\}$. We partition the set $\partial\mathcal{F}_m^k$ into several subsets, as shown in Fig. B.2, based on the similarity between the tangent cones to the set $\mathcal{F}_m^k$ at these regions, as follows:

$$\begin{aligned}
\partial\mathcal{F}_m^k &= \mathcal{S}_1 \cup \mathcal{S}_2 \cup \mathcal{S}_3 \cup \mathcal{S}_4 \cup \mathcal{G}_m^k, \\
\mathcal{S}_1 &= \left(\partial\mathcal{D}_{r_a+\gamma}(\mathcal{O}_k) \cap \mathcal{F}_m^k\right) \setminus \mathcal{G}_m^k, \\
\mathcal{S}_2 &= \mathcal{L}\left(\mathbf{0}, \mathbf{n}_{r_a+\gamma_a}^{(-m,k)}\right) \cap \mathcal{F}_m^k, \\
\mathcal{S}_3 &= \mathcal{G}_{-m}^k \cap \mathcal{F}_m^k, \\
\mathcal{S}_4 &= \partial\mathcal{D}_{r_a}(\mathcal{O}_k) \cap \mathcal{F}_m^k.
\end{aligned} \tag{B.8}$$

We proceed to prove the claims in two parts.

1. We show that if the solution $\mathbf{x}$ to the flow-only system (B.3) leaves the set $\mathcal{F}_m^k$, it cannot leave via the boundary $\partial\mathcal{F}_m^k \setminus \mathcal{G}_m^k$ *i.e.*, it can only leave the set $\mathcal{F}_m^k$ via $\mathcal{G}_m^k$. To that end, for all $\mathbf{x} \in \partial\mathcal{F}_m^k \setminus \mathcal{G}_m^k$, according to Nagumo's theorem [Aubin et al., 2011, Theorem 11.2.3], we verify the following condition:

$$\mathbf{u}(\mathbf{x}, m, k) \in \mathbf{T}_{\mathcal{F}_m^k}(\mathbf{x}) \tag{B.9}$$

where $\mathbf{T}_{\mathcal{F}_m^k}(\mathbf{x})$ is the tangent cone to the set $\mathcal{F}_m^k$ at $\mathbf{x}$.

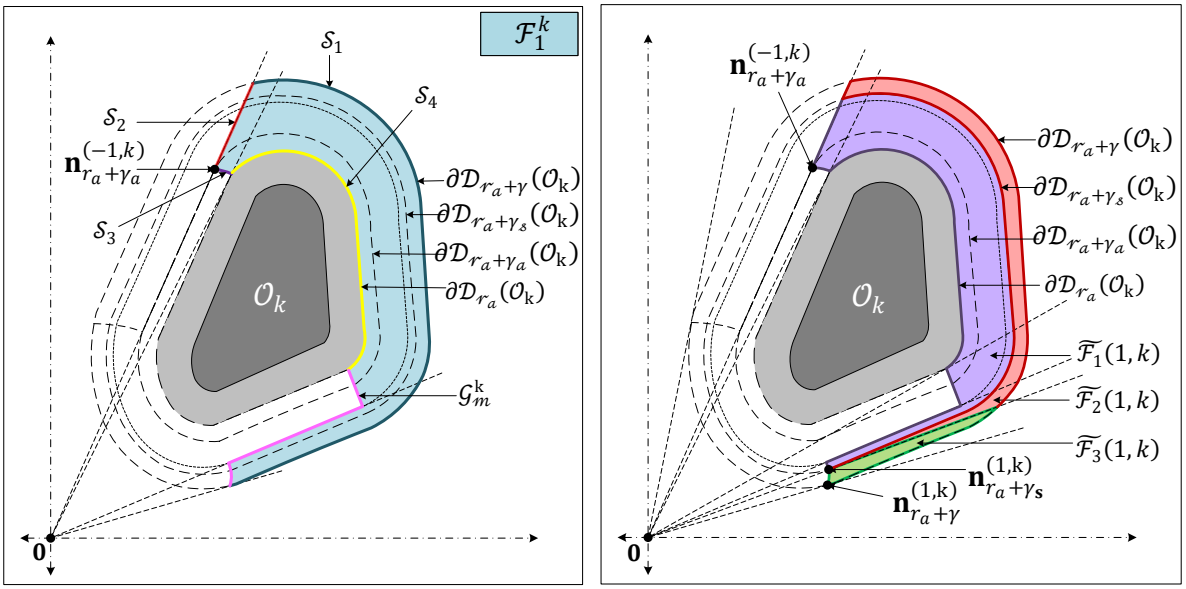

Figure B.2: The geometric representation of the *obstacle-avoidance* mode flow set $\mathcal{F}_1^k$ related to an obstacle $\mathcal{O}_k, k \in \mathbb{I}$. The left figure shows the partitions of the set $\partial\mathcal{F}_1^k$. The right figure depicts the partitions of the set $\mathcal{F}_1^k$.

2. We show that the solution $\mathbf{x}$ to the flow-only system (B.3), flowing in the set $\mathcal{F}_m^k$, away from the region $\mathcal{G}_m^k$, will always enter in the set $\mathcal{G}_m^k$ in finite time. We show that, if $\mathbf{x}(t_0) \in \mathcal{F}_m^k \backslash \mathcal{G}_m^k$ for some $t_0 \geq 0$, then $\exists T = \sup_t \text{dom } \mathbf{x} < +\infty$, $T > t_0$, such that $\mathbf{x}(T) \in \mathcal{G}_m^k$.

For $\mathbf{x} \in (\mathcal{S}_1)^\bullet$, according to Lemma 2.1, the vector $(\mathbf{x} - \Pi(\mathbf{x}, \mathcal{O}_k))$ is normal to the convex set $\mathcal{D}_{r_a+\gamma}(\mathcal{O}_k)$ at $\mathbf{x}$. Hence, the tangent cone to the set $\mathcal{F}_m^k$ at $\mathbf{x} \in (\mathcal{S}_1)^\bullet$ is given as

$$\mathbf{T}_{\mathcal{F}_m^k}(\mathbf{x}) = \mathcal{P}_{\leq}(\mathbf{0}, \mathbf{x} - \Pi(\mathbf{x}, \mathcal{O}_k)).$$

Also, for $\mathbf{x} \in (\mathcal{S}_1)^\bullet$, $\mathbf{u}(\xi) = -\kappa\mathbf{x}$, $\kappa > 0$. Since $(\mathcal{S}_1)^\bullet \notin \mathcal{R}_b^k$, according to Remark 3.1, $-\kappa\mathbf{x}^\intercal(\mathbf{x} - \Pi(\mathbf{x}, \mathcal{O}_k)) \leq 0$. Hence, one has

$$\forall \mathbf{x} \in (\mathcal{S}_1)^\bullet, \mathbf{u}(\mathbf{x}, m, k) \in \mathbf{T}_{\mathcal{F}_m^k}(\mathbf{x}). \tag{B.10}$$

For $\mathbf{x} \in (\mathcal{S}_2 \backslash \mathcal{S}_3)^\bullet$, the tangent cone to the set $\mathcal{F}_m^k$ at $\mathbf{x}$ is given by

$$\mathbf{T}_{\mathcal{F}_m^k}(\mathbf{x}) = \mathcal{P}_{\geq}(\mathbf{0}, \nu_m(\mathbf{n}_{r_a+\gamma_a}^{(-m,k)})),$$

and $\mathbf{u}(\xi) = -\kappa\sigma(\xi)\mathbf{x} + \kappa[1 - \sigma(\xi)]\mathbf{v}(\xi), \kappa > 0$. For $\mathbf{x} \in (\mathcal{S}_2 \backslash \mathcal{S}_3)^\bullet$, $\mathbf{x}^\intercal \nu_m(\mathbf{n}_{r_a+\gamma_a}^{(-m,k)}) = 0$, hence $-\kappa\sigma(\xi)\mathbf{x} \in \mathcal{P}_{\geq}\big(\mathbf{0}, \nu_m(\mathbf{n}_{r_a+\gamma_a}^{(-m,k)})\big)$. We know that $\kappa[1 - \sigma(\xi)] \geq 0$, and

$$\begin{aligned}\mathbf{v}(\xi)^\intercal \nu_m(\mathbf{n}_{r_a+\gamma_a}^{(-m,k)}) &= \frac{\|\mathbf{x}\|\nu_m(\mathbf{x} - \Pi(\mathbf{x}, \mathcal{O}_k))^\intercal \nu_m\big(\mathbf{n}_{r_a+\gamma_a}^{(-m,k)}\big)}{\|\mathbf{x} - \Pi(\mathbf{x}, \mathcal{O}_k)\|}, \\ &= \frac{\|\mathbf{x}\|(\mathbf{x} - \Pi(\mathbf{x}, \mathcal{O}_k))^\intercal \mathbf{n}_{r_a+\gamma_a}^{(-m,k)}}{\|\mathbf{x} - \Pi(\mathbf{x}, \mathcal{O}_k)\|}.\end{aligned}$$

Since for $\mathbf{x} \in (\mathcal{S}_2 \backslash \mathcal{S}_3)^\bullet$, the vectors $\mathbf{n}_{r_a+\gamma_a}^{(-m,k)}$ and $\mathbf{x}$ point in the same direction and $(\mathcal{S}_2 \backslash \mathcal{S}_3)^\bullet \notin \mathcal{R}_b^k$, according to Remark 3.1, $\mathbf{x}^\intercal(\mathbf{x} - \Pi(\mathbf{x}, \mathcal{O}_k)) \geq 0$. Hence, for $\mathbf{x} \in (\mathcal{S}_2 \backslash \mathcal{S}_3)^\bullet$, $\kappa[1 - \sigma(\xi)]\mathbf{v}(\xi) \in \mathcal{P}_{\geq}\big(\mathbf{0}, \nu_m(\mathbf{n}_{r_a+\gamma_a}^{(-m,k)})\big)$, and

$$\forall \mathbf{x} \in (\mathcal{S}_2 \backslash \mathcal{S}_3)^\bullet, \mathbf{u}(\mathbf{x}, m, k) \in \mathbf{T}_{\mathcal{F}_m^k}(\mathbf{x}). \tag{B.11}$$

For $\mathbf{x} \in (\mathcal{S}_4)^\bullet$, the tangent cone to the set $\mathcal{F}_m^k$ at $\mathbf{x}$ is given by

$$\mathbf{T}_{\mathcal{F}_m^k}(\mathbf{x}) = \mathcal{P}_{\geq}(\mathbf{0}, \mathbf{x} - \Pi(\mathbf{x}, \mathcal{O}_k)),$$

and $\mathbf{u}(\xi) = \kappa \mathbf{v}(\xi)$. Since $\mathbf{v}(\xi)^\intercal(\mathbf{x} - \Pi(\mathbf{x}, \mathcal{O}_k)) = 0$, one has

$$\forall \mathbf{x} \in (\mathcal{S}_4)^\bullet, \mathbf{u}(\mathbf{x}, m, k) \in \mathbf{T}_{\mathcal{F}_m^k}(\mathbf{x}). \tag{B.12}$$

For $\mathbf{x} \in \mathcal{S}_1 \cap \mathcal{S}_2$, the tangent cone to the set $\mathcal{F}_m^k$ at $\mathbf{x}$ is given as

$$\mathbf{T}_{\mathcal{F}_m^k}(\mathbf{x}) = \mathcal{P}_{\leq}(\mathbf{0}, \mathbf{x} - \Pi(\mathbf{x}, \mathcal{O}_k)) \cap \mathcal{P}_{\geq}(\mathbf{0}, \nu_m(\mathbf{n}_{r_a+\gamma_a}^{(-m,k)})),$$

and $\mathbf{u}(\xi) = -\kappa \mathbf{x},\ \kappa > 0$. Since $\mathcal{S}_1 \cap \mathcal{S}_2 \notin \mathcal{R}_b^k$ and the fact that the vectors $\mathbf{n}_{r_a+\gamma_a}^{(-m,k)}$ and $-\kappa \mathbf{x}$ are collinear, ensures that

$$\forall \mathbf{x} \in \mathcal{S}_1 \cap \mathcal{S}_2, \mathbf{u}(\mathbf{x}, m, k) \in \mathbf{T}_{\mathcal{F}_m^k}(\mathbf{x}). \tag{B.13}$$

Next, to show that the vector $\mathbf{u}(\mathbf{x}, m, k)$ evaluated at $\mathbf{x} \in \mathcal{S}_3$, for some $k \in \mathbb{I}$ and $m \in \{-1, 1\}$, does not point outside the set $\mathcal{F}_m^k$, we require the following lemma.

Lemma B.2 *Consider the following flow-only system:*

$$\dot{\mathbf{x}} = \mathbf{v}(\mathbf{x}, m, k),\ \mathbf{x} \in \mathcal{D}_{r_a+\gamma_a}(\mathcal{O}_k) \backslash (\mathcal{D}_{r_a}(\mathcal{O}_k))^\circ, \tag{B.14}$$

for some $k \in \mathbb{I}$ and $m \in \{-1, 1\}$. Let $d(\mathbf{x}(t_0), \mathcal{D}_{r_a}(\mathcal{O}_k)) = \beta \in [0, \gamma_a]$ for some $t_0 \geq 0$, then $\mathbf{x}(t) \in \partial\mathcal{D}_{r_a+\beta}(\mathcal{O}_k)$ for all $t \geq t_0$.

Proof According to Lemma 2.1, for $\mathbf{x} \in \partial\mathcal{D}_{r_a+\beta}(\mathcal{O}_k)$, $\mathcal{P}(\mathbf{x}, (\mathbf{x} - \Pi(\mathbf{x}, \mathcal{O}_k)))$ is a supporting hyperplane to the set $\mathcal{D}_{r_a+\beta}(\mathcal{O}_k)$ at $\mathbf{x}$. Hence, the tangent cone to the set $\partial\mathcal{D}_{r_a+\beta}(\mathcal{O}_k)$ at $\mathbf{x} \in \partial\mathcal{D}_{r_a+\beta}(\mathcal{O}_k)$ is given as $\mathbf{T}_{\partial\mathcal{D}_{r_a+\beta}(\mathcal{O}_k)}(\mathbf{x}) = \mathcal{P}(\mathbf{0}, (\mathbf{x} - \Pi(\mathbf{x}, \mathcal{O}_k)))$. Since $\mathbf{v}(\mathbf{x}, m, k)^\intercal(\mathbf{x} - \Pi(\mathbf{x}, \mathcal{O}_k)) = 0$, one has $\mathbf{v}(\mathbf{x}(t), m, k) \in \mathbf{T}_{\partial\mathcal{D}_{r_a+\beta}(\mathcal{O}_k)}(\mathbf{x}(t))$, for all $t \geq t_0$, which implies that the solution $\mathbf{x}(t)$ to the flow-only system (B.14) belongs to the set $\partial\mathcal{D}_{r_a+\beta}(\mathcal{O}_k)$ for all $t \geq t_0$.

According to Lemma B.2, the solution $\mathbf{x}(t)$ to the flow-only system (B.14), which belongs to the obstacle-free workspace within the $(r_a+\gamma_a)-$neighbourhood of an obstacle $\mathcal{O}_k, k \in \mathbb{I}$, at some time $t_0 \geq 0$, will revolve around the obstacle $\mathcal{O}_k$ in the direction decided by the parameter $m \in \{-1, 1\}$, while maintaining the same proximity $d(\mathbf{x}(t), \mathcal{O}_k)$ for all $t \geq t_0$.

Now, for $\mathbf{x} \in \mathcal{S}_3$, according to (3.4), $\mathbf{u}(\mathbf{x}, m, k) = \kappa \mathbf{v}(\mathbf{x}, m, k)$. Since the set $\mathcal{S}_3 \subset \mathcal{D}_{r_a+\gamma_a}(\mathcal{O}_k) \backslash (\mathcal{D}_{r_a}(\mathcal{O}_k))^\circ$, according to Lemma B.2, for $\mathbf{x} \in \mathcal{S}_3$, the vector $\mathbf{u}(\mathbf{x}, m, k)$ points in the direction which is tangential to the curve $\partial\mathcal{D}_{d(\mathbf{x}, \mathcal{O}_k)}(\mathcal{O}_k)$ at $\mathbf{x}$. Also, for

$\mathbf{x} \in \mathcal{S}_2 \cap \mathcal{S}_3$, according to Lemma 2.1, and (3.9), the tangent to the set $\partial\mathcal{D}_{d(\mathbf{x},\mathcal{O}_k)}(\mathcal{O}_k)$ lies along the line $\mathcal{L}(\mathbf{0}, \mathbf{n}^{(-m,k)}_{r_a+\gamma_a})$. Moreover, as $\mathcal{S}_3 \subset \mathcal{G}^k_{-m}$, $\mathbf{v}(\mathbf{x}, m, k)$ evaluated for $\mathbf{x} \in \mathcal{S}_3$ points in the direction of the vector $\mathbf{x}$, radially outward from the origin. Hence, it is straightforward to notice that for $\mathbf{x} \in \mathcal{S}_3$, $\mathbf{u}(\mathbf{x}, m, k)$ does not point outside the set $\mathcal{F}^k_m$.

According to (B.10)-(B.13), and Lemma B.2, if the solution $\mathbf{x}$ to the flow-only system (B.3) leaves the set $\mathcal{F}^k_m$, it cannot leave from the region $\partial\mathcal{F}^k_m \backslash \mathcal{G}^k_m$. Next, we show that the solution $\mathbf{x}$ to the flow-only system (B.3), flowing in the set $\mathcal{F}^k_m$, away from the region $\mathcal{G}^k_m$, will always enter in the set $\mathcal{G}^k_m$ in finite time.

We partition the set $\mathcal{F}^k_m,\ k \in \mathbb{I}$, into three subsets as follows:

$$\mathcal{F}^k_m = \tilde{\mathcal{F}}_1(m,k) \cup \tilde{\mathcal{F}}_2(m,k) \cup \tilde{\mathcal{F}}_3(m,k), \tag{B.15}$$

where

$$\begin{aligned}
\tilde{\mathcal{F}}_1(m,k) &= \left(\mathcal{F}^k_m \cap \mathcal{C}(\mathbf{n}^{(-m,k)}_{r_a+\gamma_a}, \mathbf{n}^{(m,k)}_{r_a+\gamma_s})\right) \cap (\mathcal{D}_{r_a+\gamma_s}(\mathcal{O}_k))^\circ, \\
\tilde{\mathcal{F}}_2(m,k) &= \left(\mathcal{F}^k_m \cap \mathcal{C}(\mathbf{n}^{(-m,k)}_{r_a+\gamma_a}, \mathbf{n}^{(m,k)}_{r_a+\gamma_s})\right) \backslash (\mathcal{D}_{r_a+\gamma_s}(\mathcal{O}_k))^\circ, \\
\tilde{\mathcal{F}}_3(m,k) &= \mathcal{F}^k_m \cap \mathcal{C}(\mathbf{n}^{(m,k)}_{r_a+\gamma_s}, \mathbf{n}^{(m,k)}_{r_a+\gamma}).
\end{aligned} \tag{B.16}$$

For $\mathbf{x} \in \tilde{\mathcal{F}}_3(m,k)$, the control law $\mathbf{u}(\mathbf{x}, m, k)$, according to (3.4a), is given as $-\kappa\mathbf{x},\ \kappa > 0$, *i.e.*, the solution $\mathbf{x}(t)$ will evolve along the line $\mathcal{L}(\mathbf{0}, \mathbf{x})$ towards the origin. Since $\mathbf{0} \notin \tilde{\mathcal{F}}_3(m,k)$, it is straightforward to verify that if for some $t_0 \geq 0$, $\mathbf{x}(t_0) \in \tilde{\mathcal{F}}_3(m,k)$, then there exists a finite time at which $\mathbf{x}(t)$ will leave the set $\tilde{\mathcal{F}}_3(m,k)$ via $\mathcal{G}^k_m$, see Fig. B.2.

According to (3.4a), for $\mathbf{x} \in \tilde{\mathcal{F}}_2(m,k)$, $\mathbf{u}(\mathbf{x}, m, k) = -\kappa\mathbf{x}, \kappa > 0$, hence in this region the solution will evolve towards the origin on a straight line $\mathcal{L}(\mathbf{0}, \mathbf{x})$ which implies that eventually it will enter $\tilde{\mathcal{F}}_1(m,k)$, see Fig. B.2.

Now, consider the case where $\mathbf{x} \in \tilde{\mathcal{F}}_1(m,k)$. We show that,

$$\forall \mathbf{x} \in \tilde{\mathcal{F}}_1(m,k) \backslash \mathcal{G}^k_m, \mathbf{u}(\mathbf{x}, m, k) \in \mathcal{P}_>(\mathbf{0}, \nu_m(\mathbf{x})). \tag{B.17}$$

The satisfaction of (B.17) implies that, if at some $t_0 \geq 0$, $\mathbf{x}(t_0) \in \tilde{\mathcal{F}}_1(m,k)$, the solution $\mathbf{x}$ to the flow-only system (B.3) cannot live indefinitely in the positive half-space $\mathcal{P}_>(\mathbf{0}, \nu_m(\mathbf{x}))$ since, in view of Lemma 3.1, the set $\mathcal{F}^k_m$ is closed and bounded as the obstacles are compact.

For all $\mathbf{x} \in \tilde{\mathcal{F}}_1(m,k)$, the control input vector $\mathbf{u}(\mathbf{x}, k, m)$ is given by

$$\mathbf{u}(\mathbf{x}, m, k) = -\kappa\sigma(\xi)\mathbf{x} + \kappa[1 - \sigma(\xi)]\mathbf{v}(\mathbf{x}, m, k),$$

where $\kappa > 0$. Since the vectors $-\kappa\sigma(\xi)\mathbf{x}$ and $\nu_m(\mathbf{x})$ are orthogonal, $-\kappa\sigma(\xi)\mathbf{x} \in \mathcal{P}(\mathbf{0}, \nu_m(\mathbf{x}))$. In order to check whether, $\mathbf{u}(\mathbf{x}, m, k)$ belongs to $\mathcal{P}_>(\mathbf{0}, \nu_m(\mathbf{x}))$, let us evaluate

$$\nu_m(\mathbf{x})^\intercal \mathbf{u}(\mathbf{x}, m, k) = \kappa[1 - \sigma(\xi)]\nu_m(\mathbf{x})^\intercal \mathbf{v}(\mathbf{x}, m, k),$$

where $\forall \mathbf{x} \in \tilde{\mathcal{F}}_1(m,k),\ \kappa > 0, [1 - \sigma(\xi)] > 0$. Hence, we consider

$$\begin{aligned}
\nu_m(\mathbf{x})^\intercal \mathbf{v}(\mathbf{x}, m, k) &= \nu_{-m}(\nu_m(\mathbf{x}))^\intercal \nu_{-m}(\mathbf{v}(\mathbf{x}, m, k)), \\
&= \frac{\|\mathbf{x}\|\mathbf{x}^\intercal(\mathbf{x} - \Pi(\mathbf{x}, \mathcal{O}_k))}{\|\mathbf{x} - \Pi(\mathbf{x}, \mathcal{O}_k))\|}.
\end{aligned}$$

Since $\left(\tilde{\mathcal{F}}_1(m,k)\backslash\mathcal{G}_m^k\right)\cap\mathcal{R}_b^k=\emptyset$, according to Remark 3.1, $\forall\mathbf{x}\in\tilde{\mathcal{F}}_1(m,k)\backslash\mathcal{G}_m^k$, $\mathbf{x}^\intercal(\mathbf{x}-\Pi(\mathbf{x},\mathcal{O}_k))>0$, hence (B.17) is satisfied.

B.5 Proof of Theorem 3.1

The forward invariance of the obstacle-free set $\mathcal{K}$ defined in (3.25), for the hybrid closed-loop system (3.28), is immediate from Lemma 3.2. We next prove stability of $\mathcal{A}$ using [Goebel et al., 2012, Definition 7.1]. Since $\mathcal{W}_{r_a}$ is compact by construction and $\mathbf{0}\in(\mathcal{W}_{r_a})^\circ$, $\exists\bar{\delta}>0$, such that $\mathcal{B}_{\bar{\delta}}(\mathbf{0})\cap\left(\mathcal{D}_{r_a}(\mathcal{O}_k)\right)^\circ=\emptyset$, $\forall k\in\mathbb{I}$. It can easily be shown that for each $\delta\in[0,\bar{\delta}]$, the set $\mathcal{S}:=\mathcal{B}_\delta(\mathbf{0})\times\mathbb{M}\times\mathbb{I}$ is forward invariant because $\mathcal{B}_\delta(\mathbf{0})$ is disjoint from $\mathcal{J}_0$ as for all $k\in\mathbb{I}$, $\mathcal{D}_{r_a}(\mathcal{O}_k)$ is situated between the set $\mathcal{J}_0^k$ and the target; see Fig. 3.3. Therefore, $\mathbf{x}\in\mathcal{B}_\delta(\mathbf{0})$ of the solutions evolves, after at most one jump, in the *move-to-target* mode $\dot{\mathbf{x}}=-\kappa\mathbf{x}$, $\kappa>0$. Hence, similar to [Berkane et al., 2021b, Appendix 2], the stability of $\mathcal{A}$ for the hybrid closed-loop system (3.28) is immediate from [Goebel et al., 2012, Definition 7.1]. Next, we proceed to establish almost global convergence properties of the set $\mathcal{A}$.

The next lemma helps establish the fact that the solution ξ to the hybrid closed-loop system (3.28) can enter the set $\mathcal{Z}$ only if it is initialized in the set $\mathcal{Z}_0$.

Lemma B.3 *Consider the hybrid closed-loop system (3.28) and let Assumption 3.1 hold. If $\xi(t_0,j_0)\in\mathcal{K}\backslash\mathcal{Z}_0$ for some $(t_0,j_0)\in\text{dom }\xi$, then $\xi(t,j)\notin\mathcal{Z}_0$ for all $(t,j)\succeq(t_0,j_0)$.*

Proof See Appendix B.5.1.

Lemma B.3 indicated that the solution ξ that does not belong to the set $\mathcal{Z}_0$ at some time $(t_0,j_0)\in\text{dom }\xi$ can never enter in the set $\mathcal{Z}_0$ for all $(t,j)\succeq(t_0,j_0)$. Since $\mathcal{M}\subset\mathcal{M}_0$ (3.30), it is straightforward to conclude that the solution ξ can enter the set $\mathcal{Z}$ only if $\xi(0,0)\in\mathcal{Z}_0$.

We proceed to prove that all solutions ξ to the hybrid closed-loop system (3.28) with $\xi(0,0)\in\mathcal{K}\backslash\mathcal{Z}_0$ converge towards the set $\mathcal{A}$. Towards that end we require the following lemma.

Lemma B.4 *Consider the hybrid closed-loop system (3.28) and let Assumption 3.1 hold. If $\xi(t_0,j_0)\in\tilde{\mathcal{K}}_{m^*}(\{0\})\backslash\mathcal{Z}_0$ with some $m^*\in\{-1,1\}$ for some $(t_0,j_0)\in$ dom ξ, then one of the following holds true:*

1. *$\xi(t,j)\notin\tilde{\mathcal{K}}_>(\mathbb{M})$ for all $(t,j)\succeq(t_0,j_0)$, and $\lim_{t\to\infty,j\to\infty}\xi(t,j)\to\mathcal{A}$.*
2. *there exists $(T,J)\succeq(t_0,j_0)$ such that $\xi(T,J)\in\tilde{\mathcal{K}}_>(\{-1,1\})\backslash\mathcal{Z}_0$ where $T+J<+\infty$.*

Proof See Appendix B.5.2.

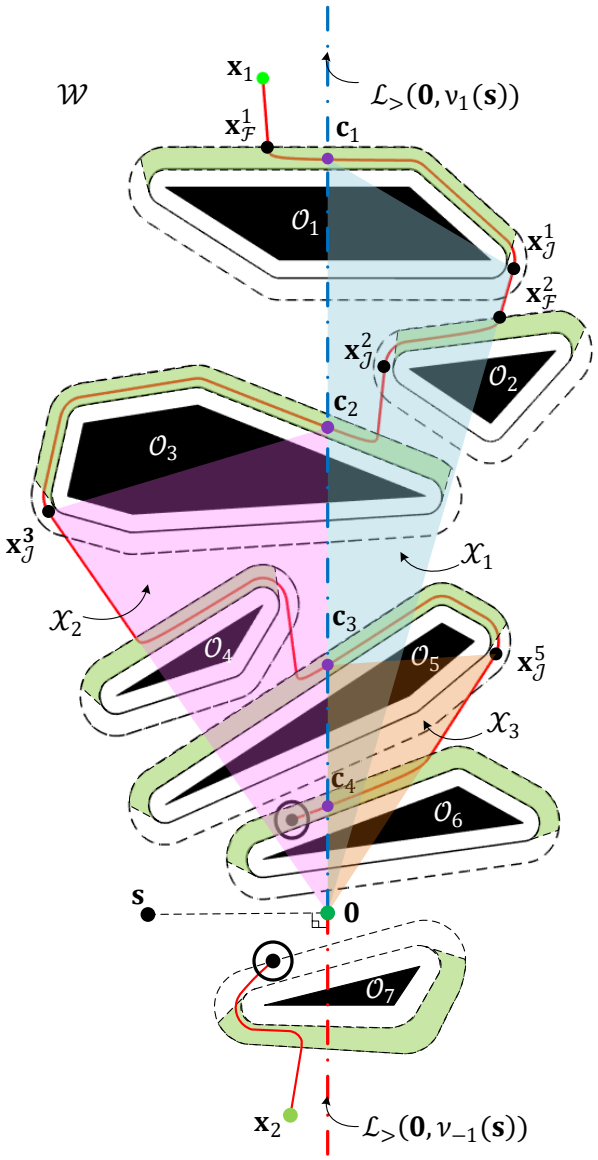

Figure B.3: 1) Trajectory $\mathbf{x}(t)$ starting from $\mathbf{x}_1$, illustrates the property stated in (B.18) *i.e.,* with consecutive intersections with the half-line $\mathcal{L}_>(\mathbf{0}, \nu_1(\mathbf{s}))$, the state $\mathbf{x}$ approaches towards the origin. 2) Trajectory $\mathbf{x}(t)$ starting from $\mathbf{x}_2$, does not intersect with the half-line $\mathcal{L}_>(\mathbf{0}, \nu_{-1}(\mathbf{s}))$, as $\mathbf{x}(0,0) \notin \mathcal{M}_0$ and $m(0,0) = 0$, as per Lemma 3.3.

Lemma B.4 shows that for the solution ξ operating in the *move-to-target* mode within the obstacle-free workspace, if $\mathbf{x}$ belongs to the interior of one of the half-spaces generated by the hyperplane $\mathcal{P}(\mathbf{0}, \mathbf{s})$ away from the set $\mathcal{M}_0$, then the solution ξ will either directly converge to the set $\mathcal{A}$ or enter the set $\tilde{\mathcal{K}}_{>}(\mathbb{M}) \cup \tilde{\mathcal{K}}_{-m^*}(\mathbb{M})$ only through the set $\tilde{\mathcal{K}}(\{-1,1\})\backslash\mathcal{Z}_0$ in finite time, while flowing in the *obstacle-avoidance* mode. For the former case, it is straightforward to establish the convergence of the solution ξ to the set $\mathcal{A}$. Therefore, focus on the latter case.

We show that for the solution ξ, initialized in the set $\mathcal{K}\backslash\mathcal{Z}_0$, if $\mathbf{x}$ intersects the half-line $\mathcal{L}_{>}(\mathbf{0}, \nu_1(\mathbf{s}))$ more than once, then with each consecutive intersection with the set $\tilde{\mathcal{K}}_{>}(\{-1,1\})\backslash\mathcal{Z}_0$, the solution ξ moves closer to the set $\mathcal{A}$.

Let $\mathbf{c}_l \in \mathcal{W}_{r_a}$, be the location where the solution ξ enters in the set $\tilde{\mathcal{K}}_{>}(\{-1,1\})\backslash\mathcal{Z}_0$, as shown in Fig. B.3. The parameter $l \in \mathbb{N}$ indicates the instance of occurrence, for example $\mathbf{c}_1 \in \mathcal{W}_{r_a}$ represents the location where the solution ξ, flowing in the *obstacle-avoidance* mode, first entered in the set $\tilde{\mathcal{K}}_{>}(\{-1,1\})\backslash\mathcal{Z}_0$. Let $(t_l^c, j_l^c) \in$ dom ξ such that $\xi(t_l^c, j_l^c) \in \mathbf{c}_l \times \{-1,1\} \times \mathbb{I}$.

We assume $\xi(t_0, j_0) \in \left(\tilde{\mathcal{K}}_{m^*}(\mathbb{M})\backslash\mathcal{Z}_0\right) \cap ((\mathcal{F}_0^*\backslash\mathcal{J}_0^*) \times \{0\} \times \mathbb{I})$ for some $(t_0, j_0) \in$ dom ξ and $m^* \in \{-1,1\}$, which can always be the case by virtue of Lemma B.1 and Lemma B.3. Furthermore, assume that for some $i \in \mathbb{I}$, $\exists (t_{\mathcal{F}}^i, j_{\mathcal{F}}^i) \succ (t_0, j_0)$ such that, according to (3.22),(3.23) and (3.27), $\xi(t_{\mathcal{F}}^i, j_{\mathcal{F}}^i) = (\mathbf{x}_{\mathcal{F}}^i, m^*, i) \in \tilde{\mathcal{K}}_{m^*}(\mathbb{M})\backslash\mathcal{Z}_0$. Hence, according to Lemma B.1 and Lemma B.3, $\exists (t_{\mathcal{J}}^i, j_{\mathcal{J}}^i) \succ (t_{\mathcal{F}}^i, j_{\mathcal{F}}^i)$ such that $\xi(t_{\mathcal{J}}^i, j_{\mathcal{J}}^i) = (\mathbf{x}_{\mathcal{J}}^i, m^*, i) \in \mathcal{K}\backslash\mathcal{Z}_0$. We assume $\xi(t_{\mathcal{J}}^i, j_{\mathcal{J}}^i) \in \tilde{\mathcal{K}}_{-m^*}(\mathbb{M})$ *i.e.*, $\exists (t_l^c, j_l^c) \in ((t_{\mathcal{F}}^i, t_{\mathcal{J}}^i] \times [j_{\mathcal{F}}^i, j_{\mathcal{J}}^i])$. This case is similar to the evolution of the robot position around obstacle $\mathcal{O}_1$ in Fig. B.3. After $(t_{\mathcal{J}}^i, j_{\mathcal{J}}^i)$, according to Lemma B.4, the solution will either directly converge to the set $\mathcal{A}$, or will again enter the set $\tilde{\mathcal{K}}_{>}(\{-1,1\})\backslash\mathcal{Z}_0$. We assume $\exists (t_{l+1}^c, j_{l+1}^c) \succ (t_{\mathcal{J}}^i, j_{\mathcal{J}}^i)$, then according to (3.22),(3.23) and (3.27), $\xi(t_{l+1}^c, j_{l+1}^c) = (\mathbf{c}_{l+1}, -m^*, i'), i' \in \mathbb{I}_l^{l+1}\backslash\{i\}$, where the set $\mathbb{I}_l^{l+1} \subset \mathbb{I}$ consists of the indices of the obstacles encountered by the solution $\xi(t, j)$, for all $(t, j) \in ([t_l^c, t_{l+1}^c] \times [j_l^c, j_{l+1}^c])$.

We show that $\exists \mu^{c_l} > 0$ such that

$$\|\mathbf{c}_{l+1}(t_{l+1}^c, j_{l+1}^c)\| \leq \|\mathbf{c}_l(t_l^c, j_l^c)\| - \mu^{c_l}. \tag{B.18}$$

The satisfaction of the (B.18) ensures that if $\mathbf{x}$ crosses the half-line $\mathcal{L}_{>}(\mathbf{0}, \nu_1(\mathbf{s}))$ more than once while operating in the *obstacle-avoidance* mode, then each consecutive intersection with the half-line $\mathcal{L}_{>}(\mathbf{0}, \nu_1(\mathbf{s}))$ is closer to the origin than the previous one. Then, by virtue of Lemma B.4 and the satisfaction of (B.18), it is straightforward to show that any solution ξ which belongs to $\mathcal{K}\backslash\mathcal{Z}_0$, at some instant of time will converge to the target set $\mathcal{A}$.

For $\xi(t_l^c, j_l^c) = (\mathbf{c}_l, m^*, i)$, we define a set $\mathcal{KT}_l := \mathcal{X}_l \times \mathbb{M} \times \mathbb{I}$, where the set $\mathcal{X}_l$ is defined as

$$\mathcal{X}_l := \mathcal{C}(\nu_1(\mathbf{s}), \mathbf{x}_{\mathcal{J}}^i) \cap \mathcal{P}_{\geq}(\mathbf{c}_l, \nu_{m^*}(\mathbf{x}_{\mathcal{J}}^i - \mathbf{c}_l)),$$

and show that $\xi(t, j) \in \mathcal{KT}_l$, $\forall (t, j) \in ([t_{\mathcal{J}}^i, t_{l+1}^c] \times [j_{\mathcal{J}}^i, j_{l+1}^c])$. This would imply that for all $(t, j) \in ([t_{\mathcal{J}}^i, t_{l+1}^c] \times [j_{\mathcal{J}}^i, j_{l+1}^c])$, the solution ξ evolves in the set $\mathcal{KT}_l$ until it enters $\tilde{\mathcal{K}}_{>}(\{-1,1\})\backslash\mathcal{Z}_0$ according to Lemma B.4, and (B.18) holds.

First, we consider a special scenario wherein $\mathbf{x}^i_{\mathcal{J}} = \mathbf{c}_l$. In this case, the set $\mathcal{X}_l$ can be represented by a line segment $\mathcal{L}_s(\mathbf{0}, \mathbf{x}^i_{\mathcal{J}})$. At $(t^i_{\mathcal{J}}, j^i_{\mathcal{J}} + 1)$ the robot enters in the *move-to-target* flow set and moves along the line segment $\mathcal{L}_s(\mathbf{0}, \mathbf{x}^i_{\mathcal{J}})$ towards the origin. Then it is straightforward to verify (B.18). Next, we consider the case wherein $\mathbf{x}^i_{\mathcal{J}} \neq \mathbf{c}_l$.

Since $\xi(t_0, j_0) \in \left(\tilde{\mathcal{K}}_{m^*}(\mathbb{M}) \backslash \mathcal{Z}_0\right) \cap ((\mathcal{F}^*_0 \backslash \mathcal{J}^*_0) \times \{0\} \times \mathbb{I})$, according to Lemma B.3, the solution $\xi(t, j) \notin \mathcal{Z}_0, \forall (t, j) \succeq (t_0, j_0)$. The boundary of the set $\mathcal{X}_l$ is defined as

$$\partial \mathcal{X}_l = \mathcal{L}_s(\mathbf{0}, \mathbf{c}_l) \cup \mathcal{L}_s(\mathbf{0}, \mathbf{x}^i_{\mathcal{J}}) \cup \mathcal{L}_s(\mathbf{c}_l, \mathbf{x}^i_{\mathcal{J}}),$$

where $\mathcal{L}_s(\mathbf{c}_l, \mathbf{x}^i_{\mathcal{J}}) \subset \mathcal{D}_{r_a+\gamma}(\mathcal{O}_i)$. According to Assumption 3.1 and (3.20), $\mathcal{F}^q_m \cap \mathcal{F}^s_m = \emptyset, \forall q, s \in \mathbb{I}, q \neq s$, for some $m \in \{-1, 1\}$. Hence, at $(t^i_{\mathcal{J}}, j^i_{\mathcal{J}} + 1)$, the solution ξ starts to flow in the *move-to-target* mode and $\mathbf{x}$ evolves along the line segment $\mathcal{L}_s(\mathbf{x}^i_{\mathcal{J}}, \mathbf{0})$. Since $\mathcal{L}_s(\mathbf{c}_l, \mathbf{x}^i_{\mathcal{J}}) \cap \mathcal{L}_s(\mathbf{x}^i_{\mathcal{J}}, \mathbf{0}) = \mathbf{x}^i_{\mathcal{J}}$, it is clear that $\mathbf{x}$ cannot enter the line segment $\mathcal{L}_s(\mathbf{c}_l, \mathbf{x}^i_{\mathcal{J}})$ from within the set $\mathcal{KT}_l$ using the stabilizing feedback $-\kappa\mathbf{x}$, $\kappa > 0$.

At $(t^i_{\mathcal{J}}, j^i_{\mathcal{J}} + 1)$, the solution ξ starts to evolve towards the origin along the line $\mathcal{L}(\mathbf{0}, \mathbf{x}^i_{\mathcal{J}})$ in the *move-to-target* mode. This solution (*i.e.,* flowing in the *move-to-target* mode) cannot leave the line segment $\mathcal{L}_s(\mathbf{0}, \mathbf{x}^i_{\mathcal{J}})$ unless it encounters $\mathcal{J}_0 \times \{0\} \times \mathbb{I}$. Let us assume $\exists (t^{i+1}_{\mathcal{F}}, j^{i+1}_{\mathcal{F}}) \succ (t^i_{\mathcal{J}}, j^i_{\mathcal{J}})$ for some $i + 1 \in \mathbb{I}^{l+1}_l \backslash \{i, i'\}$, hence, according to (3.22), (3.23) and (3.27), $\xi^{i+1}_{\mathcal{F}} = (\mathbf{x}^{i+1}_{\mathcal{F}}, -m^*, i + 1) \in \mathcal{F}^{i+1}_{-m^*} \times \{-1, 1\} \times \mathbb{I}$. At this instance, since $\mathbf{x}^{i+1}_{\mathcal{F}} \in \overline{\tilde{\mathcal{F}}_1(-m^*, i + 1)}$, defined in (B.15), (B.16), according to (B.17), $\mathbf{x}(t, j) \in \mathcal{P}_>(\mathbf{0}, \nu_{-m^*}(\mathbf{x}^{i+1}_{\mathcal{F}})), \forall (t, j) \in ((t^{i+1}_{\mathcal{F}}, t^{i+1}_{\mathcal{J}}], [j^{i+1}_{\mathcal{F}}, j^{i+1}_{\mathcal{J}}])$, and $\mathbf{x}$ enters in the interior of the set $\mathcal{X}_l$. The solution ξ does not enter the set $\mathcal{L}_s(\mathbf{0}, \mathbf{x}^i_{\mathcal{J}}) \times \mathbb{M} \times \mathbb{I}, \forall (t, j) \in ((t^{i+1}_{\mathcal{F}}, t^{i+1}_{\mathcal{J}}], [j^{i+1}_{\mathcal{F}}, j^{i+1}_{\mathcal{J}}])$.

Now, if $\mathbb{I}^{l+1}_l \backslash \{i, i + 1\} \neq \emptyset$, then for each $i'' \in \mathbb{I}^{l+1}_l \backslash \{i, i + 1\}$, according to (3.23), $m(t, j) = -m^*, \forall (t, j) \in ([t^{i''}_{\mathcal{F}}, t^{i''}_{\mathcal{J}}] \times [j^{i''}_{\mathcal{F}}, j^{i''}_{\mathcal{J}}])$. Hence, if the solution $\xi(t, j)$ enters in the *obstacle-avoidance* mode at any $(t, j) \in ([t^{i+1}_{\mathcal{J}}, t^c_{l+1}] \times [j^{i+1}_{\mathcal{J}}, j^c_{l+1}])$, it will evolve in the interior of the set $\mathcal{KL}_l$. Hence, as per Lemma B.4, it follows that the solution can only leave the set $\mathcal{KT}_l$ through $\mathcal{L}_s(\mathbf{0}, \mathbf{c}_l) \backslash \{\mathbf{c}_l\}$, which ensures that there exists some $\mu^{c_l} > 0$, such that (B.18) is satisfied. Hence, every solution starting in $\mathcal{K} \backslash \mathcal{Z}_0$ will converge to $\mathcal{A}$.

Finally, if we remove the jump set $\mathcal{J}$ from the flow set $\mathcal{F}$ to obtain the hybrid system with data $(\mathcal{F} \setminus \mathcal{J}, \mathbf{F}, \mathcal{J}, \mathbf{J})$, and thus forcing the flows over jumps [Sanfelice and Teel, 2010], the Zeno solution starting from $\mathcal{Z}_0$ is no longer a valid solution for the closed-loop system with these new data. In fact, for $\xi(0, 0) \in \mathcal{Z}_0$, the solution will flow with the *obstacle-avoidance* mode until it reaches $\mathcal{Z}$ and then flows with the *move-to-target* mode afterwards.

B.5.1 Proof of Lemma B.3

According to (3.16) and (3.30), as $\mathcal{M}_0 \subset \mathcal{J}_0$, the solution ξ with $\xi(t_0, j_0) \in \mathcal{K} \backslash \mathcal{Z}_0$, cannot enter the set $\mathcal{Z}_0$ $\forall (t, j) \succeq (t_0, j_0)$, while flowing in the *move-to-target* mode.

We consider the flow-only system (B.3), where $\mathbf{x} \in \mathcal{F}^k_m, m \in \{-1, 1\}, k \in \mathbb{I}$ *i.e.*, the case wherein the solution is flowing in the *obstacle-avoidance* mode, in the vicinity of an obstacle $\mathcal{O}_k, k \in \mathbb{I}$, and show that if $\mathbf{x}(t_0) \in \mathcal{F}^k_m \backslash \mathcal{M}_0$, then $\mathbf{x}(t) \notin \mathcal{M}_0, \forall t \geq t_0$. Since, according to Assumption 3.1, (3.19) and (3.20), the flow sets of the *obstacle-avoidance* modes for the state $\mathbf{x}$, related to different obstacles, are disjoint *i.e.*, $\mathcal{F}^p_m \cap \mathcal{F}^q_m = \emptyset, p, q \in$

$\mathbb{I}, p \neq q$, one can repeat the analysis for the solution evolving in the flow set *obstacle-avoidance* mode, related to the remaining obstacles.

Assume that $\mathbf{x}(t_0) \in \mathcal{F}_m^k$ such that $d(\mathbf{x}(t_0), \mathcal{D}_{r_a}(\mathcal{O}_k)) = \beta_1 \in (0, \gamma]$. Let $\beta_2 = \min\{\gamma_a, \beta_1\}$. According to (3.17) and (3.30), it is easy to see that the solution can enter the set $\mathcal{M}_0$ only via $\partial\mathcal{D}_{r_a+\beta_3}(\mathcal{O}_k) \cap \mathcal{F}_m^k$, where $\beta_3 \in (0, \beta_2)$. For all $\mathbf{x} \in \partial\mathcal{D}_{r_a+\beta_3}(\mathcal{O}_k) \cap \mathcal{F}_m^k$, according to (3.4), the control input $\mathbf{u}(\mathbf{x}, m, k) = \kappa\mathbf{v}(\mathbf{x}, m, k), \kappa > 0$. Hence, according to Lemma B.2, the solution $\mathbf{x}(t)$ to the flow-only system (B.3) cannot enter the set $\mathcal{M}_0$ for all $t \geq t_0$, and according to Lemma B.1, it will ultimately enter in the *move-to-target* in finite time.

B.5.2 Proof of Lemma B.4

We consider $\xi(t_0, j_0) \in \left(\tilde{\mathcal{K}}_{m^*}(\mathbb{M})\backslash\mathcal{Z}_0\right) \cap ((\mathcal{F}_0^*\backslash\mathcal{J}_0^*) \times \{0\} \times \mathbb{I})$ where $m^* \in \{-1, 1\}$ for some $(t_0, j_0) \in$ dom ξ, which can always be the case by virtue of Lemma B.1 and Lemma B.3. Also, according to Lemma B.3, $\xi(t, j) \notin \mathcal{Z}_0, \forall (t, j) \succeq (t_0, j_0)$. Then at (t_0, j_0), the state $\mathbf{x}$ will evolve along the line $\mathcal{L}(\mathbf{0}, \mathbf{x}(t_0, j_0))$ in the *move-to-target* mode. Since $\mathcal{L}(\mathbf{0}, \mathbf{x}(t_0, j_0)) \cap (\mathcal{P}(\mathbf{0}, \mathbf{s})\backslash\mathbf{0}) = \emptyset$, the control input, in the *move-to-target* mode, cannot steer ξ to the set $\tilde{\mathcal{K}}_0(\mathbb{M})$ from the set $\tilde{\mathcal{K}}_{m^*}(\mathbb{M})$. Moreover, according to Lemma 3.3, the solution will never enter the set $\tilde{\mathcal{K}}_<(\mathbb{M})$ for all $(t, j) \succeq (t_0, j_0)$. Hence, according to Lemma B.4, the only remaining possibilities, which we need to prove, are that the solution ξ with $\xi(t_0, j_0) \in \tilde{\mathcal{K}}_{m^*}(\mathbb{M})$ will either enter the set $\tilde{\mathcal{K}}_>(\{-1, 1\})\backslash\mathcal{Z}_0$ while flowing in the *obstacle-avoidance* mode or directly converge to $\mathcal{A}$ without entering the set $\tilde{\mathcal{K}}_>(\mathbb{M})$.

Let $\alpha_{-1}(\mathbf{a}, \mathbf{b})$ and $\alpha_1(\mathbf{a}, \mathbf{b})$ denote the absolute values of an angle measured from vector $\mathbf{a}$ to vector $\mathbf{b}$ in the counter-clockwise and clockwise directions, respectively. If $\xi(t, j) \notin \mathcal{J}_0 \times \{0\} \times \mathbb{I}$, $\forall (t, j) \succeq (t_0, j_0)$, then the $\mathbf{x}$ component of the solution ξ, under the influence of the stabilizing vector $-\kappa\mathbf{x}, \kappa > 0$, will asymptotically converge to the origin.

On the other hand, assume that the solution ξ encounters the jump set $\mathcal{J}_0^i \times \{0\} \times \mathbb{I}$ for some $i \in \mathbb{I}$ *i.e.*, $\exists (t_{\mathcal{F}}^i, j_{\mathcal{F}}^i) \in$ dom $\xi, (t_{\mathcal{F}}^i, j_{\mathcal{F}}^i) \succ (t_0, j_0)$. According to (3.22),(3.23) and (3.27), $\xi_{\mathcal{F}}^i = (\mathbf{x}_{\mathcal{F}}^i, m^*, i)$. Then according to Lemma B.1, $\exists (t_{\mathcal{J}}^i, j_{\mathcal{J}}^i) \succ (t_{\mathcal{F}}^i, j_{\mathcal{F}}^i)$ such that $\xi_{\mathcal{J}}^i = (\mathbf{x}_{\mathcal{J}}^i, m^*, i)$. According to Lemma B.3, the solution cannot enter the set $\mathcal{Z}_0$, hence the locations $\mathbf{x}_{\mathcal{F}}^i$ and $\mathbf{x}_{\mathcal{J}}^i$ belong to the set $(\overline{\tilde{\mathcal{F}}_1(m^*, i)}\backslash\mathcal{M}_0) \subset \mathcal{F}_{m^*}^i$, defined in (B.15), (B.16). Then, according to (B.17), $\mathbf{x}_{\mathcal{J}}^i \in \mathcal{P}_>(\mathbf{0}, \nu_{m^*}(\mathbf{x}_{\mathcal{F}}^i))$. Assuming $\xi(t_{\mathcal{J}}^i, j_{\mathcal{J}}^i) \in \tilde{\mathcal{K}}_{m^*}(\mathbb{M})$, one has

$$\alpha_{m^*}(\mathbf{x}_{\mathcal{F}}^i, \nu_1(\mathbf{s})) > \alpha_{m^*}(\mathbf{x}_{\mathcal{J}}^i, \nu_1(\mathbf{s})) > 0. \tag{B.19}$$

Hence, for any solution ξ to the hybrid closed-loop system (3.28) with $\xi(t_0, j_0) \in \left(\tilde{\mathcal{K}}_{m^*}(\mathbb{M})\backslash\mathcal{Z}_0\right) \cap (\mathcal{F}_0^*\backslash\mathcal{J}_0^*) \times \{0\} \times \mathbb{I}$ for some $(t_0, j_0) \in$ dom ξ, if there exists $(t_{\mathcal{F}}^i, j_{\mathcal{F}}^i) \succ (t_0, j_0)$ for some $i \in \mathbb{I}$ with $\xi_{\mathcal{J}}^i \in \tilde{\mathcal{K}}_{m^*}(\mathbb{M})$, then the angle between the vectors $\mathbf{x}$ and $\nu_1(\mathbf{s})$ *i.e.*, $\alpha_{m^*}(\mathbf{x}(t, j), \nu_1(\mathbf{s}))$ reduces, otherwise, if there does not exist $(t_{\mathcal{F}}^i, j_{\mathcal{F}}^i) \succ (t_0, j_0)$ for any $i \in \mathbb{I}$, *i.e.*, if the solution does not encounter the *move-to-target* mode jump set after (t_0, j_0), then it will asymptotically converge to the target set $\mathcal{A}$, under the influence of the stabilizing control input $-\kappa\mathbf{x}, \kappa > 0$.

Next, assume that the solution ξ again encounters the jump set $\mathcal{J}_0 \times \{0\} \times \mathbb{I}$ for $i+1 \in \mathbb{I}\backslash\{i\}$. Hence, $\exists(t_{\mathcal{F}}^{i+1}, j_{\mathcal{F}}^{i+1}) \succ (t_{\mathcal{J}}^{i}, j_{\mathcal{J}}^{i})$ and according to Lemma B.1, $\exists(t_{\mathcal{J}}^{i+1}, j_{\mathcal{J}}^{i+1}) \succ (t_{\mathcal{F}}^{i+1}, j_{\mathcal{F}}^{i+1})$ such that $\xi_{\mathcal{F}}^{i+1} = (\mathbf{x}_{\mathcal{F}}^{i+1}, i+1, m^*)$ and $\xi_{\mathcal{J}}^{i+1} = (\mathbf{x}_{\mathcal{J}}^{i+1}, i+1, m^*)$. Again assume $\xi_{\mathcal{J}}^{i+1} \in \tilde{\mathcal{K}}_{m^*}(\mathbb{M})$. Hence, similar to the previous case,

$$\alpha_{m^*}(\mathbf{x}_{\mathcal{F}}^{i+1}, \nu_1(\mathbf{s})) > \alpha_{m^*}(\mathbf{x}_{\mathcal{J}}^{i+1}, \nu_1(\mathbf{s})) > 0. \tag{B.20}$$

Also, as the control input corresponding to the *move-to-target* mode steers $\mathbf{x}$ straight to the origin, one has $\alpha_{m^*}(\mathbf{x}(t,j), \nu_1(\mathbf{s})) = \alpha_{m^*}(\mathbf{x}_{\mathcal{J}}^{i}, \nu_1(\mathbf{s}))$, $\forall (t,j) \in ([t_{\mathcal{J}}^{i}, t_{\mathcal{F}}^{i+1}] \times [j_{\mathcal{J}}^{i}, j_{\mathcal{F}}^{i+1}])$. As a result, one has

$$\alpha_{m^*}(\mathbf{x}_{\mathcal{F}}^{i}, \nu_1(\mathbf{s})) > \alpha_{m^*}(\mathbf{x}_{\mathcal{F}}^{i+1}, \nu_1(\mathbf{s})) > \alpha_{m^*}(\mathbf{x}_{\mathcal{J}}^{i+1}, \nu_1(\mathbf{s})) > 0$$

The angle $\alpha_{m^*}(\nu_1(\mathbf{s}), \mathbf{x}) = 0$ implies that the state $\xi \in \tilde{\mathcal{K}}_0(\mathbb{M})\backslash\tilde{\mathcal{K}}_{<}(\mathbb{M})$.

This implies that with each hybrid sequence of jumps from the *move-to-target* mode to the *obstacle-avoidance* and *vice versa*, the solution ξ, which belongs to $\tilde{\mathcal{K}}_{m^*}(\{0\})\backslash\mathcal{Z}_0$, evolve towards the set $\tilde{\mathcal{K}}(\mathbb{M}) \cup \tilde{\mathcal{K}}_{-m^*}(\mathbb{M})$, in the sense that the angle between the vectors $\mathbf{x}$ and $\nu_1(\mathbf{s})$ *i.e.*, $\alpha_{m^*}(\mathbf{x}, \nu_1(\mathbf{s}))$ decreases. Also, according to Lemma B.1, the control input corresponding to the *obstacle-avoidance* mode, always switches back to the *move-to-target* mode in finite time. Hence, it can be concluded that the solution, which belongs to the set $\tilde{\mathcal{K}}_{m^*}(\{0\}), m^* \in \{-1, 1\}$, at some time, either directly converges to the set $\mathcal{A}$ or intersects the set $\tilde{\mathcal{K}}_{>}(\{-1, 1\})$ in finite time.

B.6 Proof of Proposition 3.1

According to Lemma 3.1, the control input $\mathbf{u}(\mathbf{x}, m, k)$ in (3.4) is continuous while the robot is operating not only in the *move-to-target* mode *i.e.*, when $(\mathbf{x}, m, k) \in \mathcal{F}_0 \times \{0\} \times \mathbb{I}$ but also in the *obstacle-avoidance* mode *i.e.*, when $(\mathbf{x}, m, k) \in \mathcal{F}_z \times \{z\} \times \mathbb{I},\ z \in \{-1, 1\}$. We only need to verify the continuity of the control input $\mathbf{u}(\xi)$ at instances when the solution ξ to the hybrid closed-loop system (3.28) leaves the *move-to-target* mode and enters the *obstacle-avoidance* mode, and *vice versa*.

Note that since $\xi(t_0, j_0) \in \mathcal{K}\backslash\mathcal{Z}_0$ for some $(t_0, j_0) \in \text{dom } \xi$, according to Lemma B.3, the solution ξ cannot enter the set $\mathcal{Z}_0$ for all $(t,j) \succeq (t_0, j_0)$, and hence cannot get stuck in the Zeno behaviour for all future times.

During the *move-to-target* mode, the state $\mathbf{x}$ evolves along the line joining the center of the robot and the origin. Hence, as can be observed from Fig. 3.3, for the robot operating in the *move-to-target* mode, a solution ξ can enter in the jump set of the *move-to-target* mode for some obstacle $\mathcal{O}_i,\ i \in \mathbb{I}$, only via the region $(\partial\mathcal{D}_{r_a+\gamma_s}(\mathcal{O}_i) \cap \mathcal{J}_0^i) \times \{0\} \times \{i\}$. Let $(t_0, j_0) \in$ dom ξ such that $\xi(t_0, j_0) \in \left(\partial\mathcal{D}_{r_a+\gamma_s}(\mathcal{O}_i) \cap \mathcal{J}_0^i\right) \times \{0\} \times \{i\}$. Hence, according to (3.4), the control input vector at (t_0, j_0) is given as

$$\mathbf{u}(\xi(t_0, j_0)) = -\kappa\mathbf{x}(t_0, j_0). \tag{B.21}$$

According to (3.22), $\xi(t_0, j_0+1) \in \left(\partial\mathcal{D}_{r_a+\gamma_s}(\mathcal{O}_i) \cap \mathcal{J}_0^i\right) \times \{-1, 1\} \times \{i\}$, and the control input $\mathbf{u}(\xi(t_0, j_0+1))$, according to (3.4)-(3.8), is given as

$$\mathbf{u}(\xi(t_0, j_0+1)) = -\kappa\mathbf{x}(t_0, j_0+1). \tag{B.22}$$

Since, according to (3.28), $\mathbf{x}(t_0, j_0+1) = \mathbf{x}(t_0, j_0)$, when the solution leaves the *move-to-target* mode and enters in the *obstacle-avoidance* mode, the control vector trajectories remain continuous.

Next, we consider the case where the robot operating in the *obstacle-avoidance* mode enters in the *move-to-target* mode. According to Lemma B.1, the component $\mathbf{x}$ of the solutions, evolving in the *obstacle-avoidance* mode in the flow set $\mathcal{F}_z^i, i \in \mathbb{I}$, for some $z \in \{-1, 1\}$, will eventually leave the *obstacle-avoidance* mode via the gate region $\mathcal{G}_z^i$. Let $\xi(t_1, j_1) \in \mathcal{F}_z \times \{z\} \times \mathbb{I}$, $z \in \{-1, 1\}$ for some $(t_1, j_1) \in$ dom ξ, then according to Lemma B.1, $\exists (t_2, j_1) \succeq (t_1, j_1)$ such that $\mathbf{x}(t_2, j_1) \in \mathcal{G}_z^i$. Then according to (3.19) and (3.22), at $(t_2, j_1 + 1)$ the solution enters in the *move-to-target* mode flow set *i.e.*, $\xi(t_2, j_1 + 1) \in \mathcal{F}_0 \times \{0\} \times \mathbb{I}$. Hence, at (t_2, j_1), the control input vector $\mathbf{u}(\xi(t_2, j_1))$ is evaluated as

$$\begin{aligned}\mathbf{u}(\xi(t_2,j_1)) = &-\kappa\sigma(\xi(t_2, j_1))\mathbf{x}(t_2, j_1) \\ &+ \kappa[1 - \sigma(\xi(t_2, j_1))]\mathbf{v}(\xi(t_2, j_1)).\end{aligned} \tag{B.23}$$

According to the definition of the vector $\mathbf{v}(\xi)$ in (3.5) and the gate region $\mathcal{G}_z^i$ in (3.10), it is evident that at (t_2, j_1) the vectors $-\mathbf{x}(t_2, j_1)$ and $\mathbf{v}(\xi(t_2, j_1))$ are equal. Hence, $\mathbf{u}(\xi(t_2, j_1))$ can equivalently be expressed as

$$\mathbf{u}(\xi(t_2, j_1)) = -\kappa\mathbf{x}(t_2, j_1). \tag{B.24}$$

At $(t_2, j_1 + 1)$, according to (3.22), $\xi(t_2, j_1 + 1) \in \mathcal{F}_0 \times \{0\} \times \mathbb{I}$. Hence, the control input vector $\mathbf{u}(\xi(t_2, j_1 + 1))$ is given as

$$\mathbf{u}(\xi(t_2, j_1 + 1)) = -\kappa\mathbf{x}(t_2, j_1 + 1). \tag{B.25}$$

Since, according to (3.28), $\mathbf{x}(t_2, j_1) = \mathbf{x}(t_2, j_1 + 1)$, $\mathbf{u}(\xi(t_2, j_1)) = \mathbf{u}(\xi(t_2, j_1 + 1))$. As a result, when the solution flowing in the *obstacle-avoidance* mode, enters the *move-to-target* mode, the control vector trajectories remain continuous.

Appendix C

Proofs of Chapter 4

C.1 Proof of Lemma 4.1

Note that the following statement: "for all locations $\mathbf{x}$ with $d(\mathbf{x}, \mathcal{O}_{\mathcal{W}}^M) < \alpha$, where $\alpha \geq 0$, the set $\mathcal{PJ}(\mathbf{x}, \mathcal{O}_{\mathcal{W}}^M)$ is singleton", is equivalent to having $\mathbf{reach}(\mathcal{O}_{\mathcal{W}}^M) \geq \alpha$, as defined in Section 2.2.2. According to Remark 4.2, $\mathcal{O}_{\mathcal{W}}^M = \mathbf{M}(\mathcal{O}_{\mathcal{W}}, \alpha) = (\mathcal{W}_\alpha \oplus \mathcal{B}_\alpha^\circ(\mathbf{0}))^c$, where the closed set $\mathcal{W}_\alpha$ is defined as per (4.2) for some $\alpha \geq 0$. If one proves that $\mathbf{reach}(\mathcal{W}_\alpha) \geq \alpha$, then, according to Lemma 2.2, one has $\mathbf{reach}(\mathcal{O}_{\mathcal{W}}^M) \geq \alpha$. To that end, we make use of [Rataj and Zähle, 2019, Proposition 4.14] to show that Assumption 4.2 implies that $\mathbf{reach}(\mathcal{W}_\alpha) \geq \alpha$.

We know that for $\mathbf{x} \in \mathcal{W}_\alpha^\circ$, $\mathbf{T}_{\mathcal{W}_\alpha}(\mathbf{x}) = \mathbb{R}^2$, where $\mathbf{T}_{\mathcal{W}_\alpha}(\mathbf{x})$ denotes the tangent cone to the set $\mathcal{W}_\alpha$ at $\mathbf{x}$. Therefore, for all $\mathbf{p} \in \mathcal{W}_\alpha$, one has $\mathbf{p} - \mathbf{x} \in \mathbf{T}_{\mathcal{W}_\alpha}(\mathbf{x})$. This implies that for all $\mathbf{x} \in \mathcal{W}_\alpha^\circ$ and for all $\mathbf{p} \in \mathcal{W}_\alpha$, $d(\mathbf{p} - \mathbf{x}, \mathbf{T}_{\mathcal{W}_\alpha}(\mathbf{x})) = 0$.

Next, we consider the case where $\mathbf{x} \in \partial\mathcal{W}_\alpha$ and $\mathbf{p} \in \mathcal{W}_\alpha$. If $\mathbf{p} - \mathbf{x} \in \mathbf{T}_{\mathcal{W}_\alpha}(\mathbf{x})$, then $d(\mathbf{p} - \mathbf{x}, \mathbf{T}_{\mathcal{W}_\alpha}(\mathbf{x})) = 0$. On the other hand, when $\mathbf{p} - \mathbf{x} \notin \mathbf{T}_{\mathcal{W}_\alpha}(\mathbf{x})$, we define $\mathcal{T}(\mathbf{x}, \mathbf{p}) := \{\mathbf{t} \in \mathbf{T}_{\mathcal{W}_\alpha}(\mathbf{x}) | \mathbf{t} = \underset{\mathbf{q} \in \mathbf{T}_{\mathcal{W}_\alpha}(\mathbf{x}) \setminus \{\mathbf{0}\}}{\arg\min} |\psi(\mathbf{p} - \mathbf{x}, \mathbf{q})|\}$ as the set of all non-zero tangent vectors $\mathbf{t} \in \mathbf{T}_{\mathcal{W}_\alpha}(\mathbf{x})$ such that the absolute value of the angle measured from $\mathbf{p} - \mathbf{x}$ to $\mathbf{t}$ is the smallest. Since $\mathcal{W}_\alpha = \mathcal{W} \setminus \mathcal{D}_\alpha(\mathcal{O}_{\mathcal{W}}^\circ)$, for all $\mathbf{x} \in \partial\mathcal{W}_\alpha$, the set $\mathbf{N}_{\mathcal{W}_\alpha}(\mathbf{x}) \setminus \{\mathbf{0}\}$ is not empty, where $\mathbf{N}_{\mathcal{W}_\alpha}(\mathbf{x})$ represents the normal cone to the set $\mathcal{W}_\alpha$ at $\mathbf{x}$. Therefore, there exists $\mathbf{n} \in \mathbf{N}_{\mathcal{W}_\alpha}(\mathbf{x})$ such that $\|\mathbf{n}\| = 1$ and $\mathbf{n}^\top \mathbf{t} = 0$ for some $\mathbf{t} \in \mathcal{T}(\mathbf{x}, \mathbf{p})$.

Now, one can construct the ball $\mathcal{B}_\beta(\mathbf{x} + \beta\mathbf{n})$ for some $\beta > 0$ such that $\mathbf{p} \in \partial\mathcal{B}_\beta(\mathbf{x} + \beta\mathbf{n})$, as shown in Fig. C.1. It is clear that $\beta \geq \alpha$, otherwise, it will imply that $\mathbf{p} \in \mathcal{B}_\alpha^\circ(\mathbf{x} + \alpha\mathbf{n})$, which does not satisfy Assumption 4.2. Therefore, it can be shown that $d(\mathbf{p} - \mathbf{x}, \mathbf{T}_{\mathcal{W}_\alpha}(\mathbf{x})) = \|\mathbf{p} - \mathbf{x}\|^2/2\beta \leq \|\mathbf{p} - \mathbf{x}\|^2/2\alpha$ for any $\mathbf{x}, \mathbf{p} \in \mathcal{W}_\alpha$. Hence, according to [Rataj and Zähle, 2019, Proposition 4.14], one can conclude that $\mathbf{reach}(\mathcal{W}_\alpha) \geq \alpha$.

C.2 Proof of Lemma 4.2

Let us assume that the modified obstacle $\mathcal{O}_{i,\alpha}^M$ is not a connected set, then it implies that there exists two disjoint subsets $\mathcal{M}_1 \subset \mathcal{O}_{i,\alpha}^M$ and $\mathcal{M}_2 \subset \mathcal{O}_{i,\alpha}^M$ such that $\mathcal{M}_1 \cup \mathcal{M}_2 = \mathcal{O}_{i,\alpha}^M$ and $\mathcal{M}_1 \cap \mathcal{M}_2 = \emptyset$, [Willard, 2012, Definition 16.1]. By construction in (4.4), there

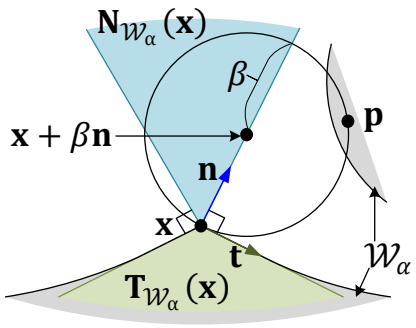

Figure C.1: Illustration of the case where $\mathbf{x} \in \partial\mathcal{W}_\alpha$ and $\mathbf{p} \in \mathcal{W}_\alpha$ such that $\mathbf{p}-\mathbf{x} \notin \mathbf{T}_{\mathcal{W}_\alpha}(\mathbf{x})$.

exists two non-empty set $\mathcal{O}_{\mathbb{C}} \subset \mathcal{O}_{i,\alpha}$ and $\mathcal{O}_{\mathbb{D}} \subset \mathcal{O}_{i,\alpha}$ such that $\mathcal{O}_{\mathbb{C}} \subset \mathcal{M}_1$, $\mathcal{O}_{\mathbb{D}} \subset \mathcal{M}_2$ and $\mathcal{O}_{\mathbb{C}} \cup \mathcal{O}_{\mathbb{D}} = \mathcal{O}_{i,\alpha}$. Note that, the distance $d(\mathcal{M}_1, \mathcal{M}_2)$ can not be greater than or equal to 2α. Otherwise, as the operator $\mathbf{M}$ is extensive, see Remark 4.1, it implies that $d(\mathcal{O}_{\mathbb{C}}, \mathcal{O}_{\mathbb{D}}) \geq 2\alpha$. However, according to (4.7), one has $d(\mathcal{O}_{\mathbb{C}}, \mathcal{O}_{\mathbb{D}}) < 2\alpha$. Hence, one can conclude that $0 < d(\mathcal{M}_1, \mathcal{M}_2) < 2\alpha$. Therefore, there exists $\mathbf{q}_1 \in \mathcal{M}_1$ and $\mathbf{q}_2 \in \mathcal{M}_2$ such that $0 < d(\mathbf{q}_1, \mathbf{q}_2) = d(\mathcal{M}_2, \mathcal{M}_2) < 2\alpha$. This implies that for $\mathbf{q} = 0.5\mathbf{q}_1 + 0.5\mathbf{q}_2 \in \mathcal{D}_\alpha(\mathcal{O}^M_{i,\alpha})$, one has $\mathbf{card}(\mathcal{PJ}(\mathbf{q}, \mathcal{O}^M_{i,\alpha})) > 1$, which cannot be the case as per Lemma 4.1. Hence, the modified obstacle $\mathcal{O}^M_{i,\alpha}$ is a connected set.

C.3 Proof of Lemma 4.3

According to Assumption 4.1, the set $\mathcal{W}^\circ_{r_a}$ is a pathwise connected set. Hence, it is evident that there exist a scalar $\bar{\delta}_1 > r_a$ such that for all $\delta \in (r_a, \bar{\delta}_1]$, the $\delta-$eroded obstacle-free workspace $\mathcal{W}_\delta$ is pathwise connected. Assumption 4.1 also assumes that the target location at the origin is in the set $\mathcal{W}^\circ_{r_a}$. Hence, the distance $d(\mathbf{0}, \mathcal{W}_{r_a}) > 0$. Then, it is straight forward to notice that there exists $\bar{\delta}_2 > r_a$ such that for any $\delta \in (r_a, \bar{\delta}_2]$ the distance $d(\mathbf{0}, \mathcal{W}_\delta) < \delta - r_a$. Then, one can choose $\bar{\alpha} = \min\{\bar{\delta}_1, \bar{\delta}_2\}$ to satisfy Lemma 4.3.

C.4 Proof of Lemma 4.4

Since the obstacle reshaping operator $\mathbf{M}$ is *idempotent*, we have $\mathbf{M}(\mathcal{O}_{\mathcal{W}}, \alpha) = \mathbf{M}(\mathcal{O}^M_{\mathcal{W}}, \alpha)$. Therefore, according to (4.4), $\mathcal{O}_{\mathcal{W}} \oplus \mathcal{B}^\circ_\alpha(\mathbf{0}) = \mathcal{O}^M_{\mathcal{W}} \oplus \mathcal{B}^\circ_\alpha(\mathbf{0})$. As a result, according to (4.2) and (4.3), the $\alpha-$eroded obstacle-free workspace $\mathcal{W}_\alpha$ is equivalent to the $\alpha-$eroded modified obstacle-free workspace $\mathcal{V}_\alpha$. Hence, if one chooses α as per Lemma 4.3, then the set $\mathcal{V}_\alpha$ is pathwise connected. As a result, the modified obstacle-free workspace $\mathcal{V}_{r_a}$ is also pathwise connected. Moreover, according to Lemma 4.3, the distance between the origin and the set $\mathcal{V}_\alpha$ is less than $\alpha - r_a$. Since the distance between the sets $\partial\mathcal{V}_\alpha$ and $\partial\mathcal{V}_{r_a}$ is $\alpha - r_a$, it is evident that the origin belongs to the interior of the modified obstacle-free workspace $\mathcal{V}_{r_a}$.

C.5 Proof of Lemma 4.5

We consider a connected modified obstacle $\mathcal{O}^M_{i,\alpha}, i \in \mathbb{I}$, as stated in Lemma 4.2, and proceed by proving the following two claims:

Claim 1: For every $\mathbf{h} \in \mathcal{J}_0^{\mathcal{W}} \cap \partial\mathcal{D}_\beta(\mathcal{O}^M_{i,\alpha}), \beta \in [r_a, r_a+\gamma_s]$ and any $\mathbf{p} \in \mathcal{PJ}(\mathbf{0}, \partial\mathcal{D}_\beta(\mathcal{O}^M_{i,\alpha}))$, one has $d(\mathbf{h}, \mathcal{B}_{2\delta}(\mathbf{p})) \geq \epsilon_h$, where

$$\epsilon_h = \sqrt{(d(\mathbf{0}, \mathcal{O}^M_{\mathcal{W}})^2 - r_a^2)} - d(\mathbf{0}, \mathcal{D}_{r_a}(\mathcal{O}^M_{\mathcal{W}})),$$

and $\delta = \min\{d(\mathbf{0}, \mathcal{O}^M_{\mathcal{W}}) - r_a, \beta - r_a\}$.

Claim 2: For $m \in \{-1, 1\}$, one has $\mathcal{H}_{\mathbf{p}} := \mathcal{B}_\delta(\mathbf{p}) \cap \mathcal{N}_\gamma(\mathcal{D}_{r_a}(\mathcal{O}^M_{i,\alpha})) \subset \mathcal{R}_a$, where the location $\mathbf{p}$ and the scalar parameter δ are defined in claim 1 above.

Claim 1 states that for any connected modified obstacle $\mathcal{O}^M_{i,\alpha}$, the distance between any point $\mathbf{h}$, which is located in the jump set of the *move-to-target* mode associated with this modified obstacle at some distance $\beta \in [r_a, r_a + \gamma_s]$ from it *i.e.*, $\mathbf{h} \in \mathcal{J}_0^{\mathcal{W}} \cap \partial\mathcal{D}_\beta(\mathcal{O}^M_{i,\alpha}), \beta \in [r_a, r_a + \gamma_s]$, and the Euclidean balls of radius 2δ centered at the set of projections of the target onto the set $\partial\mathcal{D}_\beta(\mathcal{O}^M_{i,\alpha})$ is always greater than or equal to ϵ_h *i.e.*, $d(\mathbf{h}, \mathcal{B}_{2\delta}(\mathbf{p})) \geq \epsilon_h$, where $\mathbf{p} \in \mathcal{PJ}(\mathbf{0}, \mathcal{D}_\beta(\mathcal{O}^M_{i,\alpha}))$ and the scalar parameter $\delta = \min\{\beta - r_a, d(\mathbf{0}, \mathcal{O}^M_{i,\alpha}) - r_a\}$.

Claim 2 states that the set $\mathcal{H}_{\mathbf{p}}$, which represents the intersection between the δ-neighbourhood of the set of projections of the target onto the set $\partial\mathcal{D}_\beta(\mathcal{O}^M_{i,\alpha})$ *i.e.*, $\mathcal{B}_\delta(\mathbf{p}), \mathbf{p} \in \mathcal{PJ}(\mathbf{0}, \mathcal{D}_\beta(\mathcal{O}^M_{i,\alpha}))$ and the $\gamma-$neighbourhood of the dilated modified obstacle, represented by $\mathcal{N}_\gamma(\mathcal{D}_{r_a}(\mathcal{O}^M_{i,\alpha}))$ is a subset of the *always exit* region $\mathcal{R}_a$ (4.15). This implies that if $\bar{\epsilon} \in (0, \epsilon_h]$, then $\mathcal{H}_{\mathbf{p}} \subset \mathcal{ER}^{\mathbf{h}}_m$, where the set $\mathcal{ER}^{\mathbf{h}}_m$ is defined in (4.22).

C.5.1 Proof of claim 1

We aim to obtain an expression for $\|\mathbf{h}_\beta\| - \|\mathbf{p}_\beta\|$, for $\beta \in [r_a, r_a + \gamma_s]$, where

$$\mathbf{h}_\beta = \underset{\mathbf{h} \in \mathcal{J}_0^{\mathcal{W}} \cap \partial\mathcal{D}_\beta(\mathcal{O}^M_{i,\alpha})}{\operatorname{argmin}} \|\mathbf{h}\|, \tag{C.1}$$

and the location $\mathbf{p}_\beta \in \mathcal{PJ}(\mathbf{0}, \partial\mathcal{D}_\beta(\mathcal{O}^M_{i,\alpha}))$.

Now, depending on the shape of the obstacle there can be two possibilities as follows:

Case A: When $\mathbf{h}_\beta \in \partial\mathcal{D}_\beta(\mathcal{O}^M_{i,\alpha}) \cap \mathcal{CH}(\mathbf{0}, \mathcal{O}^M_{i,\alpha})$, as shown in Fig. C.2. Notice that the line segment joining the location $\mathbf{h}_\beta$ and the origin passes through the modified obstacle $\mathcal{O}^M_{i,\alpha}$ *i.e.*, $\mathcal{L}_s(\mathbf{h}_\beta, \mathbf{0}) \cap \mathcal{O}^M_{i,\alpha} \neq \emptyset$. Hence, a part of this line segment belongs to the modified obstacle $\mathcal{O}^M_{i,\alpha}$. In other words, there exist locations $\mathbf{b}$ and $\mathbf{e}$, where $\mathbf{b}, \mathbf{e} \in \partial\mathcal{O}^M_{i,\alpha}$ such that $\mathcal{L}_s(\mathbf{b}, \mathbf{e}) \subset \mathcal{L}_s(\mathbf{h}_\beta, \mathbf{0}) \cap \mathcal{O}^M_{i,\alpha}$, as shown in Fig. C.2. We further consider two more sub-cases based on the distance between the target $\mathbf{0}$ and the modified obstacle $\mathcal{O}^M_{i,\alpha}$. Note that, as per Assumption 4.1, $d(\mathbf{0}, \mathcal{O}^M_{i,\alpha}) > r_a$.

Case A1: When $d(\mathbf{0}, \mathcal{O}^M_{i,\alpha}) \geq \beta$, as shown in Fig. C.2a, one has $\|\mathbf{h}_\beta\| - \|\mathbf{p}_\beta\| \geq \|\mathbf{h}_\beta\| - \|\mathbf{e}\| + \|\mathbf{b}\| - \|\mathbf{p}_\beta\|$.

Since $\mathbf{h}_\beta \in \partial\mathcal{D}_\beta(\mathcal{O}^M_{i,\alpha}), \{\mathbf{b}, \mathbf{e}\} \subset \partial\mathcal{O}^M_{i,\alpha}$ and $d(\mathbf{0}, \mathcal{O}^M_{i,\alpha}) \geq \beta$, one has $\|\mathbf{h}_\beta\| - \|\mathbf{e}\| \geq \beta$ and $\|\mathbf{b}\| \geq \beta + \|\mathbf{p}_\beta\|$. Hence,

$$\|\mathbf{h}_\beta\| - \|\mathbf{p}_\beta\| \geq 2\beta = 2(\beta - r_a) + 2r_a,$$

$$d(\mathbf{h}_\beta, \mathcal{B}_{2(\beta-r_a)}(\mathbf{p}_\beta)) \geq 2r_a. \tag{C.2}$$

Case A2: When $r_a < d(\mathbf{0}, \mathcal{O}^M_{i,\alpha}) < \beta$, as shown in Fig. C.2b, one has $\|\mathbf{h}_\beta\| - \|\mathbf{p}_\beta\| \geq \|\mathbf{h}_\beta\| - \|\mathbf{e}\| + \|\mathbf{b}\| - \|\mathbf{p}_\beta\|$.

Since $\mathbf{h}_\beta \in \partial\mathcal{D}_\beta(\mathcal{O}^M_{i,\alpha}), \{\mathbf{b}, \mathbf{e}\} \subset \partial\mathcal{O}^M_{i,\alpha}$, $r_a < d(\mathbf{0}, \mathcal{O}^M_{i,\alpha}) < \beta$ and by construction, as shown in Fig. C.2b, one has $\|\mathbf{h}_\beta\| - \|\mathbf{e}\| \geq \beta$ and $\|\mathbf{b}\| \geq \beta - \|\mathbf{p}_\beta\| = r_a + \|\mathbf{p}_{r_a}\|$. Hence, as $\|\mathbf{p}_{r_a}\| = d(\mathbf{0}, \mathcal{D}_{r_a}(\mathcal{O}^M_{i,\alpha}))$, one has

$$\begin{aligned} \|\mathbf{h}_\beta\| - \|\mathbf{p}_\beta\| \geq 2\beta - 2\|\mathbf{p}_\beta\| = 2\|\mathbf{p}_{r_a}\| + 2r_a, \\ d(\mathbf{h}_\beta, \mathcal{B}_{2d(\mathbf{0}, \mathcal{D}_{r_a}(\mathcal{O}^M_{i,\alpha}))}(\mathbf{p}_\beta)) > 2r_a. \end{aligned} \tag{C.3}$$

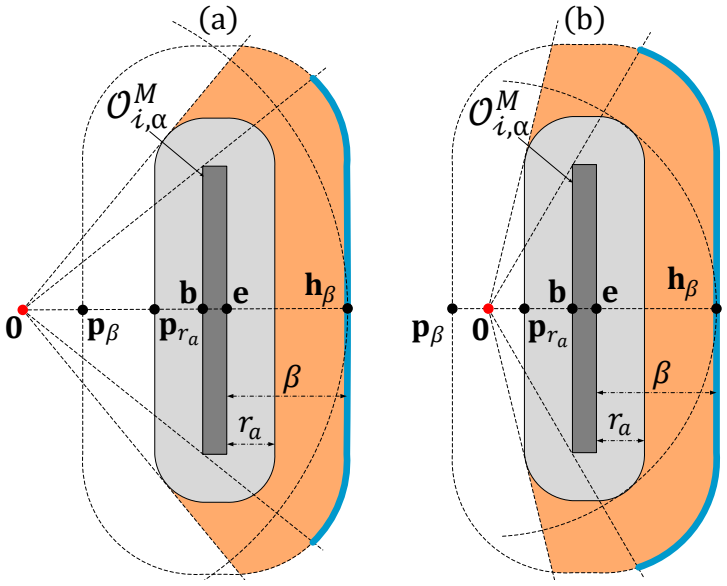

Figure C.2: The diagrammatic representation for the Case A in the proof of Lemma 4.5. (a) $d(\mathbf{0}, \mathcal{O}^M_{i,\alpha}) \geq \beta$, (b) $r_a < d(\mathbf{0}, \mathcal{O}^M_{i,\alpha}) < \beta$.

Case B: When $\mathbf{h}_\beta \in \mathcal{G}$, where the set $\mathcal{G} := \left(\partial\mathcal{D}_\beta(\mathcal{O}^M_{i,\alpha}) \cap \mathcal{CH}(\mathbf{0}, \mathcal{D}_{r_a}(\mathcal{O}^M_{i,\alpha}))\right) \setminus \mathcal{CH}(\mathbf{0}, \mathcal{O}^M_{i,\alpha})$. In other words, when the line segment joining the locations $\mathbf{h}_\beta$ and the target at the origin does not intersect with the interior of the modified obstacle $\mathcal{O}^M_{i,\alpha}$ *i.e.*, $\mathcal{L}_s(\mathbf{h}_\beta, \mathbf{0}) \cap (\mathcal{O}^M_{i,\alpha})^\circ = \emptyset$, as shown in Fig. C.2. To proceed with the proof, we use the following fact which states that the projection of the target location onto the set $\mathcal{G}$ always belongs to the intersection between the boundary of the conic hull $\mathcal{CH}(\mathbf{0}, \mathcal{D}_{r_a}(\mathcal{D}_{r_a}(\mathcal{O}^M_{i,\alpha})))$ and the set G.

Fact 2: One has $\mathcal{PJ}(\mathbf{0}, \mathcal{G}) \subset \mathcal{G} \cap \partial\mathcal{CH}(\mathbf{0}, \mathcal{D}_{r_a}(\mathcal{O}^M_{i,\alpha}))$.

Sketch of the proof: The proof is by contradiction. We assume that there exists a location $\mathbf{x}$ in the set $\mathcal{PJ}(\mathbf{0}, \mathcal{G})$ that does not belong to the intersection between the set $\mathcal{G}$ and the boundary of the conic hull to the set $\mathcal{D}_{r_a}(\mathcal{O}^M_{i,\alpha})$ *i.e.*, $\mathbf{x} \in \mathcal{PJ}(\mathbf{0}, \mathcal{G})$ and $\mathbf{x} \notin \mathcal{G} \cap \partial\mathcal{CH}(\mathbf{0}, \mathcal{D}_{r_a}(\mathcal{O}^M_{i,\alpha}))$. We know that the curve $\mathcal{G}$ belongs to the boundary of the $\beta-$dilated modified obstacle *i.e.*, $\mathcal{G} \subset \partial\mathcal{D}_\beta(\mathcal{O}^M_{i,\alpha})$. As a result, there exists a partial section of the boundary of the modified obstacle $\mathcal{O}^M_{i,\alpha}$, let say $\mathcal{M} \subset \partial\mathcal{O}^M_{i,\alpha}$ with $\mathbf{x} \in \mathcal{D}_\beta(\mathcal{M})$

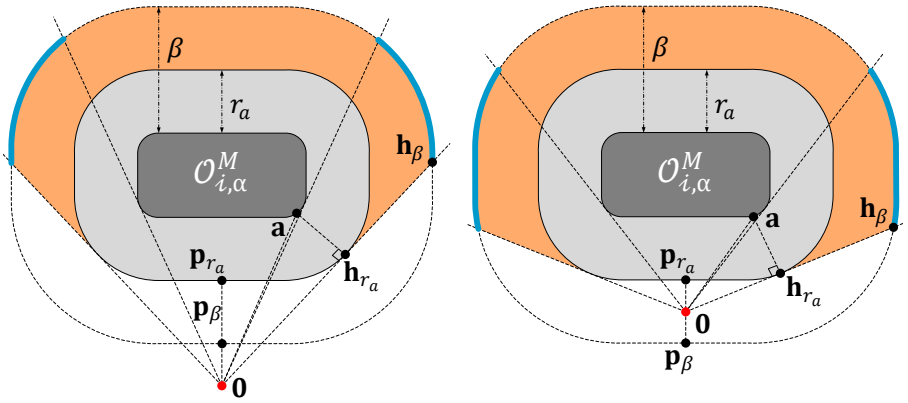

Figure C.3: The diagrammatic representation for the Case B in the proof of Lemma 4.5. (a) $d(\mathbf{0}, \mathcal{O}^M_{i,\alpha}) \geq \beta$, (b) $r_a < d(\mathbf{0}, \mathcal{O}^M_{i,\alpha}) < \beta$.

such that this curve $\mathcal{M}$ belongs to the relative complement of the conic hull $\mathcal{CH}(\mathbf{0}, \mathcal{O}^M_{i,\alpha})$ with respect to the conic hull $\mathcal{CH}(\mathbf{0}, \mathcal{D}_{r_a}(\mathcal{O}^M_{i,\alpha}))$ *i.e.*, $\mathcal{M} \in \mathcal{CH}(\mathbf{0}, \mathcal{D}_{r_a}(\mathcal{O}^M_{i,\alpha})) \setminus \mathcal{CH}(\mathbf{0}, \mathcal{O}^M_{i,\alpha})$. However, by construction of the set $\mathcal{G}$, the intersection between the modified obstacle $\mathcal{O}^M_{i,\alpha}$ and the region $\mathcal{CH}(\mathbf{0}, \mathcal{D}_{r_a}(\mathcal{O}^M_{i,\alpha})) \setminus \mathcal{CH}(\mathbf{0}, \mathcal{O}^M_{i,\alpha})$ must be an empty set. Therefore, we arrive at a contradiction.

According to Fact 2, $\mathbf{h}_\beta \in \mathcal{G} \cap \partial\mathcal{CH}(\mathbf{0}, \mathcal{D}_{r_a}(\mathcal{D}_{r_a}(\mathcal{O}^M_{i,\alpha})))$, as shown in Fig. C.3. Similar to case A, we consider two sub-cases based on the distance between the target $\mathbf{0}$ and the modified obstacle $\mathcal{O}^M_{i,\alpha}$.

Case B1: When $d(\mathbf{0}, \mathcal{O}^M_{i,\alpha}) \geq \beta$, as shown in Fig C.3a, one has

$$\|\mathbf{h}_\beta\| - \|\mathbf{p}_\beta\| = \|\mathbf{h}_\beta\| - \|\mathbf{h}_{r_a}\| + \|\mathbf{h}_{r_a}\| - \|\mathbf{p}_\beta\|. \tag{C.4}$$

Since $\mathbf{h}_\beta \in \partial\mathcal{D}_\beta(\mathcal{O}^M_{i,\alpha})$ and $\mathbf{h}_{r_a} \in \partial\mathcal{D}_{r_a}(\mathcal{O}^M_{i,\alpha})$, one has $\|\mathbf{h}_\beta\| - \|\mathbf{h}_{r_a}\| \geq \beta - r_a$. Let $\mathbf{a} \in \partial\mathcal{O}^M_{i,\alpha}$ be the location such that the lines $\mathcal{L}(\mathbf{a}, \mathbf{h}_{r_a})$ and $\mathcal{L}(\mathbf{h}_{r_a}, \mathbf{0})$ are perpendicular, as shown in Fig. C.2a. Note that, as the line $\mathcal{L}(\mathbf{h}_{r_a}, \mathbf{0})$ is tangent to the set $\mathcal{D}_{r_a}(\mathcal{O}^M_{i,\alpha})$ at $\mathbf{h}_{r_a}$, the distance $d(\mathbf{h}_{r_a}, \mathbf{a}) = r_a$. Hence, one has

$$\|\mathbf{h}_{r_a}\| = \sqrt{\|\mathbf{a}\|^2 - d(\mathbf{h}_{r_a}, \mathbf{a})^2} \geq \sqrt{d(\mathbf{0}, \mathcal{O}^M_{i,\alpha})^2 - r_a^2}. \tag{C.5}$$

After substituting (C.5) in (C.4), one gets

$$\|\mathbf{h}_\beta\| - \|\mathbf{p}_\beta\| \geq \beta - r_a + \sqrt{d(\mathbf{0}, \mathcal{O}^M_{i,\alpha})^2 - r_a^2} - \|\mathbf{p}_\beta\|.$$

Since $d(\mathbf{0}, \mathcal{O}^M_{i,\alpha}) \geq \beta$, $\|\mathbf{p}_{r_a}\| - \|\mathbf{p}_\beta\| = \beta - r_a$. Hence, one has

$$\|\mathbf{h}_\beta\| - \|\mathbf{p}_\beta\| \geq 2(\beta - r_a) + \sqrt{d(\mathbf{0}, \mathcal{O}^M_{i,\alpha})^2 - r_a^2} - \|\mathbf{p}_{r_a}\|,$$

$$d(\mathbf{h}_\beta, \mathcal{B}_{2(\beta - r_a)}(\mathbf{p}_\beta)) \geq \sqrt{d(\mathbf{0}, \mathcal{O}^M_{i,\alpha})^2 - r_a^2} - \|\mathbf{p}_{r_a}\|. \tag{C.6}$$

Case B2: When $r_a < d(\mathbf{0}, \mathcal{O}^M_{i,\alpha}) < \beta$, as shown in Fig. C.3b. According to (C.4), (C.5) and the fact that $\|\mathbf{h}_\beta\| - \|\mathbf{h}_{r_a}\| \geq \beta - r_a$, one has

$$\|\mathbf{h}_\beta\| - \|\mathbf{p}_\beta\| \geq \beta - r_a + \sqrt{d(\mathbf{0}, \mathcal{O}^M_{i,\alpha})^2 - r_a^2} - \|\mathbf{p}_\beta\|,$$

Since $r_a < d(\mathbf{0}, \mathcal{O}_{i,\alpha}^M) < \beta$, $\|\mathbf{p}_\beta\| + \|\mathbf{p}_{r_a}\| = \beta - r_a$. Hence, one has

$$\|\mathbf{h}_\beta\| - \|\mathbf{p}_\beta\| \geq 2\|\mathbf{p}_{r_a}\| + \sqrt{d(\mathbf{0}, \mathcal{O}_{i,\alpha}^M)^2 - r_a^2} - \|\mathbf{p}_{r_a}\|,$$
$$d(\mathbf{h}_\beta, \mathcal{B}_{2\|\mathbf{p}_{r_a}\|}(\mathbf{p}_\beta)) \geq \sqrt{d(\mathbf{0}, \mathcal{O}_{i,\alpha}^M)^2 - r_a^2} - \|\mathbf{p}_{r_a}\|. \tag{C.7}$$

Now, considering all the obstacles *i.e.*, for all $i \in \mathbb{I}$, according to (C.2), (C.3), (C.6) and (C.7), one has

$$d(\mathbf{h}_\beta, \mathcal{B}_{2\delta}(\mathbf{p}_\beta)) \geq \epsilon_h, \tag{C.8}$$

where $\delta = \min\left\{\beta - r_a, \min_{i\in\mathbb{I}}\{d(\mathbf{0}, \mathcal{O}_{i,\alpha}^M) - r_a\}\right\} = \min\{\beta - r_a, d(\mathbf{0}, \mathcal{O}_{\mathcal{W}}^M) - r_a\}$ and ϵ_h is evaluated as

$$\epsilon_h = \min\left\{2r_a, \min_{i\in\mathbb{I}}\left\{\sqrt{d(\mathbf{0}, \mathcal{O}_{i,\alpha}^M)^2 - r_a^2} - d(\mathbf{0}, \mathcal{D}_{r_a}(\mathcal{O}_{i,\alpha}^M))\right\}\right\},$$
$$= \min\{2r_a, \sqrt{d(\mathbf{0}, \mathcal{O}_{\mathcal{W}}^M)^2 - r_a^2} - d(\mathbf{0}, \mathcal{D}_{r_a}(\mathcal{O}_{\mathcal{W}}^M))\}. \tag{C.9}$$

It is clear that for $n > 0$, the function $f(k) = \sqrt{k^2 - n^2} - (k - n), d \in [n, \infty)$, is monotonically increasing and $\lim_{k\to\infty} f(k) = n$. Hence, according to Assumption 4.1, as $d(\mathbf{0}, \mathcal{O}_{\mathcal{W}}^M) > r_a > 0$, one has

$$\sqrt{(d(\mathbf{0}, \mathcal{O}_{\mathcal{W}}^M)^2 - r_a^2)} - d(\mathbf{0}, \mathcal{D}_{r_a}(\mathcal{O}_{\mathcal{W}}^M)) < r_a,$$

irrespective of the locations of obstacles relative to the target location. As a result,

$$\epsilon_h = \min\{2r_a, \sqrt{d(\mathbf{0}, \mathcal{O}_{\mathcal{W}}^M)^2 - r_a^2} - d(\mathbf{0}, \mathcal{D}_{r_a}(\mathcal{O}_{\mathcal{W}}^M))\}$$
$$= \sqrt{(d(\mathbf{0}, \mathcal{O}_{\mathcal{W}}^M)^2 - r_a^2)} - d(\mathbf{0}, \mathcal{D}_{r_a}(\mathcal{O}_{\mathcal{W}}^M)).$$

C.5.2 Proof of claim 2

In this proof, our goal is to show that the set $\mathcal{H}_\mathbf{p} = \mathcal{B}_\delta(\mathbf{p}) \cap \mathcal{N}_\gamma(\mathcal{D}_{r_a}(\mathcal{O}_{i,\alpha}^M))$ belongs to the *always exit* region $\mathcal{R}_a$, for any $\mathbf{p} \in \mathcal{PJ}(\mathbf{0}, \partial\mathcal{D}_\beta(\mathcal{O}_{i,\alpha}^M))$ and $\delta = \min\{d(\mathbf{0}, \mathcal{O}_{\mathcal{W}}^M) - r_a, \beta - r_a\}$, where $\beta \in [r_a, r_a + \gamma_s]$. Based on the distance of the target location from the modified obstacle $\mathcal{O}_{i,\alpha}^M$, we consider two cases as follows:

Case 1: When $d(\mathbf{0}, \mathcal{O}_{i,\alpha}^M) \geq \beta$, as shown in Fig. C.2a and Fig. C.3a. Since $d(\mathbf{0}, \mathcal{O}_{i,\alpha}^M) \geq \beta$, for any $\mathbf{p} \in \mathcal{PJ}(\mathbf{0}, \mathcal{D}_\beta(\mathcal{O}_{i,\alpha}^M))$, one has $\mathcal{B}_{\|\mathbf{p}\|+\delta}(\mathbf{0}) \subset \mathcal{B}_{d(\mathbf{0}, \mathcal{D}_{r_a}(\mathcal{O}_{i,\alpha}^M))}(\mathbf{0})$, where $\delta = \min\{\beta - r_a, d(\mathbf{0}, \mathcal{O}_{i,\alpha}^M) - r_a\} = \beta - r_a$. Hence, for any $\mathbf{p} \in \mathcal{PJ}(\mathbf{0}, \mathcal{D}_\beta(\mathcal{O}_{i,\alpha}^M))$, it is clear that $\mathcal{B}_\delta(\mathbf{p}) \subset \mathcal{B}_{d(\mathbf{0}, \mathcal{D}_{r_a}(\mathcal{O}_{i,\alpha}^M))}(\mathbf{0})$. Moreover, $\mathcal{B}_{d(\mathbf{0}, \mathcal{D}_{r_a}(\mathcal{O}_{i,\alpha}^M))}(\mathbf{0}) \cap \left(\mathcal{D}_{r_a}(\mathcal{O}_{i,\alpha}^M)\right)^\circ = \emptyset$. As a result, $\mathcal{B}_\delta(\mathbf{p}) \cap (\mathcal{D}_{r_a}(\mathcal{O}_{i,\alpha}^M))^\circ = \emptyset$. Additionally, as $\mathbf{p} \in \partial\mathcal{D}_\beta(\mathcal{O}_{i,\alpha}^M)$, where $\beta \in [r_a, r_a + \gamma_s]$, one has $\mathcal{B}_\delta(\mathbf{p}) \cap \mathcal{N}_\gamma(\mathcal{D}_{r_a}(\mathcal{O}_{i,\alpha}^M)) \neq \emptyset$. Hence, according to (4.15), one can conclude that $\mathcal{H}_\mathbf{p} \subset \mathcal{R}_a$.

Case 2: When $r_a < d(\mathbf{0}, \mathcal{O}_{i,\alpha}^M) < \beta$, as shown in Fig. C.2b and Fig. C.3b. According to Lemmas 2.3 and 4.1, $\mathbf{card}(\mathcal{PJ}(\mathbf{0}, \mathcal{D}_{r_a}(\mathcal{O}_{i,\alpha}^M))) = 1$, *i.e.*, $\Pi(\mathbf{0}, \mathcal{D}_{r_a}(\mathcal{O}_{i,\alpha}^M))$ is unique.

Since, as per Lemma 2.3, $\mathbf{reach}(\mathcal{D}_{r_a}(\mathcal{O}_{i,\alpha}^M)) = \alpha - r_a$, according to [Rataj and Zähle, 2019, Lemma 4.5], one has $(\mathcal{B}_{\alpha-r_a}(\mathbf{q}))^\circ \cap \mathcal{D}_{r_a}(\mathcal{O}_{i,\alpha}^M) = \emptyset$, where $\mathbf{q} = \Pi(\mathbf{0}, \mathcal{D}_{r_a}(\mathcal{O}_{i,\alpha}^M)) + (\alpha - r_a)\frac{\mathbf{0}-\Pi(\mathbf{0},\mathcal{D}_{r_a}(\mathcal{O}_{i,\alpha}^M))}{\|\mathbf{0}-\Pi(\mathbf{0},\mathcal{D}_{r_a}(\mathcal{O}_{i,\alpha}^M))\|}$. Now, notice that, for the location $\mathbf{p}$ in the set $\partial\mathcal{D}_\beta(\mathcal{O}_{i,\alpha}^M) \cap \mathcal{L}_s(\mathbf{q}, \Pi(\mathbf{0}, \mathcal{D}_{r_a}(\mathcal{O}_{i,\alpha}^M)))$, one has $\mathcal{B}_\delta(\mathbf{p}) \subset \mathcal{B}_{\alpha-r_a}(\mathbf{q})$, where $\delta = \min\{\beta - r_a, d(\mathbf{0}, \mathcal{O}_{i,\alpha}^M) - r_a\} = d(\mathbf{0}, \mathcal{O}_{i,\alpha}^M) - r_a < \alpha - r_a$. As a result, if one shows that $\mathbf{p} \in \mathcal{PJ}(\mathbf{0}, \partial\mathcal{D}_\beta(\mathcal{O}_{i,\alpha}^M))$ and $\mathbf{card}(\mathcal{PJ}(\mathbf{0}, \partial\mathcal{D}_\beta(\mathcal{O}_{i,\alpha}^M))) = 1$, then, according to (4.15), it is straightforward to prove that $\mathcal{H}_\mathbf{p} \subset \mathcal{R}_a$, where the set $\mathcal{H}_\mathbf{p}$ is defined in claim 2.

Let us assume that $d(\mathbf{0}, \mathcal{O}_{i,\alpha}^M) = \eta$, where $r_a < \eta < \beta < \alpha$. Notice that, $\mathbf{0} \in \mathcal{L}(\mathbf{q}, \Pi(\mathbf{0}, \mathcal{D}_{r_a}(\mathcal{O}_{i,\alpha}^M)))$. Since, $\mathbf{p} \in \mathcal{L}_s(\mathbf{q}, \Pi(\mathbf{0}, \mathcal{D}_{r_a}(\mathcal{O}_{i,\alpha}^M))) \cap \partial\mathcal{D}_\beta(\mathcal{O}_{i,\alpha}^M)$, it is clear that $d(\mathbf{p}, \Pi(\mathbf{0}, \mathcal{D}_{r_a}(\mathcal{O}_{i,\alpha}^M))) = \beta - r_a$. Therefore, one has $d(\mathbf{0}, \mathbf{p}) = \beta - \eta$. Moreover, according to Lemmas 2.2 and 4.1, the set $\mathcal{M} := (\mathcal{O}_{i,\alpha}^M \oplus \mathcal{B}_\alpha(\mathbf{0}))^c$ has the reach equal to α, *i.e.*, $\mathbf{reach}(\mathcal{M}) = \alpha$. Now, notice that, for $\beta \in [r_a, r_a + \gamma_s]$, $\partial\mathcal{D}_\beta(\mathcal{O}_{i,\alpha}^M) = \partial\mathcal{D}_{\alpha-\beta}(\mathcal{M})$. Hence, $\mathbf{0} \in \partial\mathcal{D}_{\alpha-\eta}(\mathcal{M})$ and $\mathbf{p} \in \partial\mathcal{D}_{\alpha-\beta}(\mathcal{M})$. Then, according to Lemma 2.3, one has $\mathbf{card}(\mathcal{PJ}(\mathbf{0}, \partial\mathcal{D}_{\alpha-\beta}(\mathcal{M}))) = \mathbf{card}(\mathcal{PJ}(\mathbf{0}, \partial\mathcal{D}_\beta(\mathcal{O}_{i,\alpha}^M))) = 1$. Moreover, as $d(\mathbf{0}, \mathbf{p}) = \beta - \eta$, one can conclude that $\mathbf{p} \in \mathcal{PJ}(\mathbf{0}, \partial\mathcal{D}_\beta(\mathcal{O}_{i,\alpha}^M))$.

C.6 Proof of Lemma 4.6

The flow set $\mathcal{F}$ and the jump set $\mathcal{J}$, defined in (4.25) and (4.26) are closed subsets of $\mathbb{R}^2 \times \mathbb{R}^2 \times \mathbb{M}$. The flow map $\mathbf{F}$, given in (4.29), is continuous on $\mathcal{F}_0$. For each $\mathbf{x} \in \mathcal{N}_\beta(\mathcal{D}_{r_a}(\mathcal{O}_\mathcal{W}^M)), \beta \in [r_a, \alpha)$, according to Lemma 4.1, the set $\mathcal{PJ}(\mathbf{x}, \mathcal{O}_\mathcal{W}^M)$ is a singleton. Then, for $\mathbf{x} \in \mathcal{N}_\beta(\mathcal{D}_{r_a}(\mathcal{O}_\mathcal{W}^M)), \beta \in [r_a, \alpha)$, $\Pi(\mathbf{x}, \mathcal{O}_\mathcal{W}^M)$ is continuous with respect to $\mathbf{x}$. As a result, $\mathbf{F}$ is continuous on $\mathcal{F}_m, m \in \{-1, 1\}$. Hence $\mathbf{F}$ is continuous on $\mathcal{F}$. The jump map $\mathbf{J}$, defined in (4.29), is single-valued on $\mathcal{J}_m, m \in \{-1, 1\}$ (4.28). Also, $\mathbf{J}$ has a closed graph relative to $\mathcal{J}_0$ (4.26), as it is allowed to be set-valued whenever $\mathbf{x} \in \mathcal{J}_0$. Hence, according to [Goebel et al., 2012, Lemma 5.10], $\mathbf{J}$ is outer semi-continuous and locally bounded relative to $\mathcal{J}$.

C.7 Proof of Lemma 4.7

First we prove that the union of the flow and jump sets covers exactly the obstacle-free state space $\mathcal{K}$. For $m = 0$, according to (4.20) and (4.19), by construction we have $\mathcal{F}_0^\mathcal{W} \cup \mathcal{J}_0^\mathcal{W} = \mathcal{V}_{r_a}$. Similarly, for $m \in \{-1, 1\}$, according to (4.24) and (4.21), by construction we have $\mathcal{F}_m^\mathcal{W} \cup \mathcal{J}_m^\mathcal{W} = \mathcal{V}_{r_a}$. Inspired by [Berkane et al., 2021b, Appendix 11], the satisfaction of the following equation:

$$\mathcal{F}_m^\mathcal{W} \cup \mathcal{J}_m^\mathcal{W} = \mathcal{V}_{r_a}, m \in \mathbb{M}, \tag{C.10}$$

along with (4.25) and (4.26) implies $\mathcal{F} \cup \mathcal{J} = \mathcal{K}$.

Now, inspired by [Berkane et al., 2021b, Appendix 1], for the hybrid closed-loop system (4.29), with data $\mathcal{H} = (\mathcal{F}, \mathbf{F}, \mathcal{J}, \mathbf{J})$, define $\mathbf{S}_\mathcal{H}(\mathcal{K})$ as the set of all maximal solutions ξ to $\mathcal{H}$ with $\xi(0,0) \in \mathcal{K}$. Since $\mathcal{F} \cup \mathcal{J} = \mathcal{K}$, each $\xi \in \mathbf{S}_\mathcal{H}(\mathcal{K})$ has range rge $\xi \subset \mathcal{K}$. Additionally, if every maximal solution $\xi \in \mathbf{S}_\mathcal{H}(\mathcal{K})$ is complete, then the set

$\mathcal{K}$ will be forward invariant [Sanfelice, 2021, Definition 3.13]. Since the hybrid closed-loop system (4.29) satisfies hybrid basic conditions, as stated in Lemma 4.6, one can use [Goebel et al., 2012, Proposition 6.10], to verify the following viability condition:

$$\mathbf{F}(\mathbf{x},\mathbf{h},m)\cap\mathbf{T}_{\mathcal{F}}(\mathbf{x},\mathbf{h},m)\neq\emptyset,\forall(\mathbf{x},\mathbf{h},m)\in\mathcal{F}\setminus\mathcal{J}, \tag{C.11}$$

which will allow us to establish the completeness of the solution ξ to the hybrid closed-loop system (4.29). In (C.11), $\mathbf{T}_{\mathcal{F}}(\mathbf{x},\mathbf{h},m)$ represents the tangent cone to the set $\mathcal{F}$ at $(\mathbf{x},\mathbf{h},m)$, as defined in Section 2.3.7.

Let $(\mathbf{x},\mathbf{h},m)\in\mathcal{F}\setminus\mathcal{J}$, which implies by (4.25) and (4.26) that $(\mathbf{x},\mathbf{h})\in(\mathcal{F}_m^{\mathcal{W}}\setminus\mathcal{J}_m^{\mathcal{W}})\times\mathcal{V}_{r_a}$ for some $m\in\mathbb{M}$. For $\mathbf{x}\in(\mathcal{F}_m^{\mathcal{W}})^\circ\setminus\mathcal{J}_m^{\mathcal{W}}, m\in\mathbb{M}$, $\mathbf{T}_{\mathcal{F}}(\xi)=\mathbb{R}^2\times\mathbf{T}_{\mathcal{V}_{r_a}}(\mathbf{h})\times\{0\}$, where the set $\mathbf{T}_{\mathcal{V}_{r_a}}(\mathbf{h})$ is given by

$$\mathbf{T}_{\mathcal{V}_{r_a}}(\mathbf{h})=\begin{cases}\mathbb{R}^2, & \text{if } \mathbf{h}\in(\mathcal{V}_{r_a})^\circ,\\ \mathcal{P}_{\geq}(\mathbf{0},(\mathbf{h}-\Pi(\mathbf{h},\mathcal{O}_{\mathcal{W}}^M))), & \text{if } \mathbf{h}\in\partial\mathcal{V}_{r_a},\end{cases} \tag{C.12}$$

where, according to Lemma 4.1, for $\mathbf{h}\in\partial\mathcal{V}_{r_a}$, the projection $\Pi(\mathbf{h},\mathcal{O}_{\mathcal{W}}^M)$ is unique. Since, according to (4.29), $\dot{\mathbf{h}}=\mathbf{0}$, $\dot{\mathbf{h}}\in\mathbf{T}_{\mathcal{V}_{r_a}}(\mathbf{h})$ and (C.11) holds,

For $m=0$, according to (4.19) and (4.20), one has

$$\partial\mathcal{F}_0^{\mathcal{W}}\setminus\mathcal{J}_0^{\mathcal{W}}\subset\partial\mathcal{D}_{r_a}(\mathcal{O}_{\mathcal{W}}^M)\cap\mathcal{R}_e, \tag{C.13}$$

and according to Lemma 4.1, for $\mathbf{x}\in\partial\mathcal{F}_0^{\mathcal{W}}\setminus\mathcal{J}_0^{\mathcal{W}}$, the set $\mathcal{PJ}(\mathbf{x},\mathcal{O}_{\mathcal{W}}^M)$ is a singleton *i.e.*, the projection $\Pi(\mathbf{x},\mathcal{O}_{\mathcal{W}}^M)$ is unique. Hence, $\forall\mathbf{x}\in\partial\mathcal{F}_0^{\mathcal{W}}\setminus\mathcal{J}_0^{\mathcal{W}}$,

$$\mathbf{T}_{\mathcal{F}}(\mathbf{x},\mathbf{h},0)=\mathcal{P}_{\geq}(\mathbf{0},(\mathbf{x}-\Pi(\mathbf{x},\mathcal{O}_{\mathcal{W}}^M)))\times\mathbf{T}_{\mathcal{V}_{r_a}}(\mathbf{h})\times\{0\}, \tag{C.14}$$

where $\mathbf{T}_{\mathcal{V}_{r_a}}(\mathbf{h})$ is defined in (C.12). Also, according to (4.10a), for $m=0$, $\mathbf{u}(\mathbf{x},\mathbf{h},0)=-\kappa_s\mathbf{x},\kappa_s>0$. According to (4.14), $\mathbf{u}(\mathbf{x},\mathbf{h},0)\in\mathcal{P}_{\geq}(\mathbf{0},(\mathbf{x}-\Pi(\mathbf{x},\mathcal{O}_{\mathcal{W}}^M)))$ and, according to (4.29), $\dot{\mathbf{h}}=\mathbf{0}\in\mathbf{T}_{\mathcal{V}_{r_a}}(\mathbf{h})$. As a result, viability condition (C.11) holds for $m=0$.

For $m\in\{-1,1\}$, according to (4.24) and (4.21) one has

$$\partial\mathcal{F}_m^{\mathcal{W}}\setminus\mathcal{J}_m^{\mathcal{W}}\subset\partial\mathcal{D}_{r_a}(\mathcal{O}_{\mathcal{W}}^M), \tag{C.15}$$

and according to Lemma 4.1, for $\mathbf{x}\in\partial\mathcal{F}_m^{\mathcal{W}}\setminus\mathcal{J}_m^{\mathcal{W}}, m\in\{-1,1\}$, the set $\mathcal{PJ}(\mathbf{x},\mathcal{O}_{\mathcal{W}}^M)$ is a singleton *i.e.*, the projection $\Pi(\mathbf{x},\mathcal{O}_{\mathcal{W}}^M)$ is unique and the circle $\mathcal{B}_{\|\mathbf{x}-\Pi(\mathbf{x},\mathcal{O}_{\mathcal{W}}^M)\|}(\mathbf{x})$ intersect with $\partial\mathcal{O}_{\mathcal{W}}^M$ only at the location $\Pi(\mathbf{x},\mathcal{O}_{\mathcal{W}}^M)$. Hence, $\forall\mathbf{x}\in\partial\mathcal{F}_m^{\mathcal{W}}\setminus\mathcal{J}_m^{\mathcal{W}}, m\in\{-1,1\}$,

$$\mathbf{T}_{\mathcal{F}}(\mathbf{x},\mathbf{h},0)=\mathcal{P}_{\geq}(\mathbf{0},(\mathbf{x}-\Pi(\mathbf{x},\mathcal{O}_{\mathcal{W}}^M)))\times\mathbf{T}_{\mathcal{V}_{r_a}}(\mathbf{h})\times\{0\}, \tag{C.16}$$

where $\mathbf{T}_{\mathcal{V}_{r_a}}(\mathbf{h})$ is defined in (C.12). Also for $m\in\{-1,1\}$, according to (4.10a), $\mathbf{u}(\mathbf{x},\mathbf{h},m)=\kappa_r\mathbf{v}(\mathbf{x},m),\kappa_r>0$. Since, according to (4.11), $\mathbf{u}(\mathbf{x},\mathbf{h},m)^\intercal(\mathbf{x}-\Pi(\mathbf{x},\mathcal{O}_{\mathcal{W}}^M))=0$ and, according to (4.29), $\dot{\mathbf{h}}=\mathbf{0}\in\mathbf{T}_{\mathcal{V}_{r_a}}(\mathbf{h})$, the viability condition in (C.11) holds true for $m\in\{-1,1\}$.

Hence, according to [Goebel et al., 2012, Proposition 6.10], since (C.11) holds for all $\xi\in\mathcal{F}\setminus\mathcal{J}$, there exists a nontrivial solution to $\mathcal{H}$ for each initial condition in $\mathcal{K}$. Finite escape time can only occur through flow. They can neither occur for $\mathbf{x}$ in the set

$\mathcal{F}_{-1}^{\mathcal{W}} \cup \mathcal{F}_{1}^{\mathcal{W}}$, as this set is bounded as per definition (4.24), nor for $\mathbf{x}$ in the set $\mathcal{F}_{0}^{\mathcal{W}}$ as this would make $\mathbf{x}^\intercal\mathbf{x}$ grow unbounded, and would contradict the fact that $\frac{d}{dt}(\mathbf{x}^\intercal\mathbf{x}) \leq 0$ in view of the definition of $\mathbf{u}(\mathbf{x}, \mathbf{h}, 0)$. Therefore, all maximal solutions do not have finite escape times. Furthermore, according to (4.29), $\mathbf{x}^+ = \mathbf{x}$, and from the definition of the update law in (4.27) and (4.28), it follows immediately that $\mathbf{J}(\mathcal{J}) \subset \mathcal{K}$. Hence, the solutions to the hybrid closed-loop system (4.29) cannot leave $\mathcal{K}$ through jump and, as per [Goebel et al., 2012, Proposition 6.10], all maximal solutions are complete.

C.8 Proof of Theorem 4.1

Forward invariance and stability: The forward invariance of the obstacle-free set $\mathcal{K}$, for the hybrid closed-loop system (4.29), is immediate from Lemma 4.7. We next prove stability of $\mathcal{A}$ using [Goebel et al., 2012, Definition 7.1].

According to Lemma 4.4, the target location $\mathbf{0} \in (\mathcal{V}_{r_a})^\circ$. As a result, there exists $\mu_1 > 0$ such that $\mathcal{B}_{\mu_1}(\mathbf{0}) \cap (\mathcal{D}_{r_a}(\mathcal{O}_{\mathcal{W}}^{M}))^\circ = \emptyset$. According to (4.19), there exists $\mu_2 > 0$ such that $\mathcal{B}_{\mu_2}(\mathbf{0}) \cap \mathcal{J}_0^{\mathcal{W}} = \emptyset$. We define a set $\mathcal{S}_\mu := \mathcal{B}_\mu(\mathbf{0}) \times \mathcal{V}_{r_a} \times \mathbb{M}$, where $\mu \in (0, \min\{\mu_1, \mu_2\})$. According to (4.21), the set $\mathcal{B}_\mu(\mathbf{0}) \subset \mathcal{J}_m^{\mathcal{W}}$ for $m \in \{-1, 1\}$ and $\mu \in (0, \min\{\mu_1, \mu_2\})$. As a result, for all initial conditions $\xi(0,0) \in \mathcal{S}_\mu$, the control input, after at most one jump corresponds to the *move-to-target* mode and the algorithm steers the state $\mathbf{x}$ towards the origin according to the control input vector $\mathbf{u}(\xi) = -\kappa_s\mathbf{x}, \kappa_s > 0$. Hence, for each $\mu \in (0, \min\{\mu_1, \mu_2\})$, the set $\mathcal{S}_\mu = \mathcal{B}_\mu(\mathbf{0}) \times \mathcal{V}_{r_a} \times \mathbb{M}$ is forward invariant for the hybrid closed-loop system (4.29).

Consequently, for every $\rho > 0$, one can choose $\sigma \in (0, \min\{\mu_1, \mu_2, \rho\})$ such that for all initial conditions $\xi(0,0)$ with $d(\xi(0,0), \mathcal{A}) \leq \sigma$, one has $d(\xi(t,j), \mathcal{A}) \leq \rho$ for all $(t,j) \in \text{dom}\ \xi$, where $d(\xi, \mathcal{A})^2 = \inf_{(\mathbf{0}, \bar{\mathbf{h}}, \bar{m}) \in \mathcal{A}} (\|\mathbf{x}\|^2 + \|\mathbf{h} - \bar{\mathbf{h}}\|^2 + \|m - \bar{m}\|^2) = \|\mathbf{x}\|^2$. Additionally, the target set $\mathcal{A}$, as defined in (4.30), is compact. Hence, according to [Goebel et al., 2012, Definition 7.1], the target set $\mathcal{A}$ is stable for the hybrid closed-loop system (4.29)

Convergence: Since the target set $\mathcal{A}$ is obtained by only restricting the $\mathbf{x}$ component of the state space $\mathcal{K}$ to $\mathbf{0}$, one can prove claim 2 in Theorem 4.1 by showing that for all solutions ξ to the hybrid closed-loop system (4.29) initialized in the *move-to-target* mode ($m(0,0) = 0$), the $\mathbf{x}$ component of the solution ξ converges to the origin $\mathbf{0}$. For the closed-loop system (4.29), let $\xi(t_0, j_0) \in \mathcal{F}_0$, for some $(t_0, j_0) \in \text{dom}\ \xi$. If $\xi(t,j) \notin \mathcal{J}_0, \forall (t,j) \succeq (t_0, j_0)$, then due to the stabilizing control of the form $\mathbf{u}(\mathbf{x}, \mathbf{h}, 0) = -\kappa_s\mathbf{x}, \kappa_s > 0$, the state $\mathbf{x}$ will converge to the origin. Now, assume that there exists $(t_1, j_1) \succeq (t_0, j_0)$ such that $\xi(t_1, j_1) \in \mathcal{J}_0$, then the control law switches to the *obstacle-avoidance* mode. According to (4.27), $\mathbf{h}(t_1, j_1 + 1) = \mathbf{x}(t_1, j_1)$ and $m(t_1, j_1 + 1) \in \{-1, 1\}$ *i.e.,* the state $\mathbf{x}$ will evolve either in the clockwise direction ($m = 1$) or in the counter-clockwise direction ($m = -1$). To that end, we use the following lemma to show that if the solution ξ to the hybrid closed-loop system (4.29), which has been initialized in the *move-to-target* mode, evolves in the *obstacle-avoidance* mode, then it will always enter in the jump set of that mode only through the set $\mathcal{ER}_m^{\mathbf{h}} \times \mathcal{V}_{r_a} \times \{-1, 1\}$, where, according to (4.22), the location $\mathbf{x}$ is closer to the target location than the current *hit point*.

Lemma C.1 *Let Assumptions 4.1 and 4.2 hold, and the parameter $\bar{\epsilon}$, used in (4.22), is chosen as per Lemma 4.5, then for all solutions $\xi = (\mathbf{x}, \mathbf{h}, m)$ to the hybrid closed-loop system (4.29) with $\xi(t, j-1) \in \mathcal{J}_0$, $\xi(t, j) \in \mathcal{F}_l$, for some $l \in \{-1, 1\}$ and $(t, j) \in dom\ \xi$, there exists $(p, j) \in dom\ \xi$, $(p, j) \succ (t, j)$ such that following conditions hold true:*

1. $\xi(p, j) \in \mathcal{ER}_l^{\mathbf{h}(t,j)} \times \mathcal{V}_{r_a} \times \{l\} \subset \mathcal{J}_l$,
2. $\xi(v, j) \in \mathcal{F}_l, \forall (v, j) \in ([t, p) \times j)$.

Proof See Appendix C.8.1.

According to Lemma C.1, there exists $(t_2, j_1+1) \succeq (t_1, j_1+1)$ such that $\xi(t_2, j_1+1) \in \mathcal{ER}_{m(t_1,j_1+1)}^{\mathbf{h}(t_1,j_1+1)} \times \mathcal{V}_{r_a} \times \{-1, 1\} \subset \mathcal{J}_{m(t_1,j_1+1)}$. Notice that, according to (4.21) and (4.22), $\|\mathbf{x}(t_2, j_1+1)\| < \|\mathbf{h}(t_1, j_1+1)\|$, where, according to (4.27), $\mathbf{h}(t_1, j_1+1) = \mathbf{x}(t_1, j_1)$. In other words, according to Lemma C.1, the proposed navigation algorithm ensures that, at the instance where the the control switches from the *obstacle-avoidance* mode to the *move-to-target* mode, the target location $\mathbf{0}$ is closer to $\mathbf{x}$ than to last point where the control switched to the *obstacle-avoidance* mode. Furthermore, when the control input corresponds to the *move-to-target* mode, the algorithm steers the state $\mathbf{x}$ towards the origin under the influence of the stabilizing control vector $\mathbf{u}(\xi) = -\kappa_s \mathbf{x}, \kappa_s > 0$. Consequently, given that the workspace $\mathcal{W}$ and the obstacles $\mathcal{O}_i, i \in \mathbb{I} \setminus \{0\}$, are compact, it can be concluded that the solution ξ will contain finite number of jumps and the state $\mathbf{x}$ will converge to the origin.

C.8.1 Proof of Lemma C.1

We consider a connected modified obstacle $\mathcal{O}_{i,\alpha}^M \subset \mathcal{O}_{\mathcal{W}}^M$, for some $i \in \mathbb{I}$, as stated in Lemma 4.2, where α is selected according to Lemma 4.3. Let $\xi(t, j) \in \mathcal{F}_l^{\mathcal{W}} \cap \mathcal{N}_\gamma(\mathcal{D}_{r_a}(\mathcal{O}_{i,\alpha}^M)) \times \mathcal{V}_{r_a} \times \{l\}$, for some $l \in \{-1, 1\}$. Since $m(t, j-1) = 0$ and $m(t, j) \in \{-1, 1\}$, according to (4.19), $\mathbf{x}(t, j) = \mathbf{h}(t, j) \in \partial\mathcal{D}_\beta(\mathcal{O}_{i,\alpha}^M) \cap \mathcal{J}_0^{\mathcal{W}}$, where $\beta \in [r_a, r_a + \gamma_s]$. To proceed with the proof, we need the following fact:

Fact 3: Under Assumptions 4.1 and 4.2, consider the following flow-only system:

$$\dot{\mathbf{x}} = \kappa_r \mathbf{v}(\mathbf{x}, m), \mathbf{x} \in \mathcal{N}_\gamma(\mathcal{D}_{r_a}(\mathcal{O}_{i,\alpha}^M)), \tag{C.17}$$

for some $m \in \{-1, 1\}$, where $\kappa_r > 0$ and $\mathbf{v}(\mathbf{x}, m)$ is given by (4.11). If $\mathbf{x}(t_0) \in \partial\mathcal{D}_{\beta_1}(\mathcal{O}_{i,\alpha}^M)$, $\beta_1 \in [r_a, r_a + \gamma]$, for some $t_0 \geq 0$, then $\mathbf{x}(t) \in \partial\mathcal{D}_{\beta_1}(\mathcal{O}_{i,\alpha}^M)$ for all $t \geq t_0$.

Proof According to Lemma 4.1, for $\mathbf{x} \in \partial\mathcal{D}_{\beta_1}(\mathcal{O}_{i,\alpha}^M)$ with $\beta_1 \in [r_a, r_a + \gamma]$, the closest point from $\mathbf{x}$ onto the modified obstacle $\mathcal{O}_{i,\alpha}^M$ is unique *i.e.,* $\mathbf{card}(\mathcal{PJ}(\mathbf{x}, \mathcal{O}_{i,\alpha}^M)) = 1$. Hence, according to [Rataj and Zähle, 2019, Lemma 4.5], the vector $\mathbf{x} - \Pi(\mathbf{x}, \mathcal{O}_{i,\alpha}^M)$ is normal to the set $\partial\mathcal{D}_\beta(\mathcal{O}_{i,\alpha}^M)$ at $\mathbf{x}$. As a result, the tangent cone to the set $\partial\mathcal{D}_{\beta_1}(\mathcal{O}_{i,\alpha}^M)$ at $\mathbf{x} \in \partial\mathcal{D}_{\beta_1}(\mathcal{O}_{i,\alpha}^M)$ is given by

$$\mathbf{T}_{\partial\mathcal{D}_{\beta_1}(\mathcal{O}_{i,\alpha}^M)}(\mathbf{x}) = \mathcal{P}(\mathbf{0}, \mathbf{x} - \Pi(\mathbf{x}, \mathcal{O}_{i,\alpha}^M)). \tag{C.18}$$

Since $\mathbf{v}(\mathbf{x},m)^\intercal(\mathbf{x}-\Pi(\mathbf{x},\mathcal{O}_{i,\alpha}^M))=0$, $\mathbf{v}(\mathbf{x}(t),m)\in\mathbf{T}_{\partial\mathcal{D}_{\beta_1}(\mathcal{O}_{i,\alpha}^M)}(\mathbf{x}(t))$, for all $t\geq t_0$, which implies that the solution $\mathbf{x}(t)$ to the flow-only system (C.17) belongs to the set $\partial\mathcal{D}_{\beta_1}(\mathcal{O}_{i,\alpha}^M)$ for all $t\geq t_0$.

According to Fact 3, if $\mathbf{x}$ belongs to the set $\mathcal{N}_\gamma(\mathcal{D}_{r_a}(\mathcal{O}_{i,\alpha}^M))$ at some time $t_0\geq 0$, and is solely influenced by the obstacle-avoidance control vector $\kappa_r\mathbf{v}(\mathbf{x},m)$, $\kappa_r>0$, for some $m\in\{-1,1\}$, then $\mathbf{x}(t)$ will continue to evolve within the set $\mathcal{N}_\gamma(\mathcal{D}_{r_a}(\mathcal{O}_{i,\alpha}^M))$ for all $t\geq t_0$, without changing its distance from the set $\mathcal{O}_{i,\alpha}^M$.

According to (4.10a), for $l\in\{-1,1\}$, $\mathbf{u}(\mathbf{x},\mathbf{h},l)=\kappa_r\mathbf{v}(\mathbf{x},l),\kappa_r>0$. Since $\xi(t,j)\in\mathcal{F}_l$, for some $l\in\{-1,1\}$, with $\mathbf{x}(t,j)\in\partial\mathcal{D}_\beta(\mathcal{O}_{i,\alpha}^M),\beta\in[r_a,r_a+\gamma_s]$, according to Fact 3, the state $\mathbf{x}$ will evolve along the curve $\partial\mathcal{D}_\beta(\mathcal{O}_{i,\alpha}^M)$. Since the workspace $\mathcal{W}$ and the obstacles $\mathcal{O}_i,i\in\mathbb{I}\setminus\{0\}$, $\exists(p,j)\in\operatorname{dom}\xi$, $(p,j)\succ(t,j)$ such that at (p,j), the $\mathbf{x}$ component of the solution ξ will enter the set $\mathcal{H}_\mathbf{p}=\mathcal{B}_\delta(\mathbf{p})\cap\mathcal{N}_\gamma(\mathcal{D}_{r_a}(\mathcal{O}_{i,\alpha}^M))$, where $\delta=\min\{\beta-r_a,d(\mathbf{0},\mathcal{O}_\mathcal{W}^M)-r_a\}$. Since the parameter $\bar{\epsilon}\in(0,\epsilon_h]$, where ϵ_h is defined in (4.23), according to Lemma 4.5, $\mathbf{x}(p,j)\in\mathcal{ER}_l^{\mathbf{h}(t,j)}$. Hence, according to (4.21) and (4.25), $\xi(p,t)\in\mathcal{ER}_l^\mathbf{h}\times\mathcal{V}_{r_a}\times\{l\}\subset\mathcal{J}_l$, and condition 1 in Lemma C.1 holds true.

Since $\xi(t,j)\in\mathcal{F}_l$, for some $l\in\{-1,1\}$, with $\mathbf{x}(t,j)\in\partial\mathcal{D}_\beta(\mathcal{O}_{i,\alpha}^M),\beta\in[r_a,r_a+\gamma_s]$, according to Fact 3, the state $\mathbf{x}$ evolves in the region $\mathcal{N}_\gamma(\mathcal{D}_{r_a}(\mathcal{O}_{i,\alpha}^M))$, along the curve $\partial\mathcal{D}_{r_a+\beta}(\mathcal{O}_{i,\alpha}^M)$, until it enters the set $\mathcal{ER}_l^\mathbf{h}$, which guarantees that condition 2 in Lemma C.1 holds true.

C.9 Proof of Proposition 4.1

Since the obstacles $\mathcal{O}_i,i\in\mathbb{I}\setminus\{0\}$, are convex and compact, and the pairwise distance between any two obstacles $d(\mathcal{O}_i,\mathcal{O}_j)>2r_a,\forall i,j\in\mathbb{I},i\neq j$, the r_a-dilated versions of the obstacles do not intersect with each other *i.e.*, $d(\mathcal{D}_{r_a}(\mathcal{O}_i),\mathcal{D}_{r_a}(\mathcal{O}_j))>0,\forall i,j\in\mathbb{I},i\neq j$. This ensures the pathwise connectedness of the interior of the obstacle-free workspace $\mathcal{W}_{r_a}^\circ$. In addition, since $\mathbf{0}\in\mathcal{W}_{r_a}^\circ$, Assumption 4.1 is satisfied.

Define $\bar{\alpha}=\min\limits_{i,j\in\mathbb{I},i\neq j}d(\mathcal{O}_i,\mathcal{O}_j)/2$. Since the pairwise distance between any two obstacles is greater than $2r_a$, it follows that $\bar{\alpha}>r_a$, and for any $\alpha\in(r_a,\bar{\alpha}]$, the $\alpha-$dilated versions of the obstacles do not intersect with each other *i.e.*, $d(\mathcal{D}_\alpha(\mathcal{O}_i),\mathcal{D}_\alpha(\mathcal{O}_j))>0$. Therefore, $\mathcal{W}_\alpha$, defined using (5.3), is not an empty set. Then, it is straightforward to see that for every $\mathbf{x}\in\mathcal{D}_\alpha(\mathcal{O}_\mathcal{W})\setminus\mathcal{O}_\mathcal{W}^\circ$, there is a unique closest point on the boundary of the set $\mathcal{D}_\alpha(\mathcal{O}_\mathcal{W})$ from $\mathbf{x}$. Hence, $\mathbf{reach}(\mathcal{W}_\alpha)\geq\alpha$, where $\alpha\in(r_a,\bar{\alpha}]$. Finally, by virtue of [Rataj and Zähle, 2019, Lemma 4.5], Assumption 4.2 is satisfied.

Appendix D

Proofs of Chapter 5

D.1 Proof of Lemma 5.1

Since the origin $\mathbf{0}$ belongs to the interior of the obstacle-free workspace $\mathcal{W}_{r_a}^{\circ}$, there exists some distance between the target location and the r_a-dilated obstacle $\mathcal{D}_{r_a}(\mathcal{O}_i)$. In other words, since $\mathbf{0} \in \mathcal{W}_{r_a}^{\circ}$, there exists $\bar{\delta} > 0$ such that $d(\mathbf{0}, \mathcal{D}_{r_a}(\mathcal{O}_i)) = \bar{\delta}$. Notice that, since the workspace satisfies Assumption 5.1, according to (5.12), the set $\mathcal{J}_0^{\mathcal{W}} \cap \mathcal{N}_\gamma(\mathcal{D}_{r_a}(\mathcal{O}_i))$ belongs to the *landing* region associated with obstacle $\mathcal{O}_i$ *i.e.*, $\mathcal{J}_0^{\mathcal{W}} \cap \mathcal{N}_\gamma(\mathcal{D}_{r_a}(\mathcal{O}_i)) \subset \mathcal{R}_l^i$. According to (5.9), the location $\Pi(\mathbf{0}, \mathcal{D}_{r_a}(\mathcal{O}_i))$ does not belong to the *landing region* $\mathcal{R}_l^i$. As a result, one has $d(\mathbf{0}, \mathcal{R}_l^i) > \bar{\delta}$. Hence, it is clear that $\mathcal{B}_{\bar{\delta}}(\mathbf{0}) \cap \mathcal{N}_\gamma(\mathcal{D}_{r_a}(\mathcal{O}_i)) \cap \mathcal{J}_0^{\mathcal{W}} = \emptyset$, where $\mathcal{B}_{\bar{\delta}}(\mathbf{0}) \cap \mathcal{N}_\gamma(\mathcal{D}_{r_a}(\mathcal{O}_i)) \neq \emptyset$. Hence, one can set $\bar{\epsilon} \in (0, d(\mathbf{0}, \mathcal{R}_l^i) - \bar{\delta}]$ to ensure that $\mathcal{ER}^{\mathbf{h}} \cap \mathcal{N}_\gamma(\mathcal{D}_{r_a}(\mathcal{O}_i)) \neq \emptyset$ for all $\mathbf{h} \in \mathcal{J}_0^{\mathcal{W}} \cap \mathcal{N}_\gamma(\mathcal{D}_{r_a}(\mathcal{O}_i))$, for any $\epsilon \in (0, \bar{\epsilon}]$.

D.2 Proof of Lemma 5.2

The flow set $\mathcal{F}$ and the jump set $\mathcal{J}$, defined in (4.25) are by construction closed subsets of $\mathbb{R}^3 \times \mathbb{R}^3 \times \mathbb{R}^3 \times \mathbb{R} \times \mathbb{R}$. Hence, condition 1 in Lemma 5.2 is satisfied.

Since the flow map $\mathbf{F}(\xi)$ is defined for all $\xi \in \mathcal{F}$, $\mathcal{F} \subset$ dom $\mathbf{F}$. The flow map $\mathbf{F}$, given in (5.25), is continuous on $\mathcal{F}_0$. Next, we verify the continuity of $\mathbf{F}$ on $\mathcal{F}_1$. Since $\gamma \in (0, \bar{r}_s - r_s)$, the sets $\mathcal{N}_\gamma(\mathcal{D}_{r_a}(\mathcal{O}_i))$, for all $i \in \mathbb{I}$, are disjoint. Since obstacles $\mathcal{O}_i, i \in \mathbb{I} \setminus \{0\}$ are convex, for all locations $\mathbf{x} \in \mathcal{N}_\gamma(\mathcal{D}_{r_a}(\mathcal{O}_i)), i \in \mathbb{I} \setminus \{0\}$, the closest point from $\mathbf{x}$ on the boundary of the nearest obstacle $\Pi(\mathbf{x}, \mathcal{O}_i)$ is unique. Furthermore, according to (5.17), the set $\mathcal{F}_1^{\mathcal{W}} \subset \bigcup_{i \in \mathbb{I} \setminus \{0\}} \mathcal{N}_\gamma(\mathcal{D}_{r_a}(\mathcal{O}_i))$. Hence, according to [Rataj and Zähle, 2019] [Lemma 4.1] and (5.17), $\Pi(\mathbf{x}, \mathcal{O}_{\mathcal{W}})$ is continuous for all $\mathbf{x} \in \mathcal{F}_1^{\mathcal{W}}$. Hence, the obstacle-avoidance control vector $\kappa_r \mathbf{v}(\mathbf{x}, \mathbf{a})$, used in (5.5a), is continuous for all locations $\mathbf{x} \in \mathcal{F}_1^{\mathcal{W}}$ with the unit vector $\mathbf{a}$ chosen as per (5.21). As a result, $\mathbf{F}$ is continuous on $\mathcal{F}_1$ and as such it is continuous on $\mathcal{F}$. This shows fulfillment of condition 2 in Lemma 5.2.

Since the jump map $\mathbf{J}(\xi)$ is defined for all $\xi \in \mathcal{J}$, $\mathcal{J} \subset$ dom $\mathbf{J}$. The jump map $\mathbf{J}$, defined in (4.29), is single-valued on $\mathcal{J}_1$. Hence, according to [Goebel et al., 2012, Definition 5.9 and 5.14], the jump map $\mathbf{J}$ is outer semicontinuous and locally bounded relative to $\mathcal{J}_1$.

Finally, we prove that the jump map $\mathbf{J}$ is outer semicontinuous and locally bounded

relative to $\mathcal{J}_0$. According to (4.27) and (4.29), the jump map $\mathbf{J}$ is single-valued for the state vector $(\mathbf{x}, \mathbf{h}, m, s)$ on $\mathcal{J}_0$. Consider the jump map $\mathbf{J}$ for the state $\mathbf{a}$ on $\mathcal{J}_0$. We show that the set-valued mapping $\mathbf{A} : \mathbb{R}^3 \rightrightarrows \mathbb{S}^2$, used in (5.21), is outer semicontinuous and locally bounded relative to $\mathcal{J}_0^{\mathcal{W}}$. To that end, consider any sequence $\{\mathbf{q}_i\}_{i\in\mathbb{N}} \subset \mathcal{J}_0^{\mathcal{W}}$ that converges to some $\mathbf{q} \in \mathcal{J}_0^{\mathcal{W}}$. According to (5.22), $\mathbf{p}_i = \mathbf{A}(\mathbf{q}_i) \in \mathcal{P}^{\perp}(\mathbf{q}_i) \cap \mathcal{P}^{\perp}(\mathbf{q}_i - \Pi(\mathbf{q}_i, \mathcal{O}_{\mathcal{W}}))$, where for all $\mathbf{q}_i \in \mathcal{J}_0^{\mathcal{W}}$, $\Pi(\mathbf{q}_i, \mathcal{O}_{\mathcal{W}})$ is unique. Let us assume that the sequence $\{\mathbf{p}_i\}_{i\in\mathbb{N}}$ converges to some $\mathbf{p} \in \mathbb{S}^2$. Note that $\mathbf{p}_i^{\top}\mathbf{q}_i = 0$ and $\mathbf{p}_i^{\top}(\mathbf{q}_i - \Pi(\mathbf{q}_i, \mathcal{O}_{\mathcal{W}})) = 0$ for all $i \in \mathbb{N}$. Additionally, according to (5.22), when $\mathbf{q}_i^{\times}(\mathbf{q}_i - \Pi(\mathbf{q}_i, \mathcal{O}_{\mathcal{W}})) = \mathbf{0}$, one has $\mathbf{p}_i \in \mathcal{P}^{\perp}(\mathbf{q}_i)$. Therefore, one can conclude that $\mathbf{p}^{\top}\mathbf{q} = 0$ and $\mathbf{p}^{\top}(\mathbf{q} - \Pi(\mathbf{q}, \mathcal{O}_{\mathcal{W}})) = 0$ and as such $\mathbf{p} = \mathbf{A}(\mathbf{q})$. Hence, according [Goebel et al., 2012, Definition 5.9], the mapping $\mathbf{A}$ is outer semicontinuous relative to $\mathcal{J}_0^{\mathcal{W}}$. Since rge $\mathbf{A} = \mathbb{S}^2 \subset \mathbb{R}^3$ is bounded, according to [Goebel et al., 2012, Definition 5.14], the set-valued mapping $\mathbf{A}$ is locally bounded, where the range of $\mathbf{A}$ is defined as per [Goebel et al., 2012, Definition 5.8]. Hence, $\mathbf{J}$ is outer semi-continuous and locally bounded relative to $\mathcal{J}_0$. This shows the fulfillment of condition 3 in Lemma 5.2.

D.3 Proof of Lemma 5.3

First we prove that the union of the flow and jump sets covers exactly the obstacle-free state space $\mathcal{K}$. For $m = 0$, according to (5.12) and (5.13), by construction we have $\mathcal{F}_0^{\mathcal{W}} \cup \mathcal{J}_0^{\mathcal{W}} = \mathcal{W}_{r_a}$. Similarly, for $m = 1$, according to (5.15) and (5.17), by construction one has $\mathcal{F}_m^{\mathcal{W}} \cup \mathcal{J}_m^{\mathcal{W}} = \mathcal{W}_{r_a}$. Inspired by [Berkane et al., 2021a, Appendix 11], the satisfaction of the following equation:

$$\mathcal{F}_m^{\mathcal{W}} \cup \mathcal{J}_m^{\mathcal{W}} = \mathcal{W}_{r_a}, m \in \mathbb{M}, \tag{D.1}$$

along with (5.14), (5.18) and (5.19) implies $\mathcal{F} \cup \mathcal{J} = \mathcal{K}$.

Now, inspired by [Berkane et al., 2021a, Appendix 1], for the hybrid closed-loop system (5.25), with data $\mathcal{H} = (\mathcal{F}, \mathbf{F}, \mathcal{J}, \mathbf{J})$, define $\mathbf{S}_{\mathcal{H}}(\mathcal{K})$ as the set of all maximal solutions ξ to $\mathcal{H}$ with $\xi(0, 0) \in \mathcal{K}$. Since $\mathcal{F} \cup \mathcal{J} = \mathcal{K}$, each $\xi \in \mathbf{S}_{\mathcal{H}}(\mathcal{K})$ has range rge $\xi \subset \mathcal{K}$. Additionally, if every maximal solution $\xi \in \mathbf{S}_{\mathcal{H}}(\mathcal{K})$ is complete, then the set $\mathcal{K}$ will be forward invariant [Sanfelice, 2021, Definition 3.13]. Since the hybrid closed-loop system (5.25) satisfies the hybrid basic conditions, as stated in Lemma 5.2, one can use [Goebel et al., 2012, Proposition 6.10], to verify the following viability condition:

$$\mathbf{F}(\xi) \cap \mathbf{T}_{\mathcal{F}}(\xi) \neq \emptyset, \forall \xi \in \mathcal{F} \setminus \mathcal{J}, \tag{D.2}$$

which will allow us to establish the completeness of the solution ξ to the hybrid closed-loop system (5.25). In (D.2), $\mathbf{T}_{\mathcal{F}}(\xi)$ represents the tangent cone to the set $\mathcal{F}$ at ξ.

Let $(\mathbf{x}, \mathbf{h}, \mathbf{a}, m, s) \in \mathcal{F} \setminus \mathcal{J}$, which implies by (5.14), (5.18) and (5.19) that $(\mathbf{x}, \mathbf{h}, \mathbf{a}, s) \in (\mathcal{F}_m^{\mathcal{W}} \setminus \mathcal{J}_m^{\mathcal{W}}) \times \mathcal{W}_{r_a} \times \mathbb{S}^2 \times \mathbb{R}_{\geq 0}$ for some $m \in \mathbb{M}$. For $\mathbf{x} \in (\mathcal{F}_m^{\mathcal{W}})^{\circ} \setminus \mathcal{J}_m^{\mathcal{W}}$ with $(\mathbf{h}, \mathbf{a}, m, s) \in \mathcal{W}_{r_a} \times \mathbb{S}^2 \times \mathbb{M} \times \mathbb{R}_{\geq 0}$ the tangent cone $\mathbf{T}_{\mathcal{F}}(\xi) = \mathbb{R}^3 \times \mathbf{T}_{\mathcal{W}_{r_a}}(\mathbf{h}) \times \mathcal{P}(\mathbf{0}, \mathbf{a}) \times \{0\} \times \mathbf{T}_{\mathbb{R}_{\geq 0}}(s)$, where the set $\mathbf{T}_{\mathcal{W}_{r_a}}(\mathbf{h})$ is given by

$$\mathbf{T}_{\mathcal{W}_{r_a}}(\mathbf{h}) = \begin{cases} \mathbb{R}^3, & \text{if } \mathbf{h} \in (\mathcal{W}_{r_a})^{\circ}, \\ \mathcal{P}_{\geq}(\mathbf{0}, (\mathbf{h} - \Pi(\mathbf{h}, \mathcal{O}_{\mathcal{W}}))), & \text{if } \mathbf{h} \in \partial\mathcal{W}_{r_a}, \end{cases} \tag{D.3}$$

where for $\mathbf{h} \in \partial\mathcal{W}_{r_a}$, the projection $\Pi(\mathbf{h}, \mathcal{O}_\mathcal{W})$ is unique. For $s \in \mathbb{R}_{\geq 0}$, the set $\mathbf{T}_{\mathbb{R}_{\geq 0}}(s)$ is defined as

$$\mathbf{T}_{\mathbb{R}_{\geq 0}}(s) = \begin{cases} \mathbb{R}, & \text{if } s \in \mathbb{R}_{>0}, \\ \mathbb{R}_{\geq 0}, & \text{if } s = 0. \end{cases} \tag{D.4}$$

Since, according to (5.25), $\dot{\mathbf{h}} = \mathbf{0}$ and $\dot{s} = 1$, we have $\dot{\mathbf{h}} \in \mathbf{T}_{\mathcal{W}_{r_a}}(\mathbf{h})$ and $\dot{s} \in \mathbf{T}_{\mathbb{R}_{\geq 0}}(s)$, respectively, and (D.2) holds.

For $m = 0$, according to (5.12) and (5.13), one has

$$\partial\mathcal{F}_0^\mathcal{W} \setminus \mathcal{J}_0^\mathcal{W} \subset \partial\mathcal{D}_{r_a}(\mathcal{O}_\mathcal{W}) \cap \mathcal{R}_e, \tag{D.5}$$

and for $\mathbf{x} \in \partial\mathcal{F}_0^\mathcal{W} \setminus \mathcal{J}_0^\mathcal{W}$, the projection $\Pi(\mathbf{x}, \mathcal{O}_\mathcal{W})$ is unique. Hence, $\forall \mathbf{x} \in \partial\mathcal{F}_0^\mathcal{W} \setminus \mathcal{J}_0^\mathcal{W}$,

$$\mathbf{T}_\mathcal{F}(\xi) = \mathcal{P}_\geq(\mathbf{0}, \mathbf{x}_\pi) \times \mathbf{T}_{\mathcal{W}_{r_a}}(\mathbf{h}) \times \mathcal{P}(\mathbf{0}, \mathbf{a}) \times \{0\} \times \mathbf{T}_{\mathbb{R}_{\geq 0}}(s), \tag{D.6}$$

where $\mathbf{T}_{\mathcal{W}_{r_a}}(\mathbf{h})$ and $\mathbf{T}_{\mathbb{R}_{\geq 0}}(s)$ are defined in (D.3) and (D.4), respectively, and $\mathbf{x}_\pi = \mathbf{x} - \Pi(\mathbf{x}, \mathcal{O}_\mathcal{W})$. Also, according to (5.5a), for $m = 0$, one has $\mathbf{u}(\xi) = -\kappa_s \mathbf{x}, \kappa_s > 0$. According to (5.11) and (D.5), for $\xi \in \mathcal{F}_0 \setminus \mathcal{J}_0$ with $\mathbf{x} \in \partial\mathcal{F}_0^\mathcal{W} \setminus \mathcal{J}_0^\mathcal{W}$, one can conclude that $\mathbf{u}(\xi) \in \mathcal{P}_\geq(\mathbf{0}, \mathbf{x}_\pi)$. Moreover, according to (5.25), it is clear that $\dot{\mathbf{h}} = \mathbf{0} \in \mathbf{T}_{\mathcal{W}_{r_a}}(\mathbf{h})$, $\dot{s} = 1 \in \mathbf{T}_{\mathbb{R}_{\geq 0}}(s)$ and $\dot{\mathbf{a}} = 0 \in \mathcal{P}(\mathbf{0}, \mathbf{a})$. Therefore, the viability condition (D.2) holds for $m = 0$.

For $m = 1$, according to (5.15) and (5.17) one has

$$\partial\mathcal{F}_1^\mathcal{W} \setminus \mathcal{J}_1^\mathcal{W} \subset \partial\mathcal{D}_{r_a}(\mathcal{O}_\mathcal{W}), \tag{D.7}$$

and for $\mathbf{x} \in \partial\mathcal{F}_1^\mathcal{W} \setminus \mathcal{J}_1^\mathcal{W}$, the projection $\Pi(\mathbf{x}, \mathcal{O}_\mathcal{W})$ is unique and the circle $\mathcal{B}_{\|\mathbf{x}_\pi\|}(\mathbf{x})$ intersect with $\partial\mathcal{O}_\mathcal{W}$ only at the location $\Pi(\mathbf{x}, \mathcal{O}_\mathcal{W})$. Hence, $\forall \mathbf{x} \in \partial\mathcal{F}_1^\mathcal{W} \setminus \mathcal{J}_1^\mathcal{W}$, the tangent cone

$$\mathbf{T}_\mathcal{F}(\xi) = \mathcal{P}_\geq(\mathbf{0}, \mathbf{x}_\pi) \times \mathbf{T}_{\mathcal{W}_{r_a}}(\mathbf{h}) \times \mathcal{P}(\mathbf{0}, \mathbf{a}) \times \{0\} \times \mathbf{T}_{\mathbb{R}_{\geq 0}}(s), \tag{D.8}$$

where $\mathbf{T}_{\mathcal{W}_{r_a}}(\mathbf{h})$ and $\mathbf{T}_{\mathbb{R}_{\geq 0}}(s)$ are defined in (D.3) and (D.4), respectively. Also, according to (5.5a), for $m = 1$, one has $\mathbf{u}(\xi) = \kappa_r \mathbf{v}(\mathbf{x}, \mathbf{a}), \kappa_r > 0$. From (5.8), it follows that $\eta(\mathbf{x}) = 1$ for $\mathbf{x} \in \partial\mathcal{F}_1^\mathcal{W} \setminus \mathcal{J}_1^\mathcal{W}$. As a result, according to (5.5a) and (5.6), the control vector is simplified to $\mathbf{u}(\xi) = \kappa_r \mathbf{P}(\mathbf{a})\mathbf{x}_\pi$. It can be shown that for any $\mathbf{a} \in \mathbb{S}^2$, the inner product $\mathbf{x}_\pi^\intercal \mathbf{P}(\mathbf{a})\mathbf{x}_\pi$ is always non-negative. Therefore, for $\xi \in \mathcal{F}_1 \setminus \mathcal{J}_1$ with $\mathbf{x} \in \mathcal{F}_1^\mathcal{W} \setminus \mathcal{J}_1^\mathcal{W}$, one has $\mathbf{u}(\mathbf{x}, \mathbf{h}, \mathbf{a}, 1, s)^\intercal (\mathbf{x} - \Pi(\mathbf{x}, \mathcal{O}_\mathcal{W})) \geq 0$. Moreover, according to (5.25), it is clear that $\dot{\mathbf{h}} = \mathbf{0} \in \mathbf{T}_{\mathcal{W}_{r_a}}(\mathbf{h})$, $\dot{s} = 1$ and $\dot{\mathbf{a}} = 0 \in \mathcal{P}(\mathbf{0}, \mathbf{a})$. Hence, the viability condition in (D.2) holds for $m = 1$.

Hence, according to [Goebel et al., 2012, Proposition 6.10], since (D.2) holds for all $\xi \in \mathcal{F} \setminus \mathcal{J}$, there exists a nontrivial solution to $\mathcal{H}$ for each initial condition in $\mathcal{K}$. Finite escape time can only occur through flow. They can neither occur for $\mathbf{x}$ in the set $\mathcal{F}_1^\mathcal{W}$, as this set is bounded as per definition (5.17), nor for $\mathbf{x}$ in the set $\mathcal{F}_0^\mathcal{W}$ as this would make $\mathbf{x}^\intercal\mathbf{x}$ grow unbounded, and would contradict the fact that $\frac{d}{dt}(\mathbf{x}^\intercal\mathbf{x}) \leq 0$ in view of the definition of $\mathbf{u}(\mathbf{x}, \mathbf{h}, \mathbf{a}, 0, s)$. Therefore, all maximal solutions do not have finite escape times. Furthermore, according to (5.25), $\mathbf{x}^+ = \mathbf{x}$, and from the definition of the update law in (5.21) and (5.24), it follows immediately that $\mathbf{J}(\mathcal{J}) \subset \mathcal{K}$. Hence, the solutions to the hybrid closed-loop system (5.25) cannot leave $\mathcal{K}$ through jump and, as per [Goebel et al., 2012, Proposition 6.10], all maximal solutions are complete.

D.4 Proof of Theorem 5.1

Forward invariance and stability: The forward invariance of the obstacle-free set $\mathcal{K}$, for the hybrid closed-loop system (5.25), is immediate from Lemma 5.3. We next prove the stability of $\mathcal{A}$ using [Goebel et al., 2012, Definition 7.1].

Since $\mathbf{0} \in (\mathcal{W}_{r_a})^\circ$, there exists $\mu_1 > 0$ such that $\mathcal{B}_{\mu_1}(\mathbf{0}) \cap (\mathcal{D}_{r_a}(\mathcal{O}_\mathcal{W}))^\circ = \emptyset$. According to (5.12), there exists $\mu_2 > 0$ such that $\mathcal{B}_{\mu_2}(\mathbf{0}) \cap \mathcal{J}_0^\mathcal{W} = \emptyset$. We define the set $\mathcal{S}_\mu := \{\xi \in \mathcal{K} | \mathbf{x} \in \mathcal{B}_\mu(\mathbf{0})\}$, where $\mu \in (0, \min\{\mu_1, \mu_2\})$. Notice that for all initial conditions $\xi(0,0) \in \mathcal{S}_\mu$, the control input, after at most one jump corresponds to the *move-to-target* mode and it steers the state $\mathbf{x}$ towards the origin according to the control input vector $\mathbf{u}(\xi) = -\kappa_s \mathbf{x}, \kappa_s > 0$. Hence, for each $\mu \in (0, \min\{\mu_1, \mu_2\})$, the set $\mathcal{S}_\mu$ is forward invariant for the hybrid closed-loop system (5.25).

Consequently, for every $\rho > 0$, one can choose $\sigma \in (0, \min\{\mu_1, \mu_2, \rho\})$ such that for all initial conditions $\xi(0,0)$ with $d(\xi(0,0), \mathcal{A}) \leq \sigma$, one has $d(\xi(t,j), \mathcal{A}) \leq \rho$ for all $(t,j) \in$ dom ξ, where $d(\xi, \mathcal{A})^2 = \inf_{(\mathbf{0}, \bar{\mathbf{h}}, \bar{\mathbf{a}}, \bar{m}, \bar{s}) \in \mathcal{A}} (\|\mathbf{x}\|^2 + \|\mathbf{h} - \bar{\mathbf{h}}\|^2 + \|\mathbf{a} - \bar{\mathbf{a}}\|^2 + (m - \bar{m})^2 + (s - \bar{s})^2) = \|\mathbf{x}\|^2$. Hence, according to [Sanfelice, 2021, Definition 3.1], the target set $\mathcal{A}$ is stable for the hybrid closed-loop system (5.25). Next, we proceed to establish the convergence properties of the set $\mathcal{A}$.

Attractivity: We aim to show that for the proposed hybrid closed-loop system (5.25), the target set $\mathcal{A}$ is globally attractive in the set $\mathcal{K}$ using [Sanfelice, 2021, Defintion 3.1 and Remark 3.5]. In other words, we prove that for all initial conditions $\xi(0,0) \in \overline{\mathcal{F}} \cup \mathcal{J} = \mathcal{K}$, every maximal solution ξ to the hybrid closed-loop system is complete and satisfies

$$\lim_{(t,j) \in \text{ dom } \xi, t+j \to \infty} d(\xi(t,j), \mathcal{A}) = \|\mathbf{x}(t,j)\| = 0. \tag{D.9}$$

The completeness of all maximal solutions to the hybrid closed-loop system (5.25) follows from Lemma 5.3. Next, we prove that for all initial condition $\xi(0,0) \in \mathcal{K}$, every complete solution ξ to the hybrid closed-loop system (5.25), satisfies (D.9). We consider two cases based on the initial value of the mode indicator variable $m(0,0)$.

Case 1: $m(0,0) = 0$. For the hybrid closed-loop system (5.25), consider a solution ξ initialized in the *move-to-target* mode. Let us assume $\xi(t_0, j_0) \in \mathcal{F}_0$ for some $(t_0, j_0) \in$ dom $\xi, (t_0, j_0) \succeq (0,0)$. If $\xi(t,j) \notin \mathcal{J}_0$, for all $(t,j) \succeq (t_0, j_0)$, then the control input $\mathbf{u}(\mathbf{x}, \mathbf{h}, \mathbf{a}, 0, s) = -\kappa_s \mathbf{x}$ will steer the state $\mathbf{x}$ straight towards the origin, where $\kappa_s > 0$. On the other hand, assume that there exists $(t_1, j_1) \succeq (t_0, j_0)$ such that $\xi(t_1, j_1) \in \mathcal{J}_0$. Then, according to (5.21), the control law switches to the *obstacle-avoidance* mode. As per (5.12), it is clear that $\mathbf{x}(t_1, j_1) \in \mathcal{J}_0^\mathcal{W} \cap \mathcal{N}_{\gamma_s}(\mathcal{D}_{r_a}(\mathcal{O}_i))$, for some $i \in \mathbb{I}$ and $d(\mathbf{x}(t_1, j_1), \mathcal{O}_i) = \beta$ for some $\beta \in [r_a, r_a + \gamma_s]$. At this instance, according to (5.21), the proposed navigation algorithm updates the values of the state variable $\mathbf{h}(t_1, j_1 + 1) = \mathbf{x}(t_1, j_1)$, $\mathbf{a}(t_1, j_1 + 1) \in \mathcal{P}^\perp(\mathbf{x}(t_1, j_1))$, $m(t_1, j_1 + 1) = 1$ and $s(t_1, j_1 + 1) = s(t_1, j_1) + 1$. According to (4.29), $\mathbf{h}(t_1, j_1 + 1) = \mathbf{h}(t, j)$, $\mathbf{a}(t_1, j_1 + 1) = \mathbf{a}(t, j)$ and $m(t_1, j_1 + 1) = m(t, j)$ for all $(t, j) \in (I_{j_1+1} \times j_1 + 1)$, where $I_{j_1+1} = \{t | (t, j_1 + 1) \in$ dom $\xi\}$. To proceed with the proof, we need the following lemma:

Lemma D.1 *Under Assumption 5.1, consider a solution ξ to the hybrid closed-loop system (5.25). If $\xi(t_1, j_1) \in \mathcal{J}_0$ at some $(t_1, j_1) \in$ dom ξ such that $\mathbf{x}(t_1, j_1) \in \mathcal{J}_0^\mathcal{W} \cap$*

$\mathcal{N}_\gamma(\mathcal{D}_{r_a}(\mathcal{O}_i))$ for some $i \in \mathbb{I}$, then for all $(t, j) \in (I_{j_1+1} \times j_1 + 1)$, the following statements hold true:

1. $\mathbf{x}(t, j) \in \mathcal{N}_\gamma(\mathcal{D}_{r_a}(\mathcal{O}_i)) \cap \mathcal{P}(\mathbf{h}, \mathbf{a})$,
2. *there exists $t_2 > t_1$ such that $t_2 < \infty$ and $\xi(t_2, j_1 + 1) \in \mathcal{J}_1$,*

where $\mathbf{h} = \mathbf{h}(t_1, j_1 + 1) = \mathbf{h}(t, j)$ and $\mathbf{a} = \mathbf{a}(t_1, j_1 + 1) = \mathbf{a}(t, j)$.

Proof See Appendix D.4.1.

According to Lemma D.1, when a solution ξ to the hybrid closed-loop system (5.25) evolves in the *obstacle-avoidance* mode, the state ξ eventually enters in the jump set of the *obstacle-avoidance* mode $\mathcal{J}_1$ (5.18) and the control law switches to the *move-to-target* mode.

According to Lemma D.1, there exists $(t_2, j_1 + 1) \succ (t_1, j_1 + 1)$ with $t_2 < \infty$ such that $\xi(t_2, j_1 + 1) \in \mathcal{J}_1$. Notice that, according to (5.15) and (5.16), one has $\|\mathbf{x}(t_2, j_1 + 1)\| < \|\mathbf{x}(t_1, j_1 + 1)\|$. In other words, according to Lemma D.1, the proposed navigation algorithm ensures that, at the instance where the the control switches from the *obstacle-avoidance* mode to the *move-to-target* mode, the origin is closer to the point $\mathbf{x}$ than to the last point where the control switched to the *obstacle-avoidance* mode. Furthermore, when the control input corresponds to the *move-to-target* mode, it steers the state $\mathbf{x}$ towards the origin under the influence of control $\mathbf{u}(\xi) = -\kappa_s \mathbf{x}, \kappa_s > 0$. Consequently, given that the workspace $\mathcal{W}$ and the obstacles $\mathcal{O}_i, i \in \mathbb{I} \setminus \{0\}$, are compact, it can be concluded that the solution $\xi(t, j)$ will contain finite number of jumps and will satisfy (D.9).

Case 2: $m(0, 0) = 1$. For the hybrid closed-loop system (5.25) consider a solution ξ initialized in the *obstacle-avoidance* mode. Since $m(0, 0) = 1$, according to (5.18), $\xi(0, 0) \in \mathcal{J}_1$. Therefore, according to (5.24), the control input switches to the *move-to-target* mode and $m(0, 1) = 0$. One can now use arguments similar to the ones used for case 1 to show that the solution $\xi(t, j)$ will contain finite number of jumps and will satisfy (D.9).

Hence, the target set $\mathcal{A}$ is globally attractive in the set $\mathcal{K}$ for the proposed hybrid closed-loop system (5.25). In addition, since the set $\mathcal{A}$ is stable for the hybrid closed-loop system (5.25), it is globally asymptotically stable in the set $\mathcal{K}$ for the hybrid closed-loop system (5.25) as per [Sanfelice, 2021, Remark 3.5].

D.4.1 Proof of Lemma D.1

First, we prove that when the control input corresponds to the *obstacle-avoidance* mode, one has $\mathbf{x}(t, j) \in \mathcal{N}_\gamma(\mathcal{D}_{r_a}(\mathcal{O}_i))$ for all $(t, j) \in (I_{j_1+1}, j_1 + 1)$. To that end, we make use of Nagumo's theorem [Blanchini et al., 2008, Theorem 4.7] and show that when the control input corresponds to the *obstacle-avoidance* mode, one has

$$\mathbf{u}(\xi) \in \mathbf{T}_{\mathcal{N}_\gamma(\mathcal{D}_{r_a}(\mathcal{O}_i))}(\mathbf{x}), \tag{D.10}$$

for all $\xi \in \mathcal{K}_1$, where $\mathcal{K}_1 := \{\xi \in \mathcal{K} | \mathbf{x} \in \partial\mathcal{N}_\gamma(\mathcal{D}_{r_a}(\mathcal{O}_i)), m = 1\}$. This, combined with the fact that the control input vector $\mathbf{u}(\xi)$ is continuous on $\mathcal{K}_2 := \{\xi \in \mathcal{K} | \mathbf{x} \in$

$\mathcal{N}_\gamma(\mathcal{D}_{r_a}(\mathcal{O}_i)), m = 1\}$, as stated in Lemma 5.2, ensures that $\mathbf{x}(t,j) \in \mathcal{N}_\gamma(\mathcal{D}_{r_a}(\mathcal{O}_i))$ for all $(t,j) \in (I_{j_1+1} \times j_1 + 1)$.

Note that $\partial\mathcal{N}_\gamma(\mathcal{D}_{r_a}(\mathcal{O}_i)) = \partial\mathcal{D}_{r_a}(\mathcal{O}_i) \cup \partial\mathcal{D}_{r_a+\gamma}(\mathcal{O}_i)$. For all $\mathbf{x} \in \partial\mathcal{D}_{r_a}(\mathcal{O}_i)$, one has $\mathbf{T}_{\mathcal{N}_\gamma(\mathcal{D}_{r_a}(\mathcal{O}_i))}(\mathbf{x}) = \mathcal{P}_{\geq}(\mathbf{0}, \mathbf{x}_\pi)$, where $\mathbf{x}_\pi = \mathbf{x} - \Pi(\mathbf{x}, \mathcal{O}_\mathcal{W})$ with $\Pi(\mathbf{x}, \mathcal{O}_\mathcal{W}) = \Pi(\mathbf{x}, \mathcal{O}_i)$. When the control input vector (5.5a) corresponds to the *obstacle-avoidance* mode, for $\mathbf{x} \in \partial\mathcal{D}_{r_a}(\mathcal{O}_i)$, it is given by $\mathbf{u}(\xi) = \kappa_r \mathbf{P}(\mathbf{a})\mathbf{x}_\pi$. Now, for any $\mathbf{p} \in \mathbb{R}^3$ and a unit vector $\mathbf{q} \in \mathbb{S}^2$, it can be shown that $\mathbf{p}^\top \mathbf{P}(\mathbf{q})\mathbf{p} \geq 0$. Therefore, for all $\mathbf{x} \in \partial\mathcal{D}_{r_a}(\mathcal{O}_i)$, one has $\mathbf{x}_\pi \mathbf{P}(\mathbf{a})\mathbf{x}_\pi \geq 0$. This implies that $\mathbf{u}(\xi) \in \mathcal{P}_{\geq}(\mathbf{0}, \mathbf{x}_\pi) \subset \mathbf{T}_{\mathcal{N}_\gamma(\mathcal{D}_{r_a}(\mathcal{O}_i))}(\mathbf{x})$ for $\mathbf{x} \in \partial\mathcal{D}_{r_a}(\mathcal{O}_i)$, and condition (D.10) holds true.

Next, for $\mathbf{x} \in \partial\mathcal{D}_{r_a+\gamma}(\mathcal{O}_i)$, one has $\mathbf{T}_{\mathcal{N}_\gamma(\mathcal{D}_{r_a}(\mathcal{O}_i))}(\mathbf{x}) = \mathcal{P}_{\leq}(\mathbf{0}, \mathbf{x}_\pi)$. When the control input corresponds to the *obstacle-avoidance* mode, for $\mathbf{x} \in \partial\mathcal{D}_{r_a+\gamma}(\mathcal{O}_i)$, the control vector (5.5a) is given by $\mathbf{u}(\xi) = -\kappa_r \mathbf{P}(\mathbf{a})\mathbf{x}_\pi$. As mentioned earlier, for all $\mathbf{x} \in \partial\mathcal{D}_{r_a+\gamma}(\mathcal{O}_i)$, one has $\mathbf{x}_\pi \mathbf{P}(\mathbf{a})\mathbf{x}_\pi \geq 0$. Therefore, $\mathbf{u}(\xi) \in \mathcal{P}_{\leq}(\mathbf{0}, \mathbf{x}_\pi) \subset \mathbf{T}_{\mathcal{N}_\gamma(\mathcal{D}_{r_a}(\mathcal{O}_i))}(\mathbf{x})$ for $\mathbf{x} \in \partial\mathcal{D}_{r_a+\gamma}(\mathcal{O}_i)$, and condition (D.10) holds true. As a result, since $\mathbf{x}(t_1, j_1 + 1) \in \mathcal{N}_\gamma(\mathcal{D}_{r_a}(\mathcal{O}_i))$, one can conclude that

$$\mathbf{x}(t,j) \in \mathcal{N}_\gamma(\mathcal{D}_{r_a}(\mathcal{O}_i)), \tag{D.11}$$

for all $(t,j) \in (I_{j_1+1}, j_1 + 1)$.

Next, we show that when the control input corresponds to the *obstacle-avoidance* mode, $\mathbf{x}(t,j) \in \mathcal{N}_\gamma(\mathcal{D}_{r_a}(\mathcal{O}_i)) \cap \mathcal{P}(\mathbf{h}, \mathbf{a})$ for all $(t,j) \in (I_{j_1+1}, j_1 + 1)$. When the control input corresponds to the *obstacle-avoidance* mode, it is given by $\mathbf{u}(\xi) = \kappa_r \mathbf{v}(\mathbf{x}, \mathbf{a})$, which, as per (5.6), can be expressed as a linear combination of the vectors $\mathbf{P}(\mathbf{a})\mathbf{x}_\pi$ and $\mathbf{R}(\mathbf{a})\mathbf{P}(\mathbf{a})\mathbf{x}_\pi$. Since $\mathbf{P}(\mathbf{a})$, defined in (5.7), is an orthogonal projection operator and $\mathbf{0} \in \mathcal{P}(\mathbf{h}, \mathbf{a})$, for all $\mathbf{x} \in \mathcal{N}_\gamma(\mathcal{D}_{r_a}(\mathcal{O}_i)) \cap \mathcal{P}(\mathbf{h}, \mathbf{a})$, one has $\mathbf{P}(\mathbf{a})\mathbf{x}_\pi \in \mathcal{P}(\mathbf{h}, \mathbf{a})$. Additionally, one can show that $\mathbf{R}(\mathbf{a})\mathbf{P}(\mathbf{a})\mathbf{x}_\pi \in \mathcal{P}(\mathbf{h}, \mathbf{a})$. Therefore, for all $\mathbf{x} \in \mathcal{N}_\gamma(\mathcal{D}_{r_a}(\mathcal{O}_i)) \cap \mathcal{P}(\mathbf{h}, \mathbf{a})$, one has $\mathbf{v}(\mathbf{x}, \mathbf{a}) \in \mathcal{P}(\mathbf{h}, \mathbf{a})$. As a result, since $\mathbf{x}(t_1, j_1 + 1) \in \mathcal{N}_\gamma(\mathcal{D}_{r_a}(\mathcal{O}_i)) \cap \mathcal{P}(\mathbf{h}, \mathbf{a})$, using (D.11), one can conclude that

$$\mathbf{x}(t,j) \in \mathcal{N}_\gamma(\mathcal{D}_{r_a}(\mathcal{O}_i)) \cap \mathcal{P}(\mathbf{h}, \mathbf{a}),$$

for all $(t,j) \in (I_{j_1+1}, j_1 + 1)$ and claim 1 in Lemma D.1 is satisfied.

Next, we proceed to prove claim 2 in Lemma D.1 which states that when $\xi(t_1, j_1+1) \in \mathcal{F}_1$ for some $(t_1, j_1 + 1) \in$ dom ξ, the control input steers the state ξ to the jump set $\mathcal{J}_1$ of the *obstacle-avoidance* mode in finite time $(t_2, j_1 + 1) \succ (t_1, j_1 + 1)$ with $t_2 < \infty$.

Let us define the set $\mathcal{O}_i^\mathcal{S} = \mathcal{D}_{r_a}(\mathcal{O}_i) \cap \mathcal{P}(\mathbf{h}, \mathbf{a})$, as shown in Fig. D.1. Since obstacle $\mathcal{O}_i$ is convex, the set $\mathcal{O}_i^\mathcal{S}$ is also convex. As a result, the target location has a unique closest point on the set $\mathcal{O}_i^\mathcal{S}$, represented by $\Pi(\mathbf{0}, \mathcal{O}_i^\mathcal{S})$. Let us define the set $\mathcal{LS} := \mathcal{L}_s(\mathbf{0}, \Pi(\mathbf{0}, \mathcal{O}_i^\mathcal{S})) \cap \mathcal{N}_\gamma(\mathcal{D}_{r_a}(\mathcal{O}_i))$. According to Remark 5.3, one has $\mathbf{0} \notin \mathcal{D}_{r_a+\gamma}(\mathcal{O}_i)$. Therefore, it is clear that $\mathcal{LS} \cap \partial\mathcal{D}_{r_a+\beta}(\mathcal{O}_i) \neq \emptyset$ for all $\beta \in [0, \gamma]$. Since $\mathbf{0} \in \mathcal{P}(\mathbf{h}, \mathbf{a})$, the line segment $\mathcal{LS}$ belongs to the plane $\mathcal{P}(\mathbf{h}, \mathbf{a})$. Since $\mathcal{LS} \cap \mathcal{D}_{r_a}^\circ(\mathcal{O}_i) = \emptyset$, the line segment $\mathcal{LS}$ also belongs to the *exit* region $\mathcal{R}_e$ (5.11). Since the *hit point* $\mathbf{h}$ belongs to $\mathcal{R}_l^i$, the target location $\mathbf{0}$ is closer to the location $\Pi(\mathbf{0}, \mathcal{O}_i^\mathcal{S})$ than to the *hit point* $\mathbf{h}$. Hence, for a sufficiently small value of $\bar{\epsilon}$, used in (4.22), one can ensure that the set $\mathcal{LS}$ belongs to the set $\mathcal{J}_1^\mathcal{W}$ (5.15).

Now, if one ensures that the state $\mathbf{x}$, which belongs to the set $\mathcal{N}_\gamma(\mathcal{D}_{r_a}(\mathcal{O}_i)) \cap \mathcal{P}(\mathbf{h}, \mathbf{a})$ after time (t_1, j_1), in the *obstacle-avoidance* mode around obstacle $\mathcal{O}_i$, eventually intersects the set $\mathcal{LS}$ at some finite time $(t_2, j_1 + 1) \succ (t_1, j_1 + 1)$, then it will imply that

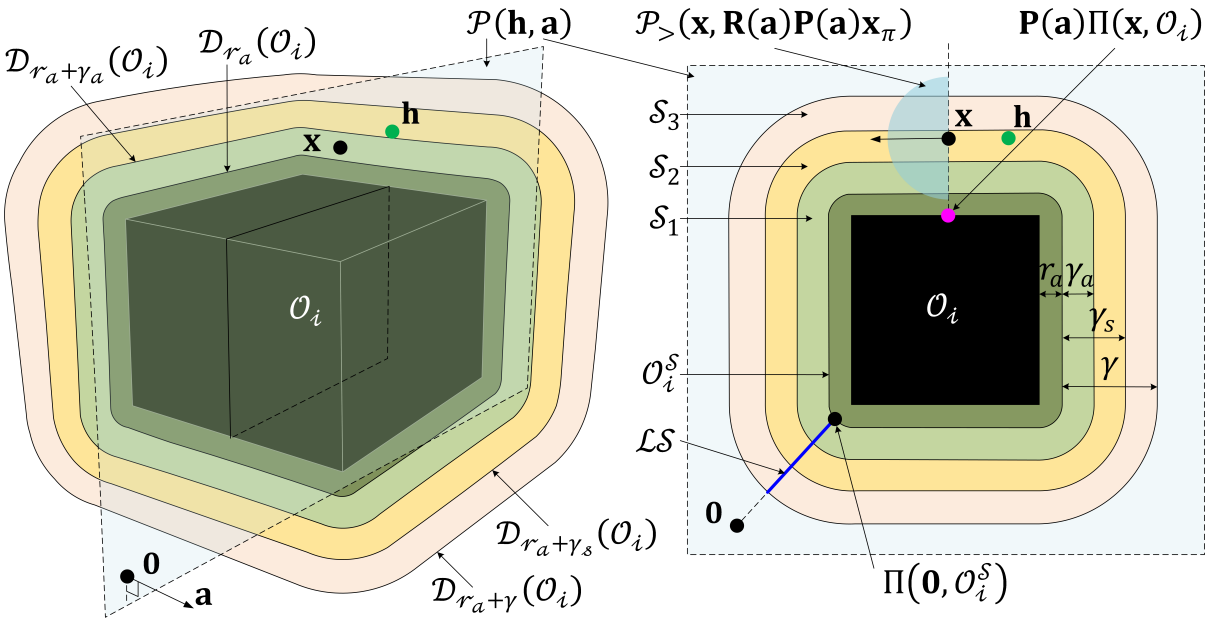

Figure D.1: The partition of the set $\mathcal{N}_\gamma(\mathcal{D}_{r_a}(\mathcal{O}_i)) \cap \mathcal{P}(\mathbf{h},\mathbf{a})$.

$\xi(t_2, j_1+1) \in \mathcal{J}_1$, and claim 2 in Lemma D.1 will be proven. To that end, let us divide the set $\mathcal{N}_\gamma(\mathcal{D}_{r_a}(\mathcal{O}_i)) \cap \mathcal{P}(\mathbf{h},\mathbf{a})$, as shown in Fig. D.1, into 3 separate subsets as follows:

$$\mathcal{N}_\gamma(\mathcal{D}_{r_a}(\mathcal{O}_i)) \cap \mathcal{P}(\mathbf{h},\mathbf{a}) = \mathcal{S}_1 \cup \mathcal{S}_2 \cup \mathcal{S}_3, \tag{D.12}$$

where the sets $\mathcal{S}_1, \mathcal{S}_2$ and $\mathcal{S}_3$ are defined as follows:

$$\begin{aligned} \mathcal{S}_1 &= \mathcal{N}_{\gamma_a}(\mathcal{D}_{r_a}(\mathcal{O}_i)) \cap \mathcal{P}(\mathbf{h},\mathbf{a}), \\ \mathcal{S}_2 &= \mathcal{N}^\circ_{\gamma_s-\gamma_a}(\mathcal{D}_{r_a+\gamma_a}(\mathcal{O}_i)) \cap \mathcal{P}(\mathbf{h},\mathbf{a}), \\ \mathcal{S}_3 &= \mathcal{N}_{\gamma-\gamma_s}(\mathcal{D}_{r_a+\gamma_s}(\mathcal{O}_i)) \cap \mathcal{P}(\mathbf{h},\mathbf{a}), \end{aligned} \tag{D.13}$$

where $0 < \gamma_a < \gamma_s < \gamma$.

We show that when the control input corresponds to the *obstacle-avoidance* mode and the state $\mathbf{x}$ belongs either in the set $\mathcal{S}_1$ or in the set $\mathcal{S}_3$, the control eventually steers the state $\mathbf{x}$ to the set $\mathcal{S}_2$. Then, we show that for all $\mathbf{x} \in \mathcal{S}_2$, the control vector $\mathbf{u}(\xi)$ belongs to the open positive half-space $\mathcal{P}_>(\mathbf{0}, \mathbf{R}(\mathbf{a})\mathbf{P}(\mathbf{a})\mathbf{x}_\pi)$. This implies that the state $\mathbf{x}$, which belongs to the set $\mathcal{N}_\gamma(\mathcal{D}_{r_a}(\mathcal{O}_i)) \cap \mathcal{P}(\mathbf{h},\mathbf{a})$ after time (t_1, j_1), in the *obstacle-avoidance* mode around obstacle $\mathcal{O}_i$, is always steered to the open positive half-space $\mathcal{P}_>(\mathbf{0}, \mathbf{R}(\mathbf{a})\mathbf{P}(\mathbf{a})\mathbf{x}_\pi)$ and will eventually reach the set $\mathcal{LS}$ at some finite time $(t_2, j_1+1) \succ (t_1, j_1+1)$.

First, we show that when the control input corresponds to the *obstacle-avoidance* mode and the state $\mathbf{x}$ is either in the set $\mathcal{S}_1$ or in the set $\mathcal{S}_3$, the control will eventually steer the state $\mathbf{x}$ to the set $\mathcal{S}_2$.

When the control input corresponds to the *obstacle-avoidance* mode and $\mathbf{x}$ belongs to the set $\mathcal{S}_1$, the control vector $\mathbf{u}(\xi)$ in (5.5a) becomes

$$\mathbf{u}(\xi) = \kappa_r \mathbf{P}(\mathbf{a})\mathbf{x}_\pi, \kappa_r > 0. \tag{D.14}$$

Let $\mathbf{x} \in \partial\mathcal{D}_{r_a+\beta}(\mathcal{O}_i) \cap \mathcal{S}_1$ for some $\beta \in [0, \gamma_a]$. We know that for $\mathbf{x} \in \partial\mathcal{D}_{r_a+\beta}(\mathcal{O}_i) \cap \mathcal{S}_1$, the tangent cone to the set $\mathcal{N}_{\gamma-\beta}(\mathcal{D}_{r_a+\beta}(\mathcal{O}_i))$ at $\mathbf{x}$ is given by

$$\mathbf{T}_{\mathcal{N}_{\gamma-\beta}(\mathcal{D}_{r_a+\beta}(\mathcal{O}_i))}(\mathbf{x}) = \mathcal{P}_{\geq}(\mathbf{0}, \mathbf{x}_\pi).$$

If we show that for all $\mathbf{x} \in \partial\mathcal{D}_{r_a+\beta}(\mathcal{O}_i) \cap \mathcal{S}_1$, one has $\mathbf{x}_\pi \mathbf{P}(\mathbf{a})\mathbf{x}_\pi > 0$, then it implies that the control input vector (D.14) steers $\mathbf{x}$ to the interior of the set $\mathcal{N}_{\gamma-\beta}(\mathcal{D}_{r_a+\beta}(\mathcal{O}_i))$. This, combined with the fact that $\mathbf{x}(t, j) \in \mathcal{P}(\mathbf{h}, \mathbf{a})$, for all $(t, j) \in (I_{j_1+1} \times j_1 + 1)$, as per claim 1 in Lemma D.1, ensures that the control input vector (D.14) steers $\mathbf{x}$ to the interior of the set $(\mathcal{S}_1 \cup \mathcal{S}_2) \setminus \mathcal{D}^\circ_{r_a+\beta}(\mathcal{O}_i)$ and eventually $\mathbf{x}$ will enter in the set $\mathcal{S}_2$. To proceed with the proof we require the following fact:

Fact 1: Let us consider a hyperplane $\mathcal{P}(\mathbf{p}, \mathbf{q})$, where $\mathbf{p} \in \mathcal{J}_0^{\mathcal{W}} \cap \mathcal{N}_\gamma(\mathcal{D}_{r_a}(\mathcal{O}_i))$, for some $i \in \mathbb{I}$ and $\mathbf{q} = \mathbf{A}(\mathbf{p})$, where the mapping $\mathbf{A}$ is defined in (5.22). Then, for all $\mathbf{x} \in \mathcal{N}_\gamma(\mathcal{D}_{r_a}(\mathcal{O}_i)) \cap \mathcal{P}(\mathbf{p}, \mathbf{q})$, one has $\mathbf{x}_\pi^\top \mathbf{P}(\mathbf{q})\mathbf{x}_\pi > 0$.

Proof This proof is by contradiction. First, note that for any vector $\mathbf{s} \in \mathbb{R}^3$, one has $\mathbf{s}^\top \mathbf{P}(\mathbf{q})\mathbf{s} \geq 0$. Let us assume that there exists $\mathbf{x} \in \mathcal{N}_\gamma(\mathcal{D}_{r_a}(\mathcal{O}_i)) \cap \mathcal{P}(\mathbf{p}, \mathbf{q})$ such that $\mathbf{x}_\pi^\top \mathbf{P}(\mathbf{q})\mathbf{x}_\pi = 0$. Since $\mathbf{x}_\pi \neq \mathbf{0}$, one has $\mathbf{P}(\mathbf{q})\mathbf{x}_\pi = \mathbf{0}$. Therefore, the vector $\mathbf{x}_\pi$ is normal to the hyperplane $\mathcal{P}(\mathbf{p}, \mathbf{q})$. This implies that the plane $\mathcal{P}(\mathbf{p}, \mathbf{q})$ is a supporting hyperplane [Boyd et al., 2004, Section 2.5.2] to the convex set $\mathcal{D}_{r_a+\beta}(\mathcal{O}_i)$ at $\mathbf{x}$, where $\beta = d(\mathbf{x}, \mathcal{O}_i) - r_a \in [0, \gamma]$. Therefore, the set $\mathcal{D}^\circ_{r_a}(\mathcal{O}_i) \cap \mathcal{P}(\mathbf{p}, \mathbf{q})$ is an empty set.

However, since $\mathbf{q} = \mathbf{A}(\mathbf{p})$, according to (5.22), one has $\mathbf{p}_\pi \in \mathcal{P}(\mathbf{p}, \mathbf{q})$ and $\mathbf{0} \in \mathcal{P}(\mathbf{p}, \mathbf{q})$. Therefore, $\mathcal{L}(\mathbf{p}, \Pi(\mathbf{p}, \mathcal{O}_i)) \subset \mathcal{P}(\mathbf{p}, \mathbf{q})$. As a result, $\mathcal{L}(\mathbf{p}, \Pi(\mathbf{p}, \mathcal{O}_i)) \cap \mathcal{D}^\circ_{r_a}(\mathcal{O}_i) \neq \emptyset$. This implies that $\mathcal{D}^\circ_{r_a}(\mathcal{O}_i) \cap \mathcal{P}(\mathbf{p}, \mathbf{q}) \neq \emptyset$, which is a contradiction.

According to Fact 1, for all $\mathbf{x} \in \partial\mathcal{D}_{r_a+\beta}(\mathcal{O}_i) \cap \mathcal{S}_1$, where $\beta \in [0, \gamma_a]$, one has $\mathbf{x}_\pi^\top \mathbf{P}(\mathbf{a})\mathbf{x}_\pi > 0$. Therefore, as discussed earlier, the control input vector (D.14) steers $\mathbf{x}$ to the interior of the set $(\mathcal{S}_1 \cup \mathcal{S}_2) \setminus \mathcal{D}^\circ_{r_a+\beta}(\mathcal{O}_i)$ and eventually $\mathbf{x}$ will enter in the set $\mathcal{S}_2$.

Similarly, when the control input corresponds to the *obstacle-avoidance* mode and $\mathbf{x}$ belongs to the set $\mathcal{S}_3$, the control vector $\mathbf{u}(\xi)$ in (5.5a) is given by

$$\mathbf{u}(\xi) = -\kappa_r \mathbf{P}(\mathbf{a})\mathbf{x}_\pi, \kappa_r > 0. \tag{D.15}$$

Let $\mathbf{x} \in \partial\mathcal{D}_{r_a+\beta}(\mathcal{O}_i) \cap \mathcal{S}_3$ for some $\beta \in [\gamma_s, \gamma]$. We know that for $\mathbf{x} \in \partial\mathcal{D}_{r_a+\beta}(\mathcal{O}_i) \cap \mathcal{S}_3$, the tangent cone to the set $\mathcal{D}_{r_a+\beta}(\mathcal{O}_i)$ at $\mathbf{x}$ is given by

$$\mathbf{T}_{\mathcal{D}_{r_a+\beta}(\mathcal{O}_i)}(\mathbf{x}) = \mathcal{P}_{\leq}(\mathbf{0}, \mathbf{x}_\pi).$$

According to Fact 1, for all $\mathbf{x} \in \partial\mathcal{D}_{r_a+\beta}(\mathcal{O}_i) \cap \mathcal{S}_3$, where $\beta \in [\gamma_s, \gamma]$, one has $\mathbf{x}_\pi^\top \mathbf{P}(\mathbf{a})\mathbf{x}_\pi > 0$. This implies that the control input vector (D.15) steers $\mathbf{x}$ to the interior of the set $\mathcal{D}_{r_a+\beta}(\mathcal{O}_i)$. This, combined with the fact that $\mathbf{x}(t, j) \in \mathcal{P}(\mathbf{h}, \mathbf{a})$, for all $(t, j) \in (I_{j_1+1} \times j_1 + 1)$, as per claim 1 in Lemma D.1, ensures that the control input vector (D.15) steers $\mathbf{x}$ to the interior of the set $(\mathcal{S}_3 \cup \mathcal{S}_2) \cap \mathcal{D}^\circ_{r_a+\beta}(\mathcal{O}_i)$ and eventually $\mathbf{x}$ will enter in the set $\mathcal{S}_2$.

Finally, we show that when the control input corresponds to the *obstacle-avoidance* mode and the state $\mathbf{x}$ belongs to the set $\mathcal{S}_2$, the control vector $\mathbf{u}(\xi)$ belongs to the open

positive half-space $\mathcal{P}_{>}(\mathbf{0}, \mathbf{R}(\mathbf{a})\mathbf{P}(\mathbf{a})\mathbf{x}_\pi)$. When the control law operates in the *obstacle-avoidance* mode and the state $\mathbf{x} \in \mathcal{S}_2$, according to (5.5), one has $\mathbf{u}(\xi) = \kappa_r \mathbf{v}(\mathbf{x}, \mathbf{a}), \kappa_r > 0$. Note that for all $\mathbf{x} \in \mathcal{S}_2$, one has $\eta(\mathbf{x}) \in (-1, 1)$. Therefore, for every $\mathbf{x} \in \mathcal{S}_2$, the vector $\mathbf{v}(\mathbf{x}, \mathbf{a})$ can be expressed as a linear combination of the vectors $\mathbf{P}(\mathbf{a})\mathbf{x}_\pi$ and $\mathbf{R}(\mathbf{a})\mathbf{P}(\mathbf{a})\mathbf{x}_\pi$ given by

$$\mathbf{v}(\mathbf{x}, \mathbf{a}) = k_1 \mathbf{P}(\mathbf{a})\mathbf{x}_\pi + k_2 \mathbf{R}(\mathbf{a})\mathbf{P}(\mathbf{a})\mathbf{x}_\pi, \tag{D.16}$$

where $k_1 \in \mathbb{R}$ and $k_2 > 0$. Additionally, according to Fact 1, for all $\mathbf{x} \in \mathcal{S}_2$, one has $\mathbf{P}(\mathbf{a})\mathbf{x}_\pi \neq \mathbf{0}$. As a result, it can be confirmed that $\mathbf{v}(\mathbf{x}, \mathbf{a})^\intercal \mathbf{R}(\mathbf{a})\mathbf{P}(\mathbf{a})\mathbf{x}_\pi > 0$, when the state $\mathbf{x}$ belongs to the set $\mathcal{S}_2$, and the proof is complete.

D.5 Proof of Theorem 5.2

Forward invariance (Safety): Note that, according to Lemma 5.4, the hybrid closed-loop system (5.29) satisfies the hybrid basic conditions. Furthermore, the modified control input vector $\mathbf{u}_s(\xi)$, as defined in (5.28), is obtained by replacing the avoidance control vector $\mathbf{v}(\mathbf{x}, \mathbf{a})$ (5.6) with $\mathbf{v}_s(\mathbf{x}, \mathbf{a})$ (5.27) in (5.5a). Hence, demonstrating that the hybrid closed-loop system (5.29) satisfies the viability condition, as mentioned in (D.2), for $m = 1$, allows one to employ similar arguments from the proof of Lemma 5.3 to establish the forward invariance of the set $\mathcal{K}$ for the hybrid closed-loop system (5.25). In other words, we want to show that for all $\xi \in \mathcal{F}_1 \setminus \mathcal{J}_1$

$$\mathbf{F}_s(\xi) \cap \mathbf{T}_{\mathcal{F}_1}(\xi) \neq \emptyset. \tag{D.17}$$

For all $\xi \in \mathcal{K}$ such that $\mathbf{x} \in (\mathcal{F}_1^{\mathcal{W}})^\circ \setminus \mathcal{J}_1$ and $m = 1$, the tangent cone $\mathbf{T}_{\mathcal{F}_1}(\xi) = \mathbb{R}^3 \times \mathbf{T}_{\mathcal{W}_{r_a}}(\mathbf{h}) \times \mathcal{P}(\mathbf{0}, \mathbf{a}) \times \{0\} \times \mathbf{T}_{\mathbb{R}_{\geq 0}}(s)$, where the sets $\mathbf{T}_{\mathcal{W}_{r_a}}(\mathbf{h})$ and $\mathbf{T}_{\mathbb{R}_{\geq 0}}(s)$ are defined in (D.3) and (D.4), respectively. Since, according to (5.29), $\dot{\mathbf{h}} = \mathbf{0} \in \mathbf{T}_{\mathcal{W}_{r_a}}(\mathbf{h})$, $\dot{s} = 1 \in \mathbf{T}_{\mathbb{R}_{\geq 0}}(s)$ and $\dot{\mathbf{a}} = \mathbf{0} \in \mathcal{P}(\mathbf{0}, \mathbf{a})$, the viability condition in (D.17) holds true for all $\xi \in \mathcal{K}$ such that $\mathbf{x} \in (\mathcal{F}_1^{\mathcal{W}})^\circ \setminus \mathcal{J}_1$ and $m = 1$.

Finally, for all $\xi \in \mathcal{K}$ such that $\mathbf{x} \in \partial\mathcal{F}_1 \setminus \mathcal{J}_1$ and $m = 1$, the tangent cone $\mathbf{T}_{\mathcal{F}_1}(\xi)$ is given by

$$\mathbf{T}_{\mathcal{F}}(\xi) = \mathcal{P}_{\geq}(\mathbf{0}, \mathbf{x}_\pi) \times \mathbf{T}_{\mathcal{W}_{r_a}}(\mathbf{h}) \times \mathcal{P}(\mathbf{0}, \mathbf{a}) \times \{0\} \times \mathbf{T}_{\mathbb{R}_{\geq 0}}(s), \tag{D.18}$$

where the sets $\mathbf{T}_{\mathcal{W}_{r_a}}(\mathbf{h})$ and $\mathbf{T}_{\mathbb{R}_{\geq 0}}(s)$ are defined in (D.3) and (D.4), respectively. According to (5.28), for $m = 1$, $\mathbf{u}_s(\xi) = \kappa_r \mathbf{R}(\mathbf{a})\mathbf{P}(\mathbf{a})\mathbf{x}_\pi, \kappa_r > 0$. Note that, for all $\mathbf{x} \in \mathcal{N}_\gamma(\mathcal{D}_{r_a}(\mathcal{O}_i))$, for each $i \in \mathbb{I} \setminus \{0\}$, one has $\mathbf{x}_\pi \in \mathcal{P}(\mathbf{0}, \mathbf{R}(\mathbf{a})\mathbf{P}(\mathbf{a})\mathbf{x}_\pi)$, where $\mathbf{a} \in \mathbb{S}^2$, and consequently $\mathbf{u}_s(\xi)^\top \mathbf{x}_\pi = 0$. Additionally, according to (5.29), $\dot{\mathbf{h}} = \mathbf{0} \in \mathbf{T}_{\mathcal{W}_{r_a}}(\mathbf{h})$, $\dot{s} = 1 \in \mathbf{T}_{\mathbb{R}_{\geq 0}}(s)$ and $\dot{\mathbf{a}} = \mathbf{0} \in \mathcal{P}(\mathbf{0}, \mathbf{a})$. Hence, the viability condition in (D.17) holds true for all $\xi \in \mathcal{K}$ such that $\mathbf{x} \in \partial\mathcal{F}_1 \setminus \mathcal{J}_1$ and $m = 1$, and as such it holds true for all $\xi \in \mathcal{F}_1 \setminus \mathcal{J}_1$.

Stability: When the mode indicator variable $m = 0$, one has $\mathbf{u}_s(\xi) = \mathbf{u}(\xi) = -\kappa_s \mathbf{x}, \kappa_s > 0$. Additionally, the target location at the origin $\mathbf{0}$ belongs to $\mathcal{W}_{r_a}^\circ$, and the definitions of the flow set $\mathcal{F}$ and the jump set $\mathcal{J}$ are the same for (5.25) and (5.29). Hence, one can use similar arguments from the proof of Theorem 5.1 to prove the stability of the target set $\mathcal{A}$.

Attractivity: If we prove that all solutions ξ to the hybrid closed-loop system (5.29) satisfy Lemma D.1, then one can use arguments similar to the ones in the proof of Theorem 5.1 to prove the attractivity of the target set $\mathcal{A}$ from any point in $\mathcal{K}$ for the hybrid closed-loop system (5.29). Consequently, we proceed to prove that every solution ξ to the hybrid closed-loop system (5.29) satisfies Lemma D.1.

Since $\xi(t_1, j_1) \in \mathcal{J}_0$, one has $\mathbf{h} \in \mathcal{J}_0^{\mathcal{W}} \cap \partial\mathcal{D}_{r_a+\beta}(\mathcal{O}_i)$ for some $i \in \mathbb{I} \setminus \{0\}$ and $\beta \in [0, \gamma]$, where $\mathbf{h} = \mathbf{h}(t_1, j_1 + 1) = \mathbf{h}(t, j)$ for all $(t, j) \in (I_{j_1+1} \times j_1 + 1)$. First, we show that $\mathbf{x}(t, j) \in \mathcal{N}_\gamma(\mathcal{D}_{r_a}(\mathcal{O}_i))$ for all $(t, j) \in (I_{j_1+1} \times j_1 + 1)$. For all $\mathbf{x} \in \partial\mathcal{D}_{r_a+\beta}(\mathcal{O}_i)$, the tangent cone to the set $\partial\mathcal{D}_{r_a+\beta}(\mathcal{O}_i)$ at $\mathbf{x}$ is given by

$$\mathbf{T}_{\partial\mathcal{D}_{r_a+\beta}(\mathcal{O}_i)}(\mathbf{x}) = \mathcal{P}(\mathbf{0}, \mathbf{x}_\pi), \tag{D.19}$$

where $\mathbf{x}_\pi = \mathbf{x} - \Pi(\mathbf{x}, \mathcal{O}_\mathcal{W})$. When the control input vector (5.28) corresponds to the *obstacle-avoidance* mode, for all $\mathbf{x} \in \partial\mathcal{D}_{r_a+\beta}(\mathcal{O}_i)$, it is given by $\mathbf{u}_s(\xi) = \kappa_r \mathbf{v}_s(\mathbf{x}, \mathbf{a})$, where $\kappa_r > 0$ and $\mathbf{a} = \mathbf{a}(t_1, j_1+1) = \mathbf{a}(t, j)$ for all $(t, j) \in (I_{j_1+1} \times j_1 + 1)$. Now, using (5.27), one can conclude that for all $\mathbf{x} \in \partial\mathcal{D}_{r_a+\beta}(\mathcal{O}_i)$, $\mathbf{v}_s(\mathbf{x}, \mathbf{a})^\top \mathbf{x}_\pi = 0$ and $\mathbf{u}_s(\xi) \in \mathbf{T}_{\partial\mathcal{D}_{r_a+\beta}(\mathcal{O}_i)}(\mathbf{x})$. Additionally, as per Lemma 5.4, the control input trajectory $\mathbf{u}(\xi(t, j))$ is continuous when it corresponds to the *obstacle-avoidance* mode. Therefore, using Nagumo's theorem [Blanchini et al., 2008, Theorem 4.7], one can conclude that for all $(t, j) \in (I_{j_1+1} \times j_1 + 1)$

$$\mathbf{x}(t, j) \in \partial\mathcal{D}_{r_a+\beta}(\mathcal{O}_i), \tag{D.20}$$

where $\beta \in [0, \gamma]$. Therefore, $\mathbf{x}(t, j) \in \mathcal{N}_\gamma(\mathcal{D}_{r_a}(\mathcal{O}_i))$ for all $(t, j) \in (I_{j_1+1} \times j_1 + 1)$.

Next, we show that $\mathbf{x}(t, j) \in \mathcal{N}_\gamma(\mathcal{D}_{r_a}(\mathcal{O}_i)) \cap \mathcal{P}(\mathbf{h}, \mathbf{a})$ for all $(t, j) \in (I_{j_1+1} \times j_1 + 1)$. Since $\mathbf{a} = \mathbf{A}(\mathbf{h})$ and obstacle $\mathcal{O}_i$ is a sphere, the hyperplane $\mathcal{P}(\mathbf{h}, \mathbf{a})$ passes through the origin and the center $\mathbf{c}_i$ of obstacle $\mathcal{O}_i$. As a result, for all $\mathbf{x} \in \mathcal{N}_\gamma(\mathcal{D}_{r_a}(\mathcal{O}_i)) \cap \mathcal{P}(\mathbf{h}, \mathbf{a})$, one has $\mathbf{x}_\pi \in \mathcal{P}(\mathbf{h}, \mathbf{a})$. Now, when the control input vector corresponds to the *obstacle-avoidance* mode, it is given by $\mathbf{u}_s(\xi) = \kappa_r \mathbf{v}_s(\mathbf{x}, \mathbf{a})$, where $\kappa_r > 0$. According to (5.27), it is clear that for all $\mathbf{x} \in \mathcal{N}_\gamma(\mathcal{D}_{r_a}(\mathcal{O}_i)) \cap \mathcal{P}(\mathbf{h}, \mathbf{a})$, $\mathbf{v}_s(\mathbf{x}, \mathbf{a}) \in \mathcal{P}(\mathbf{h}, \mathbf{a})$. As a result, since $\mathbf{x}(t_1, j_1 + 1) \in \mathcal{N}_\gamma(\mathcal{D}_{r_a}(\mathcal{O}_i)) \cap \mathcal{P}(\mathbf{h}, \mathbf{a})$, using (D.20), one can conclude that

$$\mathbf{x}(t, j) \in \mathcal{N}_\gamma(\mathcal{D}_{r_a}(\mathcal{O}_i)) \cap \mathcal{P}(\mathbf{h}, \mathbf{a}), \tag{D.21}$$

for all $(t, j) \in (i_{j_1+1} \times j_1 + 1)$ and claim 1 in Lemma D.1 is satisfied.

We proceed to prove claim 2 in Lemma D.1. We know that $\mathbf{h} \in \partial\mathcal{D}_{r_a+\beta}(\mathcal{O}_i)$ for some $i \in \mathbb{I} \setminus \{0\}$ and $\beta \in [0, \gamma]$. Additionally, according to (D.20) and (D.21), it is clear that for all $(t, j) \in (I_{j_1+1} \times j_1 + 1)$, $\mathbf{x}(t, j) \in \partial\mathcal{D}_{r_a+\beta}(\mathcal{O}_i) \cap \mathcal{P}(\mathbf{h}, \mathbf{a})$, where $\mathbf{a} = \mathbf{A}(\mathbf{h})$. Moreover, for all $(t, j) \in (I_{j_1+1} \times j_1 + 1)$, one has $\mathbf{u}_s(\xi(t, j)) \in \mathcal{P}_>(\mathbf{0}, \mathbf{R}(\mathbf{a})\mathbf{x}_\pi)$, where $\mathbf{u}_s(\xi(t, j)) = \kappa_r \mathbf{v}_s(\mathbf{x}(t, j), \mathbf{a}), \kappa_r > 0$. Therefore, since obstacle $\mathcal{O}_i$ is compact, there exists $t_2 < \infty$ and $t_2 > t_1$ such that $\mathbf{x}(t_2, j_1 + 1) = \Pi(\mathbf{0}, \partial\mathcal{D}_{r_a+\beta}(\mathcal{O}_i))$. Notice that $\Pi(\mathbf{0}, \partial\mathcal{D}_{r_a+\beta}(\mathcal{O}_i)) \in \mathcal{R}_e$ and $d(\mathbf{0}, \Pi(\mathbf{0}, \partial\mathcal{D}_{r_a+\beta}(\mathcal{O}_i))) < d(\mathbf{0}, \mathbf{h})$. Hence, for a sufficiently small value of $\bar{\epsilon}$, used in (5.16), one can ensure that $\mathbf{x}(t_2, j_1 + 1)$, which equals to $\Pi(\mathbf{0}, \partial\mathcal{D}_{r_a+\beta}(\mathcal{O}_i))$, belongs to the set $\mathcal{J}_1^{\mathcal{W}}$. This, according to (5.15) and (5.18), implies that there exists $t_2 \in I_{j_1+1}$ such that $t_2 < \infty$ and $\xi(t_2, j_1 + 1) \in \mathcal{J}_1$, and claim 2 in Lemma D.1 holds true.

Monotonic decrease of the distance $\|\mathbf{x}\|$: Monotonic decrease of $\|\mathbf{x}\|$ is trivial in the *move-to-target* mode, thus, we focus on proving the monotonic decrease in the *obstacle-avoidance* mode.

Consider a solution ξ to the hybrid closed-loop system (5.29). Let us assume that there exists $(t_1, j_1) \in \text{dom}\, \xi$ such that $\xi(t_1, j_1) \in \mathcal{J}_0$. Therefore, according to (5.14), (5.12) and (5.20), one has $\mathbf{h}(t_1, j_1 + 1) \in \mathcal{J}_0^{\mathcal{W}} \cap \partial\mathcal{D}_{r_a+\beta}(\mathcal{O}_i)$, for some $i \in \mathbb{I} \setminus \{0\}$ and $\beta \in [0, \gamma_s]$, and $\mathbf{a}(t_1, j_1 + 1) = \mathbf{A}(\mathbf{h}(t_1, j_1 + 1))$. Let $\mathbf{h} = \mathbf{h}(t_1, j_1 + 1) = \mathbf{h}(t, j)$ and $\mathbf{a} = \mathbf{a}(t_1, j_1 + 1) = \mathbf{a}(t, j)$ for all $(t, j) \in (I_{j_1+1} \times j_1 + 1)$. Consequently, according to Lemma D.1 and (D.20), under the control input $\mathbf{u}_s(\xi(t, j))$, the state $\mathbf{x}(t, j)$ belongs to the set $\partial\mathcal{D}_{r_a+\beta}(\mathcal{O}_i) \cap \mathcal{P}(\mathbf{h}, \mathbf{a})$ for all $(t, j) \in (I_{j_1+1} \times j_1 + 1)$. Moreover, $\xi(t_2, j_1 + 1) \in \mathcal{J}_1$, where $t_2 = \sup_{t \in I_{j_1+1}} t$. If one shows that for all $(t, j) \in ([t_1, t_2] \times j_1 + 1)$, $\mathbf{u}_s(\xi(t, j))^\top \mathbf{x}(t, j) \leq 0$, then it will imply that the control input vector $\mathbf{u}_s(\xi(t, j))$ guarantees a monotonic decrease of the distance $\|\mathbf{x}\|$ as the solution $\xi(t, j_1 + 1)$ flows during the interval I_{j_1+1}.
Let us divide the set $\partial\mathcal{D}_{r_a+\beta}(\mathcal{O}_i) \cap \mathcal{P}(\mathbf{h}, \mathbf{a})$ into two mutually exclusive subsets as follows:

$$\partial\mathcal{D}_{r_a+\beta}(\mathcal{O}_i) \cap \mathcal{P}(\mathbf{h}, \mathbf{a}) = \mathcal{U}_1 \cup \mathcal{U}_2, \tag{D.22}$$

where

$$\mathcal{U}_1 := \partial\mathcal{D}_{r_a+\beta}(\mathcal{O}_i) \cap \mathcal{P}(\mathbf{h}, \mathbf{a}) \cap \mathcal{P}_{\geq}(\mathbf{0}, \mathbf{R}(\mathbf{a})\mathbf{c}_i), \tag{D.23}$$
$$\mathcal{U}_2 := \partial\mathcal{D}_{r_a+\beta}(\mathcal{O}_i) \cap \mathcal{P}(\mathbf{h}, \mathbf{a}) \cap \mathcal{P}_{<}(\mathbf{0}, \mathbf{R}(\mathbf{a})\mathbf{c}_i), \tag{D.24}$$

with $\mathbf{c}_i$ being the center of obstacle $\mathcal{O}_i$.
Since $\mathbf{a}$ and $\mathbf{h}$ are chosen as per (5.20), and obstacle $\mathcal{O}_i$ is a sphere, the hyperplane $\mathcal{P}(\mathbf{h}, \mathbf{a})$ intersects both the center $\mathbf{c}_i$ of obstacle $\mathcal{O}_i$ and the target location at the origin. As a result, for all $\mathbf{x} \in \partial\mathcal{D}_{r_a+\beta}(\mathcal{O}_i) \cap \mathcal{P}(\mathbf{h}, \mathbf{a})$, one has $\mathbf{v}_s(\mathbf{x}, \mathbf{a}) = \mathbf{R}(\mathbf{a})\mathbf{x}_\pi$. Moreover, since obstacle $\mathcal{O}_i$ is a sphere, for all $\mathbf{x} \in \mathcal{U}_1$, one can conclude that $\mathbf{x}_\pi \in \mathcal{P}_{\geq}(\mathbf{0}, \mathbf{R}(\mathbf{a})\mathbf{x})$. Therefore, for all $\mathbf{x} \in \mathcal{U}_1$, it is true that $\mathbf{v}_s(\mathbf{x}, \mathbf{a})^\top \mathbf{x} \leq 0$. Now, if one shows that $\mathbf{x}(t, j) \in \mathcal{U}_1$, for all $(t, j) \in (I_{j_1+1} \times j_1 + 1)$, one can conclude that $\mathbf{u}_s(\xi(t, j))^\top \mathbf{x}(t, j) \leq 0$ for all $(t, j) \in (I_{j_1+1} \times j_1 + 1)$

Note that, for every $\mathbf{x}(t_1, j_1 + 1) \in \mathcal{J}_0^{\mathcal{W}} \cap \mathcal{N}_\gamma(\mathcal{D}_{r_a}(\mathcal{O}_i))$, the choice of the unit vector $\mathbf{a}$, as per (5.22), ensures that $\mathbf{x}(t_1, j_1 + 1) \in \mathcal{U}_1$. We know that, under the control input $\mathbf{u}_s(\xi(t, j))$, the state $\mathbf{x}(t, j)$ belongs to the set $\partial\mathcal{D}_{r_a+\beta}(\mathcal{O}_i) \cap \mathcal{P}(\mathbf{h}, \mathbf{a})$ for all $(t, j) \in (I_{j_1+1} \times j_1 + 1)$, where $\mathbf{h} \in \mathcal{J}_0^{\mathcal{W}} \cap \partial\mathcal{D}_{r_a+\beta}(\mathcal{O}_i)$, for some $\beta \in [0, \gamma_s]$. Since $\mathbf{x}(t_1, j_1 + 1) \in \mathcal{U}_1$ and $\mathbf{v}_s(\mathbf{x}, \mathbf{a})^\top \mathbf{x} \leq 0, \forall \mathbf{x} \in \mathcal{U}_1$, under control input $\mathbf{u}_s(\xi) = \kappa_r \mathbf{v}_s(\mathbf{x}, \mathbf{a})$, the state $\mathbf{x}$ can enter in the set $\mathcal{U}_2$ only from the location $\Pi(\mathbf{0}, \partial\mathcal{D}_{r_a+\beta}(\mathcal{O}_i))$. Therefore, there exists $(t_2, j_1 + 1) \succ (t_1, j_1 + 1)$ such that $\mathbf{x}(t_2, j_1 + 1) = \Pi(\mathbf{0}, \partial\mathcal{D}_{r_a+\beta}(\mathcal{O}_i)) \in \mathcal{U}_1$. Moreover, as proved earlier, for sufficiently small value of $\bar{\epsilon}$, used in (5.16), one can guarantee that $\Pi(\mathbf{0}, \partial\mathcal{D}_{r_a+\beta}(\mathcal{O}_i)) \in \mathcal{J}_1^{\mathcal{W}}$, where the set $\mathcal{J}_1^{\mathcal{W}}$ is defined in (5.15). Hence, at $(t_2, j_1 + 1)$, one has $\xi(t_2, j_1 + 1) \in \mathcal{J}_1$, which implies that $t_2 = \sup_{t \in I_{j_1+1}} t$. As a result, for all time $(t, j) \in (I_{j_1+1} \times j_1 + 1)$, one has $\mathbf{x}(t, j) \in \mathcal{U}_1$, and the proof is complete.